

2014-01-01

Fabrication Of A Nickel-Based Superalloy In Electron Beam Melting And Process Improvements Using Thermal Feedback From A Multi-Wavelength Pyrometer

Jonathan Minjares

University of Texas at El Paso, jminjares2@miners.utep.edu

Follow this and additional works at: https://digitalcommons.utep.edu/open_etd

 Part of the [Materials Science and Engineering Commons](#), [Mechanical Engineering Commons](#), and the [Mechanics of Materials Commons](#)

Recommended Citation

Minjares, Jonathan, "Fabrication Of A Nickel-Based Superalloy In Electron Beam Melting And Process Improvements Using Thermal Feedback From A Multi-Wavelength Pyrometer" (2014). *Open Access Theses & Dissertations*. 1300.
https://digitalcommons.utep.edu/open_etd/1300

This is brought to you for free and open access by DigitalCommons@UTEP. It has been accepted for inclusion in Open Access Theses & Dissertations by an authorized administrator of DigitalCommons@UTEP. For more information, please contact lweber@utep.edu.

FABRICATION OF A NICKEL-BASED SUPERALLOY IN ELECTRON BEAM
MELTING AND PROCESS IMPROVEMENTS USING THERMAL
FEEDBACK FROM A MULTI-WAVELENGTH PYROMETER

Jonathan Minjares, B.S.M.E
Department of Mechanical Engineering

APPROVED:

Ryan B. Wicker, Ph.D., Chair

Sara M. Gaytan, Ph.D.

Norman Love Jr., Ph.D.

Charles Ambler, Ph.D.
Dean of the Graduate School

Copyright ©

by

Jonathan Minjares

2014

This thesis is dedicated to my Father, my Mother, and my brother

FABRICATION OF A NICKEL-BASED SUPERALLOY IN ELECTRON BEAM
MELTING AND PROCESS IMPROVEMENTS USING THERMAL
FEEDBACK FROM A MULTI-WAVLENGTH PYROMETER

by

JONATHAN MINJARES, B.S.M.E.

THESIS

Presented to the Faculty of the Graduate School of
The University of Texas at El Paso
in Partial Fulfillment
of the Requirements
for the Degree of

MASTER OF SCIENCE

Department of Mechanical Engineering
THE UNIVERSITY OF TEXAS AT EL PASO

August 2014

ACKNOWLEDGMENTS

I would like to thank Dr. Ryan Wicker, director of the W.M. Keck Center for 3D Innovation, for giving me the opportunity to perform this research. Dr. Wicker has been my advisor during the last two years and has provided me with the needed motivation to complete this project. I would also thank David Espalin for his supervision and assistance during the completion of this work. I would like to express my gratitude to Jorge Mireles for introducing and training me in the additive manufacturing processes; his teachings, guidance, and support on the day to day operations provided me with the necessary tools to make this project feasible and made him one of my role models while working at the Keck Center. Important sections of this work were completed in collaboration with General Electric and I would like to thank William Carter for his valuable advice throughout the completion of this project.

Several other researches in the Keck Center deserve recognition for their various efforts. I would like to thank my co-workers: Cesar Terrazas, Philip Morton, Dr. Sara Gaytan, and Alejandro Hinojos, all of which have assisted importantly in the completion on this work. This research was possible because of their support.

I would also like to express my deepest appreciation to my family for being there when I needed them the most. Their support and love provided me with the opportunity to experience the journey of higher education and helping me realize that I am capable of reaching the things I aspire to achieve. Finally, I want to thank Joselyn for standing by my side during this venture and for making me understand that dreams do come true if one is dedicated to make them happen and puts all their energy and heart into it.

ABSTRACT

The focus of this research was to fabricate parts composed of a nickel-based superalloy containing high levels of aluminum and titanium (NSAT) by using electron beam melting (EBM) additive manufacturing (AM) technology and utilizing thermal feedback from a multi-wavelength pyrometer to perform process improvements leading to near defect-free parts. EBM is an AM technology that utilizes metal powder to fabricate parts in layer-by-layer manner. A multi-wavelength pyrometer was implemented in an Arcam S12 (Arcam AB, Sweden) EBM system to observe and record surface temperatures throughout fabrication. Temperature data from the EBM system and the multi-wavelength pyrometer were graphed using MATLAB (The MathWorks, Inc., Natick, MA) to obtain temperature feedback leading to cooling rate determination with the ultimate goal of modifying EBM build parameters to fabricate defect-free NSAT parts. Metallography of fabricated parts was performed to detect defects such as cracks and porosity.

Nickel-based superalloy materials are of special interest to aerospace and nuclear industries due to their mechanical properties that allow such alloys to withstand severe operating conditions such as high temperature and pressure. Their best properties include creep resistance, high tensile strength, and oxidation resistance (Ekrami et al, 2006). However, nickel-based superalloy materials are susceptible to surface cracking during traditional fabrication processes such as casting due to thermal stresses during solidification (Wang et al, 2011). Processing of such alloys by utilizing an advanced manufacturing method such as AM powder bed fusion technology can further help control processing, reduce time-to-market, and reduce fabrication costs. NSAT alloys are challenging to process in powder bed fusion systems due to their propensity to crack during solidification or immediately after solidification. By minimizing thermal gradients throughout the part (e.g. by using powder bed fusion that preheats powder before melting), it was hypothesized that thermal stresses would be decreased which would lead

to fabrication of parts containing reduced cracking. It was the ultimate goal of this research to determine if EBM could fabricate defect-free NSAT parts.

A main objective of this research was to fabricate parts from NSAT powder precursor using the EBM process. To achieve dense parts and continuously improve the system parameters in an effort to reduce cracking, a multi-wavelength pyrometer was externally installed atop an Arcam S12 EBM system. The multi-wavelength pyrometer is a non-contact device capable of measuring the temperature of an object without the need of knowing emissivity, or the object's surface ability to emit radiant energy (Felice, 2002). To automatically determine an emissivity, the instrument measured the target object's wavelengths to calculate a temperature whose radiance curve is compared to an ideal Planck curve. If the curve matches, the target is said to be an ideal blackbody (emissivity=1), otherwise the radiance corresponds to a non-blackbody and emissivity is automatically calculated to match a Planck curve. Since the Arcam S12 system emits X-rays, the installation of the multi-wavelength pyrometer included a radiation shield to safely protect the operator from radiation exposure. The instrument allowed the characterization of the EBM process that consisted of various steps during fabrication (e.g., heating of the start plate, raking, powder distribution, and melting).

The EBM system parameter modifications examined included beam speed, beam current, beam focus, line order, line offset, number of repetitions, and the preheat cycle (all of which affect thermal behavior during fabrication). Systematic modification of these system parameters was explored to identify parameters that significantly reduce the amount of cracking observed in fabricated parts when compared to the initial parameters. Two major modifications were found that produced a significant reduction in cracking which included utilizing unidirectional scanning and performing multiple melt cycles. It was theorized that unidirectional scanning reduces the thermal gradient between hatch lines (due to the scanning pattern that inherently reduces localized heating) and that the multiple melt cycles re-melt the forming surface which has shown to reduce defects such as porosity (Medina, 2013). The work presented here showed the strategy

for developing system parameters used, the improved parameters developed for reduction in cracking, as well as possible recommendations for future work.

TABLE OF CONTENTS

ACKNOWLEDGMENTS	v
ABSTRACT.....	vi
TABLE OF CONTENTS.....	ix
LIST OF TABLES	xi
LIST OF FIGURES	xii
CHAPTER 1 INTRODUCTION	1
1.1 Project overview	1
1.2 W.M. Keck Center for 3D Innovation	4
1.3 Additive Manufacturing.....	5
1.4 Electron Beam Melting	6
1.5 Research Motivation	7
1.7 Thesis outline	10
CHAPTER 2 LITERATURE REVIEW	11
2.1 Additive Manufacturing.....	11
2.3 Characterization of materials	13
2.2 Nickel-based superalloys	15
2.3 Thermal radiation and pyrometer fundamentals	17
2.4 Feedback methods in Additive Manufacturing.....	25
CHAPTER 3 SYSTEM.....	27
3.1 Cylindrical build tank envelope	28
3.2 Fabrication process	30
3.3 Parameter modification capabilities of the EBM system.....	32
CHAPTER 4 METHODOLOGY	40
4.1 Powder characterization.....	40
4.2 Multi-wavelength pyrometer	45
4.3 Optical metallography.....	46
4.4 Description of custom experiments	47

CHAPTER 5 THERMAL RADIATION AND PYROMETRY	54
5.1 Multi-wavelength pyrometer	54
5.2 Installation.....	55
5.3 Characterization of the EBM process using the multi-wavelength pyrometer	61
CHAPTER 6 RESULTS	67
6.1 Discussions	133
6.2 Best parameters modifications.....	133
6.3 Best Parameters.....	135
6.4 Possible Experiments	136
CHAPTER 7 CONCLUSIONS	138
7.1 Summary	138
7.2 Recommendations.....	139
REFERENCES	141
Appendix	146
CURRICULUM VITA	166

LIST OF TABLES

Table 1-1 Alloy chemistry for NSAT	10
Table 4-1 Metal powder properties.....	45
Table 6-1 Preheat theme	135
Table 6-2 Melt theme.....	136

LIST OF FIGURES

Figure 1-1 EBM system	6
Figure 2-1 Stress vs temperature curves for rupture in 1000h for select nickel-based alloys (Bradley, 1988)	16
Figure 2-2 Electromagnetic Spectrum	18
Figure 2-3 Spectral blackbody emissive power	22
Figure 3-1 Arcam S12 system.....	27
Figure 3-2 Rene 125 start plates	29
Figure 3-3 Build tank envelopes	30
Figure 3-4 illustrates the mini-vat installed in the Arcam S12.	30
Figure 3-5 Example of squares and contours of a cuboid.....	31
Figure 3-6 Focus offset parameter	33
Figure 3-7 Line offset and line order parameters.....	34
Figure 3-8 Snake parameter	35
Figure 3-9 Example of an inflection point from the thickness function	38
Figure 4-1 Gas atomization process.....	40
Figure 4-2 Metallography of NSAT metal powder.....	41
Figure 4-3 Powder distribution of NSAT metal powder	43
Figure 4-4 Powder distribution of Ti-6Al-4V metal powder.....	43
Figure 4-5 Formula for apparent density and Hall flowmeter	44
Figure 4-6 Pyrometer schematic	46
Figure 4-7 Nine cubes	47
Figure 4-8 Stainless steel mask.....	48

Figure 4-9 Thin rectangular blocks.....	49
Figure 4-10 Five hollow cylinders.....	50
Figure 4-11 Single hollow cylinder	51
Figure 4-12 Hollow cylinders with a solid cylinder	51
Figure 4-13 Single solid cylinder.....	52
Figure 4-14 Electron beam pass experiment.....	53
Figure 5-1 Schematic of the multi-wavelength pyrometer developed by FAR Associates (Felice, 2002)	55
Figure 5-2 Pyrometer and Fixture.....	56
Figure 5-3 The multi-wavelength pyrometer components.....	57
Figure 5-4 Quartz glass	58
Figure 5-5 Experiment Setup	59
Figure 5-6 Radiation shield.....	60
Figure 5-7 Experiment for comparison of surface temperature between the multi-wavelength pyrometer and the system's thermocouple.	62
Figure 5-8 Temperature graphs from the thermocouple and the multi-wavelength pyrometer....	63
Figure 5-9 Characterization of the EBM process using the multi-wavelength pyrometer; a) solid cylinder; b) Temperature graph; c) surface temperature pattern; d) characterization of the EBM process.....	65
Figure 5-10 Example of cooling rates.....	66

CHAPTER 1 INTRODUCTION

1.1 PROJECT OVERVIEW

The focus of this research was to fabricate parts composed of a nickel-based superalloy containing high levels of aluminum and titanium, which will be refer as NSAT, by using electron beam melting (EBM) additive manufacturing (AM) technology and utilizing thermal feedback from a multi-wavelength pyrometer to perform process improvements leading to defect-free parts. EBM is a technology that utilizes metal powder to fabricate parts in a layer-by-layer manner. A multi-wavelength pyrometer was externally installed atop an Arcam S12 (Arcam AB, Sweden) EBM system that allowed surface temperature measurements throughout fabrication to be obtained. Graphs of temperature data obtained were studied to determine a correlation between cooling rates and the presence of cracks observed by metallography. Microstructures of fabricated parts were analyzed to identify defects such as cracks and porosity.

The main objective of this research was to fabricate parts from NSAT powder precursor using the EBM process. Nickel-based superalloy materials are widely used in applications where the operating conditions are extreme and need to withstand high temperatures. Their best properties include creep resistance, high tensile strength, and oxidation resistance (Ekrami et al, 2006). Nickel-based superalloy materials are extensively used in the aerospace industry to manufacture components such as turbine blades. Turbine blades must resist severe conditions such as high temperature, high pressure, and stresses during operation. However, nickel-based superalloy materials are susceptible to cracking during traditional fabrication processes such as casting due to thermal stresses during solidification process (Wang et al, 2011). Processing of such alloys by utilizing an advanced manufacturing method such as AM powder bed fusion technology can further help control processing, reduce time-to-market, and reduce fabrication costs. Thus, EBM can enable fabrication of reliable parts without cracks as well as implement fabrication procedures that are cost effective and time efficient.

The first step of this research was to safely install the pyrometer on an Arcam S12 system. The multi-wavelength pyrometer is a non-contact device capable of measuring the temperature of an object without the need of knowing the emissivity, or the object's surface ability to emit radiation energy (Felice, 2002). To automatically determine an emissivity, the instrument measured the target object's wavelengths to calculate a temperature whose radiance curve is compared to an ideal Planck curve. If the curve matches, the target is said to be an ideal blackbody (emissivity=1), otherwise the radiance corresponds to a non-blackbody and emissivity is automatically calculated to match a Planck curve. Since the EBM process emits X-rays (Arcam AB, 2011) during fabrication, and the pyrometer points towards the inside of the system through a quartz window, a lead shield was designed and fabricated to prevent radiation exposure emerging from the window to the system operator. Once installed, the instrument allowed the characterization of the EBM process that consisted of various steps during fabrication (e.g., heating of the start plate, raking, powder distribution, and melting). Micrographs were analyzed to correlate the effect of the change of thermal behavior and further understand possible methods to reduce prevalent fabrication issues such as porosity and cracking.

One of the objectives of this research was to use the multi-wavelength pyrometer to compare the cooling rates using different system parameters and analyze the surface temperature effect on the presence of cracking. The pyrometer allowed the researchers to understand surface temperatures of each build and helped identify temperature decay due to raking, melting temperature of the material, and minimum and maximum temperatures during the preheat step. Temperature data were graphed using MATLAB (The MathWorks, Inc., Natick, MA) and graphs were analyzed to implement parameter changes in an effort to achieve near defect-free NSAT parts.

The system parameter modifications that were implemented for fabrication of NSAT parts by the EBM process included beam speed, beam current, beam focus, line order, line offset, number of repetitions, and the preheat cycle. Modifications of these system parameters were

achieved by using the thermal feedback from the multi-wavelength pyrometer and significantly reduced the amount of cracking of a part when compared to initial parameter development. The work presented here showed the strategy for developing system parameters used, the improved parameters for reduction in cracking obtained, as well as possible recommendations for future work.

1.2 W.M. KECK CENTER FOR 3D INNOVATION

The work for this research was performed at the W.M. Keck Center for 3D Innovation (Keck Center) located at The University of Texas at El Paso (UTEP). The laboratory was recently awarded a grant from the Texas Emerging Technology Fund (ETF), from the University of Texas System, which has allowed the expansion of the laboratory to over 13,000 square feet (Office of research and sponsored projects, 2012). The Keck Center is dedicated to advanced manufacturing technology that offers services to manufacturers, researchers, and professionals in the medical and mechanical fields.

Currently, the Keck Center has over 40 AM machines for research use. The work done at the Keck Center is focused in three main areas. The first is Engineered Structural Materials; where research is concentrated in finding ways to improve and create commonly used materials in models and prototypes by using AM machines such as fused deposition modeling, stereolithography, laser sintering, and, the main focus of this research, EBM. The next area of interest is Additive Manufacturing Technology Development where the Keck Center relies on the development and creative use of AM technologies for producing functional end-use devices (Wicker, 2012). The main focus relies on the development of new processes and systems to address the challenges faced during fabrication of parts involving multiple materials. The main emphasis for this research is to advance in the development of AM, allowing the production of more complicated components and systems, reducing both costs of fabrication machinery, energy requirements, and, environmental impacts (Wicker, 2012). The Keck Center's third research concentration is the development of 3D printed electronic devices to produce mechanical structures with embedded electronics.

Researchers in the Keck Center have various publications and patents covering AM technologies and systems. The Keck Center's researchers have access to combined facilities for advanced manufacturing; micro-dispensing; reverse engineering, metrology and inspection; materials characterization and testing; experimental fluid mechanics; and tissue engineering (Wicker, 2012).

1.3 ADDITIVE MANUFACTURING

During the first stages of development, this technology was titled Rapid Prototyping (RP) as this process allowed to build a prototype, or scale model, from digital data to test the development process and conceptual design for a specific product and provide feedback before producing the final product (Gibson *et al*, 2009). As the technology continues to develop, improvements in the fabrication process were implemented and more applications appeared that allowed for functional parts to be created. Since some of the parts manufactured by using this process were fully functional, the name of rapid prototyping was no longer representative of this technology. The layer-by-layer process technology adopted the name of Additive Manufacturing by the ASTM F42 Committee in 2009 (Wohlers, 2009).

AM processes consist of adding layers of a material to create a solid 3D object starting from a computer-aided design (CAD), whether the material is plastic, paper, wax, ceramic or powder metal (Sclater and Chironis, 2006). AM processes have an advantage in terms of part complexity over other common fabrication methods such as milling and injection molding, because AM part fabrication takes place directly from a CAD model without any tool constraints. After the model is designed in CAD, it is sliced into single layered sections and converted into digital data. This information is used by the machine's software to describe the 2D cross section of each layer and output the tool path to fabricate the part layer-by-layer. Some recent advanced applications of AM include high efficiency temperature sensors, mounting brackets for airplanes, pulleys in a mechanical assembly, and biomedical implants (Gibson *et al*, 2009).

AM technologies are categorized by the type of process and material utilized. AM processes consist of material extrusion that uses thermoplastics; material jetting that utilizes photopolymers and wax; directed energy deposition, such as laser-engineering net shaping, that uses metal alloys; powder bed fusion, for example, EBM, selective laser melting, and direct metal laser sintering (Wohlers,2013); sheet lamination manufacturing that uses metal foil or plastic films; and vat photopolymerization methods that use photopolymers such as

stereolithography (Gibson *et al*, 2010). In AM, each process has different characteristics in terms of part accuracy, material properties, post-processing time, part size, and fabrication cost (Wohlers, 2013).

1.4 ELECTRON BEAM MELTING

EBM is an AM process first commercialized by Arcam AB (Gibson et al, 2010) that uses an electron beam to melt metal powder particles ($10\mu\text{m} - 160\mu\text{m}$ in diameter) to build a dense part in a layer-by-layer manner. A schematic of EBM and its components are illustrated in **Error! Reference source not found..** The EBM system uses 60,000V to heat a tungsten filament at $2,000^\circ\text{C}$ (Arcam AB, 2011). The energy density of the electron beam is capable of reaching $106\text{kW}/\text{cm}^2$. The electrons are then accelerated to about 0.1 to 0.4 times the speed of light caused by the electric field between the filament and the anode. The electrons are focused, deflected magnetically, and travel in a vacuum chamber (10^{-4}torr) to prevent collisions with gas atoms. The electrons have kinetic energy when accelerated, which is converted to thermal energy when the electrons collide with the metal powder particles (Gibson et al, 2010). This heat melts the 2D cross section of the geometry corresponding to the CAD model at that particular

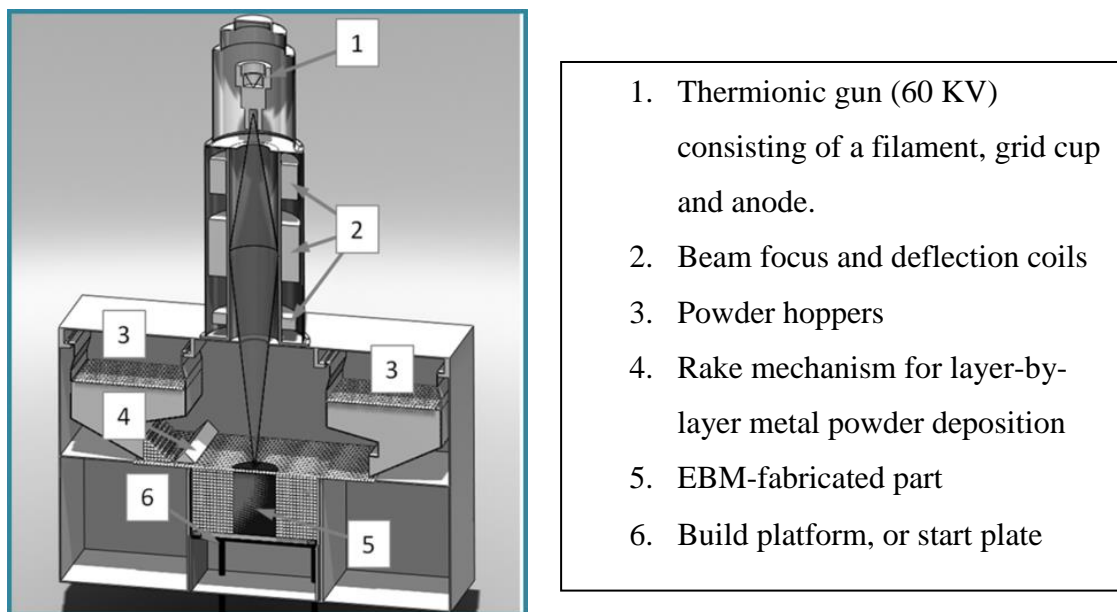


Figure 1-1 EBM system

layer.

The EBM process has several steps to fabricate a part that primarily involve raking, preheating, and melting. First, a layer of powder is deposited into the start plate by the raking mechanism. The electron beam preheats the powder to about 50% of the melting temperature of the alloy being used. The preheat step is used to sinter the powder around the part that serves as support for holding the part during the fabrication process (Cormier *et al*, 2004). Preheating helps decrease the thermal gradient between layers and throughout the overall part (Cormier *et al*, 2004). After the preheat cycle, the electron beam melts the metal powder following the 2D cross section from the CAD model. The start plate is lowered by the thickness of one layer and the steps of raking, preheating, and melting are repeated until the fabrication is complete (Cormier *et al*, 2004). Helium is purge into the vacuum chamber to accelerate the cooling process of the part. The operator can remove the part from the machine when the temperature underneath the start plate is below 100°C to avoid oxidation of the metal powder. After the part is taken out from the system it is cleaned in the powder recovery system to remove the sintered powder around the parts and recover powder to re-use for future builds. Post-processing methods such as hot isostatic pressing (HIP) can be used to decrease porosity in parts or heat treatments such as annealing to relieve internal stresses (Distefani, 1990). In order to accomplish this work, a mini-vat that was previously developed by the Keck Center was utilized which provided a maximum build envelope of 70mm in diameter by 80mm in height (Medina, 2013). This system configuration allowed for faster system set-up.

1.5 RESEARCH MOTIVATION

The EBM process is an encouraging technology to develop end use metal components in industries such as aerospace, biomedical, electrical, and automotive (Gibson *et al*, 2010). Arcam is continuously improving the technology and process by developing new machines capable of fabricating parts faster and with improved surface finish (Wohlers, 2013). Material development on this system is of significant interest since only few materials have been made commercial.

Currently, Arcam commercially offers Titanium Ti6Al4V, Titanium Ti6Al4V ELI, Titanium Grade 2, and Cobalt-Chrome- ASTM F75.

The EBM process has demonstrated that it is capable of reducing cost of titanium parts by decreasing the use of raw material and machining time when compared to other conventional methods such as casting. EBM-fabricated metal parts approach 100% density which makes its mechanical properties after fabrication comparable to its wrought counterpart. When using these metal parts in applications of cyclic stresses, porosity within parts might act as a locations for crack initiation (Wei, 2008). The main effect of not having fully dense metal parts is that mechanical properties are compromised such as fracture toughness and fatigue. Compromising these mechanical properties could cause premature failure during operating conditions (Wohlers, 2013).

Arcam completed a study using EBM-fabricated parts to characterize the properties of Ti-6Al-4V. The study indicated that EBM metal parts had equivalent properties as parts fabricated with conventional methods such as investment cast and wrought forms (Wohlers, 2013). Industries are looking to produce end-use parts using EBM technology due to the advantages of AM and the ability to build more complex geometries. Aerospace industries have become interested in nickel-based super-alloys such as NSAT for components including turbines blades. For the EBM process to be reliable in the fabrication of NSAT, the parts must not have defects such as porosity or cracks. A multi-wavelength pyrometer was implemented with the EBM system to gain sense of parameter modifications needed to fabricate solid parts with limited cracks. The multi-wavelength pyrometer was used to monitor surface temperature profiles during the EBM fabrication process.

In EBM systems, the temperature reading process includes a single thermocouple that measures the temperature below the start plate and not of the forming layer. Since this is a layer-by-layer process, the temperature readings below the start plate do not accurately represents the surface temperatures to perceive any effect on microstructure. In this project, a multi-wavelength pyrometer was externally implemented atop an Arcam S12 EBM system to monitor the surface

temperature during the fabrication process. The pyrometer allowed the characterization of the EBM process such as raking, preheat, melting, and cooling during the fabrication of the forming layer. This information is relevant when developing and improving parameters for a new material or improve its mechanical properties by further controlling the thermal environment during fabrication. In this research, the pyrometer was used to analyze temperature data to determine which system parameters produced better microstructure of EBM- fabricated NSAT parts.

1.6 Material

The need to develop superalloys that combine corrosion resistance with long-lasting mechanical strength have surged forward as a means to increase the efficiency and performance of contemporary power generation systems by allowing these to operate at higher temperatures. Nickel-based superalloys are widely used in applications where extreme operating conditions exist and the material needs to withstand high temperatures, creep, high tensile strength, and oxidation resistance (Ekrami *et al*, 2006). Such alloys are also extensively used in the aerospace industry to manufacture components for aircraft gas turbines parts such as blades, disks, rings, shafts, and many compressors and diffuser components (Bradley, 1988). Turbine blades must resist severe conditions such as thermal fatigue, oxidation, corrosion, and creep during operation (Shahsvari *et al*, 2007). Nickel-based superalloy materials are susceptible to surface cracking during traditional fabrication processes such as casting due to the thermal stress during solidification (Wang *et al*, 2011). Processing of such alloys by utilizing an advanced manufacturing method such as AM powder bed fusion technology can further help control processing, reduce time-to-market, and reduce fabrication costs.

One type of nickel-based superalloy that is operational in commercial and military jet engines is NSAT, which is a directionally solidified (with columnar grains) turbine airfoil alloy. NSAT has high strength, oxidation resistance, and lower part costs when compared to other common air-foil materials with directionally solidified single crystal characteristics (without grains) such as Rene N4, PWA 1480, and CMSX-3 (Ross and O'Hara, 1992). Table 1-1

describes the alloy chemistry of NSAT used for this project. These cracks may potentially result in a significant reduction of part's service life or capital loss (Wang *et al*, 2011).

Table 1-1 Alloy chemistry for NSAT

Alloy Chemistry												
Alloy	Ni	Co	Cr	Al	Ta	W	Re	Mo	C	Hf	B	Zr
NSAT	57.84	12	6.8	6.15	6.35	4.9	2.8	1.5	0.12	1.5	0.015	0.02

* By weight percent

1.7 THESIS OUTLINE

The following chapters provide further details of the research pursued for this thesis, including background theory, experiments, and results and conclusions. Chapter 2 covers a literature review on AM technology, material characterization, nickel-based superalloy materials, thermal radiation, pyrometry fundamentals, and a discussion on previously achieved temperature feedback methods specific to AM. Chapter 3 gives an in-depth explanation of the system used and the parameter modification capabilities of EBM. Chapter 4 describes the multi-wavelength pyrometer process and the installation of the radiation shielding setup for user safety. Chapter 5 describes in detail the design of experiments performed and the strategy to improve system parameters. Chapter 6 describes the results of the experiments performed, temperature data from the EBM system and pyrometer (where applicable), and microstructural analysis of fabricated parts. Finally, Chapter 7 is a final discussion of this project, conclusions, and recommendations.

CHAPTER 2 LITERATURE REVIEW

To understand the context of this project, a background of AM focusing on EBM technology, material characterization, and the multi-wavelength pyrometer as a monitoring method for evaluation of an object's temperature needs to be further discussed. A literature review presented in this chapter will explain current work related to EBM technology as well as current feedback methods in AM to monitor surface temperatures of layer-by-layer fabrication.

2.1 ADDITIVE MANUFACTURING

AM is a process of adding material layer upon layer to create a 3D solid object from digital data. The AM process begins from a 3D CAD model that is sliced into layers of specific thickness. Typically, a stereolithography (STL) file is derived from the CAD software and used by AM systems (Gibson *et al*, 2009). The STL file is then transferred to the machine's software and, depending on the presence of overhanging features on the part, a support structure is generated in STL format. The machine's software then outlines the path of fabrication necessary to complete manufacture.

There are different materials in AM technology, but the most widely used are polymers and metals. The first materials to appear in AM technology were polymers and for that reason there are more polymers materials than metals used in AM processes. The AM processes that use polymers are stereolithography (SL), fused deposition modeling (FDM), selective laser sintering (LS) (Wohlers, 2013). SL utilizes a photopolymer resin, or polymer that is cured when exposed to ultraviolet light. FDM uses a polymer filament that is deposited layer-by-layer using a nozzle that preheats the material to allow for layer deposition. The LS process uses a high power laser to sinter or melt material in powder form. Sintering is defined by heating without material liquefaction and it is commonly used to give support to parts in powder bed fusion systems or to minimize internal stresses on the forming layer (Gibson *et al*, 2009).

AM processes that utilize metals are primarily selective laser melting (SLM) and EBM. SLM works like LS but instead of using polymer powder it utilizes metal powder to fabricate the

parts by using a high power. LS operates in an inert gas environment of nitrogen or argon (Gibson *et al*, 2009). Instead of using a laser, EBM utilizes an electron beam for part fabrication. The electron beam is also used to selectively melt the layer of metal powder according to the 2D cross section from the CAD model. The electron beam can be used at high scan speed ($\sim 14,600\text{mm/s}$) and low power ($\sim 8.8\text{mA}$) to maintain the build platform at a certain temperature during the fabrication process and help reduce the thermal gradient of the part upon melting (Wohlers, 2013). The process starts with heating of the build platform up to 50% of the material's melting point ($\sim 760^\circ\text{C}$ for Ti-6Al-4V). The build platform is usually heated above the melted temperature of the metal powder to achieve a stable temperature during the process. During the first few layers of the process, the temperature under the build platform experiences a decrease in temperature until it becomes stable as noted by the thermocouple below the build platform. The build platform is lowered by one layer thickness that can be in the range of 0.05 to 0.020mm. The rake is used to evenly spread the powder over the built platform. The electron beam starts preheating the forming layer to sinter the powder. The preheating step uses a high speed ($\sim 14,600\text{mm/s}$ for Ti-6Al-4V) and lower beam current ($\sim 8.8\text{mA}$ for Ti-6Al-4V) compared to the melting step (Arcam AB, 2011). The electron beam melts the 2D cross section of each layer and solidifies when cooled (Wohlers, 2013). This process is repeated layer-by-layer until the build is complete. After the build is complete Helium is purged into the chamber to allow for rapid cooling of the powder.

The EBM process allows features such as internal channels in heat exchangers and lattice structures to be incorporated in the build without the need for machining (Wohlers, 2013). EBM has been primarily used in the biomedical industry and has been granted seven FDA certifications for orthopedic implants such as long-term hip and spine implants (Wohlers, 2013). Approximately 30,000 hip (acetabular) implants fabricated on EBM systems have been implanted in patients (Wohlers, 2013). The EBM system on fabrication of acetabular implants has proof to be more cost effective than machining with $\sim 31\text{USD}$ of estimated savings (Wohlers, 2013). Arcam released the Arcam Q10 EBM system in 2013. The new Q10 EBM system was

specifically designed for manufacture of orthopedic implants. The Q10 system has features for industrial manufacturing such as volume production, increased productivity, higher resolution, and a new camera-based monitoring system implemented for continuous quality assurance called Arcam LayerQam (Wohlers, 2013). Arcam and Manufacturing Demonstration Facility at Oak Ridge National Laboratory have a cooperation agreement whose plans are to develop process monitoring and closed loop controls as well as develop new materials such as nickel-based superalloys and stainless steel on EBM systems. The major focus is to improve the reliability of EBM-fabricated parts (Wohlers, 2013).

2.3 CHARACTERIZATION OF MATERIALS

2.3.1 Grain boundaries

A crystal is the material's atoms arranged in a periodic manner. When a material has many crystals, the crystals are called grains. The region between grains is known as grain boundary. The characteristics of grains such as size and shape as well as the grain boundaries affect the mechanical properties of materials (Askeland and Phule, 2006). For example, equiaxed grain structures in casting are not desired for components used in turbines engines such as blades and vanes since these components fail in a transversal direction. These components are fabricated utilizing precision investment casting and they are commonly made of titanium, cobalt or nickel-based superalloys (Askeland and Phule, 2006). Creep and fatigue mechanical properties are improved by using the directional solidification growth method. During the directional solidification process, the part achieves columnar microstructure with all of the grain boundaries growing in the longitudinal direction (i.e. no grain boundaries exist in the transversal direction). This columnar microstructure is produced by the mold being cooled by a chill from one point and heated from the opposite point (Askeland and Phule, 2006). Production of single crystals produce improved mechanical properties compared to parts that are directionally solidified. A single crystal utilizes a chill from one point where the chill uses a helical

connection to the part allowing growth to only one columnar grain on the part (i.e. no grain boundaries exist on single crystal casting) (Askeland and Phule, 2006).

Defects during the fabrication process can occur such as cracking and formation of pores. Crack is a rupture occurring on the part at or below the solidification temperature caused by thermal stresses. Porosity is the appearance of tiny empty cavities on the material. Porosity is unfavorable to the mechanical properties of materials since pores can act as a pre-existing location of crack initiation (Askeland and Phule, 2006).

2.3.2 Metallography

Optical microscopy is a method to expose and observe microstructural features such as grain boundaries and defects such as porosity and cracking. A metallic sample of the material to be analyzed is sanded and polished to a mirror finish. The microstructure features of the surface of interest are revealed by etching, or by a chemical attack. This etching attacks the grain boundaries more destructively than to the rest of the grains. The optical microscope sends light to sample and the sample surface reflects the light that produces the etched microstructural features such as grain boundaries which appear dark. Metallography is the process of preparing the metallic sample, observing the surface using a microscope, and recording the sample's microstructure (Askeland and Phule, 2006). Scanning Electron Microscopy (SEM) is a microscope that utilizes electron to form an image instead of light which is used by the optical microscope. The advantages of the SEM over other common microscopes are depth of field, and higher resolution.

2.3.3 Hardness

The hardness test measures the resistance of penetration of a material surface using a hard object. The hardness of a material is a qualitative measure of its strength. On a Rockwell hardness test, the depth of penetration of the hard object (commonly a diamond cone) is automatically measured by the testing machine and adapted to a Rockwell hardness number (HR) that has no units. Rockwell hardness testing has several variations. For example, the

Rockwell C (HRC) test is utilized for hard steel and Rockwell F (HRF) can be utilized for aluminum (Askeland and Phule, 2006).

2.2 NICKEL-BASED SUPERALLOYS

A superalloy is defined by an alloy developed to withstand severe mechanical stresses ($\sim 350\text{MPa}$), and elevated temperatures ($\sim 850^\circ\text{C}$) (Bradley, 1988). These alloys present exceptional heat resistance, corrosion resistant, and creep resistance when compared to conventional alloys. Figure 2-1 illustrates various nickel-based superalloys in a stress vs temperature curve for rupture in 1000 hours showing the properties of these alloys. Superalloys consist of various combinations of iron, nickel, cobalt, chromium, and small amounts of tungsten, tantalum, niobium, titanium, and aluminum. The applications of superalloys are wide. Such applications include components for aircraft, chemical plant equipment, and petrochemical equipment (Bradley, 1988). Some applications are components on aircraft and industrial gas turbines such as disks, bolts, blades, and thrust reversers. Steam-turbine power plants use nickel-based superalloys for stack-gas re-heaters. Applications for this material can extend to components for reciprocating engines such as turbochargers, exhaust valves, and hot plugs. In nuclear power plants, these alloys are used to fabricate ducting, springs, valve systems and control-rod drive mechanisms. Finally, nickel-based superalloys have been used on metal processing for hot work tools and cast dies and chemical and petrochemical industries for piping, reactions vessels, and pumps (Bradley, 1988).

Nickel is a metal with a silver-white color that is commonly used to fabricate stainless steel and other alloys. Nickel was discovered as a unique element in 1751 by a Swedish mineralogist and chemist by the named of Baron Axel Fredrik Cronstedt. When working with nickel metal or nickel compounds, safety precaution must take place because they have been proven to cause cancer (Boland, 2012). Since nickel has high corrosion resistance and good mechanical properties, it is used to create superalloys that can withstand harsh environments such as those in chemical plants, petroleum refineries, jet engines, power generation facilities,

and offshore installation. Other uses of nickel alloys are batteries for portable computers, power tools, hybrid vehicles, and electric vehicles (Boland, 2012).

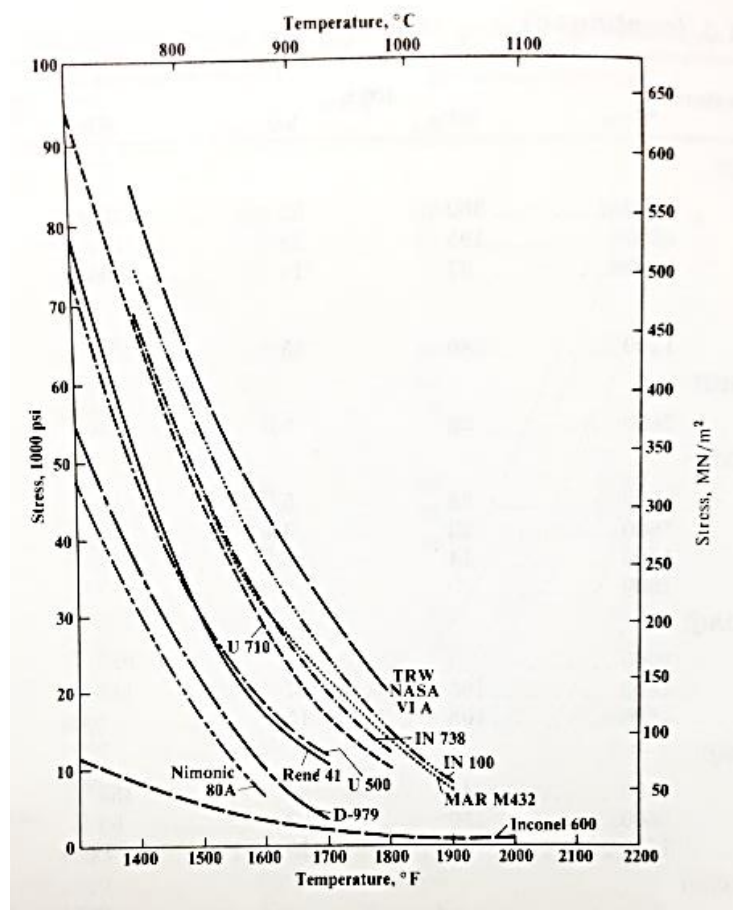


Figure 2-1 Stress vs temperature curves for rupture in 1000h for select nickel-based alloys (Bradley, 1988)

Generally, nickel-based superalloys are composed of nickel as a major component along with chromium, cobalt, iron, molybdenum, tungsten, tantalum, aluminum, titanium, and niobium. Castings are stronger than forgings at higher temperatures. Upon casting, the material develops coarse grains when compared to forging where the material develops fine-grains. The coarse grains of these superalloys improve the strength at high temperatures. Higher strengths on nickel-based superalloy may be attained by increasing the aluminum and titanium contents or by decreasing the chromium content (Bradley, 1988). Chromium has a negative effect on high-temperature strength. By decreasing chromium, hot corrosion and oxidation resistance is

reduced. The higher the melting point of the alloy indicates the high-temperature strength of the material (Bradley, 1988).

Nickel-based superalloys are widely used in hostile environments where high temperature and pressure are present, particularly in aircraft engines (Bradley, 1988). Since castings are stronger than forgings at high temperatures, the commonly used is investment cast for nickel-based superalloys such as INCO 713, INCO 100, B-1900, MAR-M 247, and MAR-M 200 are used for high temperature service conditions such as in turbine blades. When the material is needed to withstand severe conditions for rotating parts on turbine blades, directionally solidified or single-crystal structures are used. Some examples are B-1900, MAR-M 247 and MAR-M200 nickel-based superalloys (Bradley, 1988).

Since the nickel-based superalloys are extensively used on aerospace industries, there are interests in building these parts using AM processes. Arcam is collaborating with Oak Ridge National Labs to develop these superalloys on EBM systems and EOS released nickel alloy IN625 for fabrication on their system. EOS is a German company producing systems that utilize DMLS technology. Nickel alloy IN625 is used for aerospace, chemical, motorsports, and marine applications. Fabricated parts have high strength, good processability, and corrosion resistance as stated by EOS (Wohlers, 2013).

2.3 THERMAL RADIATION AND PYROMETER FUNDAMENTALS

2.3.1 Thermal radiation

Radiation is the energy emitted by objects in the form of electromagnetic waves due to the atomic and molecular agitation (Harrison, 1960). Substances at higher temperatures of absolute zero (0K) have atoms and molecules rotating and moving because of the energy associated with the substance temperature, resulting in radiation being emitted. Radiation energy emitted by a substance only increases when the temperature of the substance increases. Heat transfer by radiation moves at the speed of light (Cengel, 2011). For solids with opaque surfaces such as metals, radiation is considered to be a surface phenomenon, since radiation being emitted

by the inside of the metallic body will never reach the surface, and the incident radiation is absorbed within a few microns (Cengel, 2011).

2.3.1.1 The electromagnetic spectrum

The electromagnetic radiation encompasses an extensive range of wavelengths. The electromagnetic spectrum covers wavelengths from cosmic rays that are less than $10^{-10}\mu\text{m}$ to electrical power waves that are more than $10^{10}\mu\text{m}$. The electromagnetic spectrum includes cosmic rays, gamma rays, X-rays, ultraviolet radiation, visible light, infrared radiation, thermal radiation, microwaves, radio waves and electrical power waves. Thermal radiation is the type of electromagnetic waves emitted by matter caused by the energy transition of molecules, atoms, and electrons. Temperature indicates the strength of these motions at the microscopic level. Thermal radiation covers the electromagnetic waves from about $0.1\mu\text{m}$ to $100\mu\text{m}$ from the electromagnetic spectrum, since a substance emits radiation almost entirely between this wavelengths range (Cengel, 2011). Figure 2-2 Electromagnetic Spectrum describes the electromagnetic spectrum.

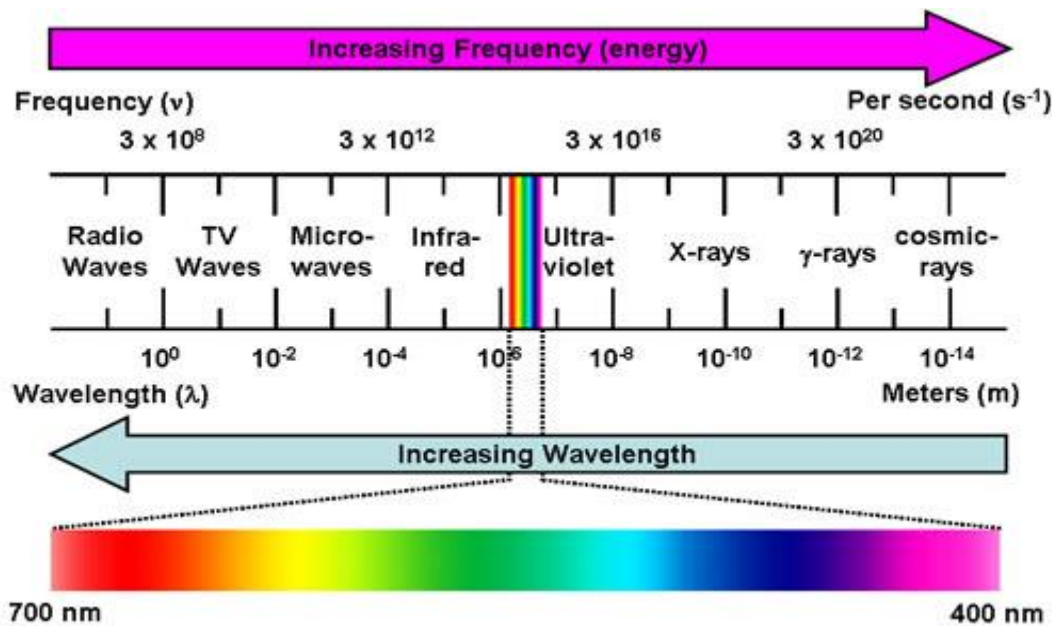


Figure 2-2 Electromagnetic Spectrum

2.3.1.2 Absorptivity, reflectivity, and transmissivity.

When a substance is exposed to radiation, a part is absorbed, a part is reflected, and the rest is transmitted. However, different objects have different radiant energy absorption abilities that are dependent upon their composition, surface, and in their dimensions if these are non-opaque substances. This ability to absorb incident radiant energy is linked to their own relative ability to radiate energy. It is important to understand that when analyzing problems involving heat exchanged between two or more objects in stable thermal communication within a completely enclosed and insulated chamber, such objects tend to reach a state of equilibrium in which of the objects and walls of the enclosed chamber are at the same temperature. These reach equilibrium temperature that will remain constant thereafter. Since the driving force for heat transfer is a change in temperature, no heat will flow either by conduction or convection from one object to another. However, regardless what the state is, there will be a continuous exchange of radiant energy by the chamber walls and the objects inside. Right before a state of equilibrium is reached, a given unit volume of one of the enclosed object temperatures will increase or decrease depending on its rate to absorb and emit radiant energy. A state of equilibrium will be proclaimed once all the objects inside the chamber have reached the same temperature. At this state, each unit volume of every enclosed object will absorb radiant energy at same rate that it emits it. So convection and conduction will no longer exists (Harrison, 1960)

To analyze the interchange of radiant energy accurately when measuring surface temperature, it is important to be able to identify certain characteristics. Most materials in engineering applications do not behave like blackbodies; in this case, it is important to know the material's absorption, reflection, and transmission characteristics to make precise measurements. These material properties, or variables, are defined as dimensionless quantities, all between values between zero and one (Cengel, 2011). The surfaces of interest in this study are opaque surfaces, such as metals, which will be examined in more detail for which the transmittance is zero. The summation of the absorbed, reflected, and transmitted radiation is equal to that of the incident radiation as stated by the first law of thermodynamics (Cengel, 2011).

2.3.1.3 Emissivity

The radiant intensity of an object may be expressed as the fraction of the radiation emitted by the object at a given temperature to the radiation emitted by a blackbody at the same temperature (Harrison, 1960). This fraction is called emissivity and defines an object's ability to emit energy. The emissivity is denoted by the symbol ε and varies between zero and one (Cengel, 2011). The emissivity describes how the object approximates a blackbody, for which emissivity is one.

The emissivity of an object is not constant, since the emissivity depends on various factors such as composition, size, shape, temperature, surface condition, and the wavelengths or the band of wavelengths for which the ratio (emissivity) applies (Harrison, 1960). The spectral directional emissivity is defined as the fraction of the intensity of radiation emitted by the surface at a certain wavelength and direction to the intensity of radiation emitted by a blackbody at the same temperature and wavelength. Defined by:

$$\varepsilon_{\lambda,\theta}(\lambda, \theta, \phi, T) = \frac{I_{\lambda,e}(\lambda, \theta, \phi, T)}{I_{b\lambda}(\lambda, T)}$$

In radiation analysis, objects are approximated by assuming to have gray or diffuse surfaces since radiation analysis considering direction and wavelength dependence of properties is very complex. A gray surface has properties independent of wavelength (λ) and a diffuse surface has properties independent of direction (θ). When the surface is assumed to have gray and diffusive surfaces, the emissivity is independent of direction and wavelength. This is a valid approximation since the total radiation emission from a gray surface should be equal to the total radiation emission of the real surface at the same temperature (Cengel, 2011).

2.3.1.4 Blackbody radiation

The amount of radiation energy emitted from a surface at a given wavelength is dependent on its material, surface condition, and surface temperature. Defining an idealized body, called a blackbody, allows the determination of the maximum amount of radiation that can be emitted by a unique surface or material at a given temperature. A blackbody is defined as a

perfect emitter and absorber of radiation, since at a specific temperatures and wavelength no surface can emit more energy than a blackbody (Cengel, 2011). A blackbody is an instrument that absorbs all irradiated energy from any direction and wavelength. This instrument also has the ability to reemit this energy until reaching thermodynamic equilibrium with its surroundings, also earning the name of a perfect radiator (Cengel, 2011). The amount of radiation energy emitted by a blackbody per unit time and per unit surface area is defined by

$$E_b(T) = \sigma T^4$$

This equation is known as the Stefan-Boltzmann law, in which $\sigma = 5.670 \times 10^{-8} \text{ W/m}^2 \text{ K}^4$ is known as the Stefan-Boltzmann constant, T is the absolute surface's temperature in Kelvin, and E_b is the blackbody emissive power (Cengel, 2011). The emissivity power is the addition of the radiation emitted over the entire range of wavelengths. The spectral (dependence on wavelength) blackbody emissivity power is defined as the amount of radiation energy emitted by a blackbody at a certain temperature and at a specific wavelength. Planck's law describes the spectral blackbody by

$$E_b(\lambda, T) = \frac{C_1}{\lambda^5 (\exp(\frac{C_2}{\lambda T}) - 1)}$$

Where:

$$C_1 = 3.74177 \times 10^8 \text{ W } \mu\text{m}^4/\text{m}^2$$

$$C_2 = 1.43878 \times 10^4 \mu\text{m K}$$

The variation of the blackbody emissive power with wavelength for several temperatures is illustrated in Figure 2-3.

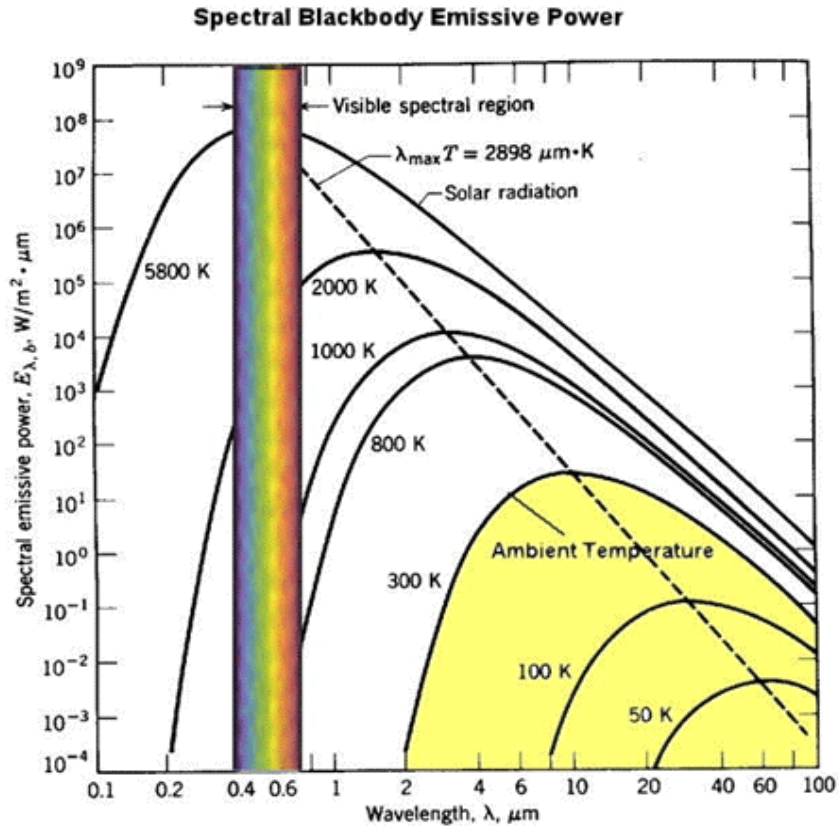


Figure 2-3 Spectral blackbody emissive power

2.3.2 Pyrometry

A pyrometer is a device capable of measuring radiant energy that can be converted into temperature. Thermal radiation is transfer of energy in forms of electromagnetic waves. The process of using radiant energy data to calculate the temperature is called pyrometry. The pyrometer is a non-contact instrument used to measure high temperatures of objects when the environment is hostile, or the area of interest is difficult to access using another kind of thermopile. There are three types of pyrometers: brightness pyrometer (single-color), ratio pyrometer (two-colors), and multi-wavelength pyrometer (three-colors or more) (Felice, 2002).

Brightness pyrometry consists of absorbing a known portion of radiation from a particular source at a specified angle. Ratio pyrometry depends on the material's grey-body behavior and uses Planck's law and two wavelengths to calculate the temperature of a given

material. In both of these conventional methods of pyrometry, it is imperative to obtain the correct wavelengths. If the wavelengths are incorrect, then temperature and emissivity measurements may vary by a large amount. The multi-wavelength pyrometer uses a large amount of wavelengths from a circular spot size and calculates temperature values, and if a wavelength does not correspond to the spectra, the value is ignored and only common wavelengths are used in the calculation (avoiding the inaccuracy caused by obtaining incorrect wavelengths). The pyrometer used during this project was a multi-wavelength pyrometer developed and commercialized by FAR Associates in 1997 (Felice, 2002).

2.3.3 Multi-wavelength pyrometer

The multi-wavelength pyrometer utilizes a spectrophotometer as its detector of thermal radiation, or the electromagnetic radiation emitted by an object when it is heated above absolute zero. This radiation is detected by the pyrometer and relates it to a look-up table which utilizes the theory of Planck's Law (Felice, 2002). Planck's Law describes an ideal blackbody radiator. This law is used to define the amount of electromagnetic energy with a definite wavelength radiated by a blackbody through the following formula:

$$L_{\lambda} = \frac{2 h c^2}{\lambda^5} \left[e^{\frac{h c}{\lambda k_B T}} - 1 \right]^{-1}$$

Where L_{λ} is the radiance in energy per unit time per steradian per unit wavelength interval, h is Planck's constant, c is the speed of light, λ is the wavelength of radiation, k_B is Boltzmann's constant and T is the absolute temperature of the material. For a non-blackbody, the equation simply becomes:

$$H_{\lambda} = \epsilon L_{\lambda}$$

Where H_{λ} is the radiation emitted and ϵ is the emissivity of the material. Using the short-wavelength-temperature assumptions and solving Planck's law for temperature by dividing the intensities at two different wavelengths, the following formula is obtained:

$$T_{12} = \frac{C_2 \left(\frac{1}{\lambda_1} - \frac{1}{\lambda_2} \right)}{\ln R - 5 \ln(\lambda_2 / \lambda_1)}$$

Where C_2 is the second radiation constant, and R is the ratio of intensities at the two wavelengths. The method used by the multi-wavelength pyrometer is the calculation of all possible values of T_{ij} for a collection of distinct wavelength and intensity pairs that are then averaged (Felice, 2002). This method is most appropriate for noise-free collected data of greybody or blackbody sources (Felice, 2002).

By using standard deviation, or the pyrometer's tolerance output, the results can be characterized accordingly. If the result is a single value, it means that the tested specimen is a greybody where the absorptions are insignificant (Felice, 2002). However, if the calculated value is large, i.e. greater than a single value result, it may indicate one of the following: 1) the emissivity is a function of wavelength, 2) atmospheric absorptions are present, 3) the temperature is not a single value, or 4) optical elements have changed characteristics (Felice, 2002). The first two among these can be corrected once detected. As un-oxidized metals normally display an emissivity that decreases with wavelength, it can be drawn from previous work that a three-wavelength pyrometer is capable of solving for the temperature if the emissivity dependence of temperature is linear (Felice, 2002). For the reason that the device is able to detect several wavelengths, a correction that assumes emissivity can be expressed by a linear function. This assumption is to remain true if the result is shown to be a single value (Felice, 2002).

The multi-wavelength pyrometer was directed to the inside of Arcam's vacuum chamber pointing to the middle of the build platform to record temperature data during the fabrication process. The EBM process consists on several steps (e.g. movement of raking mechanism, spreading of powder, pre-heating, and melting) that may vary the emissivity of the material with each step. The multi-wavelength pyrometer is a valuable instrument to measure the surface temperature of the build since it is capable of detecting several wavelengths and correct for emissivity in real time during the fabrication process.

2.4 FEEDBACK METHODS IN ADDITIVE MANUFACTURING

In research it is very important to understand the thermal behavior when fabricating metals to improve their mechanical properties. Methods of understanding the temperature of the forming layer allow improvements to enable the improvement of the system to produce quality parts.

An infrared camera has been used to study the thermal effects during the fabrication process of directed energy deposition (Griffith, *et al*, 1999). On SLM, an infrared camera has been utilized to monitor the temperature during the fabrication process (Xiong *et al*, 2009). On a laser-based system, a camera with high frame rate (800 frame/s) was implemented to acquire infrared images of the melt pool (Hu *et al*, 2002). These methods allowed observing infrared images of builds permitting analyzing the thermal behavior of parts during the fabrication process in AM systems. Additional methods to analyze the surface temperature of builds must be implemented on AM systems to have a fully understand of thermal behavior during fabrication and allow real simulation and quality control on AM fabricated parts.

2.4.1 Temperature monitor in EBM

As mentioned before, since the current technology of EBM uses a single thermocouple underneath the start plate to measure the temperature of the build, the temperature displayed by the machine does not accurately represents the surface temperature of the build. The interest is now in the temperature of the forming layer during the fabrication process. If in the fabrication process the temperature of the forming layer is known, the operator can adjust some parameters such as beam current and speed to attempt to obtain the desired temperature. An infrared thermal imager was used in an EBM system to analyze the melt pool sizes, temperature distribution around the melting area at various configurations (Price *et al*, 2013). Another method to record the temperature of the forming layer in real-time was utilizing an infrared (IR) camera on the Electron Beam system performed by the W.M. Keck Center (Rodriguez, 2013). With a specified emissivity value the IR camera is capable of recording thermal images while fabricating parts

and displaying the surface temperature of the build as well as detecting defects on parts such as porosity. During the fabrication process the rake passes to spread the layer of powder, the electron beam melts the layer and a shutter mechanism opens to allow the IR camera to take a thermal image of the layer. This process is repeated in every layer throughout the entire part. In addition, the process permits implementation of automated control on fabricated parts to correct defects such as porosity (Mireles, 2013). The difficulty with this method is that in order to achieve accurate results, the emissivity of the material has to be known. Many times when working with parameter development the emissivity of the material is not known and it may vary during the fabrication process.

CHAPTER 3 SYSTEM

The EBM Arcam S12 system was used during this project. Like other AM technologies, EBM fabricates parts directly from CAD in a layer-by-layer manner. The S12 model was modified to fabricate materials with high temperature melting points. The Arcam S12 system has a larger heat shield, and an additional stainless steel plate to protect the front window in comparison to the Arcam A2 system that is also available at UTEP. Also, the distance between the gun and the forming layer is larger to prevent the column from overheating (the maximum temperature of the column should not exceed $\sim 80^{\circ}\text{C}$). The basic components of the Arcam S12 system are the vacuum chamber, powder hoppers, heat shield, build tank, rake mechanism, thermocouple, powder pulse sensors, and start plate. The main components of the system are illustrated in Figure 3-1.

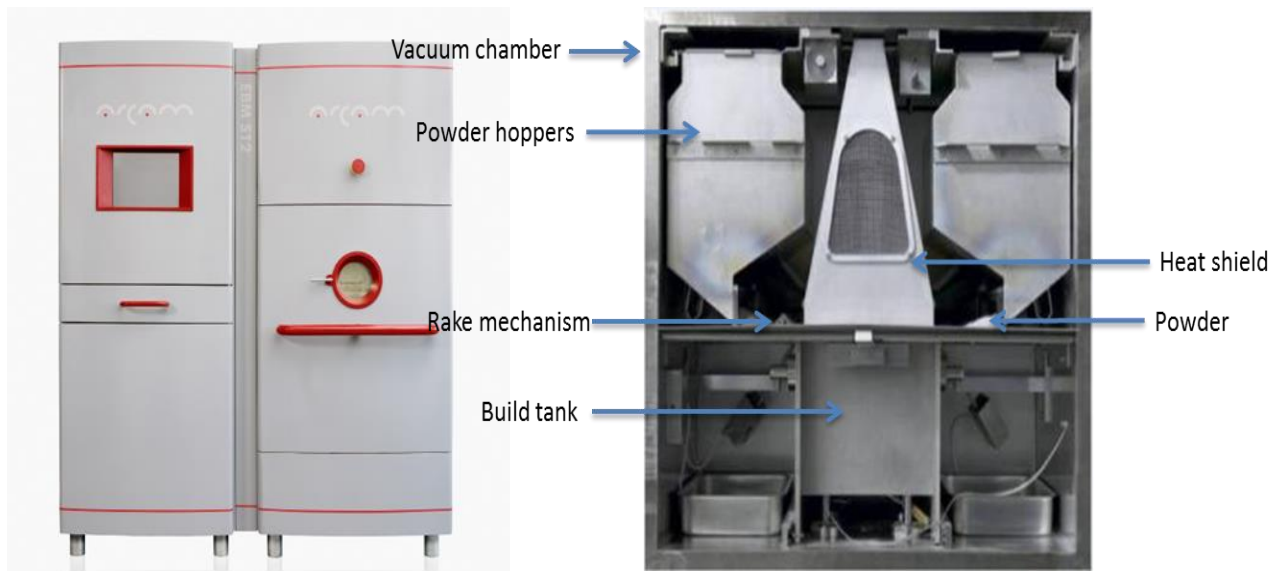


Figure 3-1 Arcam S12 system

On the Arcam S12 system, the general set-up procedure the operator needs to follow includes:

- 1) Filling the hoppers with previously sifted powder metal that is sufficient to complete the required build.
- 2) Filling the build tank with powder metal approximately 2 inches in height.

- 3) Place the build platform surrounded by powder metal onto the build tank.
- 4) Calibrate the raking system to fetch enough powder and ensure it spreads the metal powder evenly onto the start plate.
- 5) Verify the filament has enough life to complete the build (life of filament: ~80hrs).
- 6) Verify the beam path in the column is free of any impurities.
- 7) Examine the front window for sufficient observance (metallization on glass occurs during fabrication).
- 8) Place the heat shield in its proper position.
- 9) Clean and close the chamber door.
- 10) Activate the turbo pumps to put the system into vacuum.

These series of steps are followed every time the operator attempts to fabricate a part with the system. When developing parameters for a new material, reducing time in set-up procedures and during fabrication is beneficial because it allows the user to attempt more builds, and thus, perform more experiments and have more results.

In the following sections, design modifications to reduce time in set-up procedures and fabrication processes are discussed. The fabrication of small start plates and the implementation of a cylindrical build tank envelope are presented. Also, detailed parameter capabilities on the EBM system and the strategy for parameter development used are further explained.

3.1 CYLINDRICAL BUILD TANK ENVELOPE

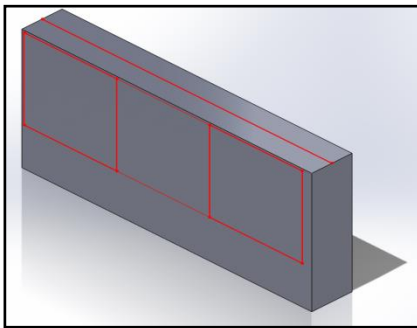
The start plates as well as the build tank envelope play important roles in set up and building times to develop system parameters for new materials. During the fabrication process, the first step is to heat the start plate to about 80% of the melting temperature of the material (~1100°C for NSAT). The larger the surface area of the start plate, the more time the electron beam scans the surface to reach the desired temperature. The second step is to sinter the powder under the start plate to hold it in place and prevent it from moving during raking of new powder.

The more powder there is in the build tank envelope, the more time the system takes to sinter the powder appropriately.

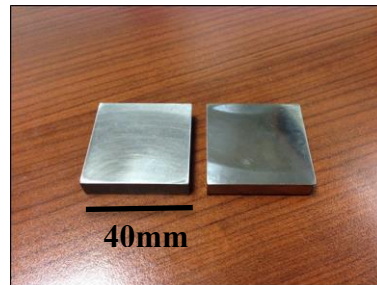
The first task to reduce time in set-up and building processes was to decrease the surface area of the start plate. Small start plates permitted reducing the time in the heating and sintering process. In its commercial state, the standard start plates are composed of stainless steel and measure from 100x100x10mm to 210x210x10mm. A block of Rene 125 was provided by GE and small start plates were machined out of the block using wire EDM. The alloy chemistry for Rene 125 is showed in Table 2-1 (Sexton et al, 2002). The small start plates measure 40x40x10mm. Figure 3-2 illustrates the block design and the start plates made of Rene 125.

Table 2-1 Alloy chemistry for Rene 125

Alloy Chemistry												
Alloy	Ni	Cr	Co	Mo	Fe	C	Ti	Al	B	Zr	Hf	Ta
Rene 125	58.8	9	10	2	0.32	0.1	2.8	4.8	0.015	0.05	1.6	3.8



a) Block design of Rene 125



b) Start plates of Rene 125

Figure 3-2 Rene 125 start plates

Since small start plates were machined for the experiments, there was also a necessity to reduce the volume of the build tank. Decreasing the volume of the build tank allowed the use of less powder material to hold the start plate which also reduced the time of set-up and the material sintering process during fabrication. The original design for the build tank envelope required about 1,830 cm³ of metal powder to do the set-up of the system. The W.M. Keck Center for 3D innovation designed and fabricated a cylindrical build tank envelope (mini-vat) for new material

parameter development purposes. The mini-vat has a 120mm inner diameter and a build height of 150mm (Medina, 2013). The mini-vat is used to decrease the amount of powder required to accommodate the start plate from about $1,830\text{cm}^3$ to 153cm^3 . Then mini- vat was also useful to reduce the amount of powder during the fabrication process. Figure 3-3 illustrates a comparison between the standard build tank envelope and the mini-vat.

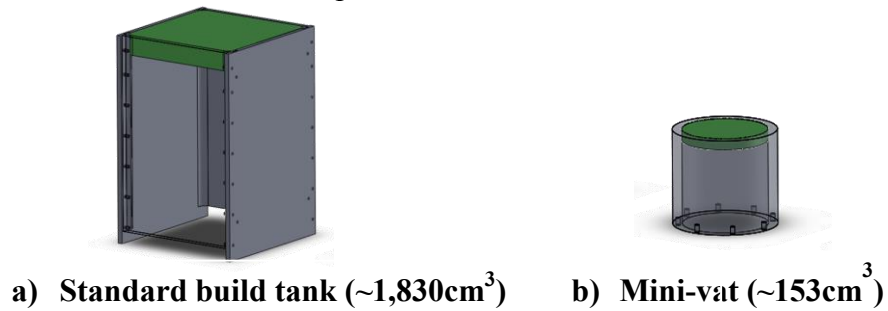


Figure 3-3 Build tank envelopes

The mini-vat was installed in the Arcam S12 for development of NSAT. The design of the mini-vat was focused on developing system parameters to fabricate quality parts; thus, primary focus was given to the manufacturing parameters and how they changed the fabrication process. Therefore, it was useful to build faster using small parts and analyzing the effect on them due to the system parameters.

Error! Reference source not found. Figure 3-4 illustrates the mini-vat installed in the Arcam S12.

3.2 FABRICATION PROCESS

The Arcam S12 system uses different parameters to fabricate parts. The system software allowed the operator to change parameters before and during the fabrication process. Before the fabrication process starts, the operator chooses the steps of the process (commonly being, the preheat theme, wafer support theme, and the melt theme). During the fabrication process the preheat theme is used to sinter the powder for three main reasons: 1) to hold the part in place, 2)

to reduce thermal stresses, and 3) to increase the surface temperature allowing the electron beam to properly melt the metal powder. If the geometry has overhanging features then support is needed to build the part without deformation. The wafer support theme fabricates supports around the part to prevent deformation. After the part is out of the machine the supports can be removed easily by hand or by using the powder recovery system (PRS) from Arcam. The melt theme describes the parameters for the electron beam to melt the 2D cross section of the forming layer of metal powder.

During the EBM fabrication process, each layer is preheated and melted. Under the preheat theme the operator can specify the preheat area (box size) to use. Commonly, the preheat area has larger surface area than the part. The melt step divides the part into contours and hatching. The hatch is the inside of the part during the forming layer, or the fragment portion inside the contours to be melted. Under the melt theme, the operator can choose the number of contours and whether to first melt the contours or the hatch. The software changes the hatch direction every layer to prevent deformation of parts and evenly distribute heat (Cormier *et al*, 2004). **Error! Reference source not found.** describes an example of the software's segmentations (contours and squares) considering a cuboid part.

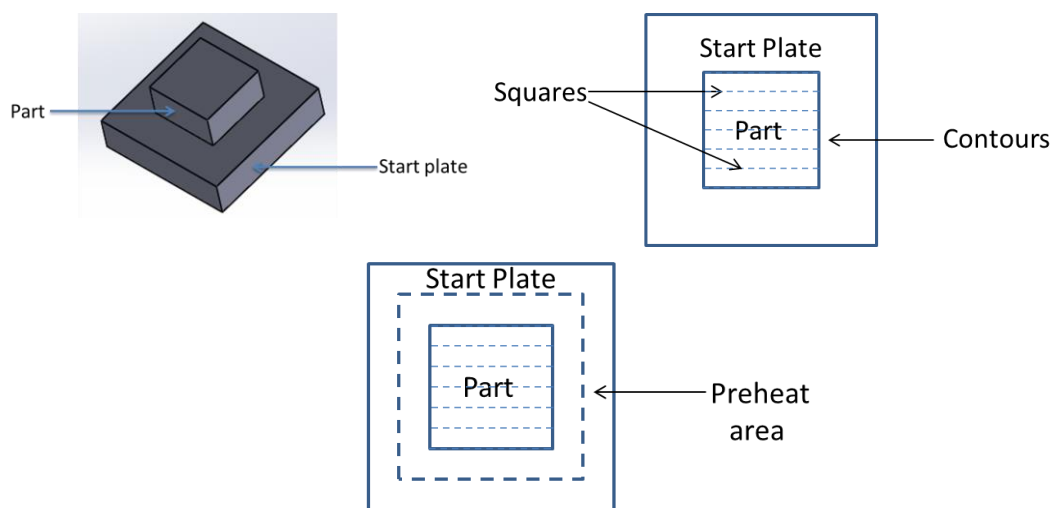


Figure 3-5 Example of squares and contours of a cuboid

Throughout the fabrication process the system used a calculation for energy balance to keep a proper constant build temperature and maintain a low thermal gradient that helps reduce residual stresses. Powder particles increase in negative charge when gaining electrons by the electron beam. If the electron beam does not increase the negative charge in a proper manner, it may cause two undesirable effects during the fabrication process:

1) The frictional and gravitational forces holding the particles together might be overcome by the repulsive force of the negatively charged particles on the powder bed, causing rapid ejections of the powder particles (powder explosions).

2) If the powder particles increase in negative charge, a diffuse beam can be formed due to the repelling force between the powder and electron beam (Gibson *et al*, 2010).

3.3 PARAMETER MODIFICATION CAPABILITIES OF THE EBM SYSTEM

The preheat theme is divided into two sections, preheat I and preheat II. Preheat I is used to begin sintering the powder at a low current (~10mA for NSAT) and high speed (25,000mm/s for NSAT). This is used to prevent powder explosions by slowly increasing the energy of the layer. Preheat II increases the sintering on the powder with high current (~40mA for NSAT) and low speed (~7,000mm/s for NSAT). This preheat theme increases the temperature of the layer at least 80% or more of the melting point of the material (~1,100°C for NSAT). Increasing the temperature of the layer using preheat II prevents metal powder particles from being rapidly expelled from the melt pool as well as formations of melt balls during the melting process. The melt theme is divided into two main sections; contours and hatch. Each section of the melt theme has its own parameters that the operator can modify if necessary to fabricate the part in a correct manner.

The most commonly used system parameters that the operators can modify under the preheat theme are beam focus, beam current (minimum, average, and maximum), beam speed, line offset, preheat area and number of repetitions. Description of parameters is as follows:

- Beam focus: the beam focus describes how narrow the electron beam will be. The narrower it is, the more energy it deposits over a certain area. When the beam is wide, the beam energy covers a large area and less energy is focused over that area and vice versa. Figure 3-6 (a) illustrates a narrow beam and (b) describes a wide beam due to an increase in beam focus.

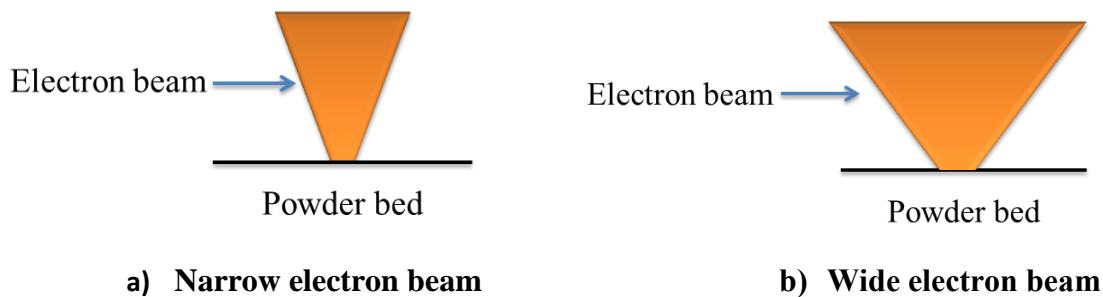


Figure 3-6 Focus offset parameter

- Beam current: The beam current parameter allows the operator to specify the minimum and maximum current in units of mA. When the electron beam preheats the layer, it uses a range between the minimum and maximum.
- Beam speed: Beam speed specifies the speed of the electron beam in units of mm/s.
- Line offset: During the preheat step, several lines of the electron beam heat the layer at the same time. Line offset describes the distance between these electron beam lines in units of mm.
- Preheat area: Defines the size of the area heated by the electron beam with a user defined number of repetitions. Number of repetitions describes the number of times the lines of the electron beam pass over the same layer.

The most commonly used system parameters under the melt theme are focus offset, beam current (minimum, average, and maximum), beam speed, line offset, line order, snake, and randomized hatch. Focus offset, beam current and beam speed are the same as described in the preheat theme.

- Line offset: During the melting process, the electron beam melts the 2D geometry one line at a time. These lines are called hatch lines. The line offset specifies the distance between hatch lines in mm. Figure 3-7 (a) describes the line offset between hatch lines.
- Line order: This parameter specifies the number of sections in a layer. Initially the electron beam melts the first hatch line of each section, then, the second hatch line of each section, and the electron beam follows this pattern until it melts the entire layer. Figure 3-7 (b) describes the line order divided into three sections. First the electron beam melts all the red hatch lines, followed by green, yellow, and purple hatch lines.

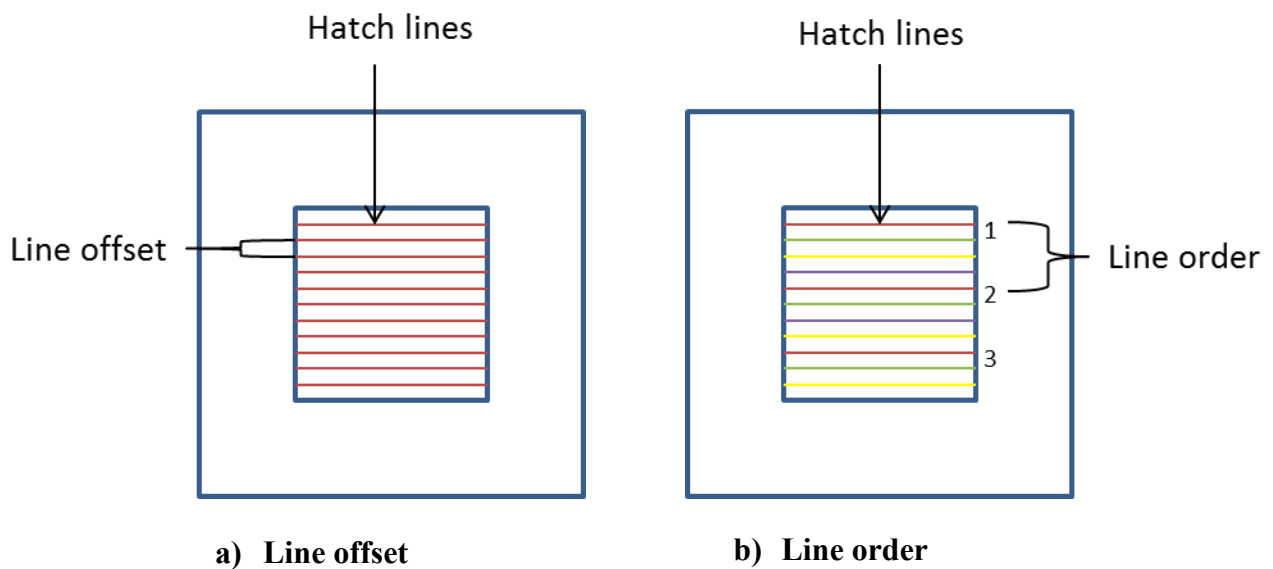


Figure 3-7 Line offset and line order parameters

- **Snake:** The snake parameter describes the pattern the electron beam follows. If the snake is on, the hatch line will move in the opposite direction to the previous hatch line. For example, if the first hatch line moves from left to right, the second hatch line would move from right to left and the electron beam would follow this pattern to melt the entire part. If the snake is off, the hatch lines would be unidirectional. For example, if the first hatch line moves from top to bottom, all the consecutive hatch lines would follow the same pattern. **Error! Reference source not found.** (a) shows the electron beam melting pattern when the snake is off and (b) when the

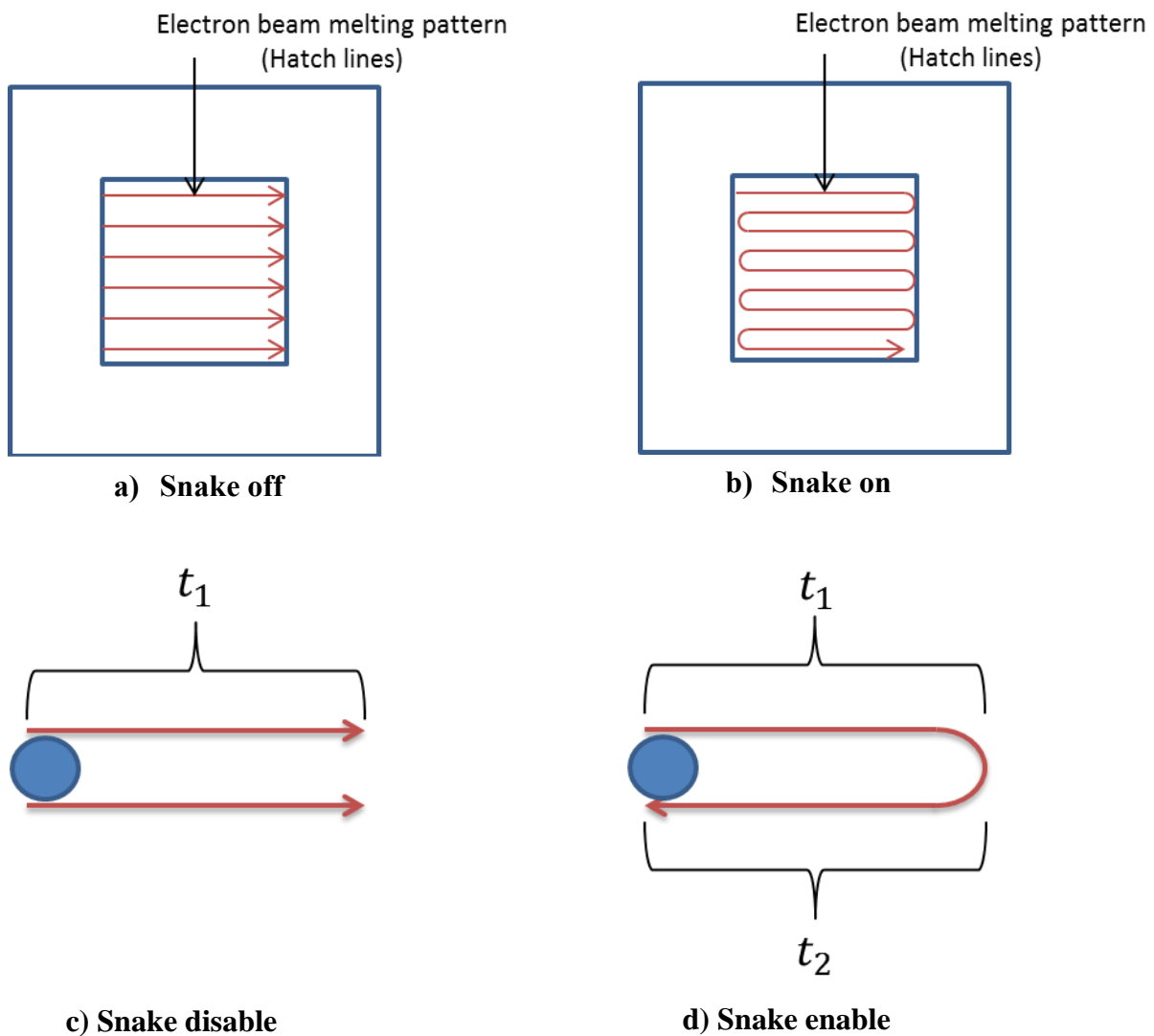


Figure 3-8 Snake parameter

snake is on. This unidirectional hatch distributes the heat more evenly through the layer. Consider two hatch lines that describe the beam pattern during melting, where the point of origin is the blue circle (**Error! Reference source not found.** c and d). If the snake parameter is disabled (**Error! Reference source not found.** c) the electron beam takes time t_1 to reach the point of origin. If the snake parameter is enabled, (**Error! Reference source not found.** d) the electron beam doubles the time (t_1+t_2) to reach the point of origin. Thus, the snake being disabled distributes heat more evenly during the melt than the snake being enabled.

- Randomized hatch: Hatch randomization describes the direction the electron beam will scan the hatch lines in each layer. If the randomized hatch is off, the electron beam follows a pattern between each layer to melt (right to left, top to bottom, left to right, and bottom to top). If the randomized hatch is on, it will randomize each layer with arbitrary directions.

3.3.1 Manual and automatic mode

Another useful parameter is the manual or automatic mode. If the system is in manual mode, it makes a calculation with the specified beam currents and uses a constant energy on each layer and throughout the build. If the system is in automatic mode the operator needs to specify a desired temperature. The system makes calculations based on the specified beam currents and the thermocouple temperature, and it increases or decreases the beam energy in each layer based on the desired temperature.

3.3.1.1 Preheat automatic mode

If automatic mode is selected for the preheat, the software calculates the beam settings by computing the following:

$$Speed = \frac{\text{Min length of lines before beam returns to adjacent line}}{\text{Time elapsed before beam returns to adjacent line}_{Ref}}$$

$$\text{Min current} = \frac{\text{Min current}_{Ref} \times \text{Speed}}{\text{Speed}_{Ref}}$$

$$\Delta \text{Current} = \frac{(\text{Max current}_{Ref} - \text{Min current}_{Ref}) \text{Speed}}{\text{Speed}_{Ref} \times \text{Number of repetitions}_{Ref}}$$

$$\Delta \text{Temp}_{Ref} = \frac{\text{Total time}_{Ref} (\text{Max current}_{Ref} - \text{Min current}_{Ref})}{2 \text{Area}_{ref} (\text{Layer thickness} \times \text{Density} \times \text{Cp} + \text{total time} \times \text{HeatLossFactor})}$$

$$\text{Required energy} = \text{Area}_{ref} \times \Delta \text{Temp}_{Ref} \times \text{Layer thickness} \times \text{Density} \times \text{Cp}$$

where:

Speed = Actual beam speed

Min length of lines before beam returns to adjacent line = the length of the preheat area

Time elapsed before beam returns to adjacent line_{Ref} = Specified time between adjacent lines

Min current_{Ref} = Specified min current on the preheat theme

Speed_{Ref} = Specified speed on the preheat theme

ΔCurrent = Increase in current during the preheat step

Number of repetitions_{Ref} = Specified number of repetitions during the preheat step to ramping up the current from minimum current to maximum current.

ΔTemp_{Ref} = Increase in temperature during the preheat step

Total time_{Ref} = Specified time on the preheat theme

Max current_{Ref} = Specified max current on the preheat theme

Area_{Ref} = Specified preheat area

Density = Specified metal powder density under the material theme

Cp = Specified heat capacity of the metal powder

Layer thickness = Specified layer thickness for fabrication

Heat loss factor = This factor describes the loss of heat through the surface down into the material.

These calculations are computed to increase the energy of the layer by increasing the number of repetitions until the deposited energy is equal to the required energy or until the maximum number of repetitions is reached. If the density and heat capacity values are not specified, the software uses the default values for Ti-6Al-4V. The automatic mode of the preheat calculates the required energy to heat each layer and modifies the beam speed and beam current to achieve that energy.

3.3.1.2 Melt automatic mode

The user specified parameter for desired temperature is used to control the automatic calculation. The objective of this calculation is to maintain a constant surface temperature through the build by adjusting the power depending upon the geometries of the model. The speed function is used to control the speed when melting in automatic mode (the higher the specified value the higher the speed). The speed function is a function of current that is obtained by interpolation in a look-up table. When the Z distance from the surface of the build to the

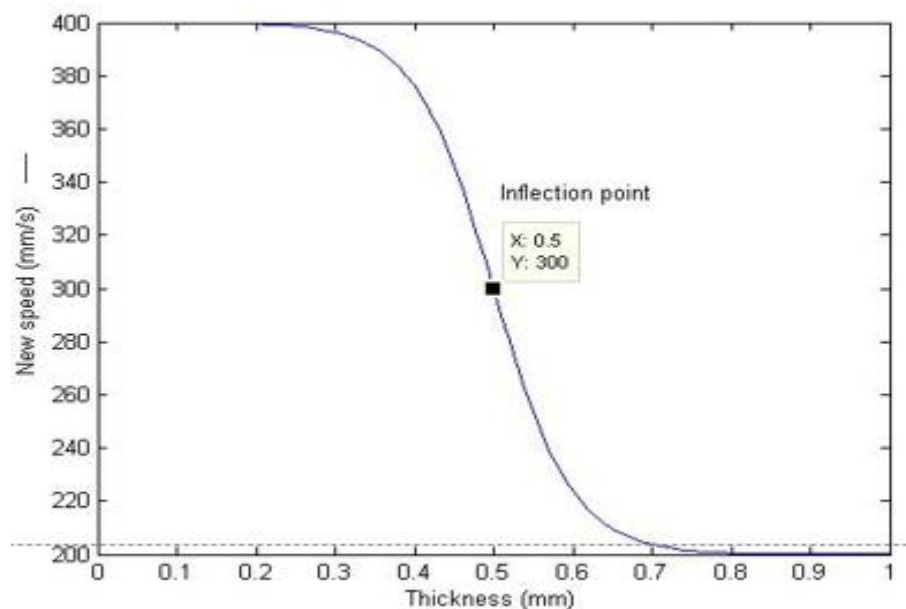


Figure 3-9 Example of an inflection point from the thickness function

substrate is small, the system uses a thickness function to calculate the speed by correlating the thickness of the build and the speed and finding an inflection point (Figure 3-9 illustrates an example of an inflection point of 300 mm/s) using the following formula:

$$New\ speed = speed \left(1 + \frac{Speed\ factor}{Exp (Expfactor (Thickness - Thickness\ factor)) + 1} \right)$$

Where:

Speed = The speed used in the previous layer

Speed factor = A pre-exponential scale factor used for computing how much the speed will affect the thickness function

Exponent factor = an exponential factor used for computing how fast the depth contribution will decay. This factor controls the slope of the curve at the inflection point

Thickness factor = an exponential factor used for calculating how deep the depth contribution will affect the thickness function. This factor controls the position of the inflection point

CHAPTER 4 METHODOLOGY

The purpose of these experiments was to develop system parameters for fabrication of NSAT parts. A multi-wavelength pyrometer was used to record surface temperature data during the fabrication process. First characterization of the metal powder was performed to compare with Ti-6Al-4V, a commercially available material for fabrication in the EBM system. Experiments were designed to start developing system parameters and fabricate NSAT parts. Each custom experiment gave valuable information to attempt new educated system parameter modifications. On all experiments containing fabricated parts, micrographs were recorded and analyzed to observe differences in cracking.

4.1 POWDER CHARACTERIZATION

NSAT powder was manufactured using gas atomization technology. The gas atomized process is utilized to produce high quality spherical metal powder. The equipment used during this process is illustrated in **Error! Reference source not found.**. During the process, the material is melted in a vacuum induction chamber. The liquid metal passes through a nozzle and inert gas is dispersed by a high velocity jet (air, nitrogen, argon, or helium) atomizing the powder into fine droplets (Inoue et al, 1988). The droplets fall in the atomizing powder. The droplets cool down as they fall and spherical powder particles are formed. Powder particles are collected in a collection chamber. Inert gases are utilized in the atomization process to avoid oxidation of reactive materials such as superalloys (Wan X et al, 1998). Gas atomization processes provide quality spherical morphology of metal powders particles at high purity levels.

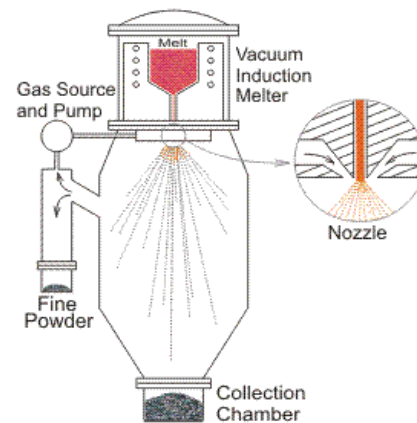
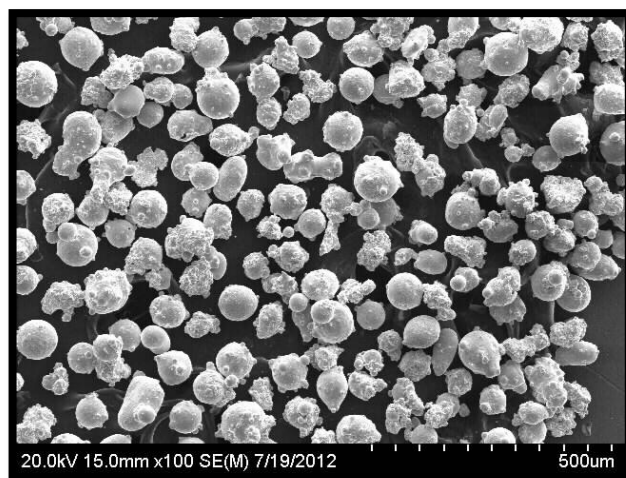
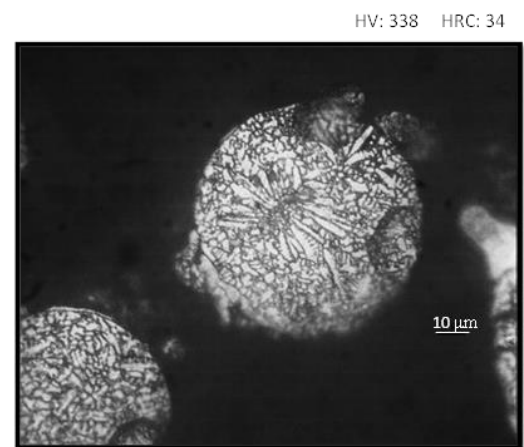


Figure 4-1 Gas atomization process

To characterize the NSAT powder, microstructural analysis was performed. A Hitachi S4800 Ultra-High Resolution Field-Emission Scanning Electron Microscopy (SEM) (Hitachi High-Technologies Corporation, Tokyo, Japan) was utilized to analyze the powder particles. Figure 4-2 (a) shows a SEM picture of NSAT metal powder particles. The morphology of NSAT contains spherical, semi-spherical, satellites, and some agglomerations of particles. Optical metallography of NSAT particles was performed using an AmScope Microscope MD600 digital camera (United Scope LLC, Irvine, CA). Figure 4-2 (b) shows the optical image of a sphere powder particle. The microstructure of the spherical particle is dendritic. Also, Vickers micro-indentation hardness (HV) testing was done on the powder particles utilizing a Shimadzu HMV-2000 micro-indentation tester (Shimadzu Corporation, Tokyo, Japan) for comparison between the powder and a solid part fabricated in EBM. The HV of the powder was 338, corresponding to a HRC (Rockwell C Scale) value of 34. The hardness of the NSAT solid part has been shown to be 41 HRC (Murr *et al*, 2013). This value of hardness implies high strength. Previous research has demonstrated that NSAT turbine blades had twice the rupture life than CF6-80C HP turbine blades at a temperature of 982°C (Murr *et al*, 2013).



a) SEM Picture



b) Optical Image

Figure 4-2 Metallography of NSAT metal powder

Powder distribution analysis was performed using SEM pictures at low magnification. Arcam recommended using metal powders with a normal distribution curve and with powder particles between 30 to 120 μm . To avoid fire and health hazard, powder particles must not contain particles less than 10 μm (Medina, 2013).

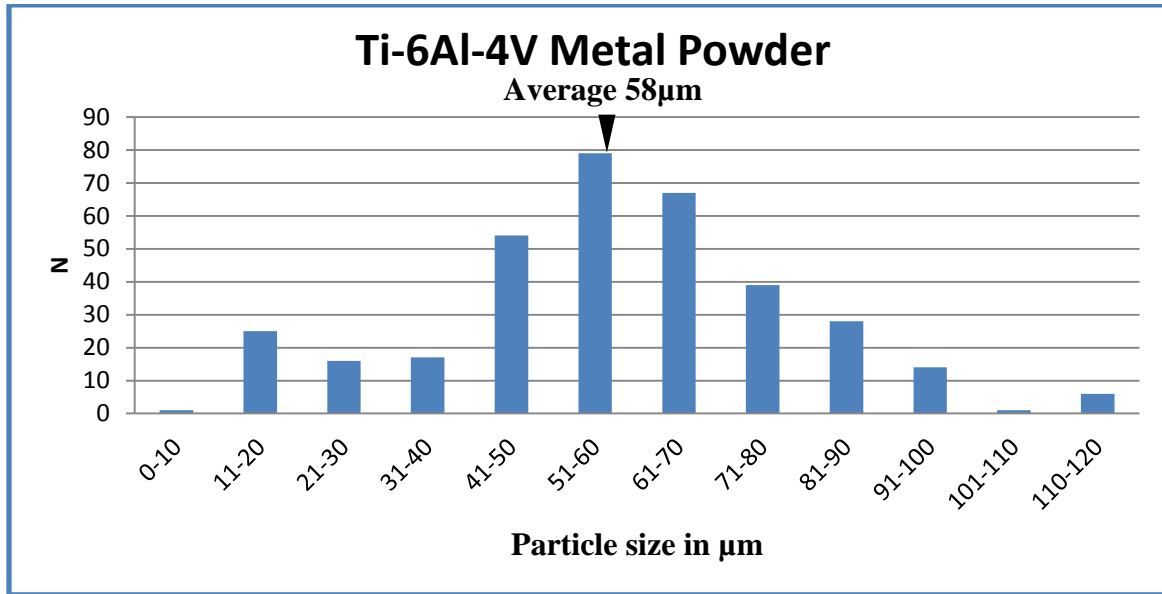


Figure 4-4 illustrates the powder distribution analysis of NSAT. The histogram describes a normal distribution curve and a mode between 60 to 69 μm . To predict the behavior of the powder inside the system during the fabrication process, some properties had to be known such as apparent density (AD), solid density, percent density change, and flow rate. It is desirable that these properties are similar to Ti-6Al-4V since this material is well developed using the EBM process. Figure 4-4 illustrates the powder distribution of Ti-6Al-4V

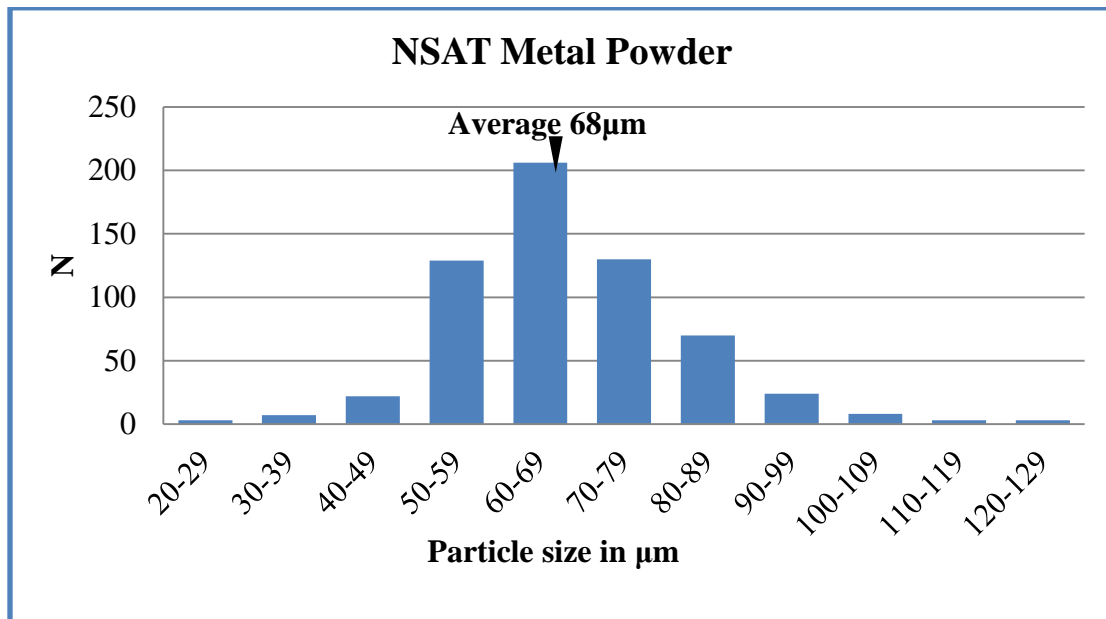


Figure 4-3 Powder distribution of NSAT metal powder

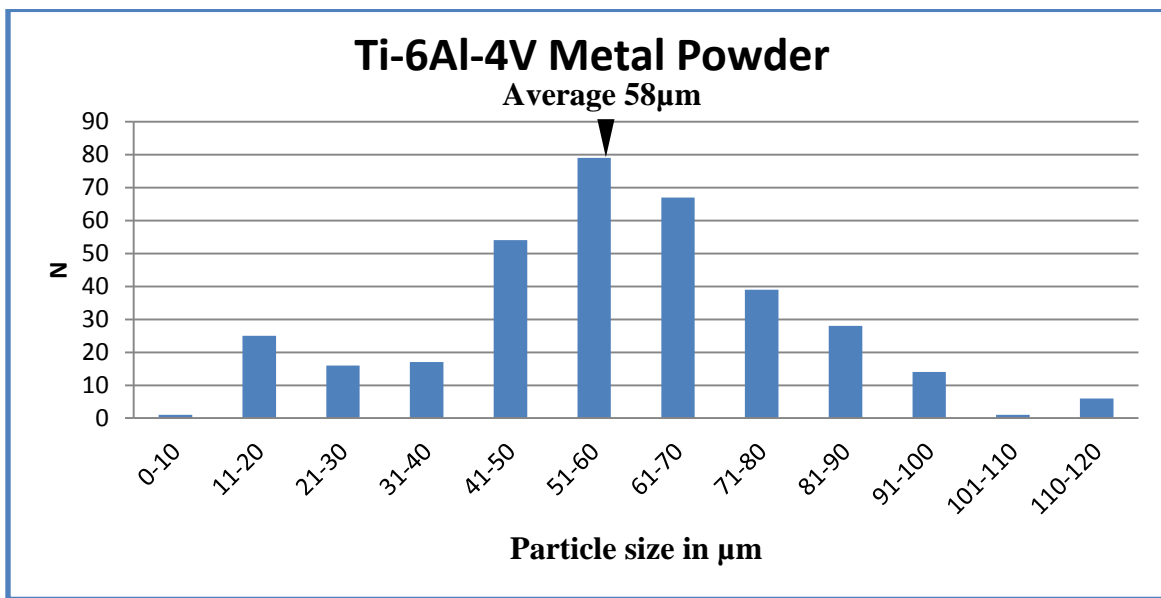


Figure 4-4 Powder distribution of Ti-6Al-4V metal powder

To calculate the apparent density, the ASTM B212-13 standard was followed. The apparent density allowed measuring the amount of mass to fill a fixed volume (ASTM Standard). The ASTM B212-13 standard procedure was essentially comprised of: 1) filling a container of a

known volume (25cm³) with metal powder using a hall flowmeter funnel illustrated in Figure 4-5, 2) weighing the mass of the powder inside the container, and, 3) calculating the apparent density using the following formula:

$$AD = M/V$$

where:

M = mass of powder in the density container in
V = Volume of the density container, cm³
AD = apparent density, g/cm³

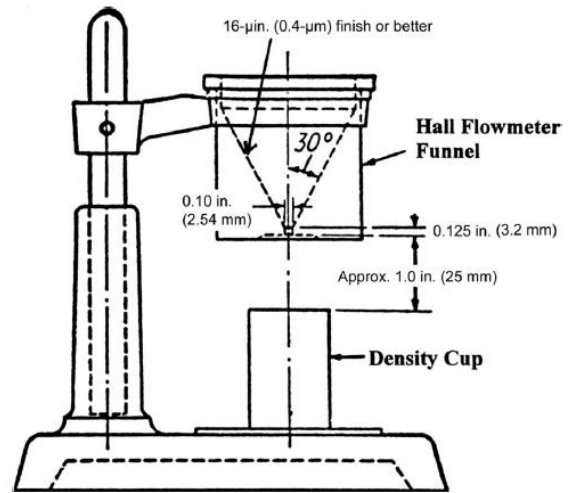


Figure 4-5 Formula for apparent density and Hall flowmeter

The solid density of NSAT was provided by GE. The percent density change is the change in density from powder form to solid form of a material. The following formula was used:

$$\% \text{ Density Change} = \text{abs} \left(\left(\frac{SD - AD}{SD} \right) 100 \right)$$

where:

SD = Solid density in g/cm³,
AD = Apparent density in g/cm³

The flow rate was measured using the ASTM B213-13 standard. This test measured flow properties of metal powders that affect homogeneity of compacted parts and production rates (ASTM Standard). The ASTM B213-13 standard procedure consisted of filling the hall flowmeter container with 50g of metal powder. The powder was discharged through an orifice in

the container. Time was recorded for the metal powder to empty the container. The units of flow rate are in s/50g that refers to how many seconds 50g of metal powder takes to empty the container. Table 4-1 illustrates a comparison of apparent density, solid density, percent density change, and flow rate between NSAT and Arcam's Ti-6AL-4V metal powders.

Table 4-1 Metal powder properties

Metal powder analysis						
Material	Manufacturer	Mass (g)	AD g/cc	Solid density (g/cc)	% Density change	Flow rate X Avg (s/50 g)
NSAT	CARPENTER	100.25	4.01	8.64	53.56	18.17
Ti-6Al-4V	ARCAM	60.75	2.43	4.42	54.98	24.99

4.2 MULTI-WAVELENGTH PYROMETER

The multi-wavelength pyrometer was installed in the Arcam S12. The pyrometer was directed to the vacuum chamber through a quartz glass window. For all the experiments, the pyrometer was pointed to the middle of the start plate and the temperature data recorded corresponded to the part fabricated in that particular place. Figure 4-6 illustrates the position of the pyrometer where the green point is the spot size (~2mm) of the pyrometer.

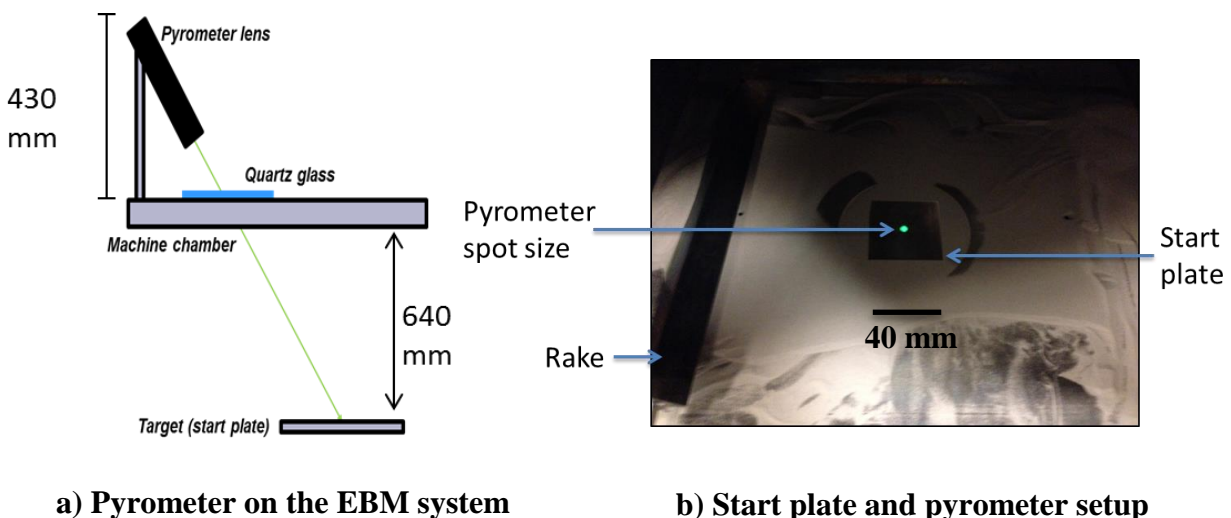


Figure 4-6 Pyrometer schematic

4.3 OPTICAL METALLOGRAPHY

Optical metallography was performed on samples fabricated in EBM utilizing a Leica Reichert MEF4 A/M (Leica Microsystems Inc., Buffalo Grove, IL) metallography microscope and photographs were recorded utilizing an Am Scope MD600 microscope (United Scope LLC, Irvine, CA) . Micrographs from samples were compared to observe the way that cracks are formed on parts during the fabrication process. The sample preparation for optical metallography was performed by the following process: First, the sample was cut from the start plate using a precision cutter powercut 10 abrasive cut-off saw (Allied high-tech products, Inc, Rancho Dominguez, CA). The sample was placed in a container of 3cm in depth with the zone of interest facing down. The sample was mounted using Koldmount (CMP Industries LLC, Albany, NY) that is a mixture of polyester and liquid solvent. Koldmount was poured into the container and solidified after 30min. The sample was then polished by placing the zone of interest on a standard 203mm rotating wheel using grinding paper. Silicon carbide grinding paper was used to polish the samples, starting from a coarse grit to a fine grit (80, 120, 180, 220, 320, 500, 800, 1000, and 1200). The sample was rotated 90° and exposed to water during polishing to obtain even planes and avoid sample heating that can change microstructure. After grinding, the sample was polished using a soft cloth with 1µm and 0.5µm alumina. The polishing process provided the sample with a mirror finish.

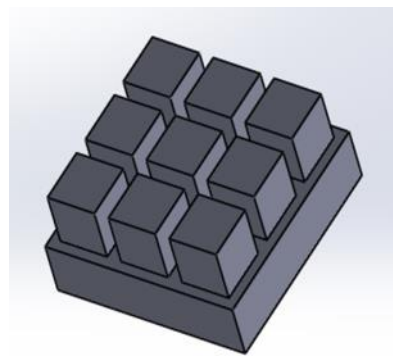
The next step of metallography was to etch the sample. Etching was used to reveal the grain boundaries of the sample's microstructure. The etchant solution used for NSAT samples consisted of 20mL of water (H₂O), 20mL of nitric acid (HNO₃), and 20mL of hydrofluoric acid (HF). The samples were exposed to an etchant solution for about 5 to 10 seconds. After etching, the sample was cleaned using an ultrasonic system and rinsed with isopropanol alcohol. After cleaning, the sample was positioned under the microscope to observe the microstructure and record photographs.

4.4 DESCRIPTION OF CUSTOM EXPERIMENTS

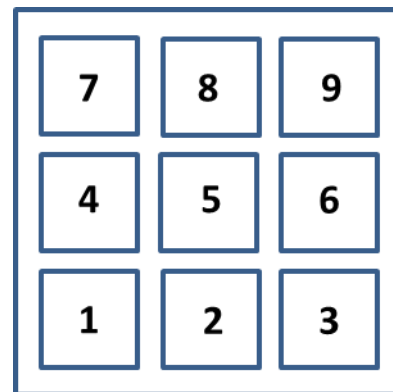
The melting point of the material needed to be known to start developing system parameters and begin fabricating parts. The melting temperature of NSAT is about 1,300°C. Initially, the experiments were focused on properly melting of the material with primary concentration on focus offset, beam speed, and beam current. Once these parameters were known, the experiments guided the modification of preheat and melting parameters that lead to improved part quality.

4.4.1 Nine cubes

The first approach was to attempt the fabrication of nine cubes of 10mm sides on a stainless steel start plate (40x40x10mm). Each of the nine cubes had different parameters focusing on beam speed, average beam current, and focus offset. The experiments were performed using the system in automatic mode. The cubes were numbered from one to nine to correlate each one with a microstructure if necessary. Figure 4-7 illustrates the experiment.



CAD model



Layer cross section

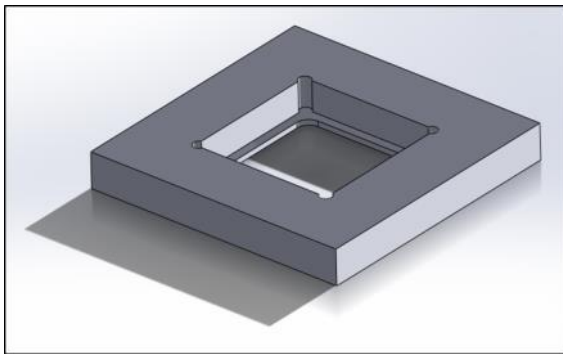
Figure 4-7 Nine cubes

It was noticed that the parameters used in the first experiments with stainless steel start plates deformed and expanded due to the parameters used. It was decided to continue with the same experiments using 40x40x10mm Rene 125 start plates to avoid deformation and expansion

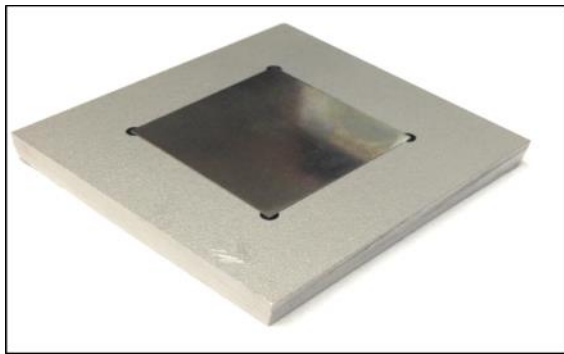
of stainless steels start plates. Re-use of Rene 125 start plates was required due to limited availability of start plate resources. The re-use of the Rene 125 start plates consisted of the following procedure: 1) the fabricated part was cut from the start plate, 2) the start plate was machined to get an even top surface and the surface was polished using 320grit grinding paper, and 3) the plate was rinsed with ethanol, dried, and ready to re-use.

4.4.2 Stainless steel mask

The Rene 125 start plate also expanded during the preheat step. A design for a mask within the start plate was fabricated to prevent the thermal expansion. The mask was made out of stainless steel since it is the material used for standard start plates from Arcam. The mask consisted of a cavity in the middle to hold the start plate. The cavity was machined with a tolerance of 0.003” for press-fit of the start plate. Figure 4-8 is an illustration of the mask. Experiments were continued with the fabrication of the nine blocks to attempt improving system parameters.



CAD model



Stainless steel mask

Figure 4-8 Stainless steel mask

4.4.3 Thin rectangular blocks

After development of system parameters to fabricate dense parts using the experimental procedure described above, one experiment was conceived to change the geometry of parts to observe any effect on the fabrication process using the same parameters. The experiment consisted of nine thin rectangular blocks. The rectangular blocks were numbered for reference. Figure 4-9 represents the design of test setup with the thin rectangular blocks.

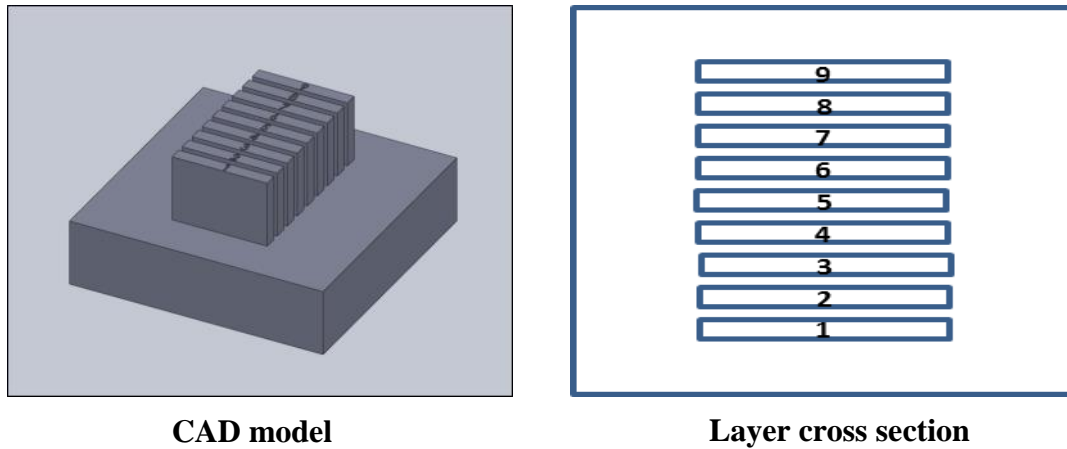


Figure 4-9 Thin rectangular blocks

4.4.4 Hollow cylinders

After some attempts to improve the system parameters, the experiments changed to a different geometry in an attempt to reduce cracking. The experiments consisted of five hollow cylinders of thickness of 1mm and height of 2.5mm. Each thin walled cylinder had different system parameters. The best parameters from the previous experiments were used but the parameters were not effective in building the parts due to the different geometry utilized. Other attempts consisted of melting hollow cylinders using only contours. Furthermore, fabrication of hollow cylinders using contours for melt and low current hatch lines was attempted to reduce the cooling rate of the forming layer. Figure 4-10 represents the design of the test setup for the hollow cylinders.

From previous experiments, it was suspected that the cracking could also initiate from the start plate and propagate to the build. A single crystal start plate material was needed to test this hypothesis. N5 single crystal cuboids were obtained to build a thin wall cylinder on top of it. The cuboid measured 17x17x10mm. Rene 125 cuboids of the same dimensions were fabricated. The experiment consisted of fabrication of the hollow cylinder using a N5 single crystal and Rene 125 cuboids to have a valuable comparison. Figure 4-11 represents the design of the test piece for this experiment.

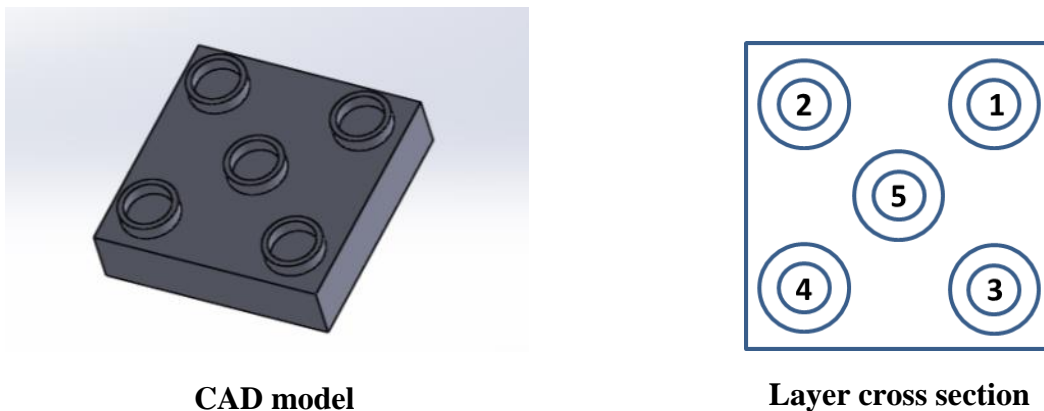
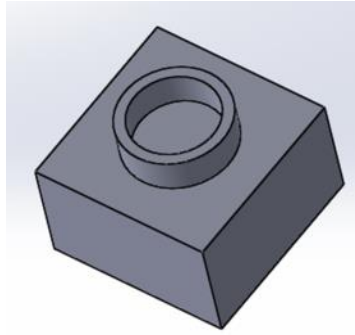
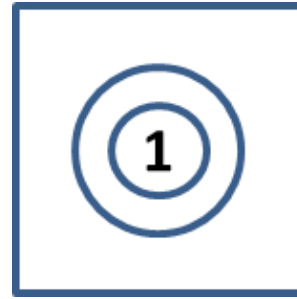


Figure 4-10 Five hollow cylinders



CAD model

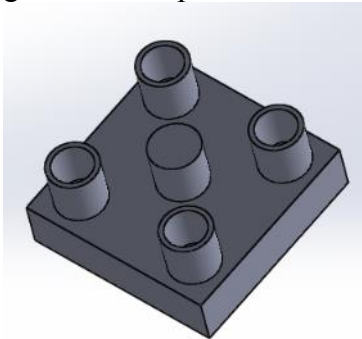


Layer cross section

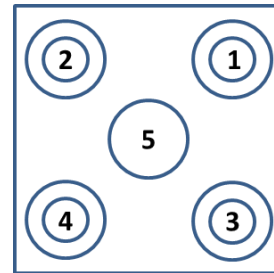
Figure 4-11 Single hollow cylinder

4.4.5 Solid cylinder

After some attempts to improve the system parameters using the five hollow cylinders, part 5 was changed to a solid cylinder that allowed observation of any difference in crack density when compared to the hollow cylinders. The height of the build changed from 2.5mm to 10mm to detect if cracks were continuous throughout the parts. Figure 4-12 shows a representation of this design of the test part.



CAD model



Layer cross section

Figure 4-12 Hollow cylinders with a solid cylinder

The solid cylinder was fabricated alone on Rene 125 start plates in an attempt to improve the system parameters and further reduce the crack density. The same experiments were done

using N5 single crystal start plates (17x17x40mm) to compare any effect on reduction in cracking. Figure 4-13 shows a representation for this test piece design.

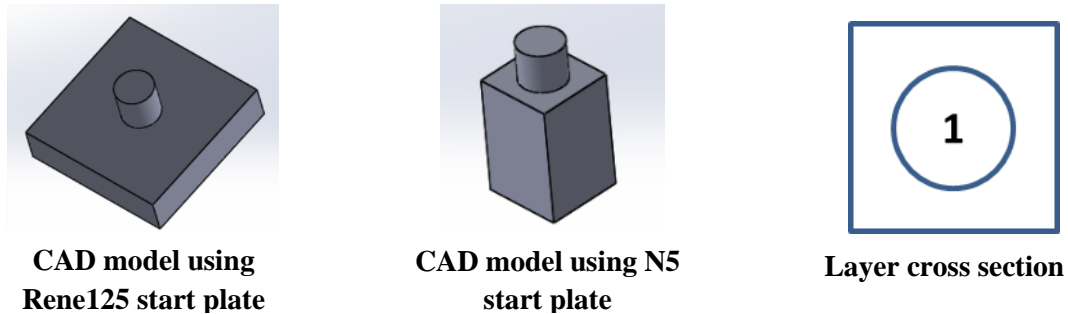


Figure 4-13 Single solid cylinder

4.4.6 Electron beam passes

To better understand the behavior of the electron beam on the NSAT material, a beam pass experiment was performed. This experiment consisted of fabricating a 40x40x10mm NSAT start plate. After fabricating the NSAT start plate, ten single electron beam passes were made on the top of the start plate, each one with different parameters focusing on changes to beam speed and beam current. This experiment allowed the analysis of hatch line depth of the electron beam on the material. Figure 4-14 illustrates the design of the test part for building NSAT start plates and the electron beam single pass experiment.

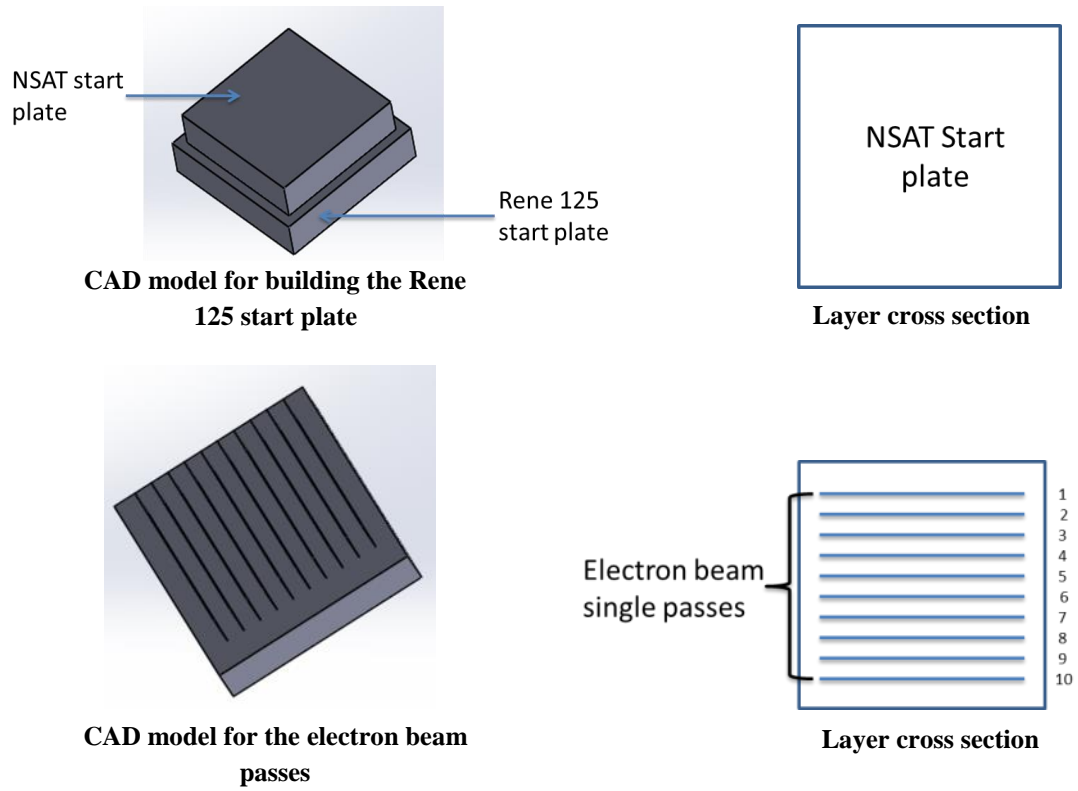


Figure 4-14 Electron beam pass experiment

CHAPTER 5 THERMAL RADIATION AND PYROMETRY

Radiant energy, or thermal radiation, is emitted by all objects when its temperature is above absolute zero. This is caused by the atomic and molecular motion related to object's temperature. With the increase in temperature the rate of emission of radiant energy per unit area increases. Therefore, the temperature of an object can be obtained by a device capable of measuring radiant energy (Harrison, 1960).

A radiation pyrometer is a device capable of measuring temperature by detecting radiant energy and displaying the temperature value (Harrison, 1960). The pyrometer is used to measure temperature of an object without being in contact with the surface of the object. This allows measuring the temperature of objects that are moving or physically inaccessible. The pyrometer needs to have a detector for radiant energy. Often the radiation detectors sense a constrained range of wavelengths. These kinds of pyrometers are used only for measuring high temperatures corresponding to those wavelengths (Harrison, 1960). The pyrometer used during this research was a multi-wavelength pyrometer developed by FAR Associates in 1997 (Felice, 2002).

5.1 MULTI-WAVELENGTH PYROMETER

The multi-wavelength pyrometer is able to measure temperatures in the range of 300°C to 2,000°C. The spectrophotometer operates in the spectral range of 500 – 1,700 nm with a spectral resolution of 1nm for a range of 500-1,000nm and 3nm for the range of 1,000-1,700nm. While measuring, the pyrometer displays and records temperature of the target object (in °C), tolerance of the measured temperature (standard deviation), and signal strength (an emissivity value at a certain wavelength) (Felice, 2002).

The multi-wavelength pyrometer functions by using a fiber optic cable that directs laser light to the object whose temperature is being measured, and detects the wavelengths emitted by using a spectrophotometer that separates the detected wavelengths. By employing an electrical transmission line, the information is sent to the device's analog-to-digital conversion system, producing computation, and finally releasing information (temperature, tolerance, and signal strength) that is displayed by a desktop computer. Figure 5-1 illustrates the schematic of the multi-wavelength pyrometer from FAR Associates.

5.2 INSTALLATION

In its commercial state, the Arcam S12 system contains a standard video camera to observe part fabrication. The camera is installed externally on the top of the chamber and looks through the inside of the system through a lead glass window. The camera is installed using a stainless steel bracket that fully encloses both the camera and the glass window. To install the multi-wavelength pyrometer through the camera window, the camera components were removed from the system. Figure 5-2 (a) illustrates the pyrometer looking thorough the inside of the

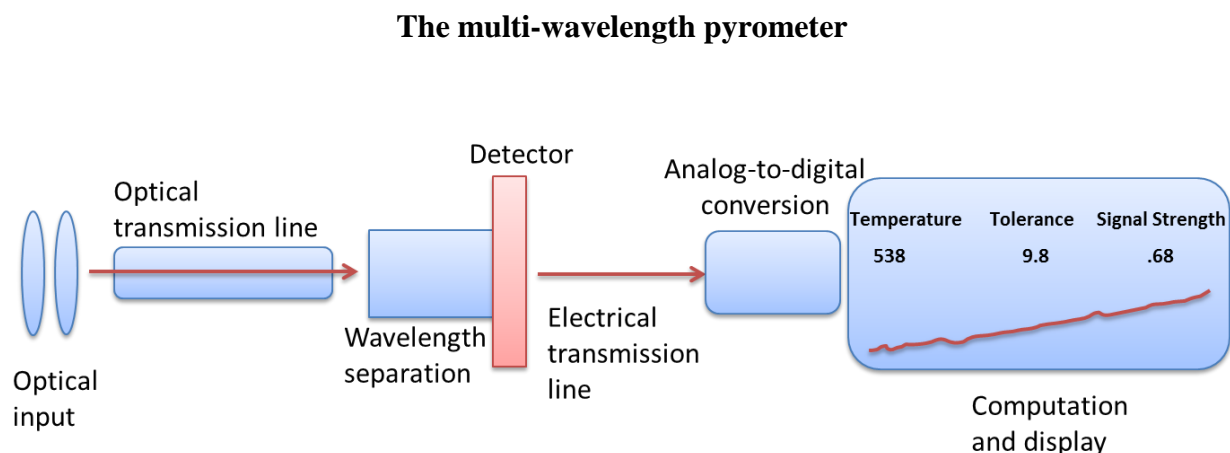
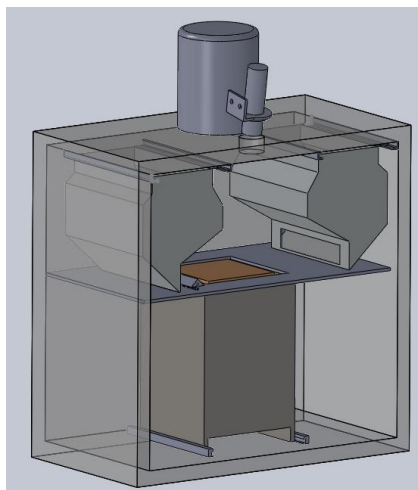


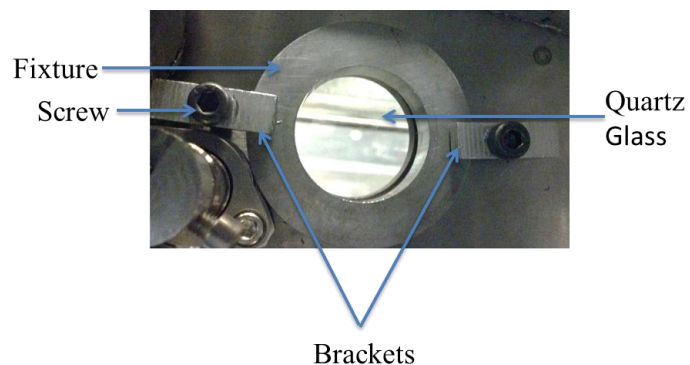
Figure 5-1 Schematic of the multi-wavelength pyrometer developed by FAR Associates (Felice, 2002)

system. FAR Associates recommended using quartz glass for optimum measurements since quartz glass transmission spectrum covers the spectral range that the multi-wavelength pyrometer (500 – 1,700 nm) is capable of detect. Quartz glass windows were manufactured as the same dimensions as the open view port. Fixtures and brackets were designed and fabricated to maintain a good seal on the top of the chamber and ensure the system was able to obtain appropriate vacuum levels for fabrication ($\sim 10^{-4}$ torr). The fixture consisted of a stainless steel ring fitting the outside contour of the quartz glass. Two aluminum brackets press the fixture onto the glass using screws. Figure 5-2 (b) describes the fixture and the bracket installed on the system and in section 5.2.2 a radiation shield is discussed.

The multi-wavelength pyrometer from FAR Associates consisted of the device console, a fiber optic cable, and the focusing lenses. Figure 5-3 illustrates the components of the multi-wavelength pyrometer. The fiber optic is very delicate; thus, if bent more than a 6in (152mm) radius the cable will break and the system will stop working. The position of the fiber optic cable is important to maintain a safe range of bending and avoid damage. For this reason, the console was positioned on the top of the machine's frame and the fiber optic cable was connected to the lenses by a small drilled hole on the top of the frame. The pyrometer displays the information



a) Pyrometer pointing inside the EBM system



b) Fixture and brackets installed on the EBM System

Figure 5-2 Pyrometer and Fixture

(temperature, tolerance, signal strength) to the operator by using a laptop computer. The computer records these data in log files according to the date and time.



a) Multi-wavelength pyrometer console



b) Fiber optic cable



c) Lens assembly with angle bracket

Figure 5-3 The multi-wavelength pyrometer components

5.2.1 Quartz glass metallization

The pyrometer points to the inside of the EBM system from a quartz glass window. The quartz glass measured 65.85mm in diameter and 9.52mm in thickness. Each quartz glass cost about 37 USD. The quartz glass must be clean and free from any impurities when preparing the system for fabrication to obtain optimum data using the pyrometer. During the preheat step, powder explosions occur occasionally due to a rapid increase in negative charge of metal powder particles. These rapid expulsions of metal powder particles might cover a part of the quartz glass, affecting the pyrometer's measurements. When the electron beam is melting the powder, elements with low melting temperatures (e.g. aluminum) vaporize causing metallization on the quartz glass. After a certain period of time, metallization will decrease the accuracy of the pyrometer to the extent where the pyrometer stops displaying data. The time of the quartz glass metallizing completely depends on the size of the layer being formed. The larger the cross

section being melted, the greater the vaporization that causes the quartz glass metallizing faster. For this reason, a process to remove metallization was implemented. The procedure consisted of cleaning the quartz glass with isopropanol alcohol. Then, the quartz glass was polished in a standard 8 inch (203mm) rotating wheel using a soft cloth and alumina of 1 μ m. The glass was rotated 90° to have an even surface and polished until metallization was reduced. Figure 5-4 illustrates a metallized and a polished quartz glass. During the experiments four quartz glasses were available. After each experiment the quartz glass was metallized and polished was needed.

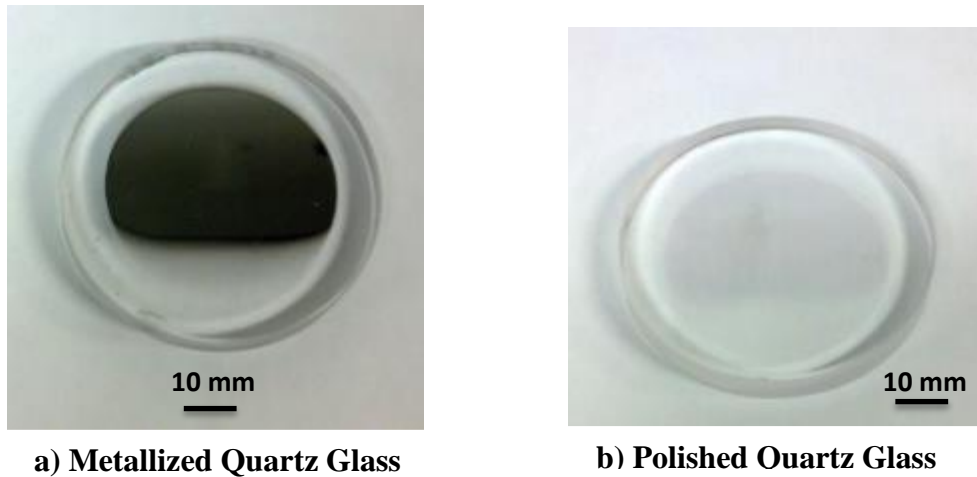


Figure 5-4 Quartz glass

An experiment was performed to compare if there was any effect on the pyrometer's measurements between using a new and a polished quartz glass. The experiment consisted of pointing the pyrometer to a digital hot plate set to ~530°C. When the pyrometer temperature measurement was stable, a new quartz glass was placed between the pyrometer and the hot plate. Then, the new quartz glass was removed and replaced with a polished quartz glass. In both cases, the pyrometer displayed only a 1°C temperature change, concluding that polished quartz glass can be used for experiments. Also, a metallized window was placed between the pyrometer and the hot plate to observe the effect on the measurements. The pyrometer displayed “signal below range” meaning that the pyrometer was not detecting temperature above 300°C. Thus, pyrometer

readings are not reliable when quartz glass is metallized. Figure 5-5 represents the setup for the quartz glass experiment.

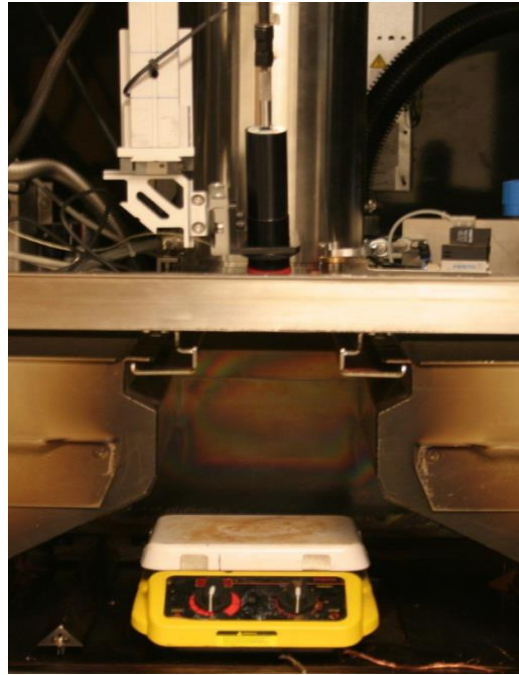
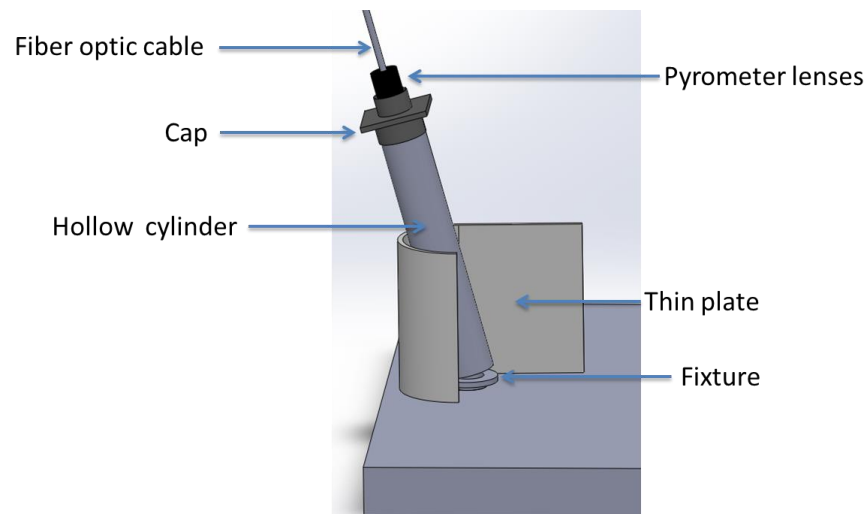


Figure 5-5 Experiment Setup

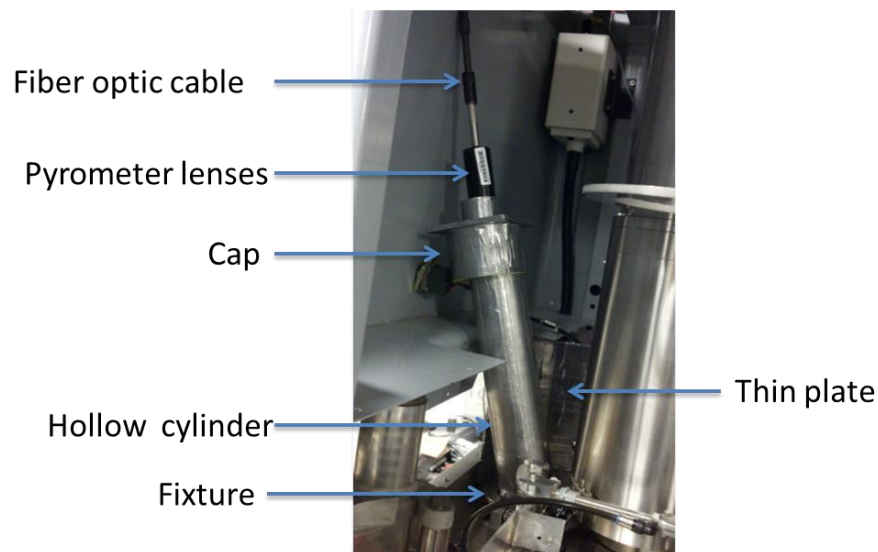
5.2.2 Radiation shielding

During the fabrication process, X-rays are emitted by electrons generated from the electron beam (Arcam AB, 2011). The vacuum chamber, the lead-coated glass windows, and the heat shields are specifically designed to enclose the emitted X-rays allowing the external emissions to remain within approved levels (Arcam AB, 2011). The human body has living tissue that can be damaged by ionizing radiation. Alpha and beta particles, gamma and X-rays are common types of ionizing radiation (U.S. Environmental Protection Agency, 2012). Radiation causes negative effects in human health by producing nausea, weakness, hair loss, skin burns, diminishing organ functions, changes in DNA, and cancer (U.S. Environmental Protection Agency, 2012).

Since the bracket from the camera was removed, and the lead-coated glass was replaced with a quartz glass, a radiation shield was crucial to prevent radiation exposure to the EBM user. Being that the space around the quartz glass was limited; the radiation shield had to be thin. The design also needed a curvature for optimum protection due to the limited space. The shield design consisted of a thin plate with a curvature around the quartz glass fixture and a hollow cylinder on top of the fixture to prevent radiation exposure and hold the pyrometer in place.



a) Radiation shield CAD model



b) Radiation shield installed in the Arcam S12 system

Figure 5-6 Radiation shield

Since lead is most commonly used for radiation shielding due to its high density, high atomic number, and its ability to scatter or absorb radiation, a thin (0.0047in) lead foil was purchased. The lead foil is used to protect parts from x-rays, radiation, dust, and chemicals. The temperature range for the lead foil is from -34°C to 107°C. It was decided to use stainless steel for both the thin plate and the hollow cylinder and cover each with lead foil. A cap was designed to fill the space between the hollow cylinder and the pyrometer. The cap was fabricated by AM using a U-print system and also covered with lead foil post-fabrication. Figure 5-6(a) illustrates the CAD model for the radiation shield. Figure 5-6 (b) describes the radiation shield installed on the Arcam S12 EBM system. The department of Environmental Health and Safety at The University at El Paso (UTEP) was contacted to measure the radiation levels with specialized radiation equipment Fluke 481 radiation detection meter (Fluke Corporation, Everett, WA) while the machine was in operation to ensure there was no harmful radiation was emitted from the system. The equipment did not detect harmful levels of radiation (0.04 $\mu\text{Sv/h}$) emitted by the EBM system during operation.

5.3 CHARACTERIZATION OF THE EBM PROCESS USING THE MULTI-WAVELENGTH PYROMETER

5.3.1 Validation of the multi-wavelength pyrometer

To understand the accuracy of the multi-wavelength pyrometer, an experiment was performed that consisted of drilling a hole in the middle of a standard start plate (150x150x10mm) to expose the system thermocouple to the surface. The multi-wavelength pyrometer was pointed to the start plate with the spot size next to the thermocouple to compare temperature readings. The start plate was heated by the electron beam and the process was stopped and the plate was allowed to cool. Figure 5-7 illustrates the results from the experiment. To compare the temperature measurements between the multi-wavelength pyrometer and the system's thermocouple, the temperature data were graphed utilizing MATLAB. Figure 5-8 is a MATLAB graph of temperature (in °C) vs time (in seconds). The red plot is the thermocouple and the blue plot is the multi-wavelength pyrometer. The initial peak on the blue plot is due to

the pyrometer calibrating itself. Initially, the temperature data are proximate, then, the thermocouple data intersects with the pyrometer data showing a higher temperature than the pyrometer. One possible explanation is following: First, the electron beam was heating the start plate and the thermocouple. Then, the start plate reached a stable temperature of about 940°C and the electron beam continued to heat the thermocouple. The average percent difference between the thermocouple and the pyrometer graphs during the heating of the start plate is 3.08% and during the cooling process is 1.9%. After the process was stopped both temperatures were approximately equal, thus it was concluded that the temperature measurements from the pyrometer meet an approximate temperature value that is coherent to the thermocouple data obtained.

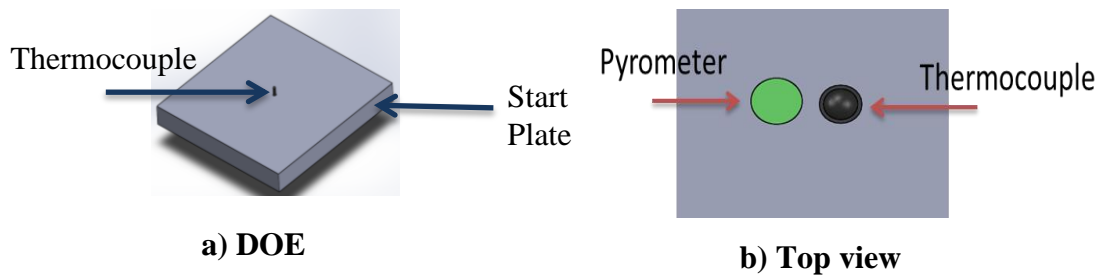


Figure 5-7 Experiment for comparison of surface temperature between the multi-wavelength pyrometer and the system's thermocouple.

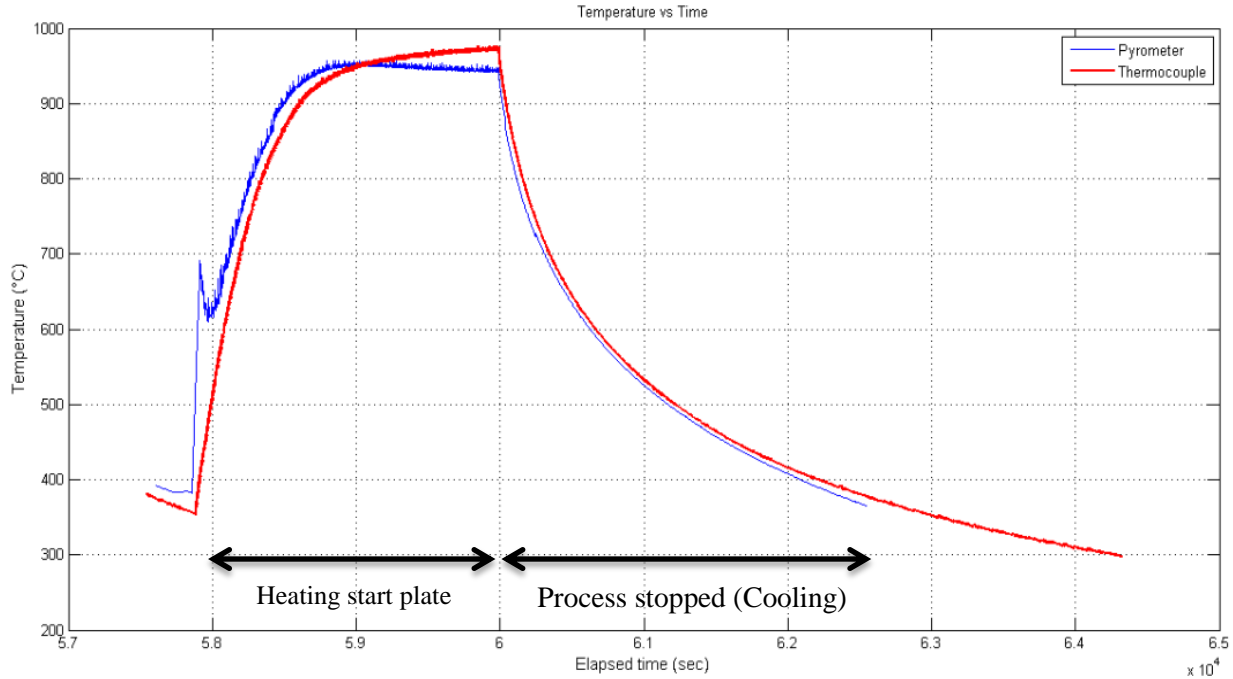
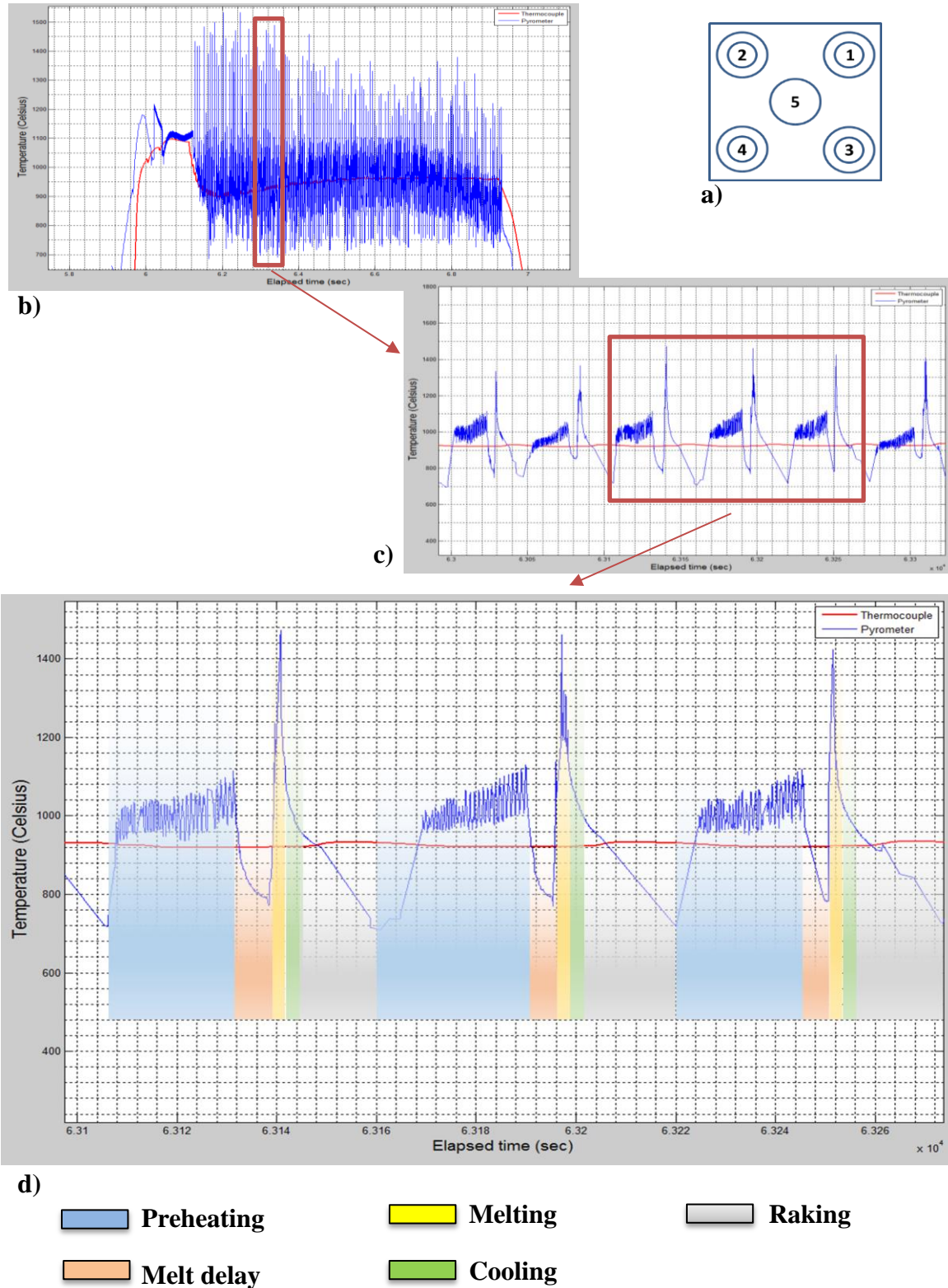


Figure 5-8 Temperature graphs from the thermocouple and the multi-wavelength pyrometer

5.3.2 Characterization of the EBM process

One of the advantages of utilizing the multi-wavelength pyrometer with the EBM system is the user ability to identify surface temperatures of the build during the fabrication. The surface temperature of the build during the fabrication process is important information when developing parameters for novel materials. This information allowed the determination of the temperature to ensure an appropriate sinter of the material (~50% of the material's melting point) was reached, ensure the melting point of the material was achieved for appropriate melting, measure the temperature before melting, cooling rates, and temperature decay due to raking; all which affect part fabrication. The thermal feedback from the multi-wavelength pyrometer allowed the modification of parameters based on temperature during fabrication steps to obtain desired surface temperature on each step. For example, if the temperature after the preheat step is not at least 50% of the material's melting point, formation of melt balls can occur. With the multi-wavelength pyrometer, the operator can ensure that a desired surface temperature is obtained after each step to help improve the quality of the parts.

To characterize the EBM process, a test was performed using the ‘solid cylinder’ experiment explained in chapter 4 (Figure 5-9). The multi-wavelength pyrometer was pointing to the middle of part 5. Figure 5-9(a) is a layer cross section of the experiment. Figure 5-9(b) is the MATLAB graph with the multi-wavelength pyrometer plot (blue) and the thermocouple plot (red). Figure 5-9 (c) is a zoomed view from the graph in Figure 5-9 (b) to observe the surface temperature pattern during the fabrication process. Figure 5-9 (d) is the characterization of the EBM process during this experiment. The process consisted of preheating, part melt delay, melting, cooling, and raking. The melt delay occurred because part 5 was the last part to be melted by the electron beam, thus, the melt delay is evident when the electron beam was melting part 1, 2, 3, and 4.



**Figure 5-9 Characterization of the EBM process using the multi-wavelength pyrometer;
a) solid cylinder; b) Temperature graph; c) surface temperature pattern; d)
characterization of the EBM process**

5.3.3 Cooling Rates

To gain a sense of the rate of the solidification process for the part measured by the pyrometer, the cooling rate was calculated by using the temperature graphs. This calculation is only an approximation and was done to compare cooling rates between experiments. To calculate the cooling rate, the following formula was used:

$$C.R. = \frac{\Delta \text{Temperature}}{\Delta \text{Time}}$$

Where:

C.R. = Cooling rate in $^{\circ}\text{C/s}$

$\Delta \text{Temperature}$ = Change in temperature in $^{\circ}\text{C}$ from the peak during melting to raking

ΔTime = Change in time in seconds between the peak during melting to raking

A MatLab code was developed to calculate the cooling rates. The code consisted in finding a linear regression from the temperature vs time graph by defining a time range. The time range was defined by two points. The first point was the highest point during the melt process. The last point was taken from the graph before the slope changed dramatically, implying that raking process has begun. The code calculated the slope of the linear equation or cooling rate. Figure 5-10 describes two examples of cooling rates.

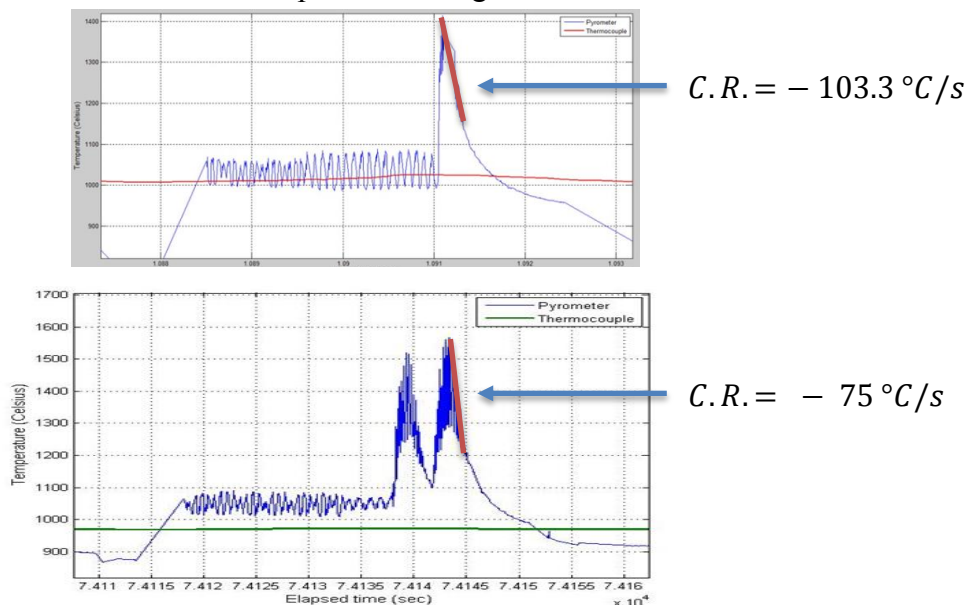


Figure 5-10 Example of cooling rates

CHAPTER 6 RESULTS

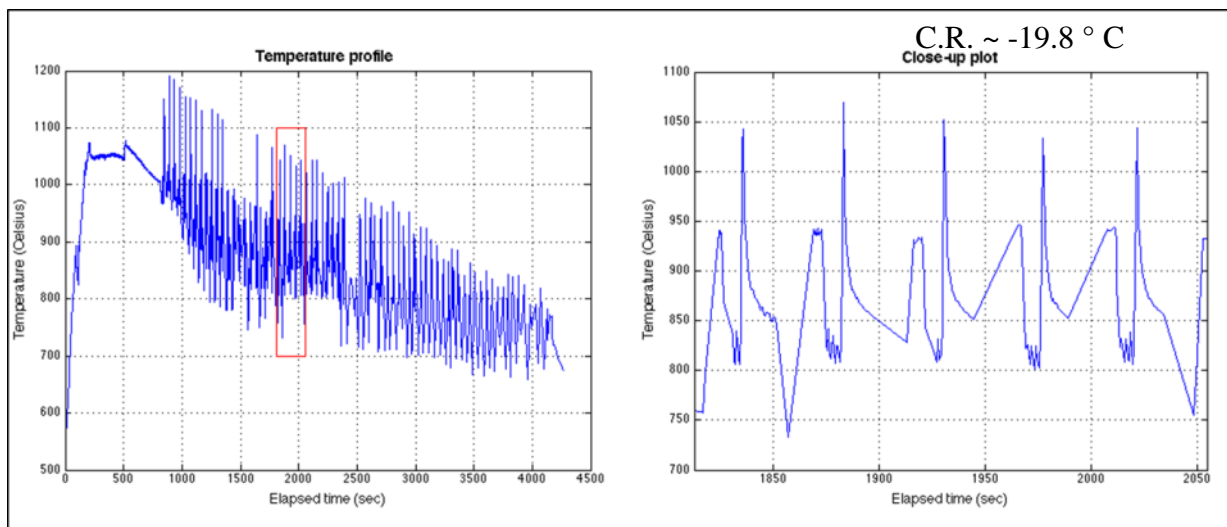
Results presented in this section represent experiments (builds) performed for GE to achieve crack free parts of NSAT alloy via fabrication using EBM technology. Each experiment is divided by date (in red) and depicts the parameters utilized, resulting part, temperature graphs (from system's bottom temperature and pyrometer where applicable), and noteworthy microstructure. It is important to note that various other experiments were performed with failed results and without successful fabrication. Such failed attempts are not shown in this chapter (included on appendix) but allowed for improved experiments that resulted in near crack-free parts. Since the focus of these experiments was to reduce crack and crack growth, initial parameter development for NSAT is not shown in this chapter (included on appendix). It is important to note that these experiments may not render the same results if a different setup is utilized including, but not limited to: system configuration, system model, start plate size, and start plate composition.

Date: 10/23/13

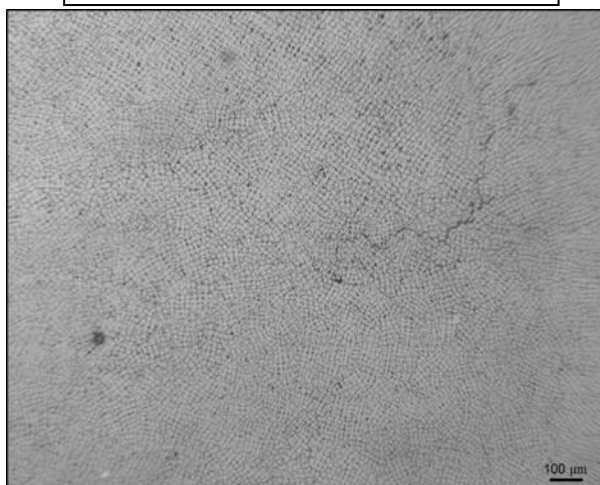
After finding workable parameters and build temperature ranges, experiments were performed to find the optimal speed, current and focus offset parameters. An experiment, consisting of 9 parts,

ng of 9	SP: 200 AC: 5 FO: 17	SP: 200 AC: 5 FO: 19	SP: 200 AC: 5 FO: 21
parts,			
was	SP: 175 AC: 5 FO: 17	SP: 175 AC: 5 FO: 19	SP: 175 AC: 5 FO: 21
develop			
ed and	SP: 150 AC: 5 FO: 17	SP: 150 AC: 5 FO: 19	SP: 150 AC: 5 FO: 21

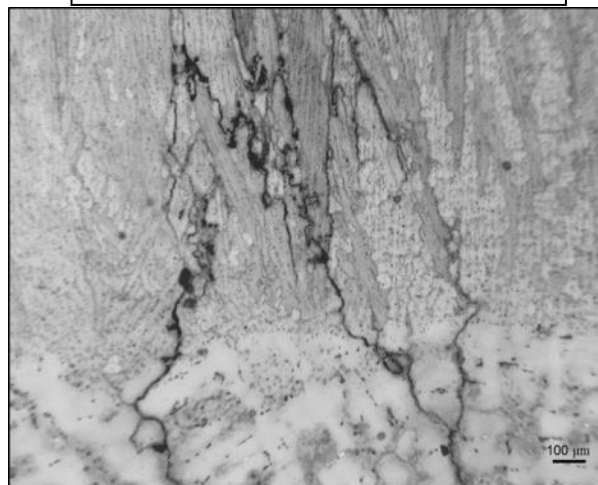




Horizontal micrographs of part 1

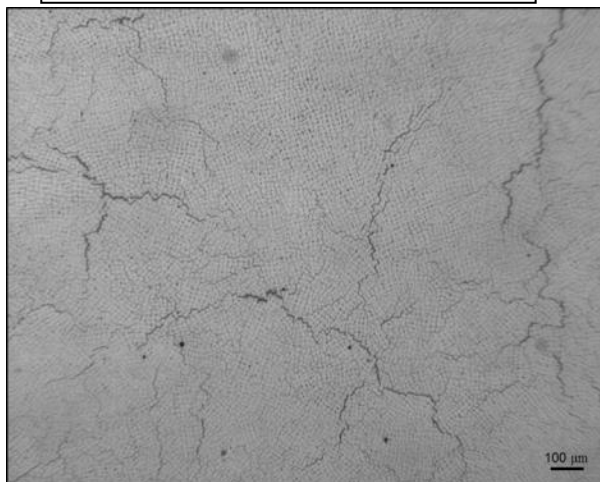


Vertical micrographs of part 1

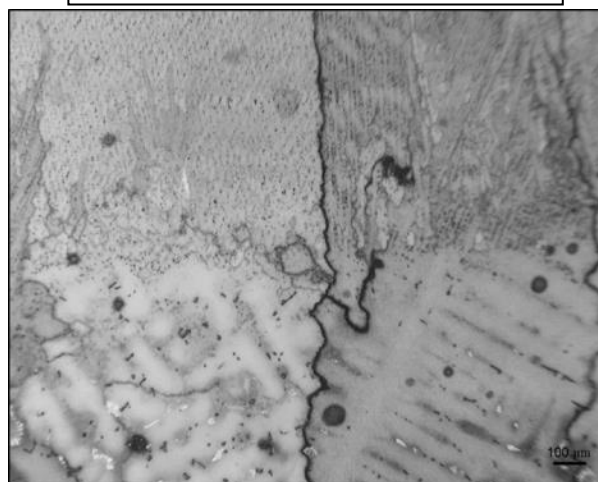


parameters of the test are as follows:

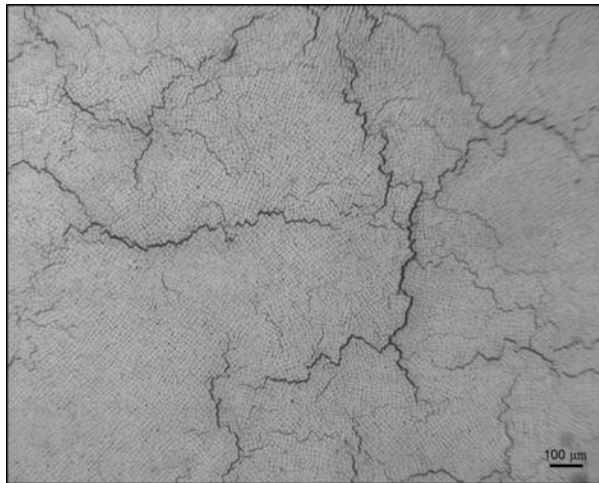
Horizontal micrographs of part 4



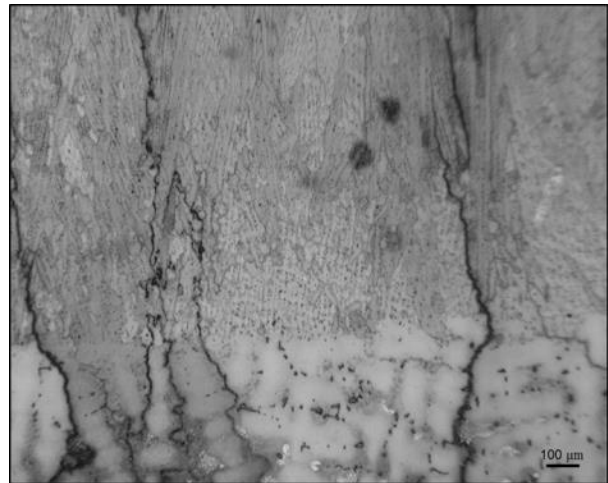
Vertical micrographs of part 4



Horizontal micrographs of part 7



Vertical micrographs of part 7



Date: 10/31/13

As shown by the previous experiment, noteworthy cracking was evident in the microstructure. For this build, the helium purge was delayed in an attempt to reduce the thermal decay post fabrication. In its commercial state, the EBM system purges helium into the vacuum chamber to expedite cooling time; however this additional cooling medium was thought to add thermal stresses that affected crack density for NSAT. Upon microstructure examination, the parts did not show improvement in crack density.

SP: 75
AC: 4.25
FO: 17

SP: 75
AC: 4.25
FO: 19

SP: 75
AC: 4.25
FO: 21

SP: 100
AC: 4.25
FO: 17

SP: 100
AC: 4.25
FO: 19

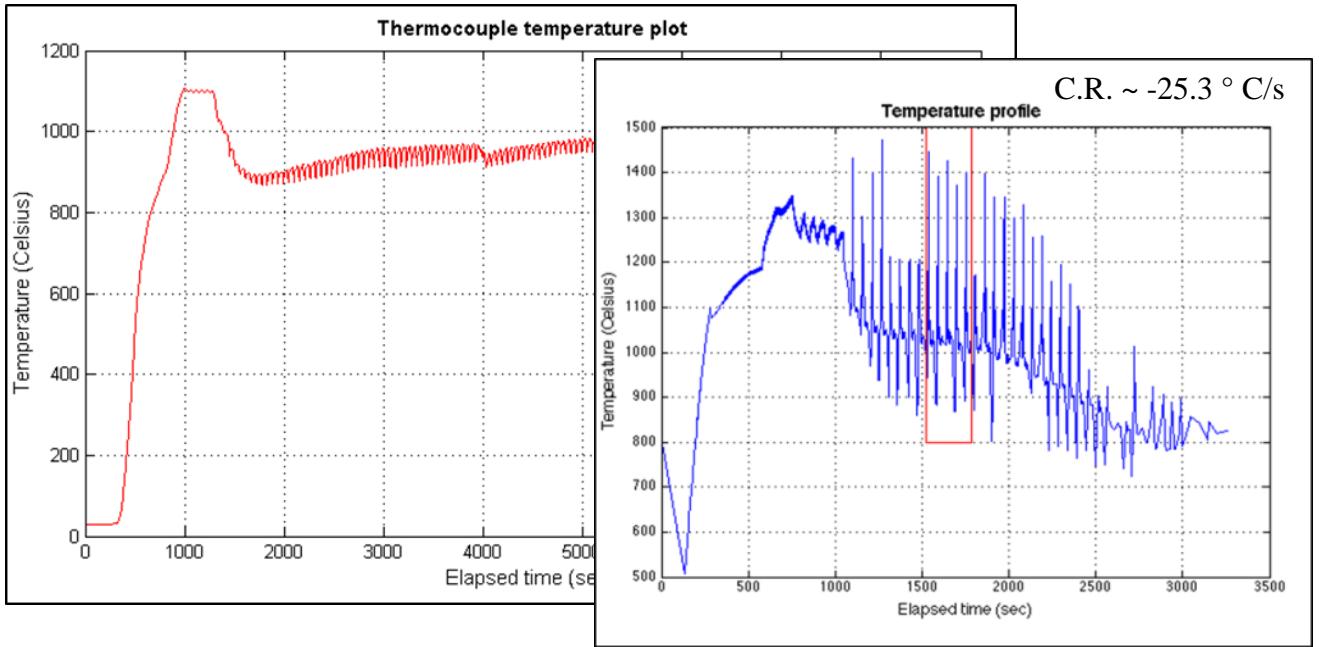
SP: 100
AC: 4.25
FO: 21

SP: 125
AC: 4.25
FO: 17

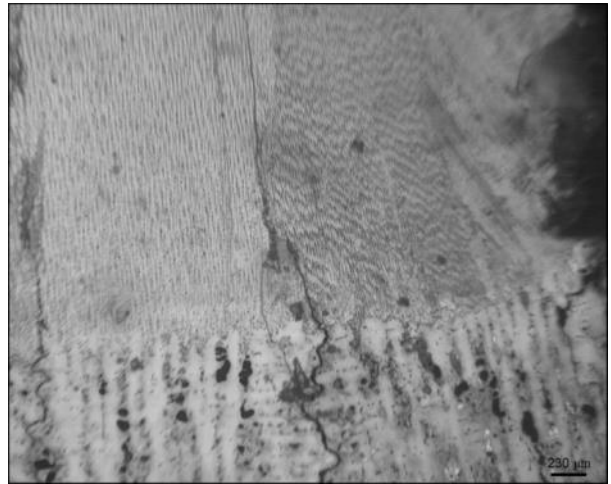
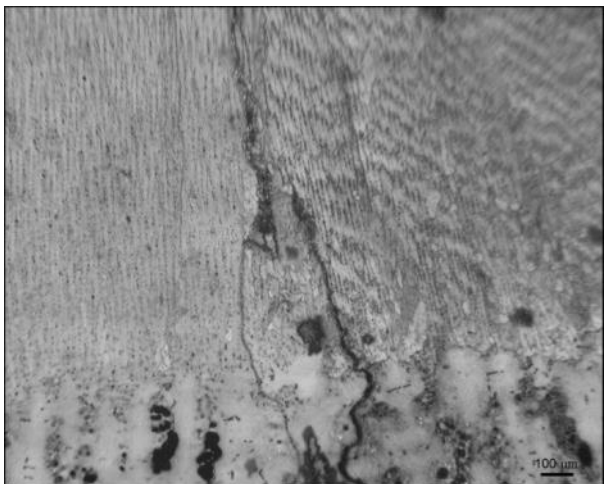
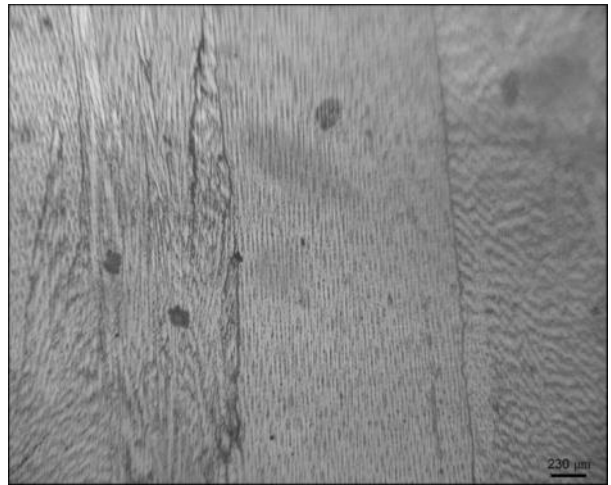
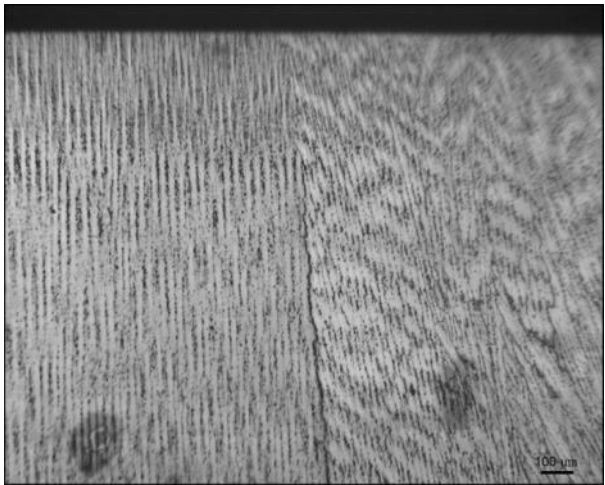
SP: 125
AC: 4.25
FO: 19

SP: 125
AC: 4.25
FO: 21





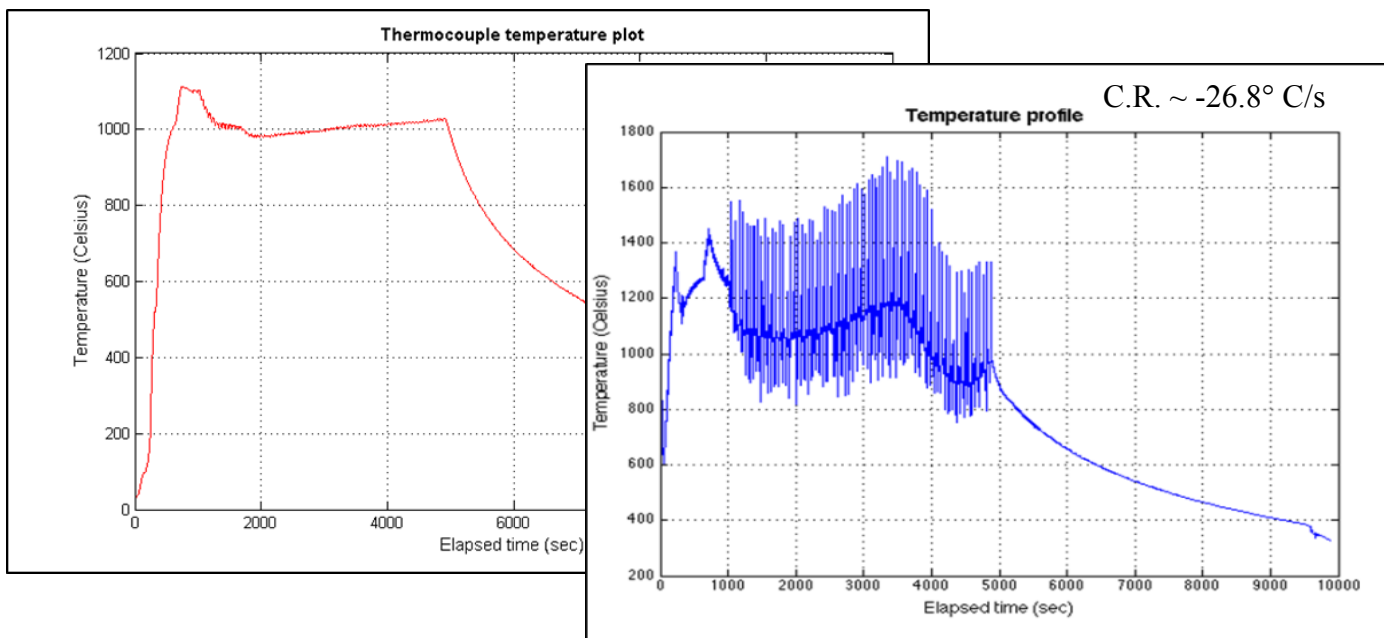
Vertical micrographs of part 5



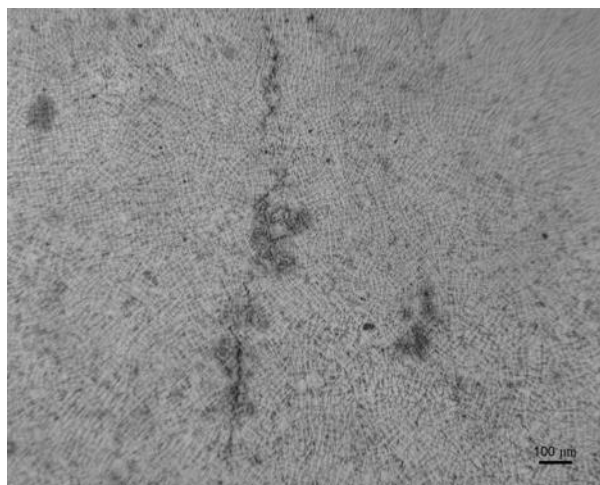
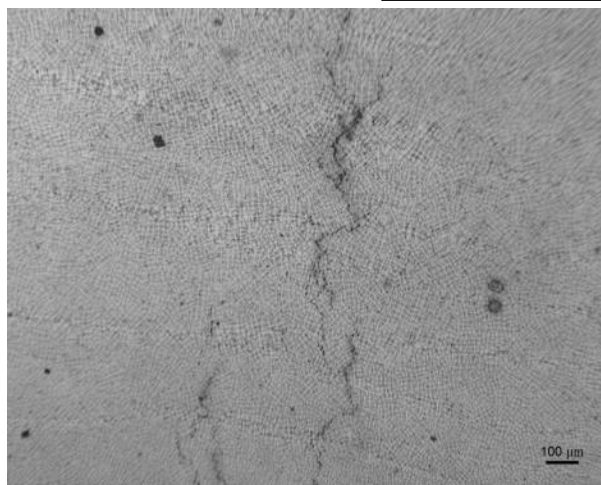
Date: 11/07/13

The melt order for this build was changed and is as follows: 5, 1, 3, 9, 7, 2, 6, 8, and 4. This was performed primarily to optimize acquisition of pyrometer measurements since the spot for measurement was focused on part 5 and further notice the effect of scan sequence (to see if melting immediately after preheating had a noteworthy effect on crack density). The scanning sequence does have some effect on the cracks seen in the horizontal micrographs. Part 5 did not present cracks on the horizontal micrographs.

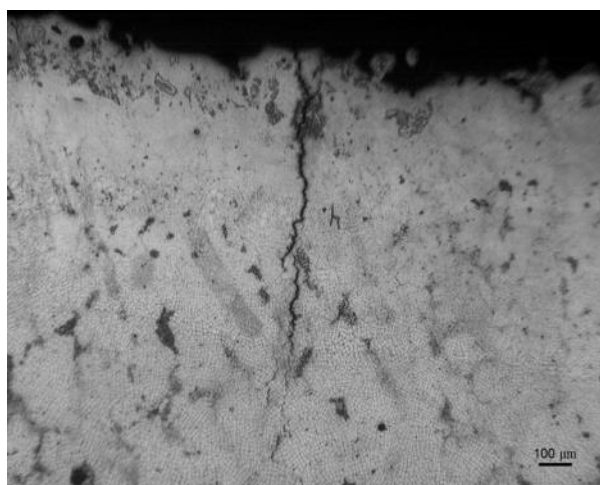
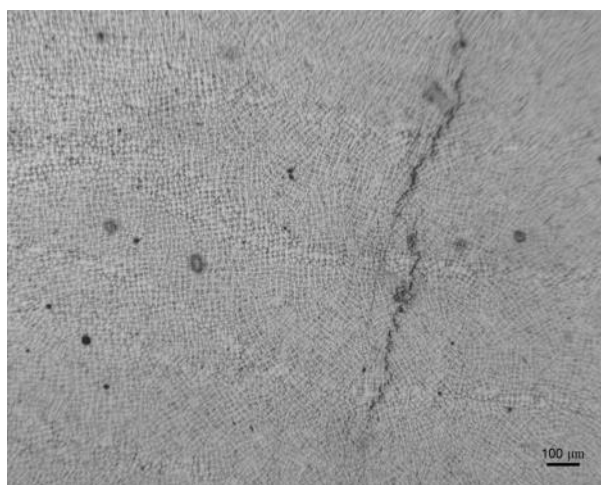
SP: 80 AC: 4.0 FO: 19	SP: 100 AC: 4.25 FO: 19	SP: 80 AC: 4.0 FO: 20
SP: 100 AC: 4.25 FO: 19	SP: 100 AC: 4.25 FO: 19	SP: 100 AC: 4.25 FO: 19
SP: 90 AC: 4.25 FO: 19	SP: 100 AC: 4.25 FO: 19	SP: 90 AC: 4.25 FO: 20



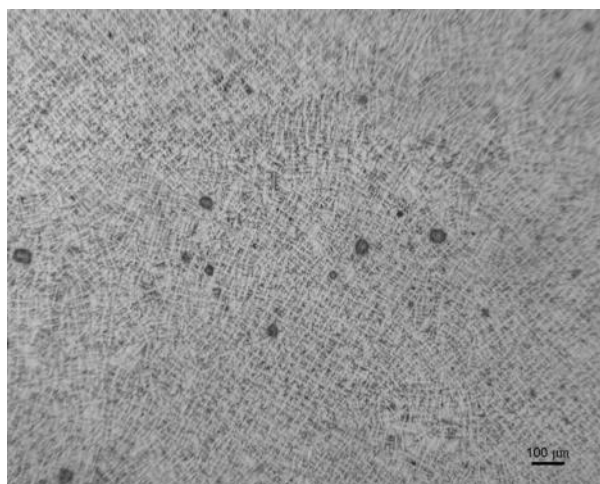
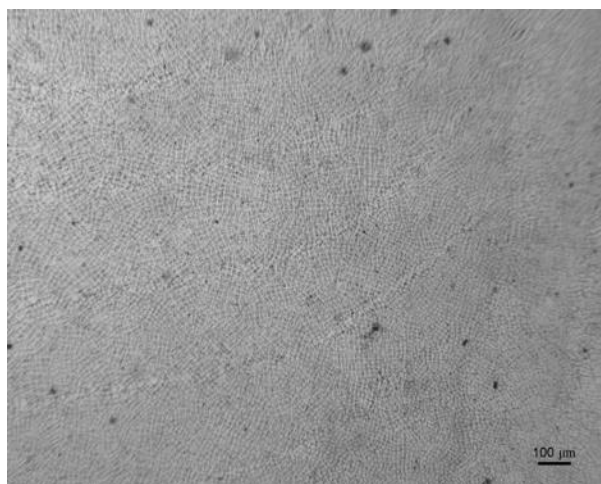
Horizontal micrographs of part 2



Horizontal micrographs of part 4



Horizontal micrographs of part 5



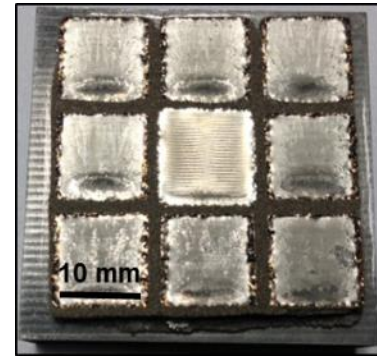
Date: 11/18/13

Additional melts were used to attempt and reduce the cooling rate of each layers melt step allowing for reduced thermal stresses. Sixteen melt steps were used for part five, starting at 4.25 mA each subsequent melt reduced the current by 0.25 mA. The powder bed was cooling too fast, the process was stopped and the start plate heating was done to increase the temperature. Afterward, 6 of the melt steps were disabled for part 5. Cracks were still evident upon microstructure analysis.

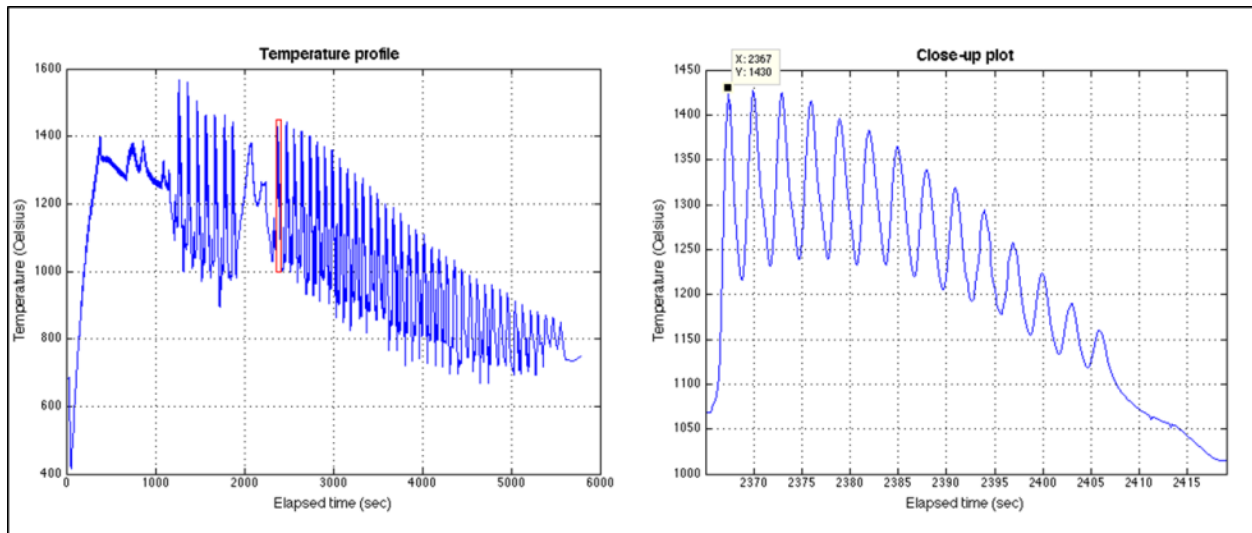
SP: 75 AC: 4.25 FO: 17	SP: 75 AC: 4.25 FO: 19	SP: 75 AC: 4.25 FO: 21
SP: 100 AC: 4.25 FO: 17	SP: 100 AC: 4.25 FO: 19	SP: 100 AC: 4.25 FO: 21
SP: 125 AC: 4.25 FO: 17	SP: 125 AC: 4.25 FO: 19	SP: 125 AC: 4.25 FO: 21

SP: 100
AC: 4.0 → 0.25
FO: 19

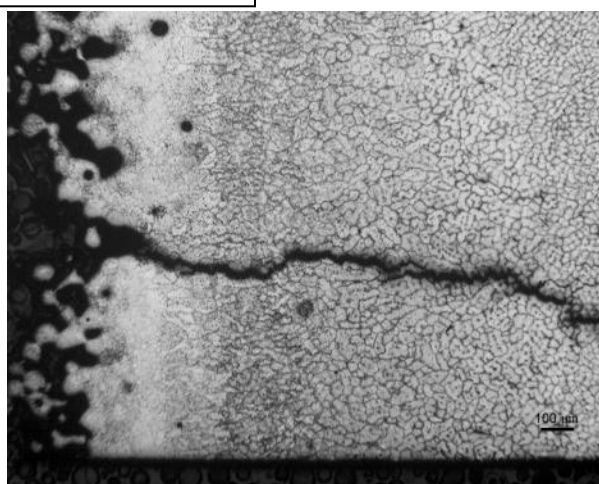
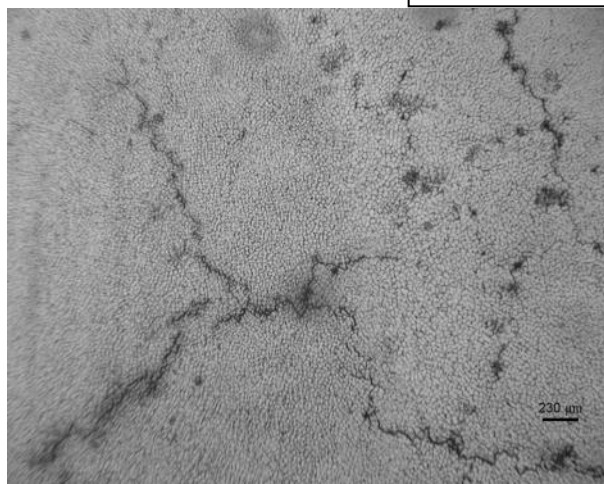
x 16



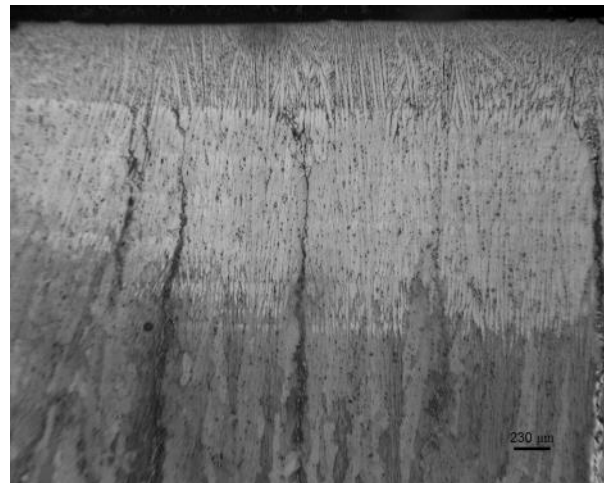
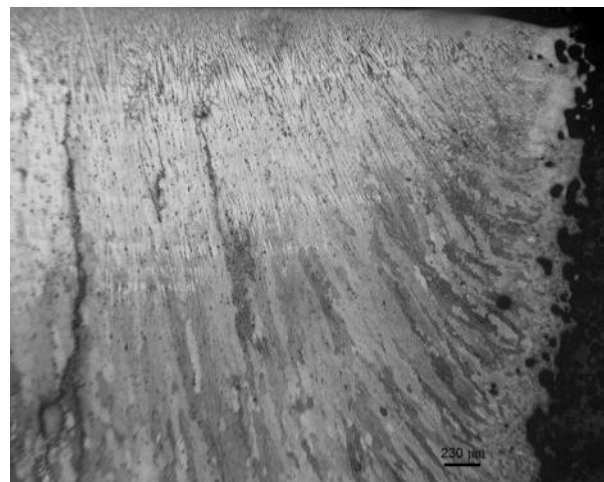
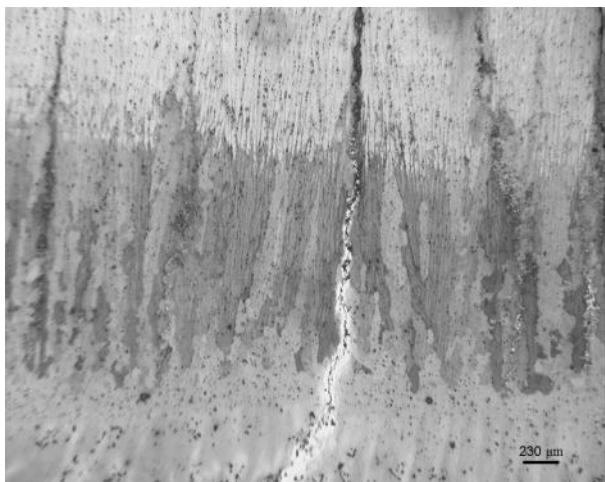
C.R. ~ -18.6° C/s



Horizontal micrographs of part 5



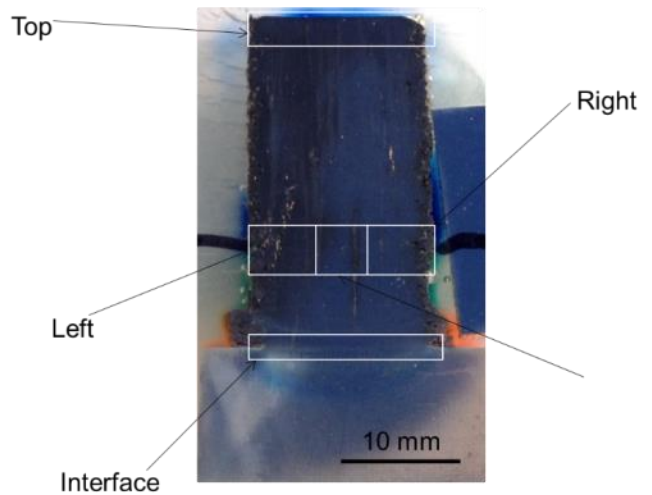
Vertical micrographs of part 5



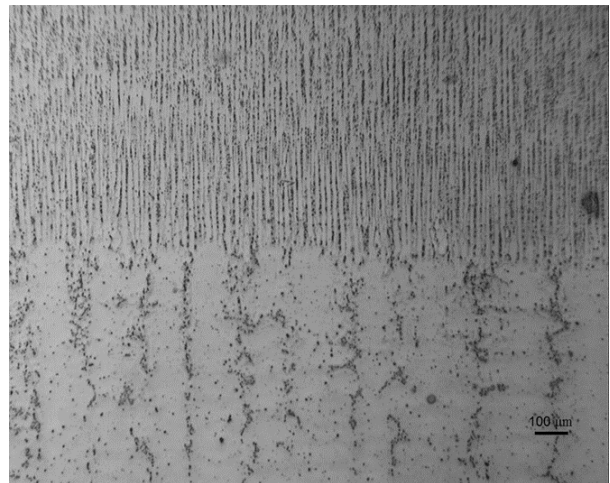
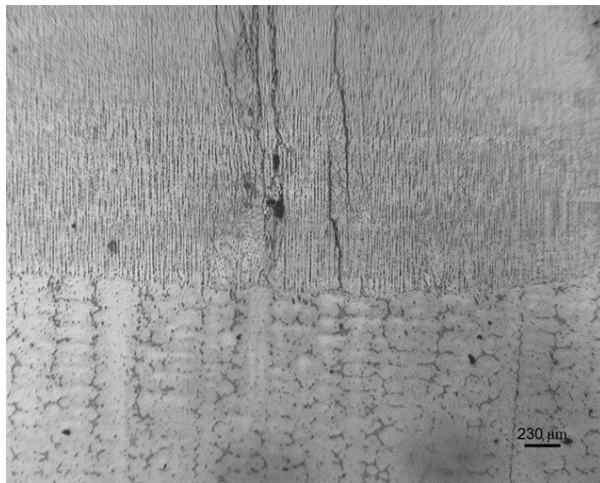
Date: 11/25/13

Automatic mode was used for seven parts using cylindrical N5 start plates and sent to GE. One build failed due to an Arcam internal error. The total height of each build was 30mm. An extra part was fabricated and sectioned by UTEP. The following microstructure showed noteworthy cracks throughout the part. Automatic mode was effective in fabrication of these parts; however to maintain a higher level of control, and observe the effect on part quality due to individual system parameters, manual mode was used for most experiments.

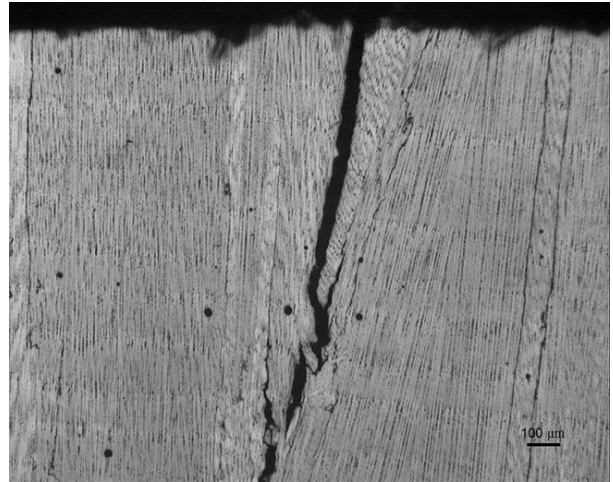
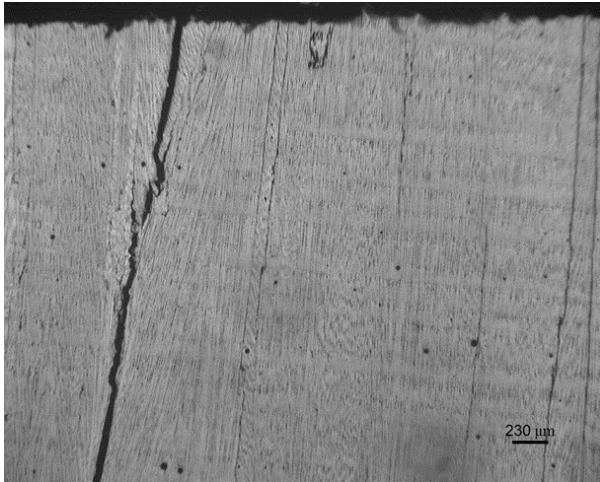
Automatic Mode Parameters:
Surface Temperature: 1400° C
Speed function: 28
Max. Current: 50 mA



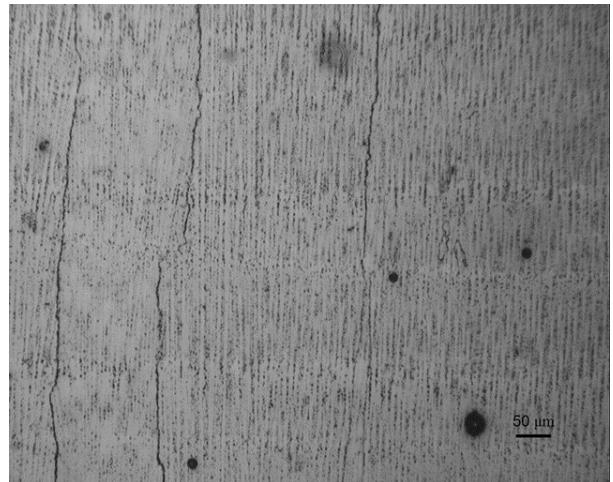
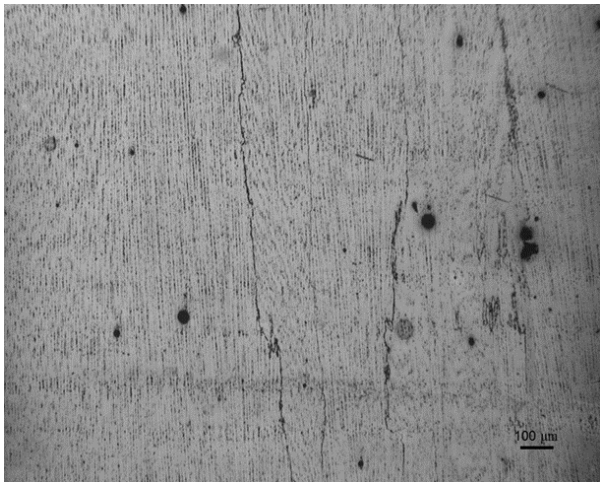
Interface micrographs



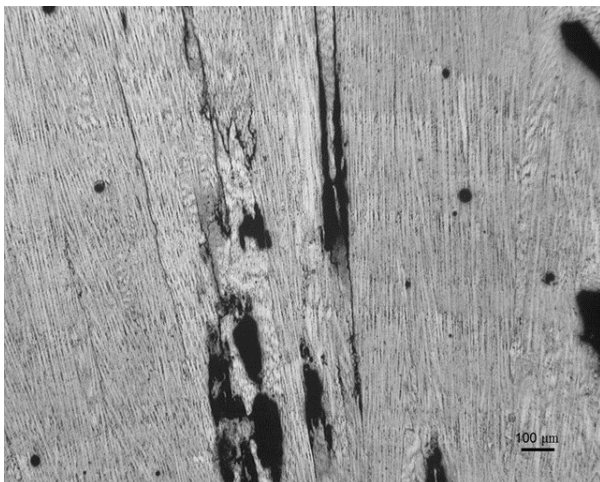
Top micrographs



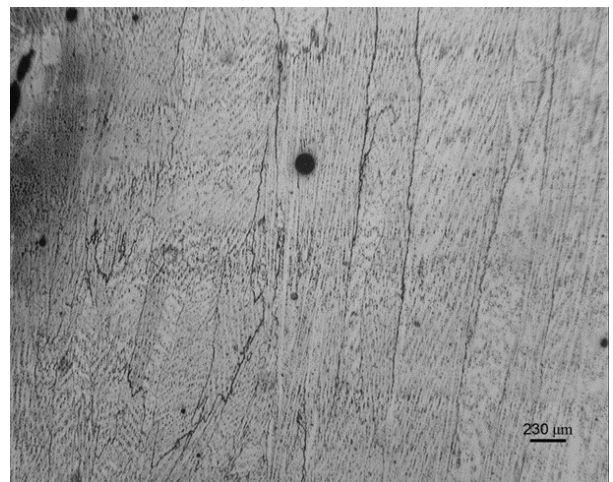
Center micrographs



Left micrographs



Right micrographs



Date: 1/07/14

Additional melt steps were added to each part using different parameters in order to try and reduce the cooling rate of the parts. The bottom thermocouple temperature was not stable and as a result the process had to be stopped and additional heating was added.

First melt Current: 4 mA

First melt speed: 100 mm/s

7

S.P. 250, 450
A.C. 3, 2

8

S.P. 200, 300
A.C. 3, 2

9

S.P. 150, 200
A.C. 3, 2

4

S.P. 250, 450
A.C. 1.5, 1

5

S.P. 200, 300
A.C. 1.5, 1

6

S.P. 150, 200
A.C. 1.5, 1

1

S.P. 250, 450
A.C. 2, 1

2

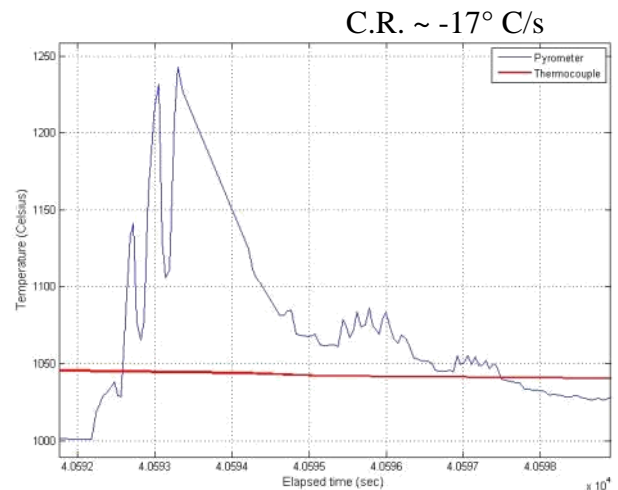
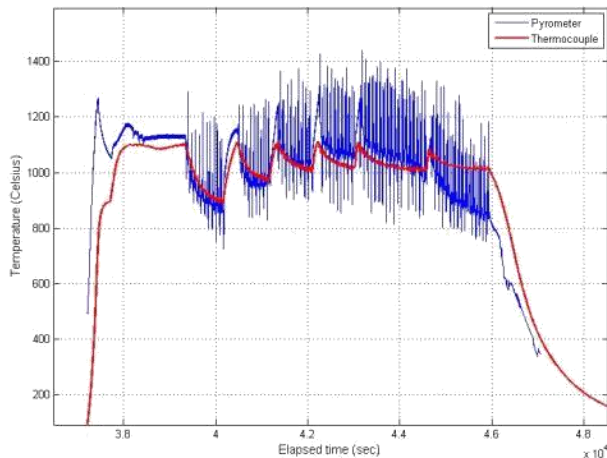
S.P. 200, 300
A.C. 2, 1

3

S.P. 150, 200
A.C. 2, 1

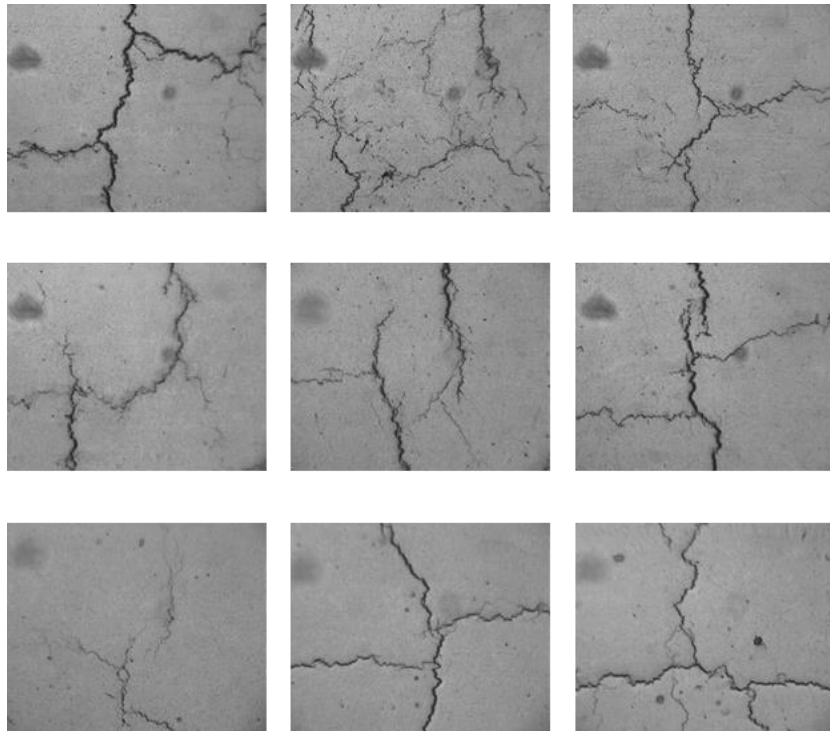


As-fabricated picture

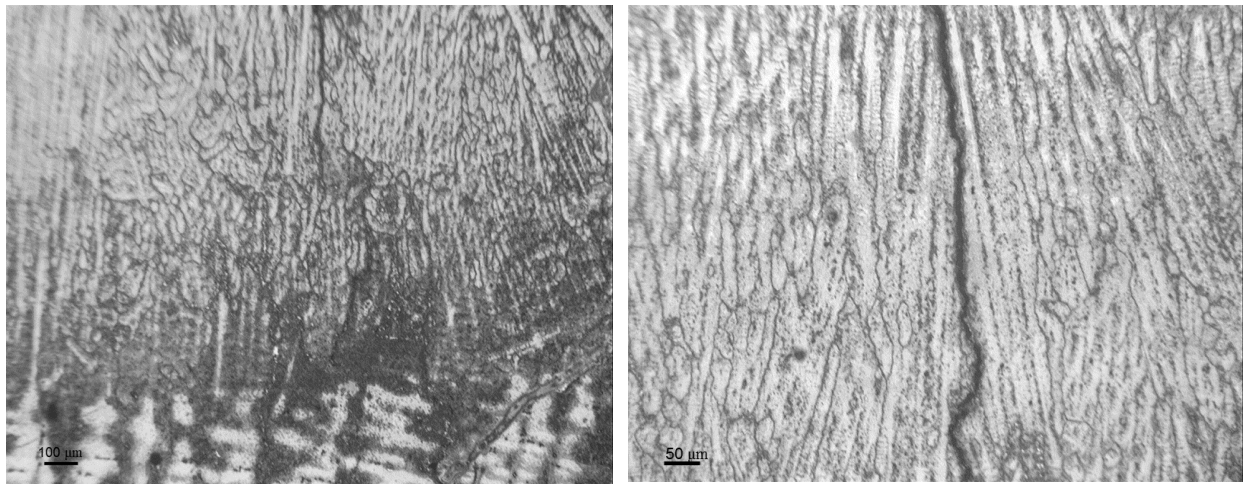


Temperature plots for the pyrometer were focused on part 5. Full plot on the left and a zoomed in image of the melt to the right

Horizontal micrographs of all parts



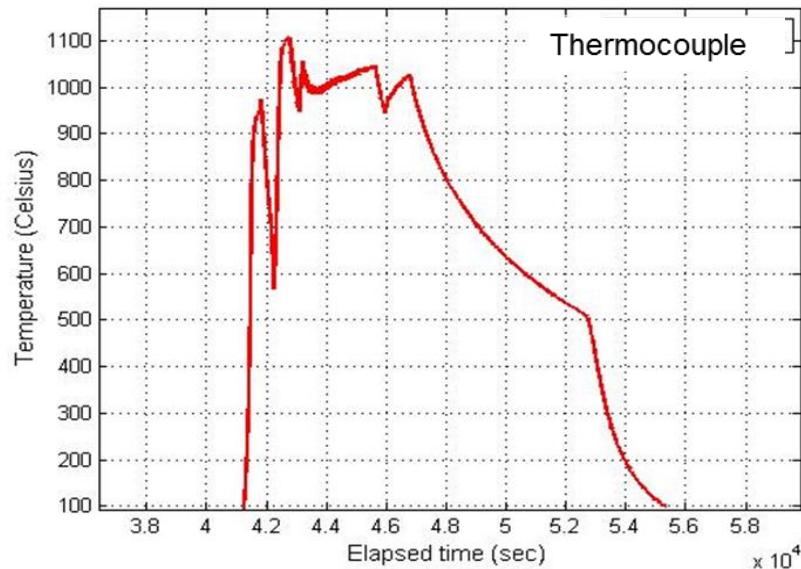
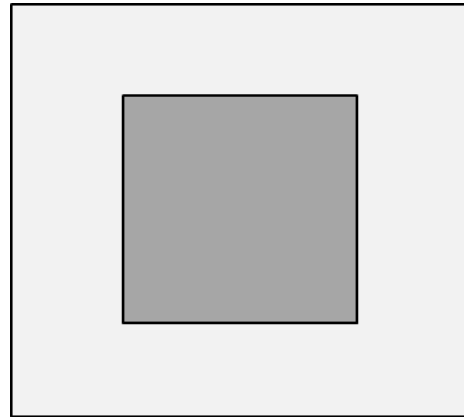
Vertical micrographs for part 1



Date: 1/09/14

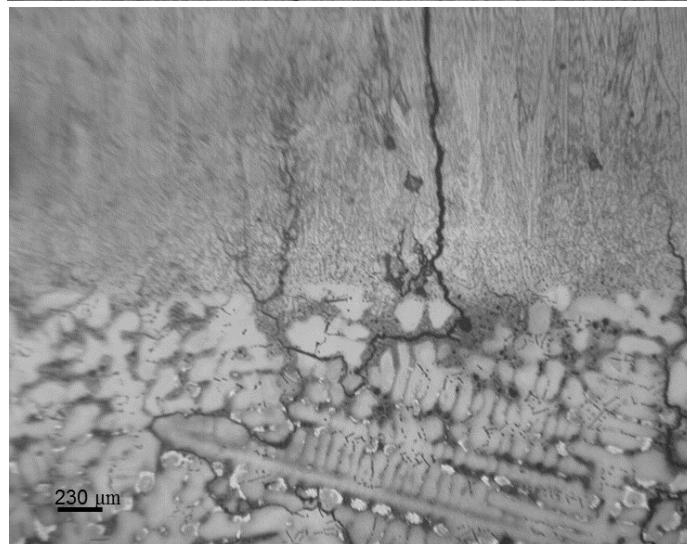
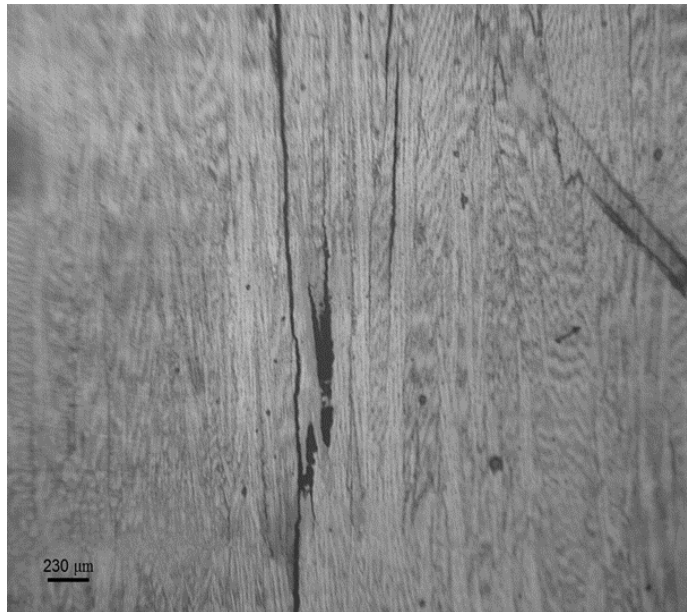
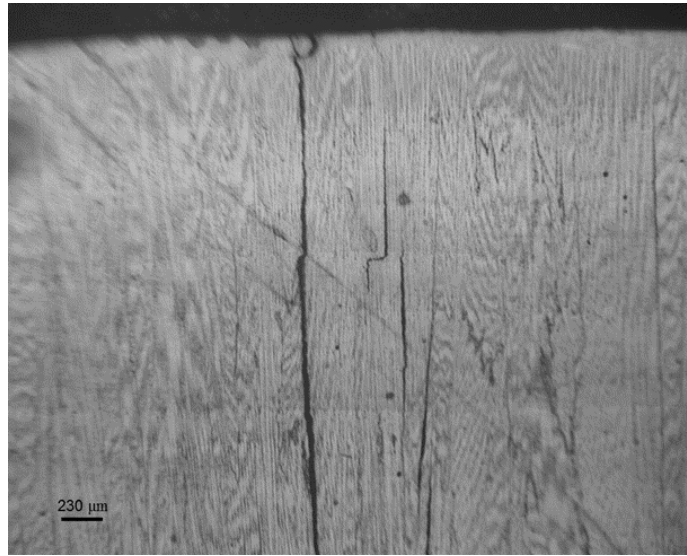
Fabrication of a single part with 3 melt steps was attempted to control the cooling rate. An error occurred with the pyrometer and did not output data. The fabricated part's sintered powder was solid (no as-fabricated picture is available). Dips in the thermocouple plot were caused by the process being stopped, to change parameters (beginning) or allowing the system to cool.

Melt	Scan Speed (mm/s)	Current (mA)
1	100	4
2	250	2
3	450	1



Above is the thermocouple temperature plot

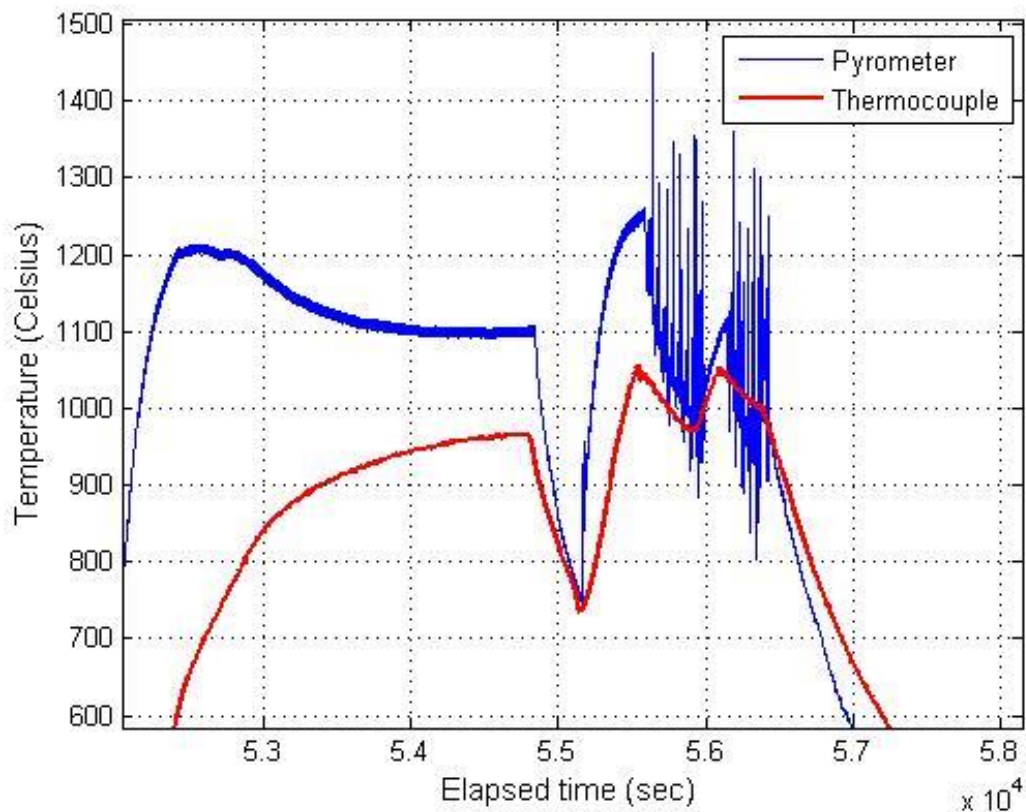
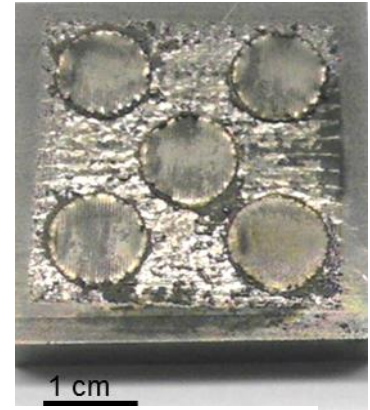
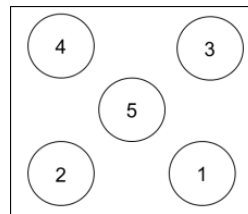
Vertical micrographs



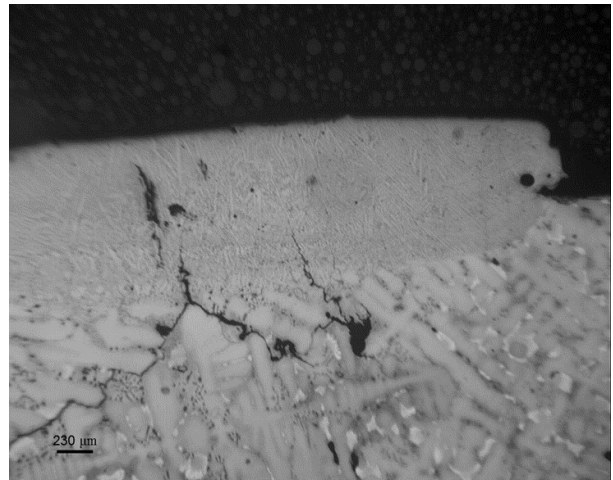
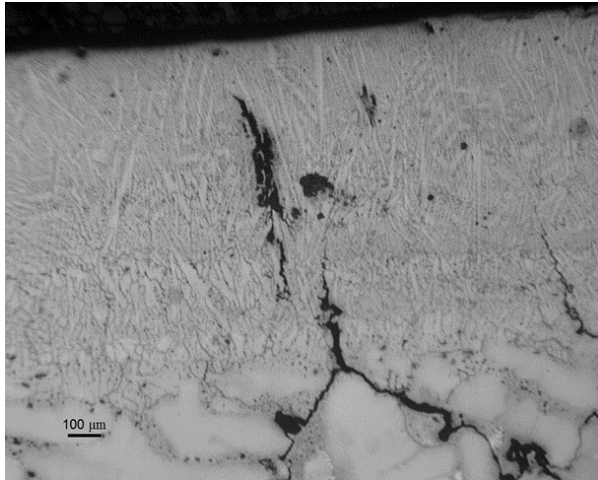
Date: 1/14/14

Part geometry was changed to cylindrical parts (1mm in height) in order to see if geometry affects crack density. Cracking was still clearly visible in these short builds. Comparing part 1 to parts 2 and 5, no conclusion can be drawn to the effect of the additional cooling melt steps in this experiment. The build stopped and heating was performed to raise the bottom temperature, possibly contributing to the crack density.

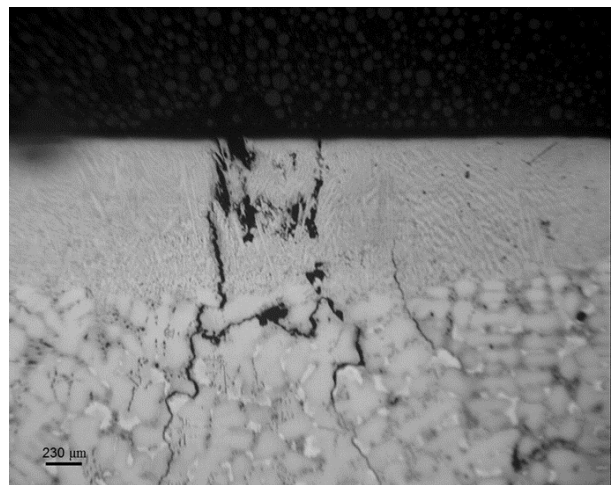
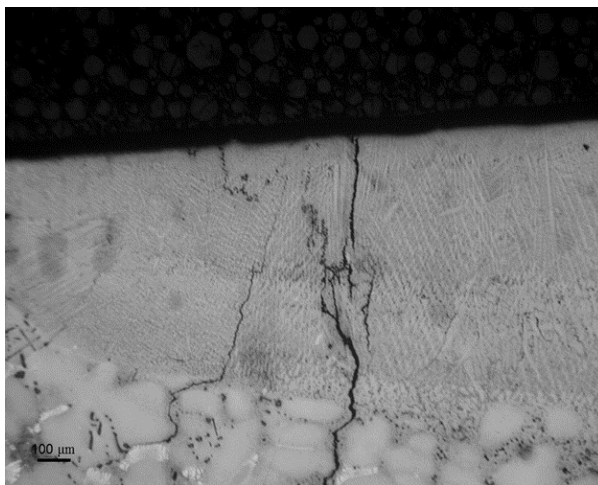
Part #	Melt 1		Melt 2		Melt 3	
	AC (mA)	SP (mm/s)	AC	SP	AC	SP
1	4	100	N/A	N/A	N/A	N/A
2	4	100	2.25	250	1.25	350
3	4	100	2.25	350	1.25	300
4	4	100	1.5	250	1	350
5	4	100	1.5	200	1	300



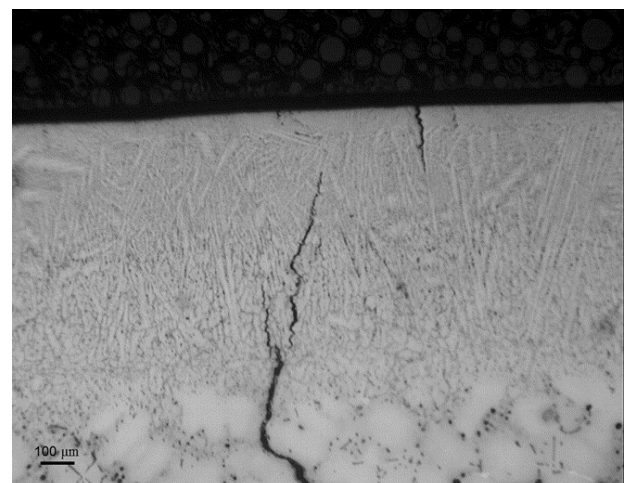
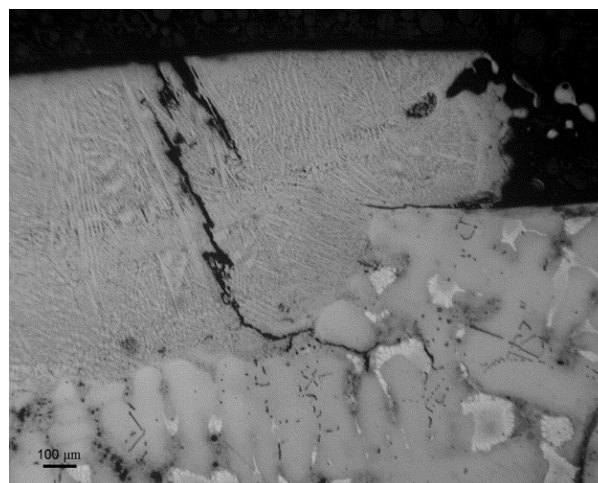
Part 1 Vertical micrographs



Part 2 Vertical micrographs



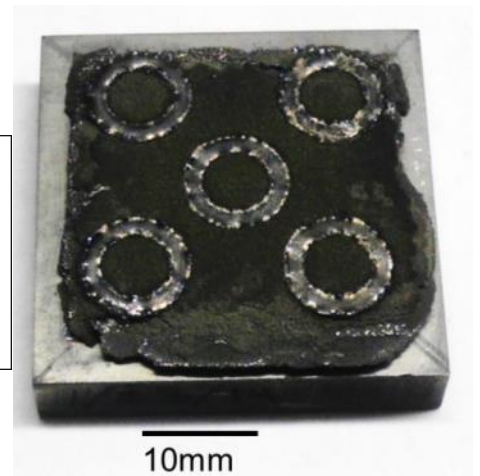
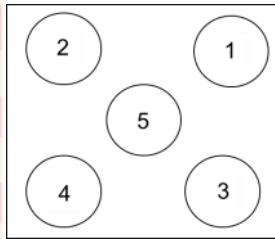
Part 5 Vertical micrographs



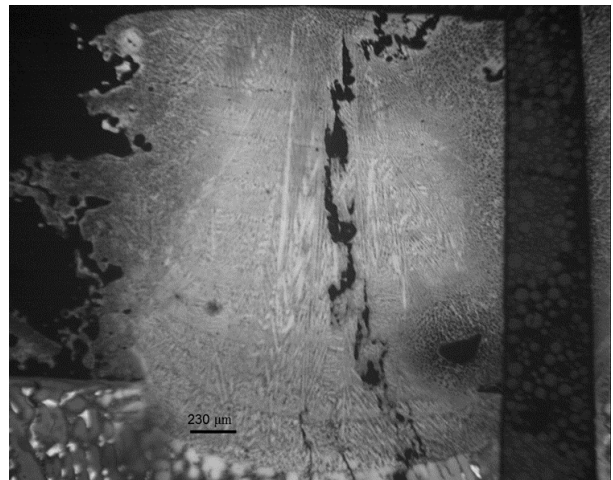
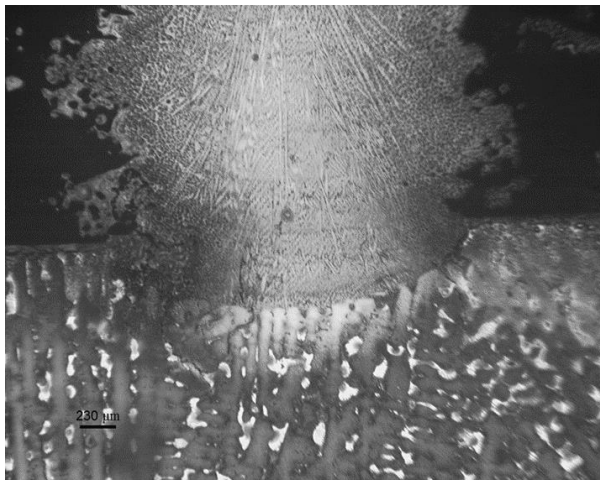
Date: 1/22/14

Part geometry was changed to further investigate the effect of part geometry on crack density. Rings with dimensions of inner diameter of 9 mm, outer diameter 10 mm, and a height of 3 mm were fabricated. Such rings were expected to prevent a center spot where heat can accumulate (a phenomena expected from fabrication of solid cylinders). An error occurred in the thermocouple that prevented the log file from being analyzed. The process was maintained steady above $\sim 1000^{\circ}\text{C}$. The process was stopped in middle of the build to allow the build to cool down to prevent the temperature from increasing above $\sim 1100^{\circ}\text{C}$. The powder surrounding the parts was nearly solid, meaning the pre-heat was too hot and nearly melted the powder.

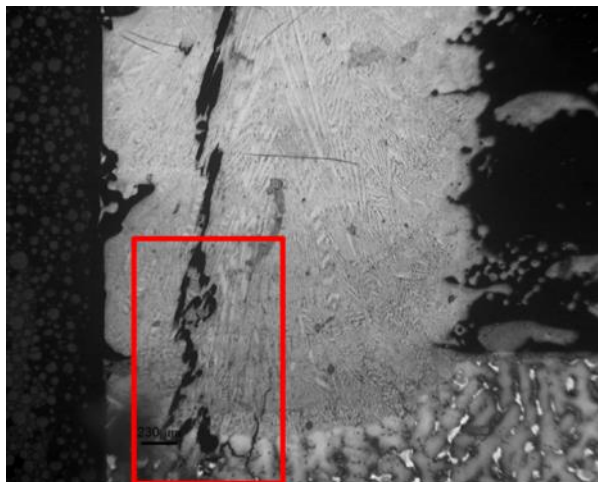
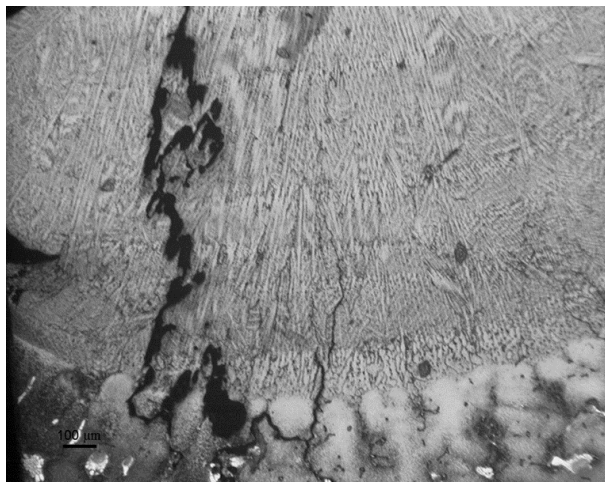
Part #	Melt 1		Melt 2		Melt 3	
	AC (mA)	SP (mm/s)	AC	SP	AC	SP
1	4	100	N/A	N/A	N/A	N/A
2	4	100	2.25	250	1.25	350
3	4	100	2.25	350	1.25	300
4	4	100	1.5	250	1	350
5	4	100	1.5	200	1	300



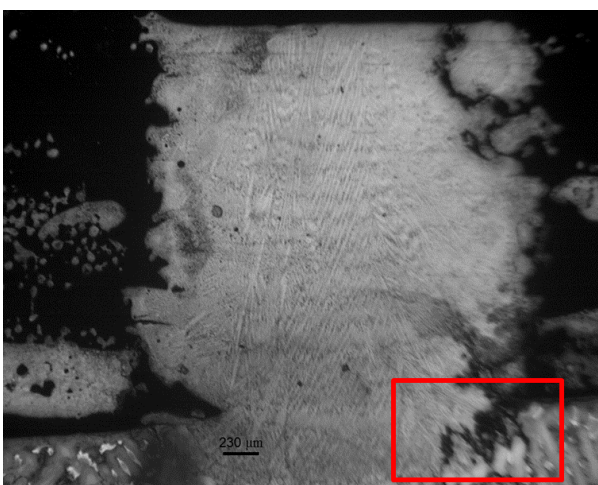
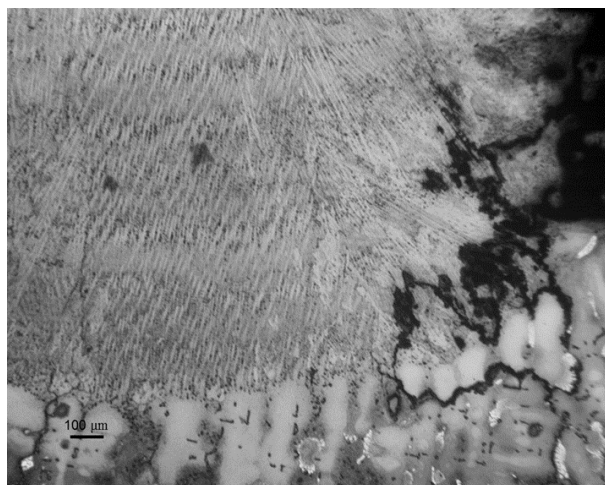
Part 1 Vertical micrographs



Part 3 Vertical micrographs

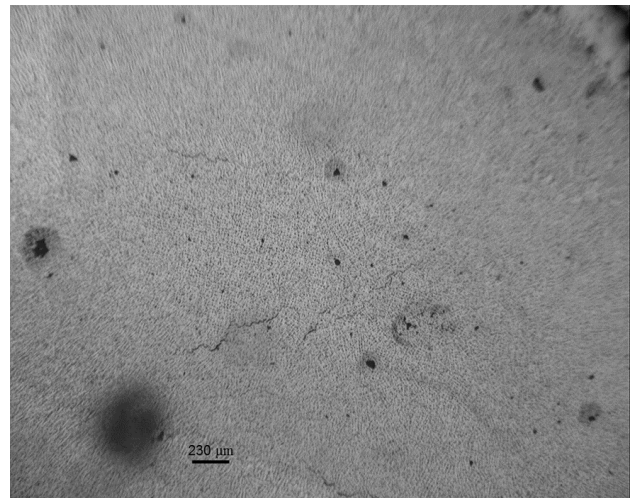
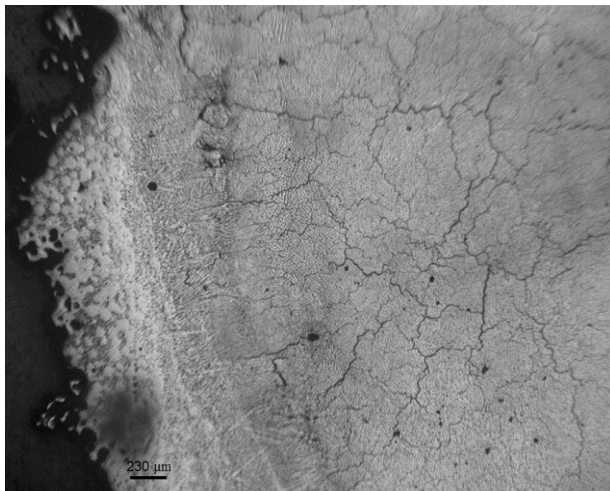
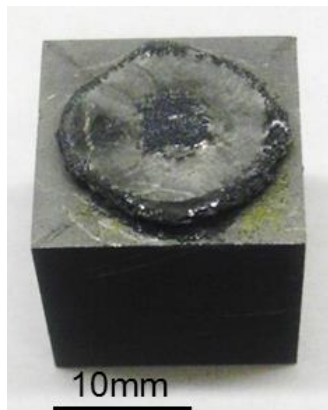


Part 5 Vertical micrographs



Date: 1/28/14

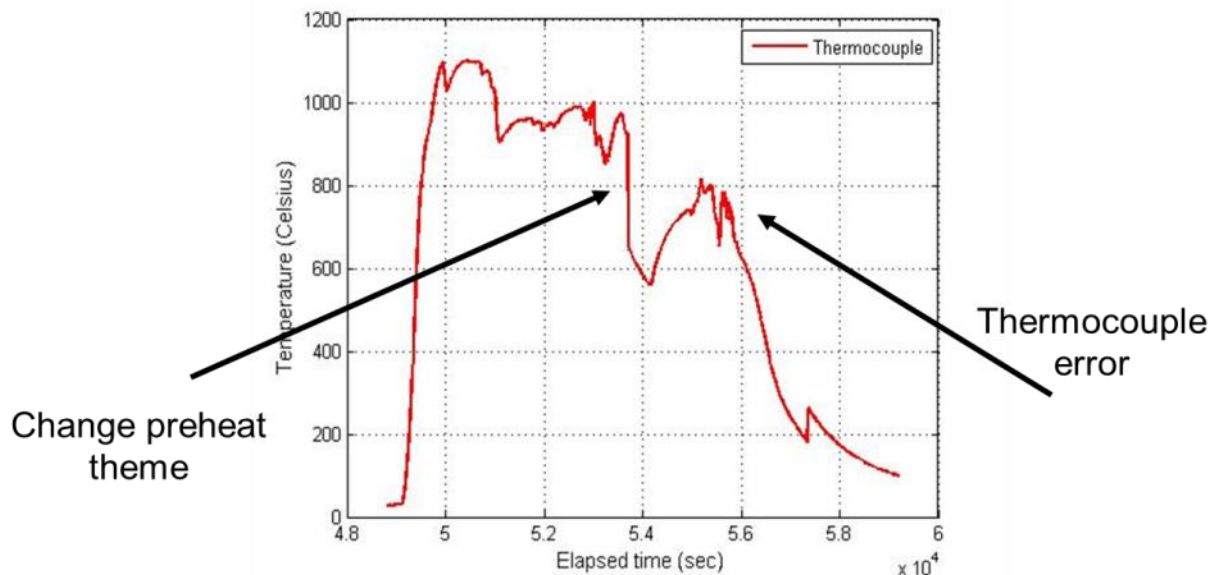
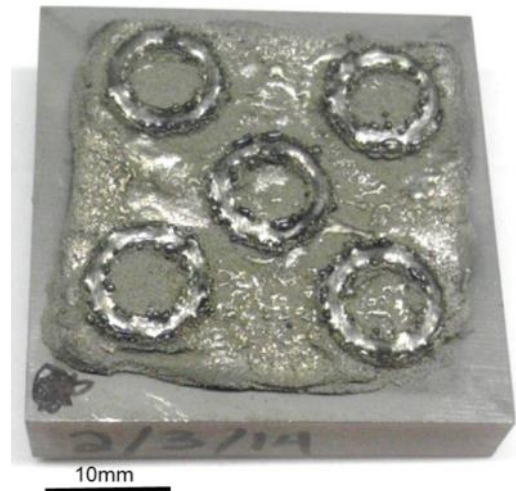
Single parts with same geometry of 1/22/14, the speed, and current were greatly reduced to build on the smaller cube start plates (16 x 16 x 16 mm). A switch in start plate material (N5 vs. R125) Parameters were changed many times throughout the build and ended with speed of 20 mm/s, current 2 mA, and focus offset of 20 mA. Multiple attempts were done to work with the smaller cube start plates; however, the use of the smaller start plates was abandoned due to the increased time required to develop functional parameters.



Date: 2/3/14

Contour beam paths were used for the initial melt. Contour beams follow a circular path compared to melting which typically follows a hatch pattern that is linear. Changes in beam caused an increase of balling defects and caused the geometry to swell and top surface to dome. Thermocouple data showed not stable temperature behavior possibly due to some kind of thermocouple damage. The thermocouple was replaced after the build.

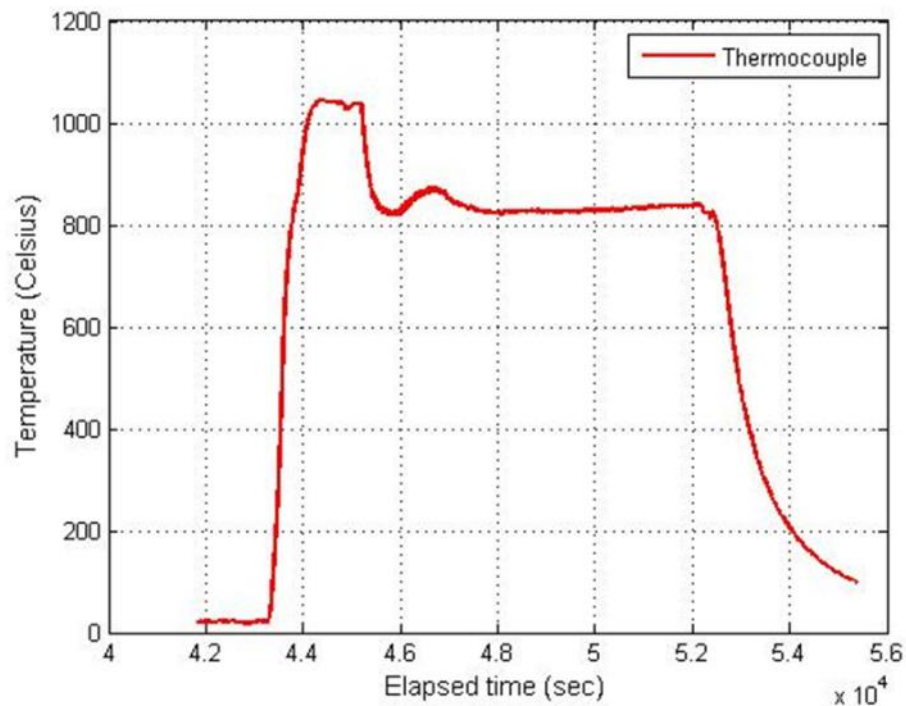
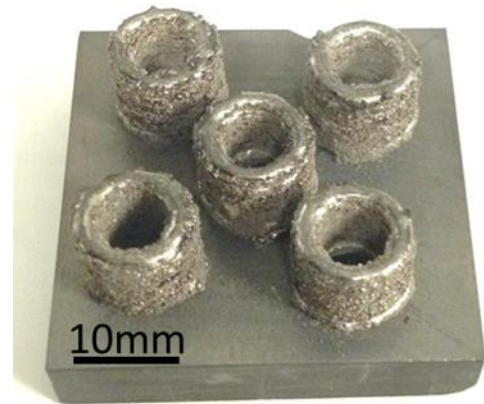
Part #	Melt 1		Melt 2		Melt 3	
	AC (mA)	SP (mm/s)	AC	SP	AC	SP
1	4	100	N/A	N/A	N/A	N/A
2	4	100	2.25	250	1.25	350
3	4	100	2.25	350	1.25	300
4	4	100	1.5	250	1	350
5	4	100	1.5	200	1	300



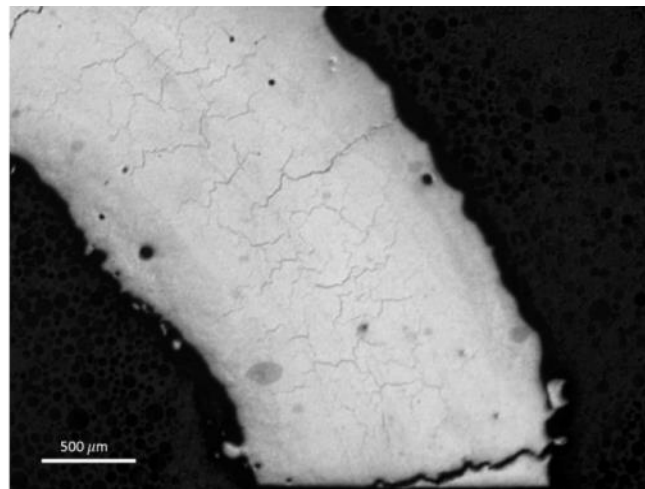
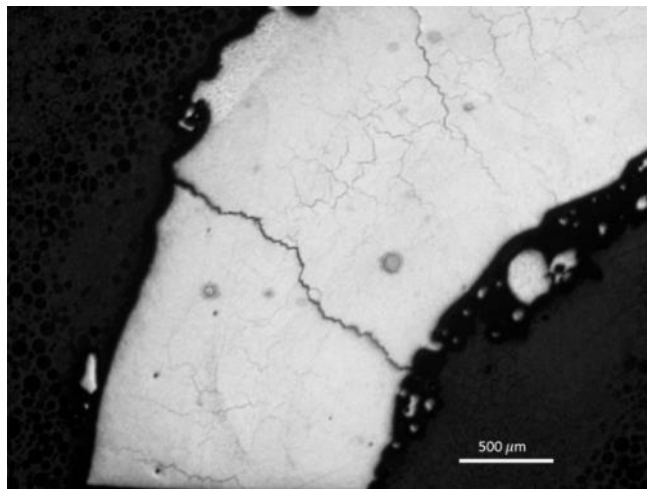
Date: 2/07/14

Contour tool paths were used in the initial melt and subsequent cooling rate reduction melts were implemented using a typical hatch tool path. Build height was increased up to 10mm in order to increase the amount of surface seen in the micrographs and the same ring geometry was used for these builds. The pre-heat was adjusted to a slow speed and lower current. The sintered powder was easily removable and the process was stable with a thermocouple temperature of $\sim 860^{\circ}\text{C}$.

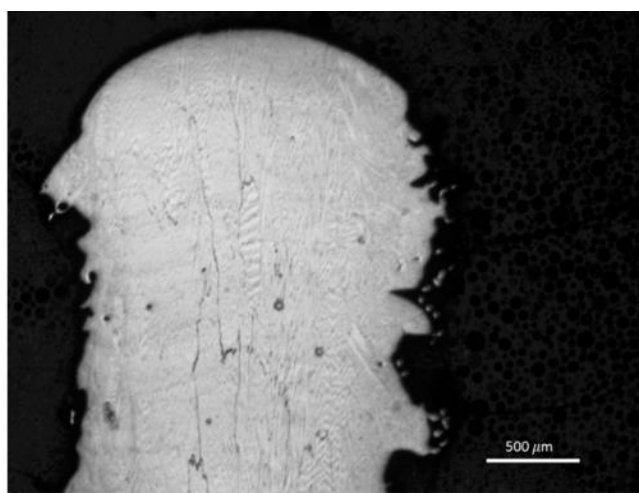
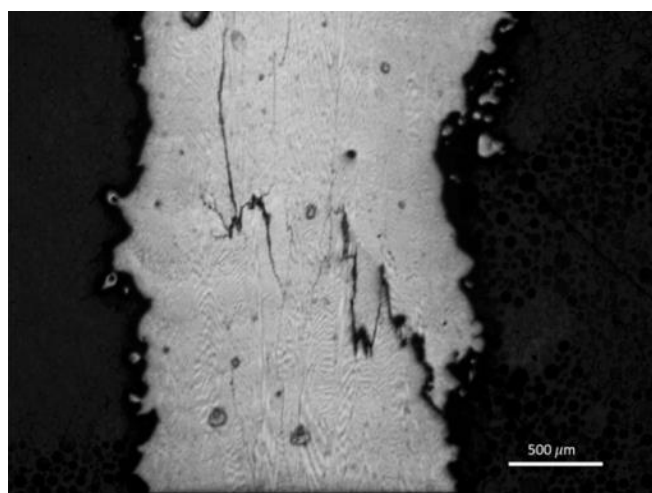
Part #	Melt 1		Melt 2		Melt 3	
	AC (mA)	SP (mm/s)	AC	SP	AC	SP
1	4	100	N/A	N/A	N/A	N/A
2	4	100	2.25	250	1.25	350
3	4	100	2.25	350	1.25	300
4	4	100	1.5	250	1	350
5	4	100	1.5	200	1	300



Part 2 micrographs (Horizontal)



Part 2 micrographs (Vertical)

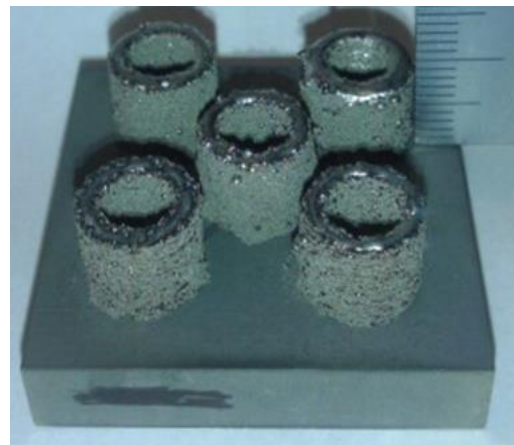


Date: 2/10/14

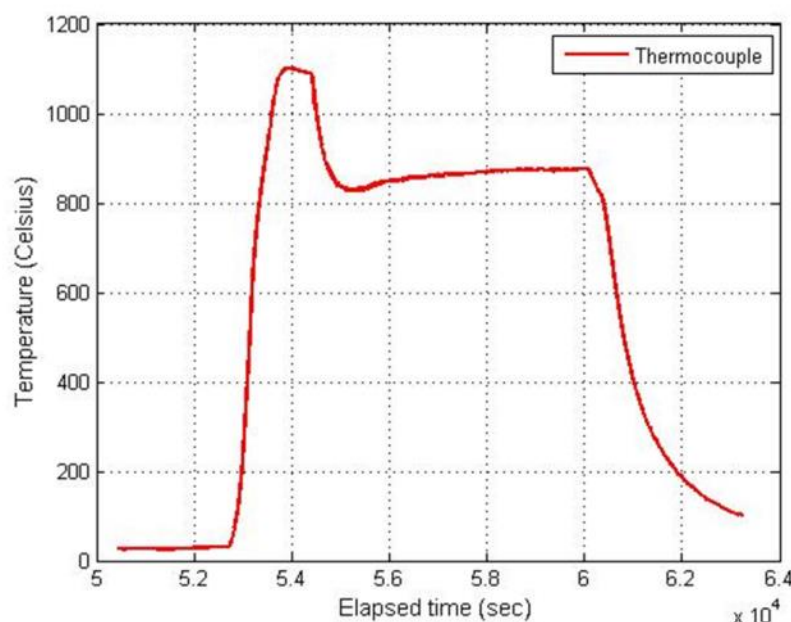
An experiment was performed to find the effect of altering the tool path offsets on crack density. A single baseline melt theme was used with a different variation for each of the five parts. The first melt used contour passes and subsequent melts used hatch patterns. Parts were fabricated using a contour offset of 1 mm with 2 passes to melt part and spacing of 0.4 mm as well as a contour offset of 0.1 mm using 8 passes with 0.1mm spacing. All 5 parts showed cracking from inner diameter to outer diameter and part 1 showed the least amount of cracking.

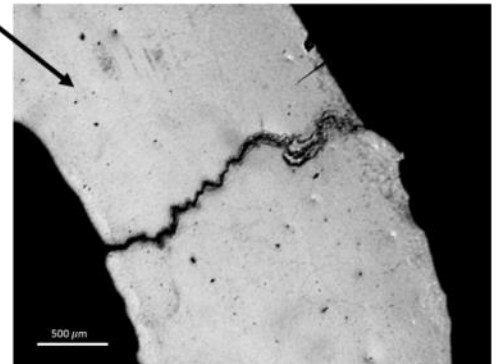
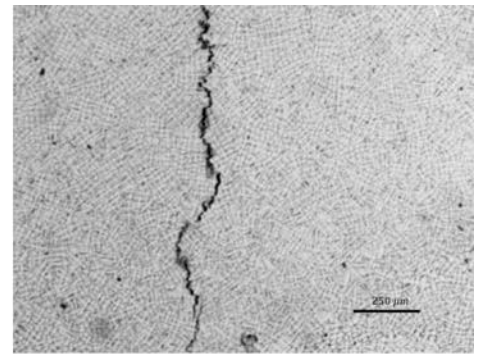
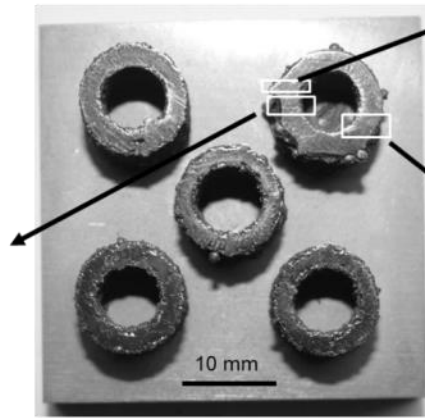
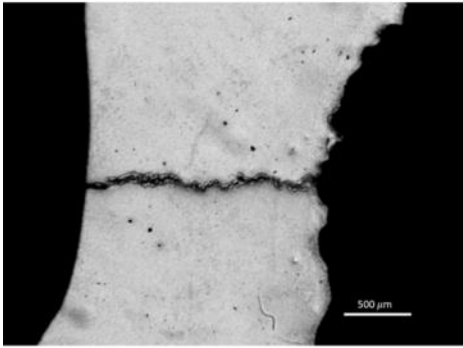
Baseline melt theme:
Current: 3mA
Scan Speed: 100mm/s
Focus Offset: 19mA
Contour Offset: 0.2 mm

Part	Variations
1	Contour Offset = 1 mm Scan Speed = 20 mm/s
2	Contour Offset = 0.1 mm
3	Scan Speed = 150 mm/s Current = 3.5 mA
4	Focus Offset = 25 mA
5	Focus Offset = 15 mA



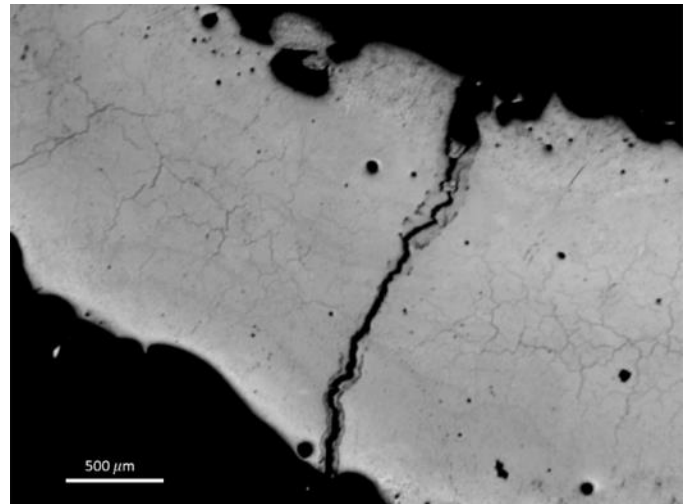
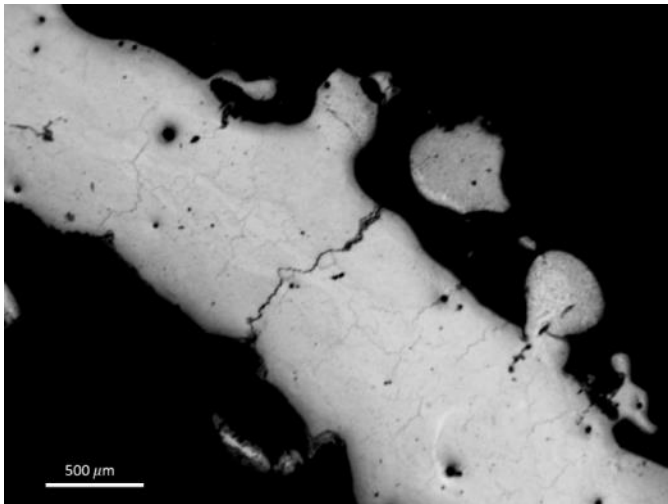
Cooling rate reduction melts
parameters:
Currents: 2.25, 1.25mA
Speed: 250, 350mm/s
Focus Offset: 19, 19mA





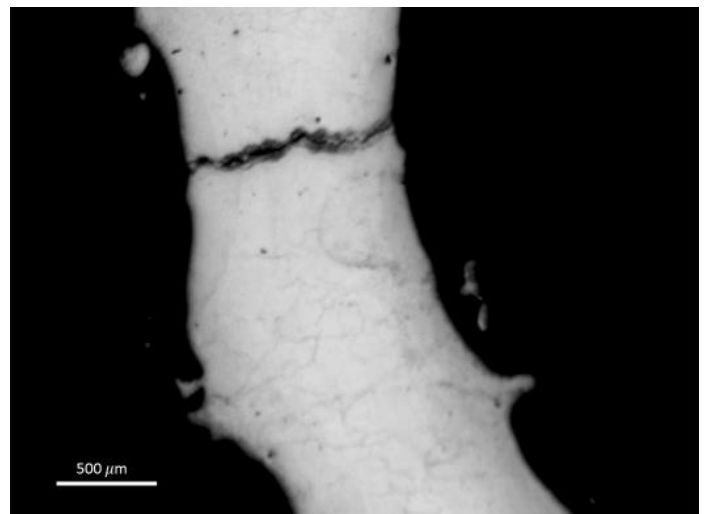
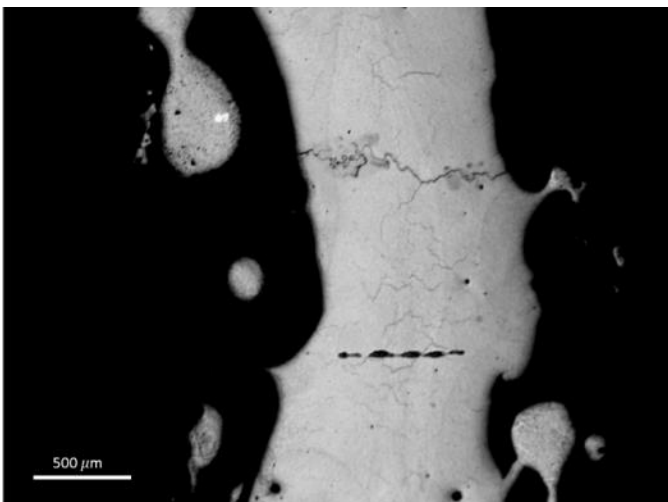
Part 2

Part 3



Part 4

Part 5

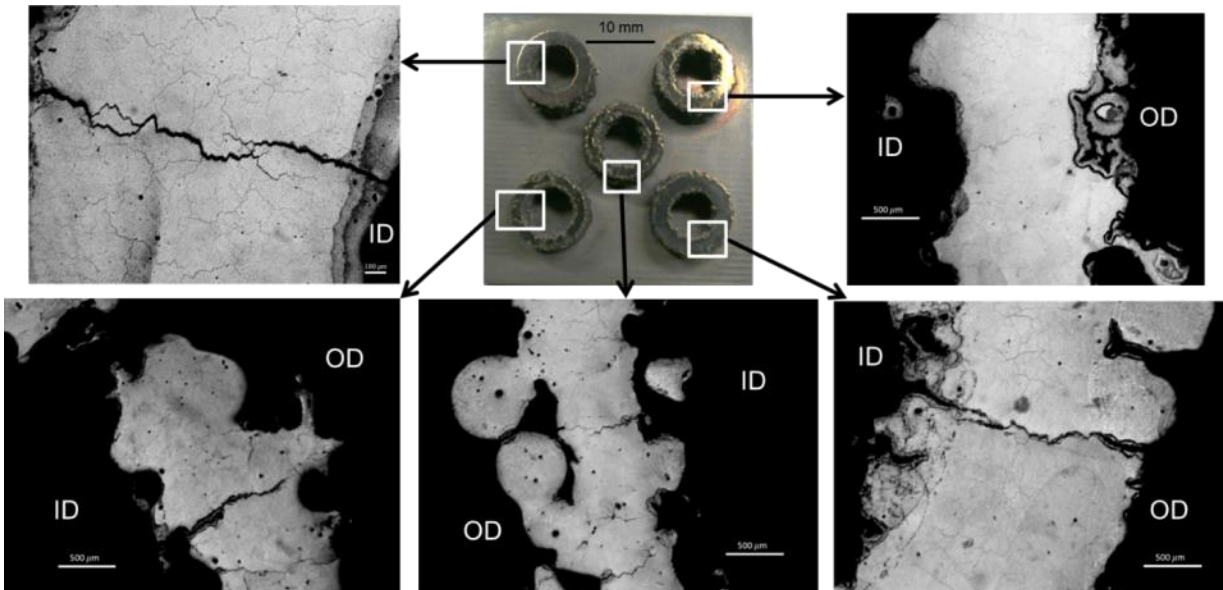
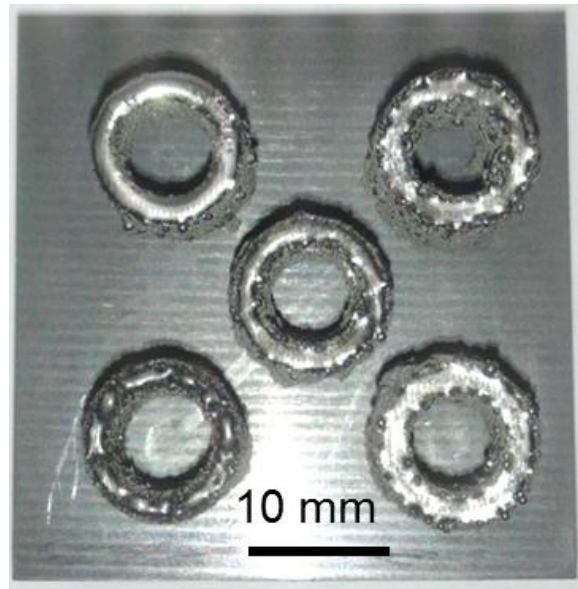


Date: 2/11/14

No thermocouple data were available for this build; however, temperature was expected to be similar to the previous build (2/10/14) since the same preheating parameters were used. Cracking from the inner diameter to outer diameter was evident in all parts. This type of cracking was commonly observed in builds using contour beam passes. The build the parameters of part 1 were changed during fabrication to a current of 3.7 mA and a speed of 175 mm/s.

Baseline melt theme:
Current: 3mA
Scan Speed: 100mm/s
Focus Offset: 19mA
Contour Offset: 0.2 mm

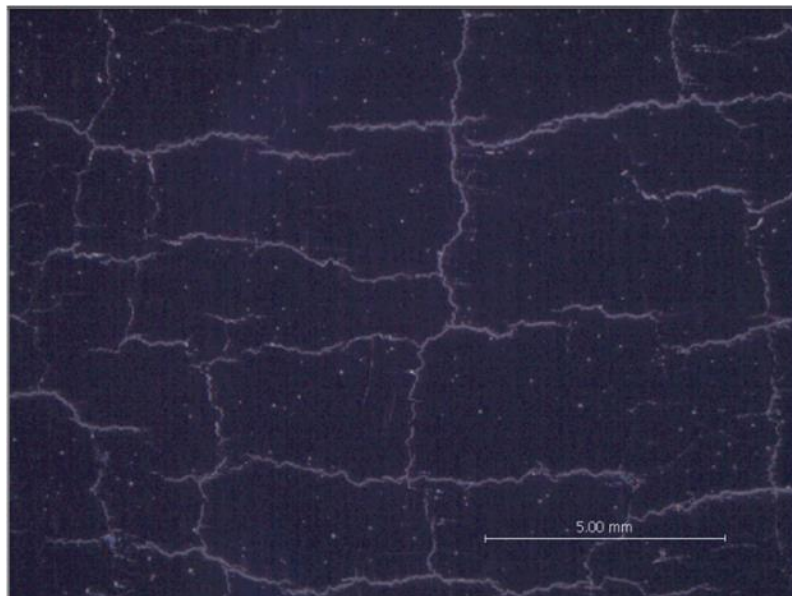
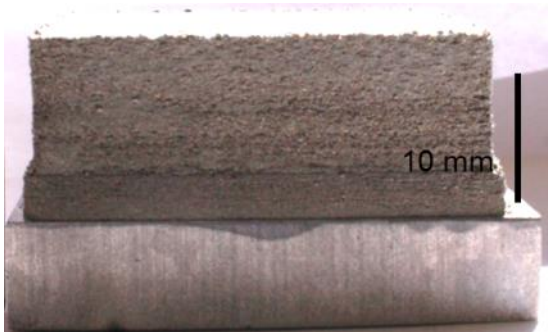
Part	Variations
1	Contour Offset = 0.1 mm Scan Speed = 150 mm/s
2	Contour Offset = 1 mm Scan Speed = 20 mm/s Current = 2.6 mA
3	Contour Offset = 0.1 mm Current = 2.6 mA
4	Contour Offset = 0.1 mm Current = 2.6 mA Scan Speed = 150 mm/s
5	Contour Offset = 1 mm Scan Speed = 20 mm/s (Same as Part 1, 2/10)



Date: 2/14/14

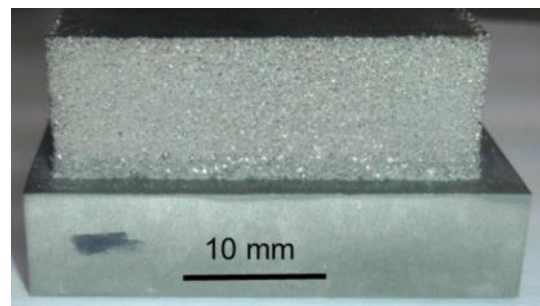
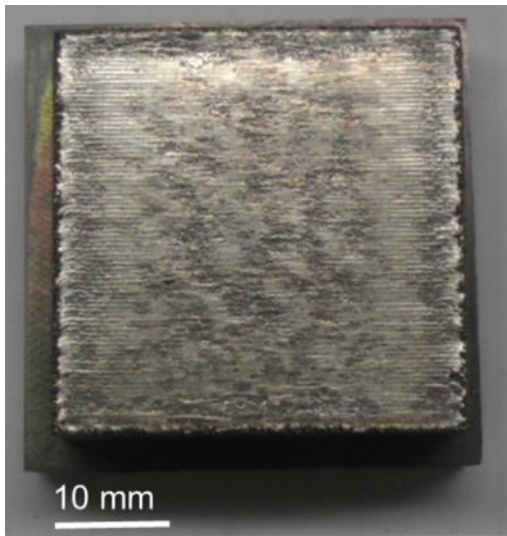
A 35 x 35 x 15 mm start plate was built, using parameters that were previously used in May – 2013. During the build, the contour melting speed had to be reduced to reduce powder explosions. This build plate was primarily fabricated to be used in later experiments (2/21/14).

Automatic mode
Current ~ 3.7mA
Speed ~ 178mm/s
Focus Offset = 19
mA



Date: 2/19/14

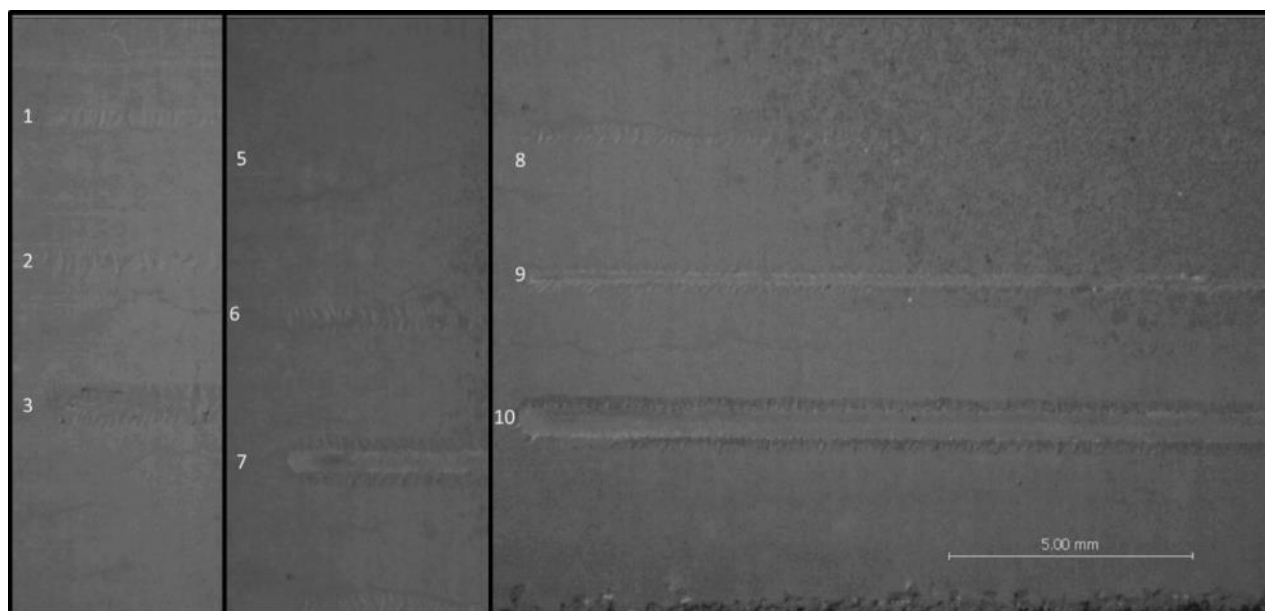
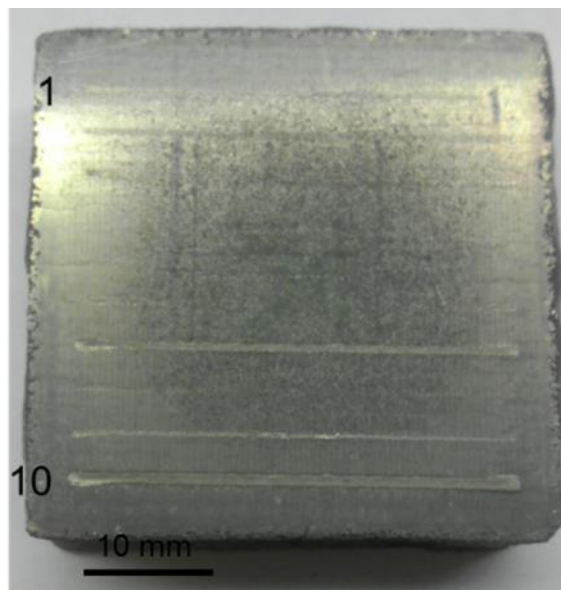
An additional start plate was built using the adjusted parameters from 2/17/14. Current from the contours was reduced to prevent powder explosion during the build. The preheat theme was also adjusted to a lower current and slowed to prevent powder explosions during the build. This plate was used later for beam pass experiment (3/17/14).

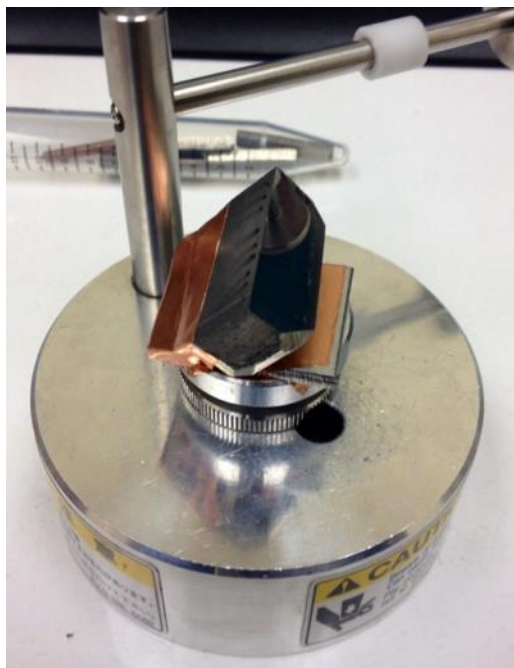


Date: 2/21/14

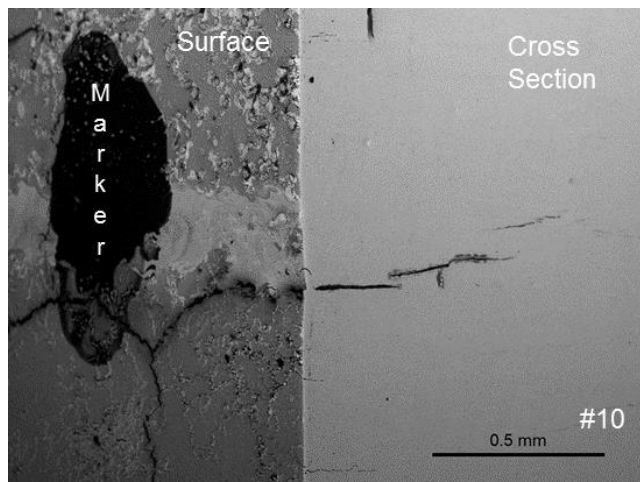
A single beam pass on the R142 start plate fabricated from 2/17/14 was performed. 10 beam passes were done with varying beam speed and beam current. The plate was cross sectioned in an attempt to observe the depth of the beam; however, only some of the heat affected zones were visible using optical microscopy after preparation using a glyceresia etchant. A tabletop SEM was initially used; however, no heat affected zone or melt pool was visible. A second attempt was done tilting the specimen and placing markers directly on the beam pass, to pinpoint the melted area.

Pass number	Current (mA)	Scan Speed (mm/s)
1	2	300
2	2	100
3	2	20
4	3	500
5	3	300
6	3	100
7	3	20
8	4	300
9	4	100
10	4	20



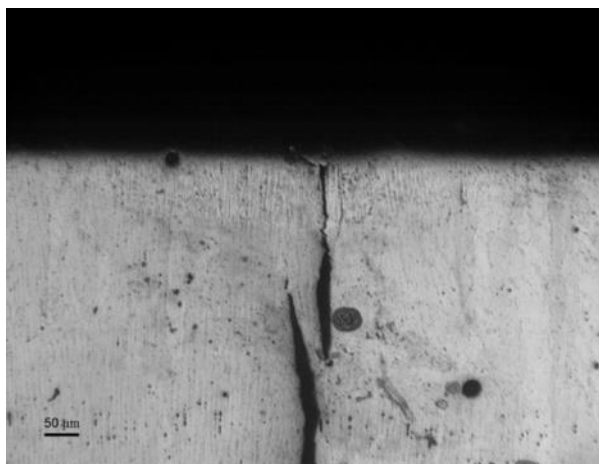


Using the glyceresia etchant

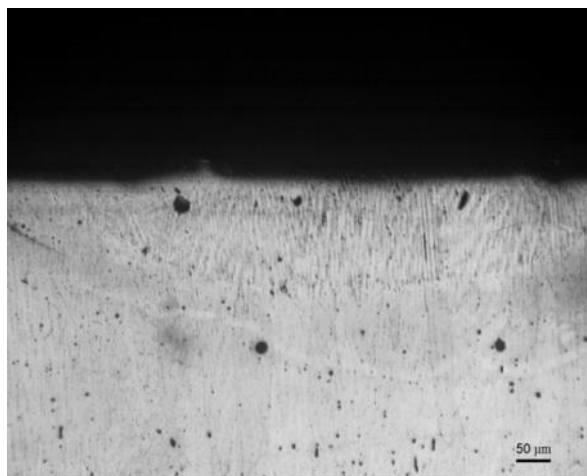


Left: Mounted specimen used that was placed in the SEM

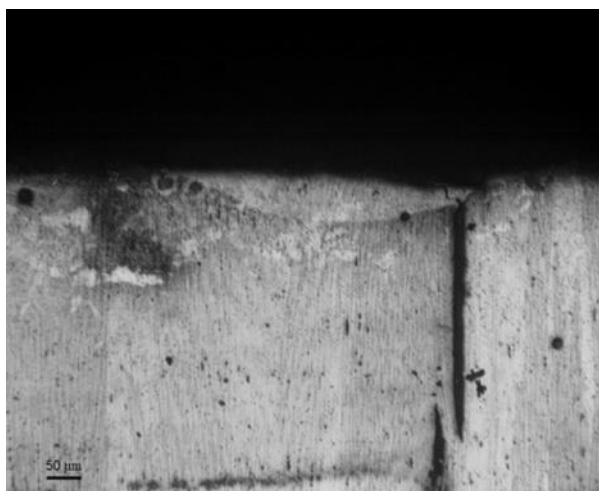
Above: Image showing the marker, with no sign of a melted region



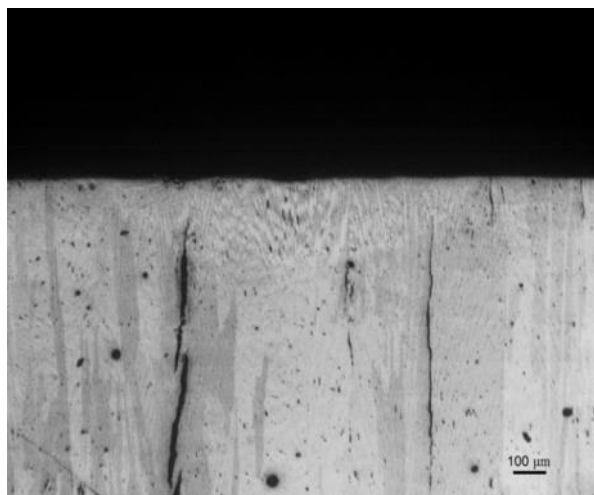
Pass #3



Pass #7



Pass #9

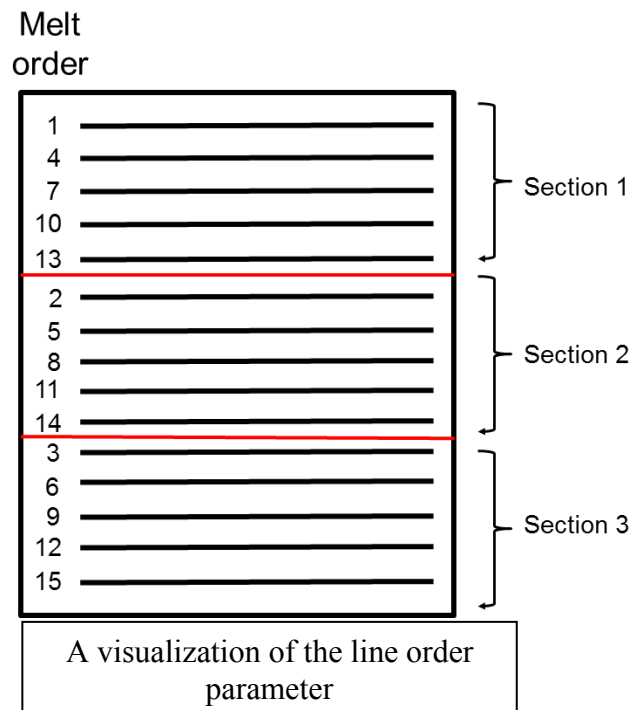
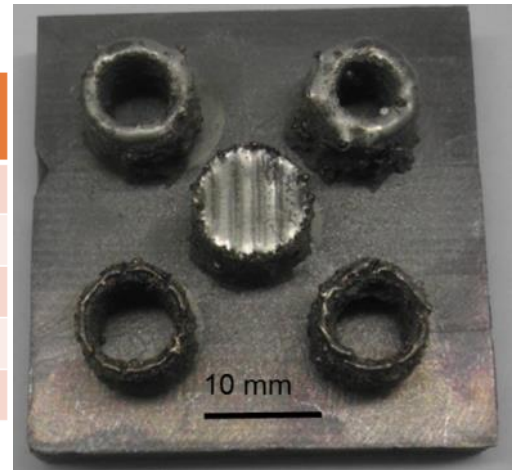


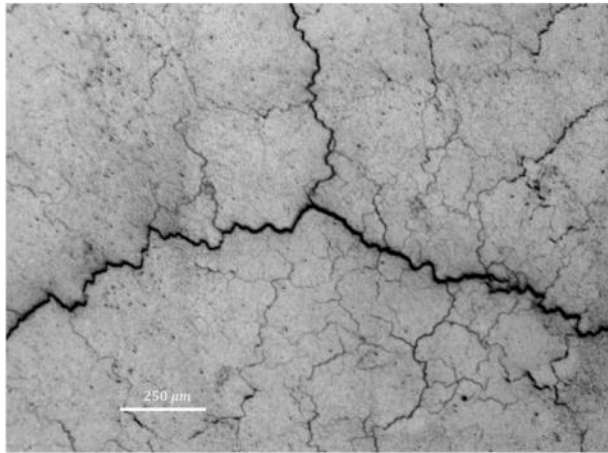
Pass #10

Date: 2/25/14

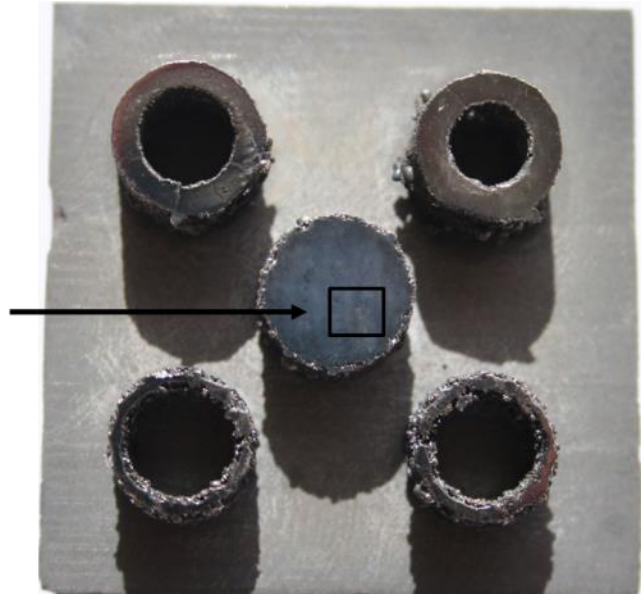
For this experiment the snake parameter was disabled and the line order parameter was changed to 10 for part 5. Line order parameter dictates the order in which hatch lines are melted. The total number of hatch lines is divided into sections of the line order number. Each section is numerically melted (see the below figure). Only one crack was macroscopically visible after polishing on the horizontal surface of part 5.

Part #	Current (mA)	Scan Speed (mm/s)
1	4	20
2	3	20
3	4	100
4	3	100
5 (Hatch)	4	100

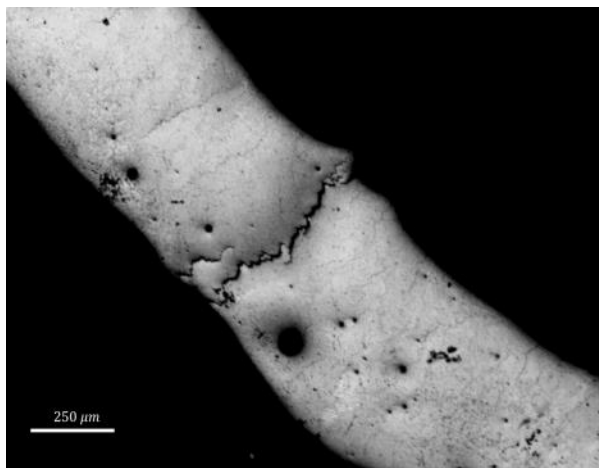




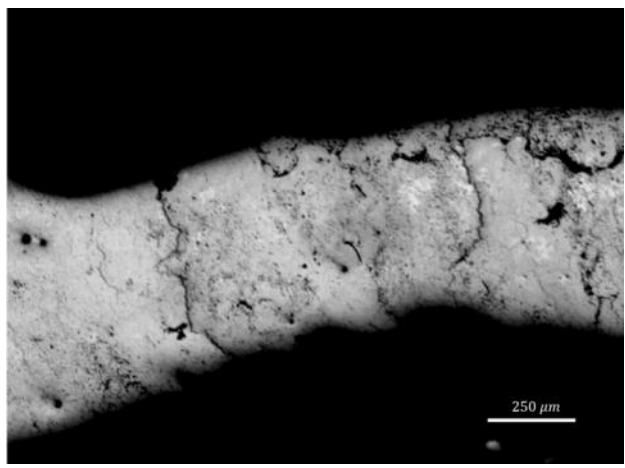
Part 1



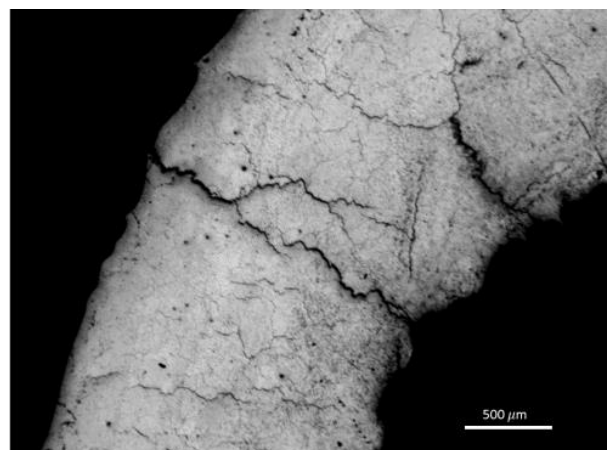
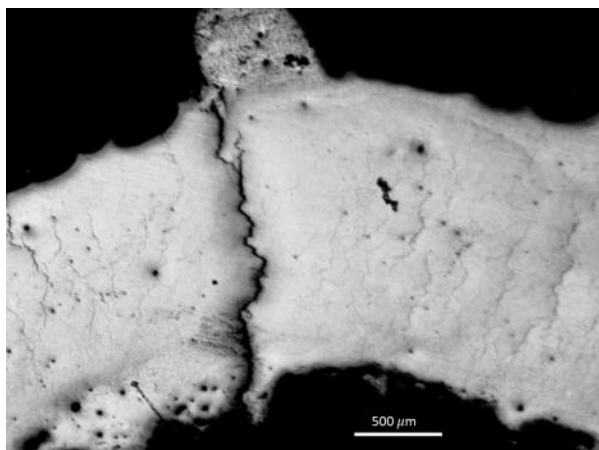
Part 2



Part 3



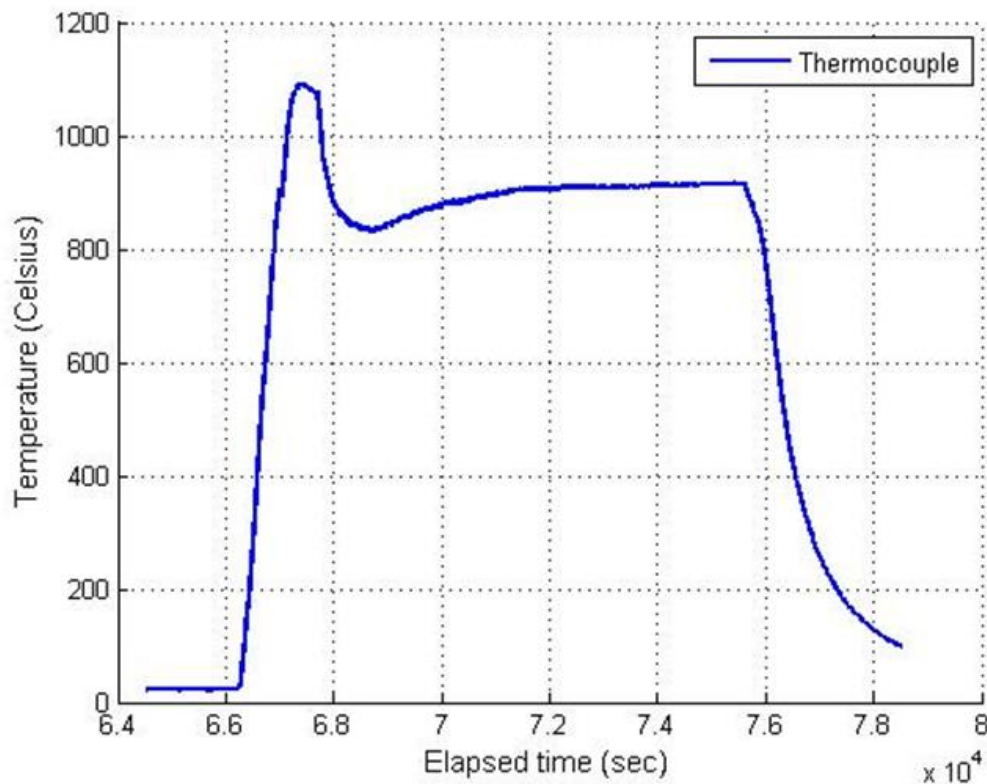
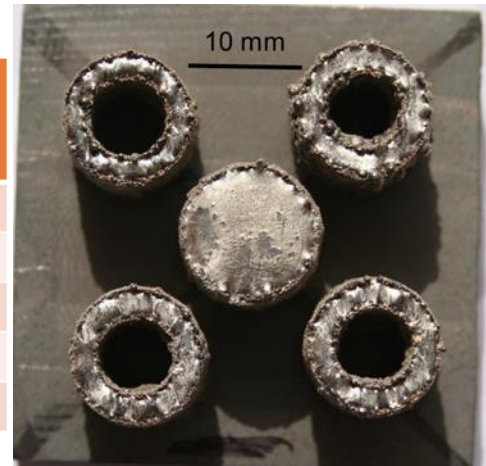
Part 4



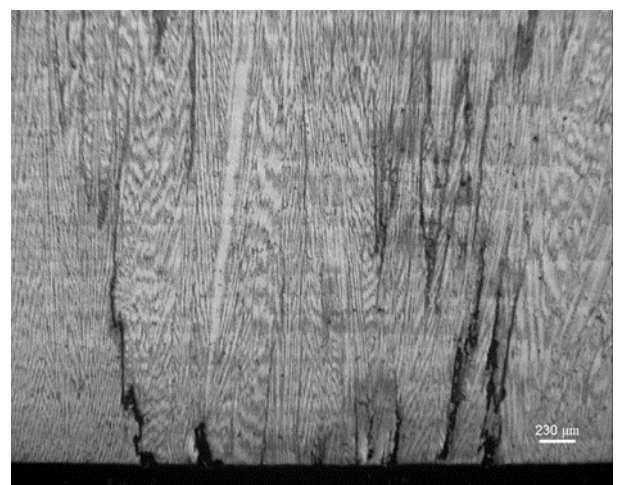
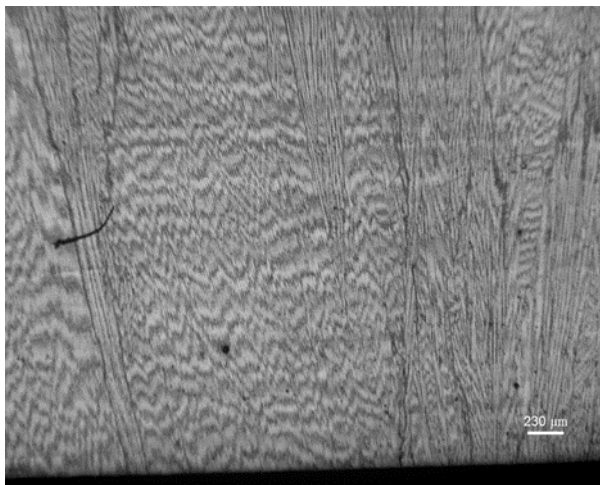
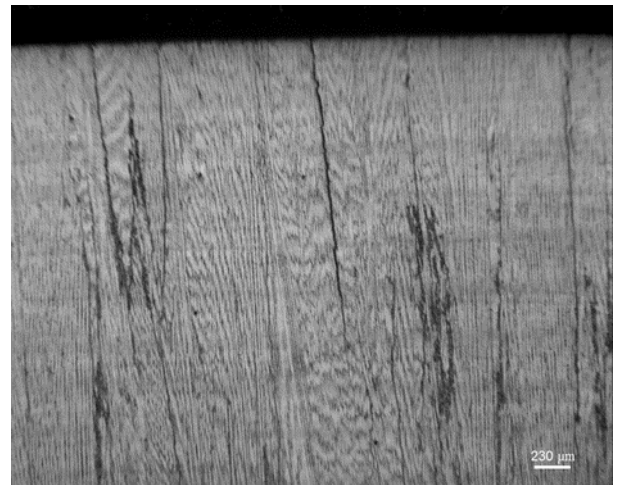
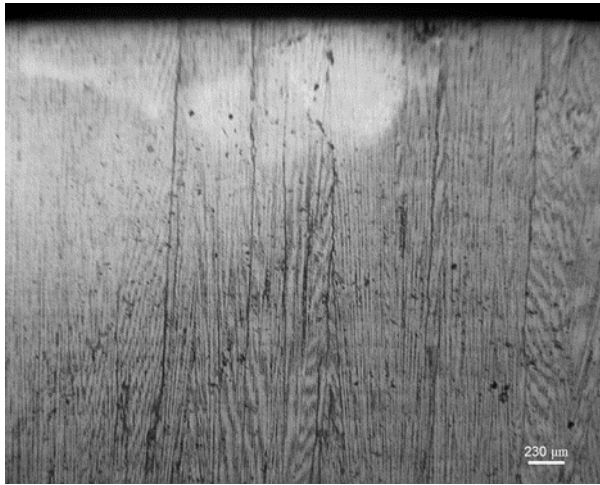
Date: 3/3/14

Building on the results of 2/25/14, the next build was achieved by varying the line order parameter to see if further improvements to crack density could be made. The snake parameter was disabled for part 5 and was the same for all future builds. This was also the first experiment in a set that was intended to find a relation between build temperature and crack density while keeping parameters for part 5 consistent in all experiments.

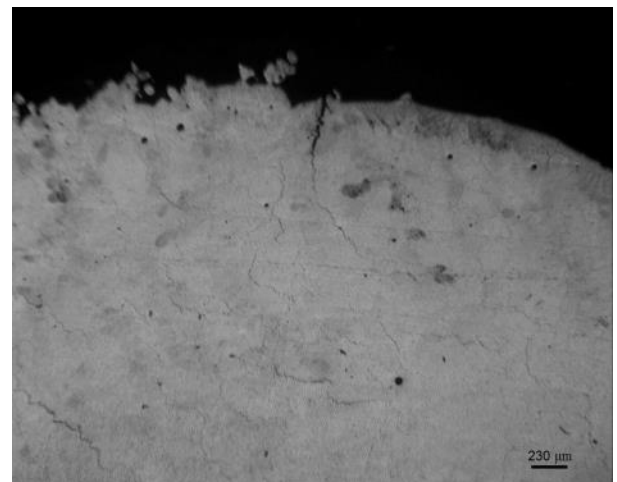
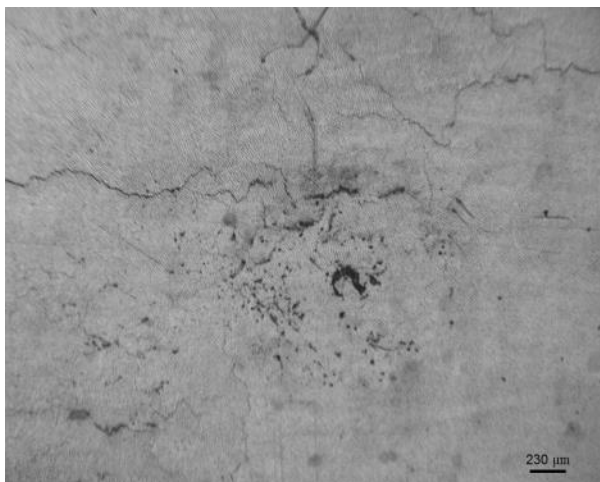
Part #	Current (mA)	Scan Speed (mm/s)	Line order
1	4	100	5
2	3	100	10
3	4	100	10
4	4	100	15
5	4	100	1



Vertical micrographs of part 5



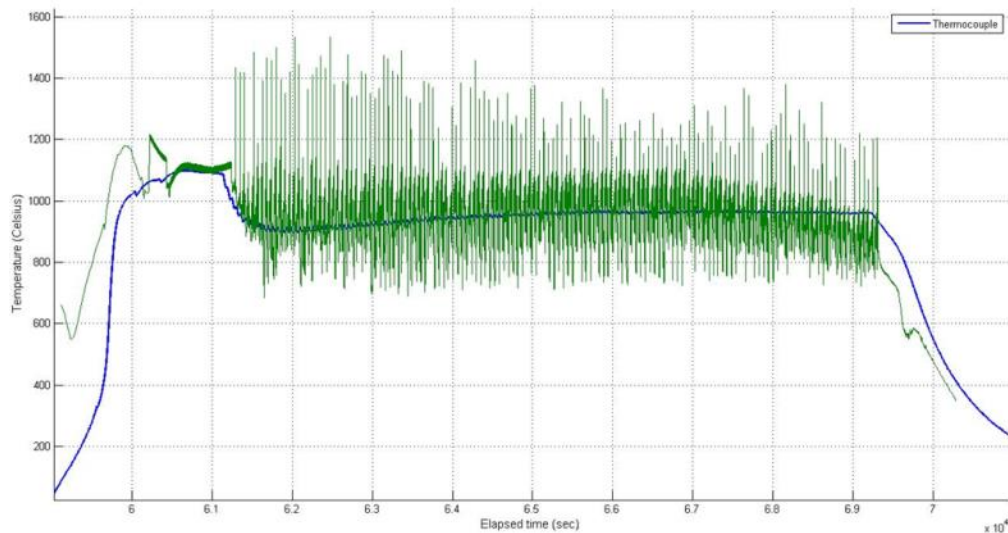
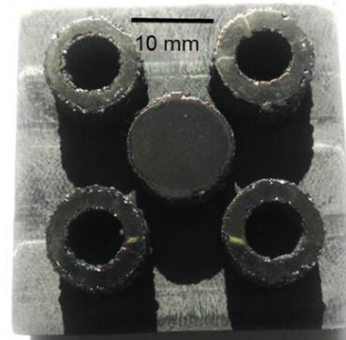
Horizontal micrographs of part 5



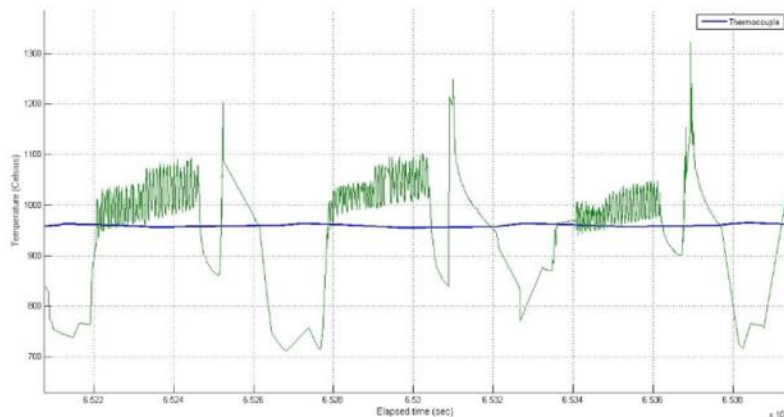
Date: 3/4/14

The build temperature was increased by increasing the beam current of the preheat theme. The parameters for part 5 were kept the same as the previous build (3/3/14); snake disabled, current and speed shown in the table below. Pyrometer data were available for this build (green line shown in the temperature graphs below). The build temperature was stable around 900°C.

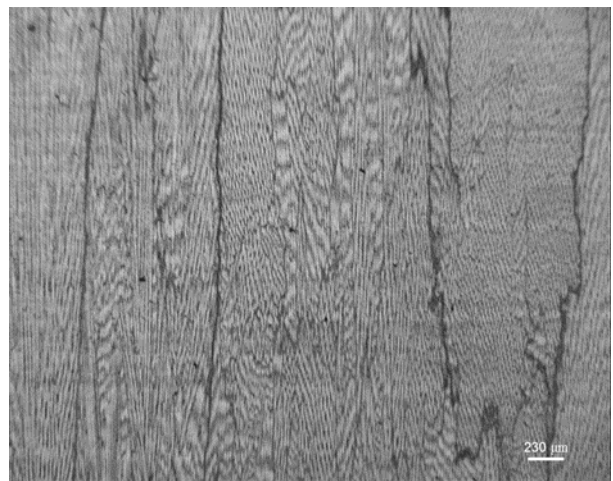
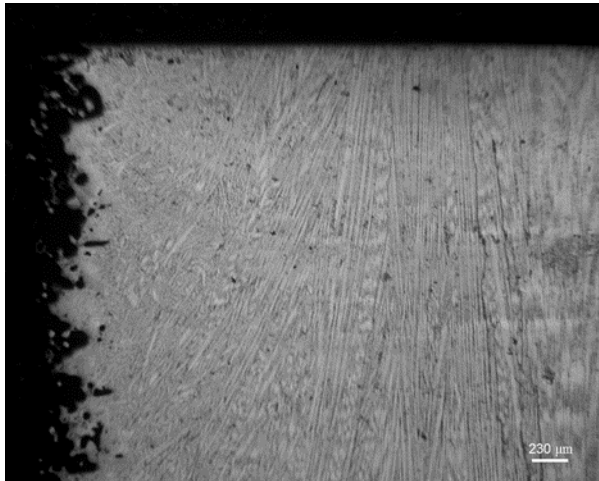
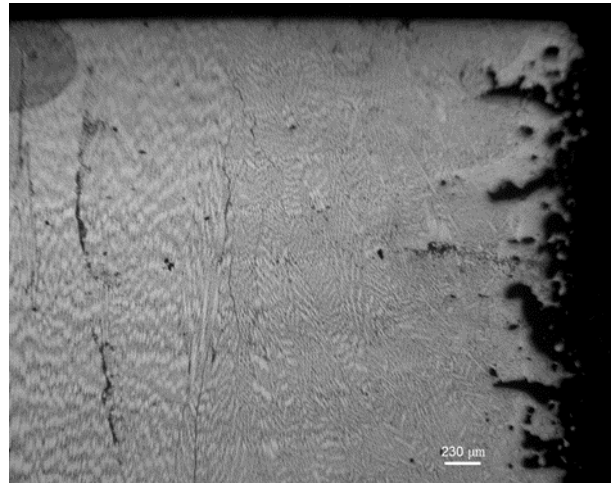
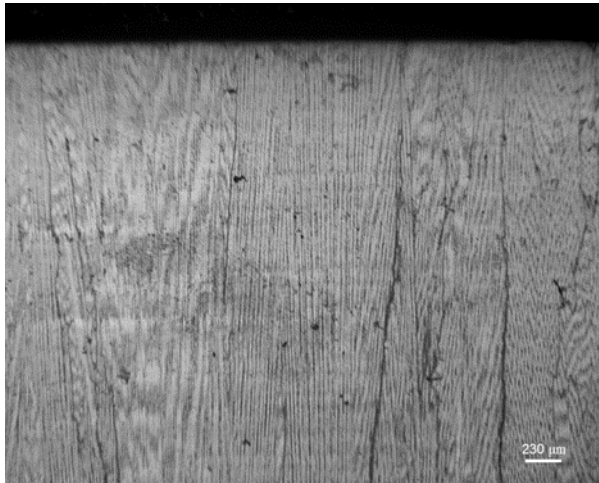
Part #	Current (mA)	Scan Speed (mm/s)	Line order
1	4	100	2
2	2.5	100	1
3	3.5	100	10
4	4	200	1
5	4	100	1



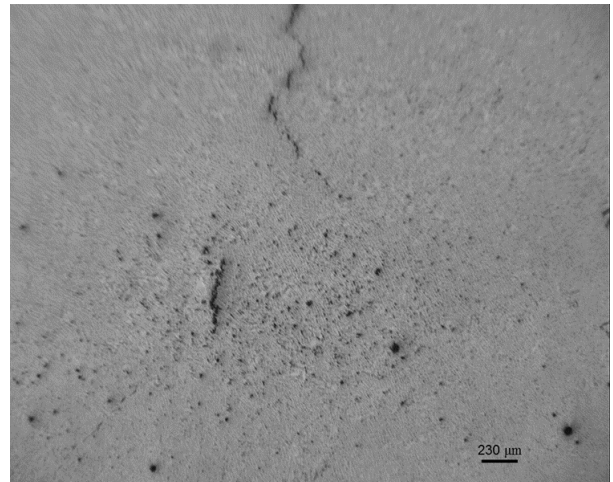
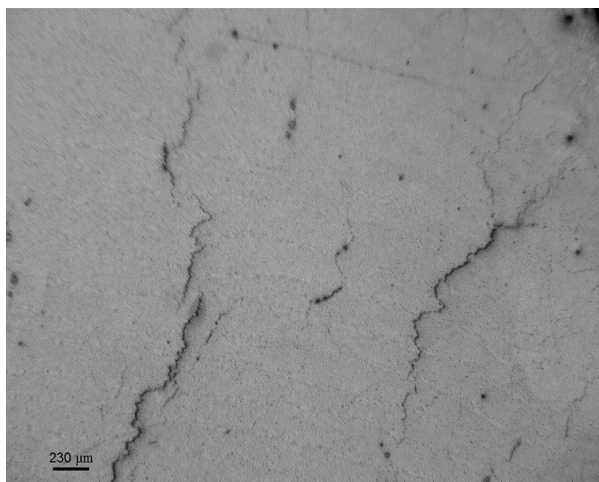
C.R. $\sim -25^\circ \text{C/s}$



Vertical micrographs of part 5



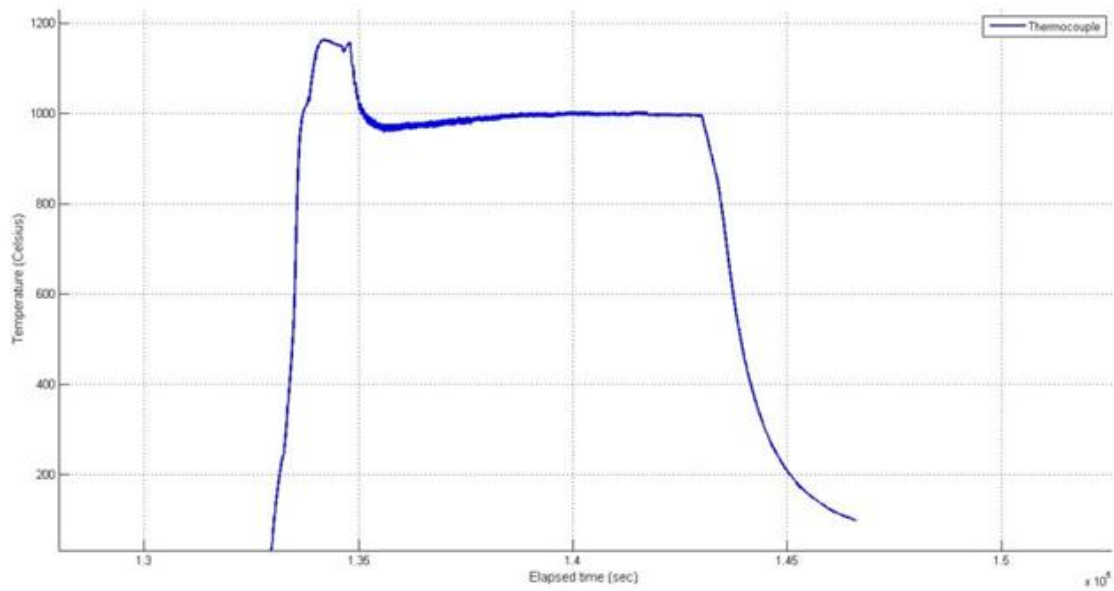
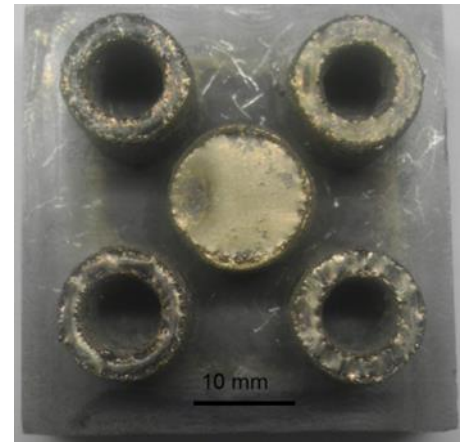
Horizontal micrographs of part 5



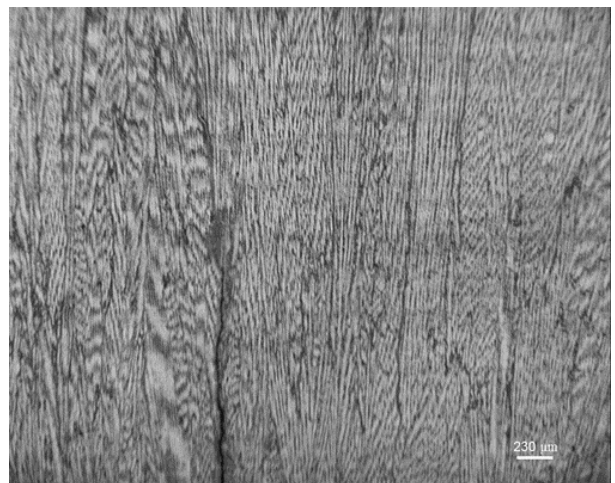
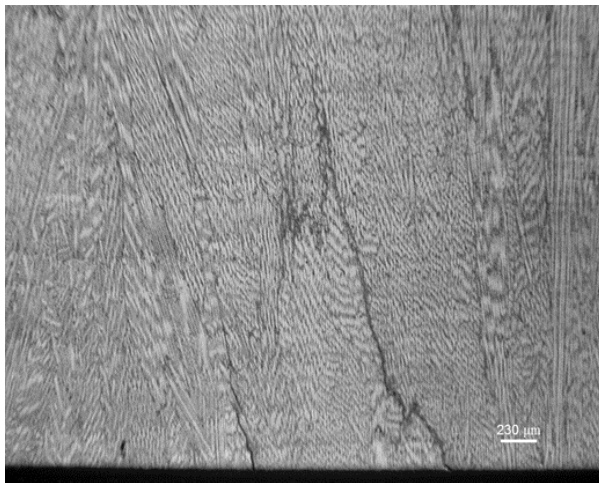
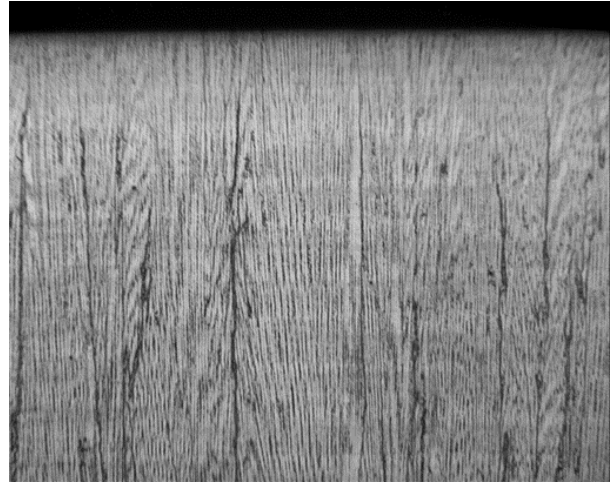
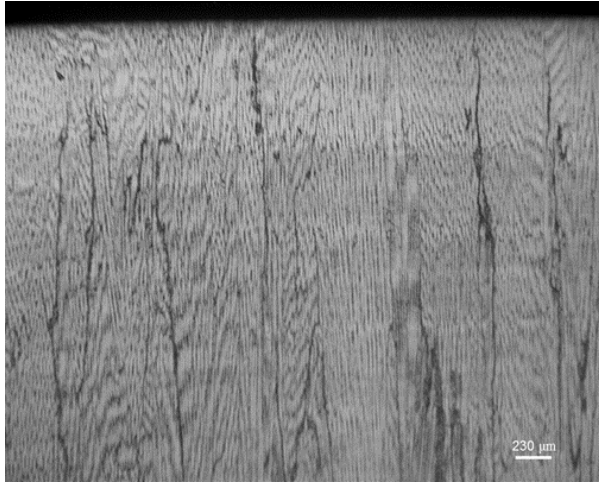
Date: 3/6/14

The processing temperature for this build was approximately 1000°C. Part 5 was built using the same parameters as the previous two builds (snake disabled). Movement of the pyrometer led to incorrect pyrometer data for this build. No significant change in crack density was observed when changing the build temperature.

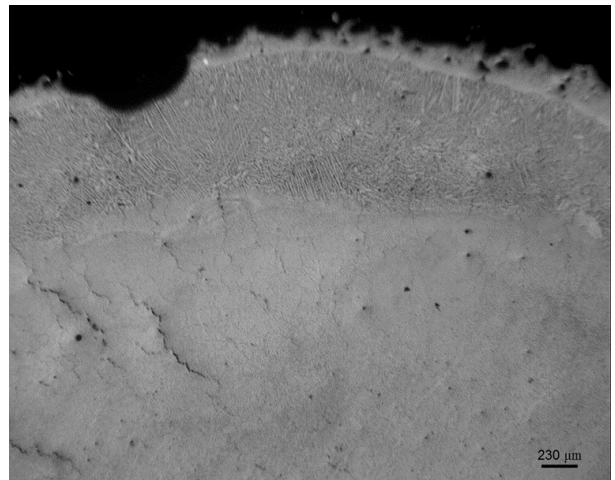
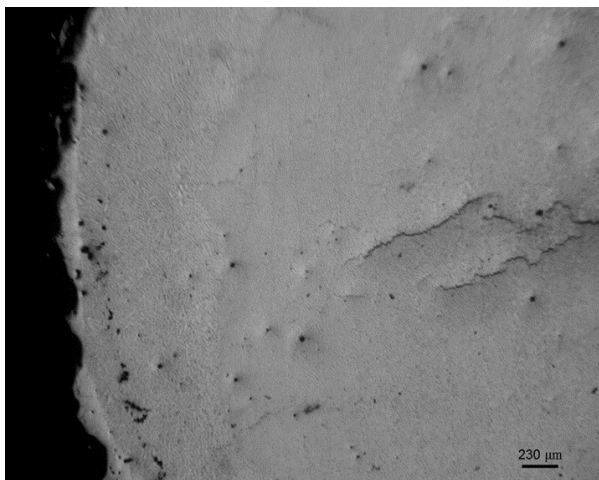
Part #	Current (mA)	Scan Speed (mm/s)	Line order
1	4	100	5
2	2.5	100	10
3	3.5	100	10
4	4	200	1
5	4	100	1



Vertical micrographs of part 5



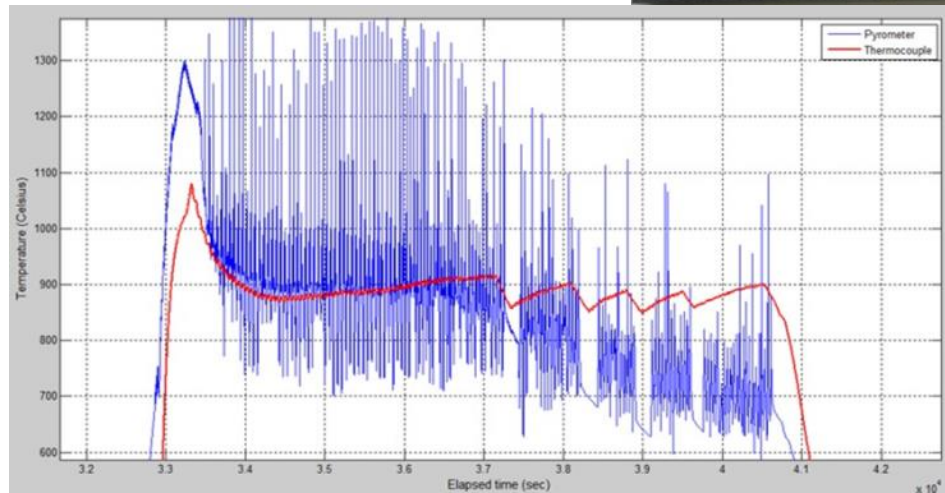
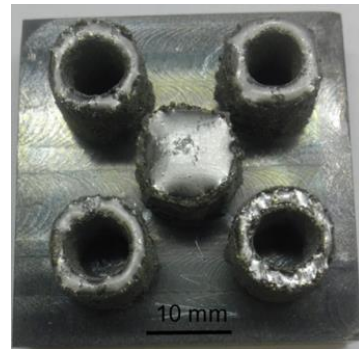
Horizontal micrographs of part 5



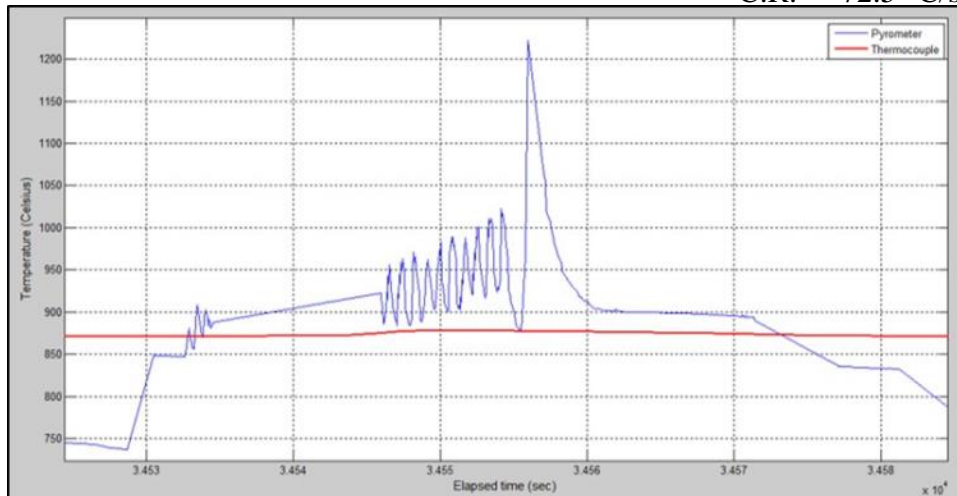
Date: 3/12/14

A replication of the low ($\sim 860^{\circ}\text{C}$) temperature build was attempted. Upon completion the build, part 5 showed visible warping and the sides of the part were sloped downward. The build temperature increased during the build above the targeted $\sim 860^{\circ}\text{C}$. The process was stopped (4 times) and allowed to cool in an attempt to reduce the building temperature. This phenomenon can be seen in the thermocouple temperature readings.

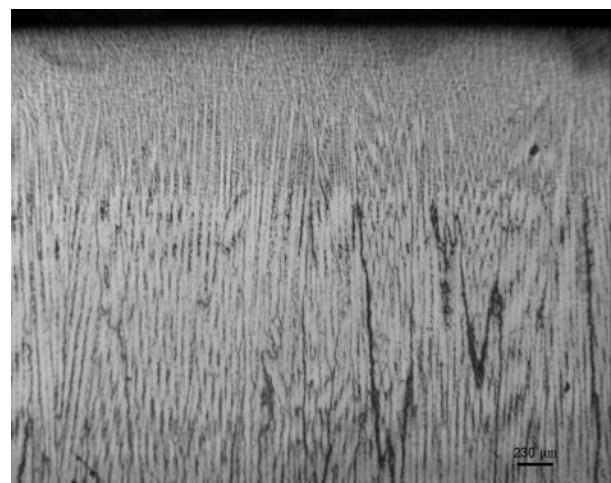
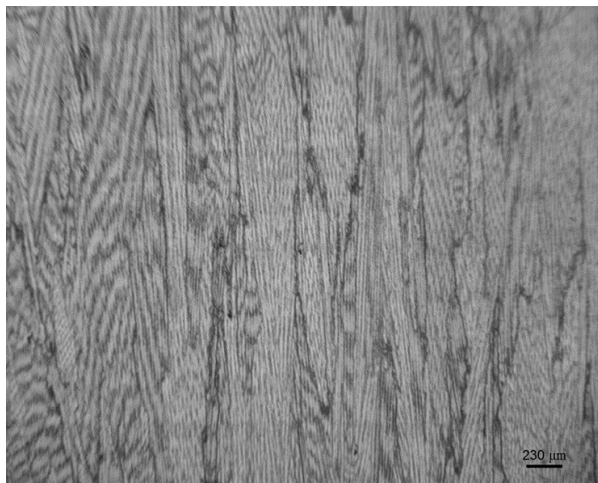
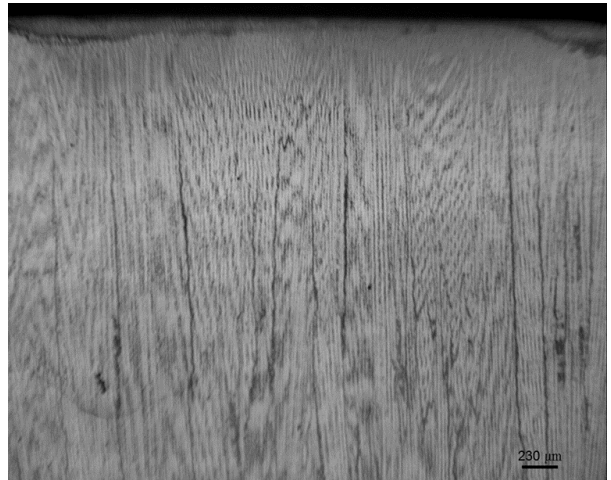
Part #	Current (mA)	Scan Speed (mm/s)	Line order
1	4	80	1
2	3	100	10
3	4	100	10
4	3.5	100	15
5	4	100	1



C.R. $\sim -72.5^{\circ}\text{C/s}$



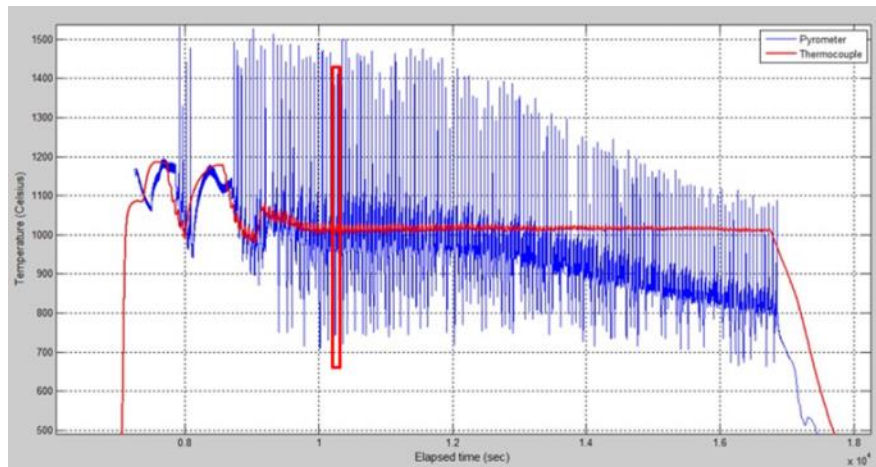
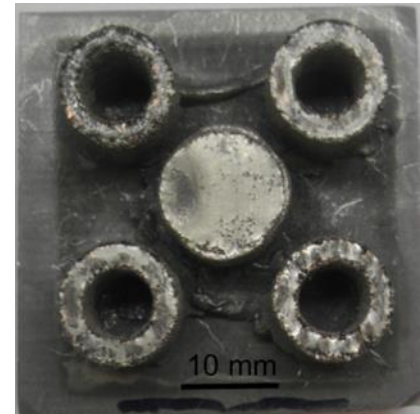
Vertical micrographs of part 5



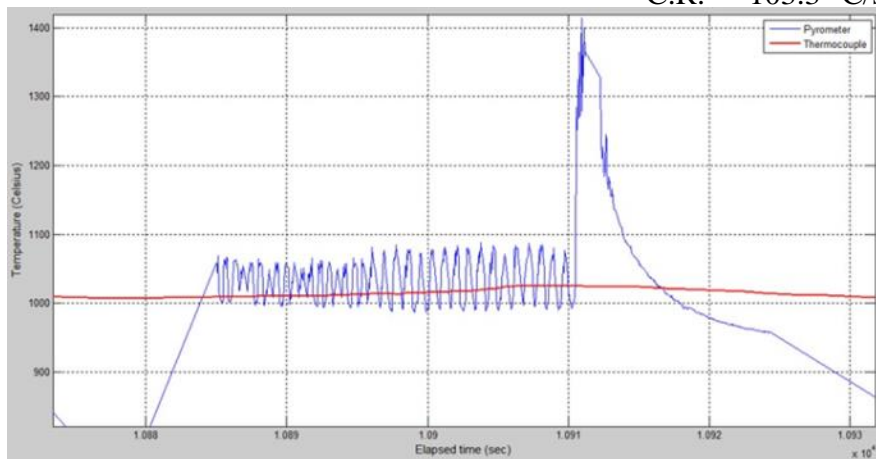
Date: 3/13/14 (1)

In order for further increase the temperature before the melt step of part 5, the melt order was changed for part 5 to be melted first. The pyrometer showed this was an effective way to maintain a higher temperature before melting.

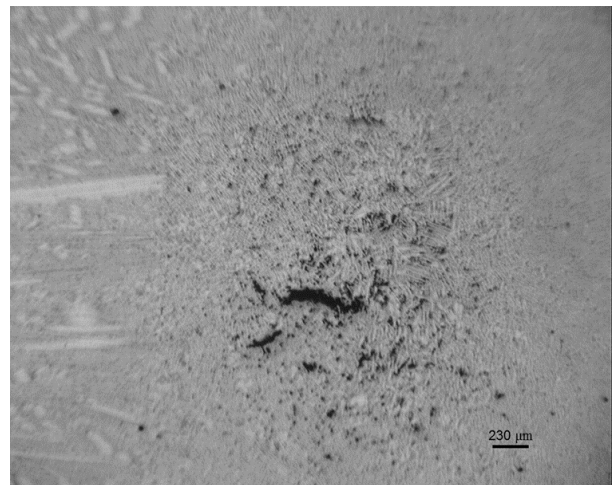
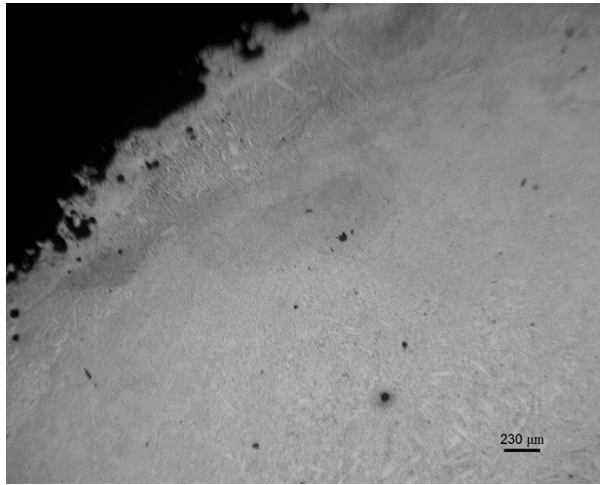
Part #	Current (mA)	Scan Speed (mm/s)	Line order
1	3.5	100	1
2	2	100	1
3	3.5	100	10
4	4	100	10
5	4	100	1



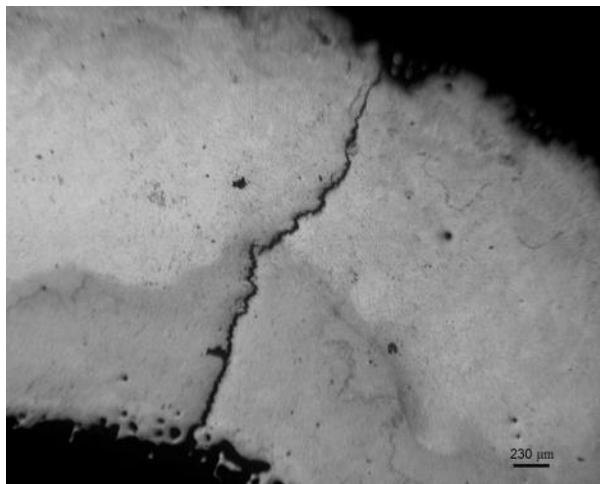
C.R. $\sim -103.3^{\circ}\text{C/s}$



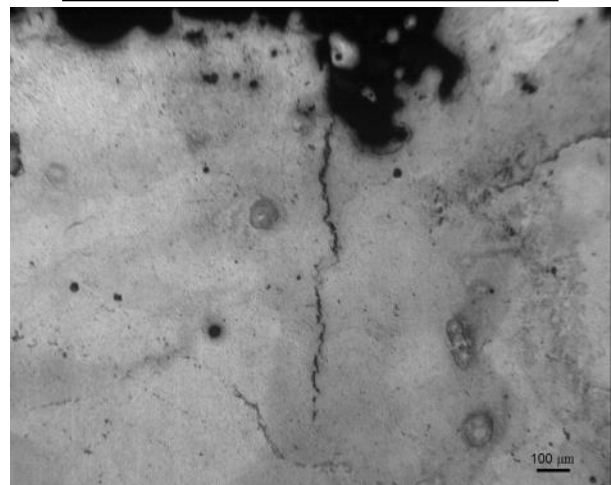
Horizontal micrographs of part 5



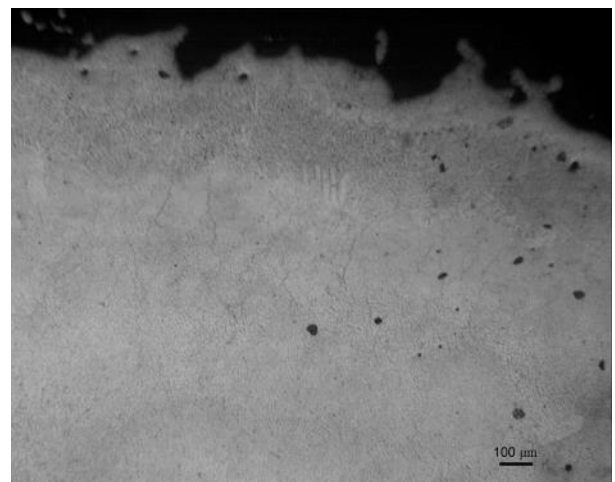
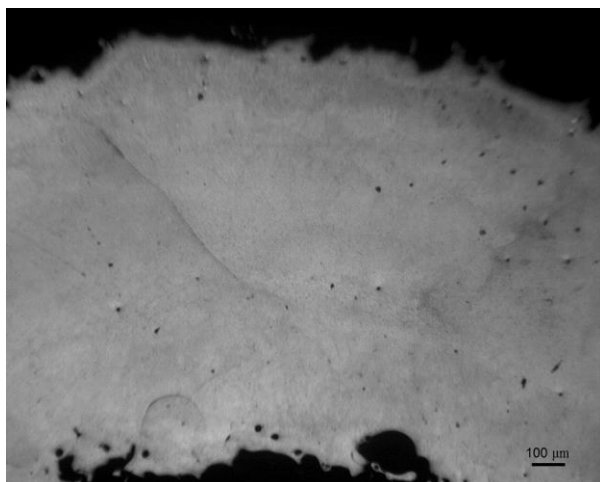
Horizontal Micrograph of part 1



Horizontal Micrograph of part 2



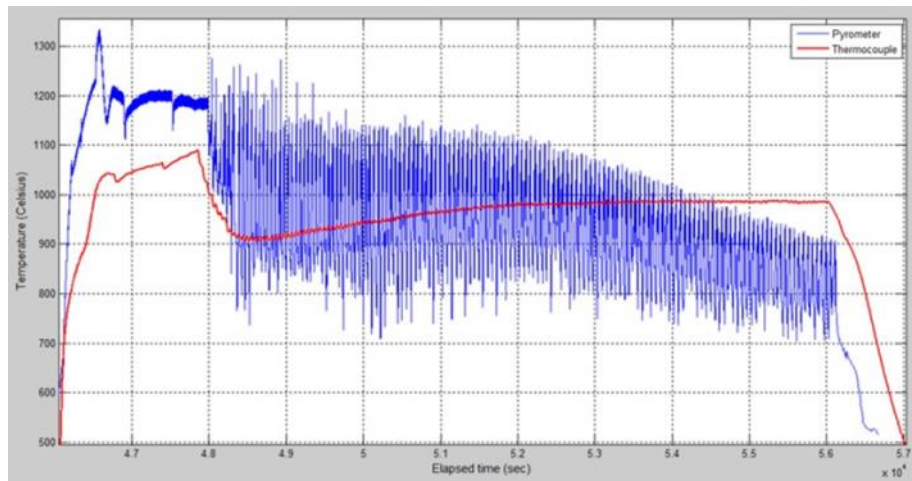
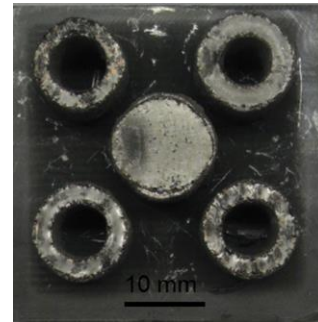
Horizontal Micrograph of part 4



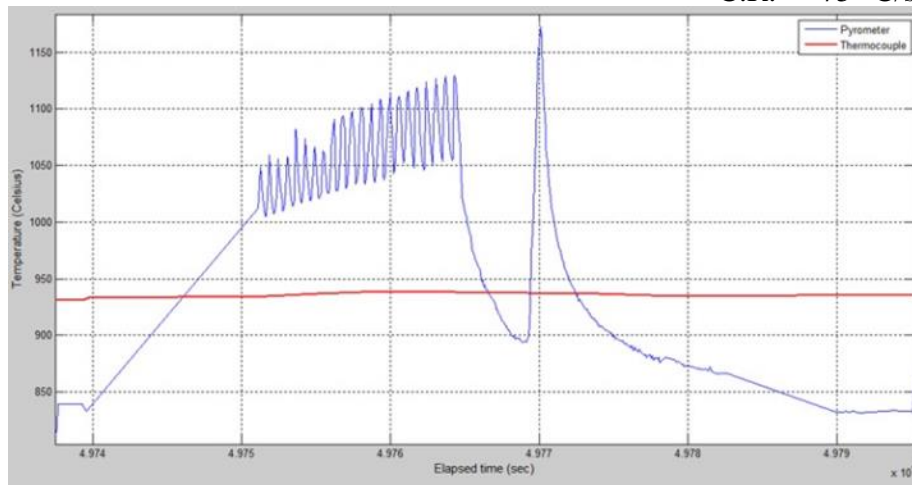
Date: 3/13/14 (2)

In this build, the pyrometer aim was shifted to part three during fabrication. Part 5 was melted first; however, the pyrometer data (below) shows a large temperature drop prior to melting. The temperature of the powder prior to the melting of part 5 was assumed to be approximately the same temperature reading from the pyrometer directly after preheating. Making this assumption that the temperature prior to melting is greater than the previous build (3/13 (1)) by $\sim 50^{\circ}\text{C}$.

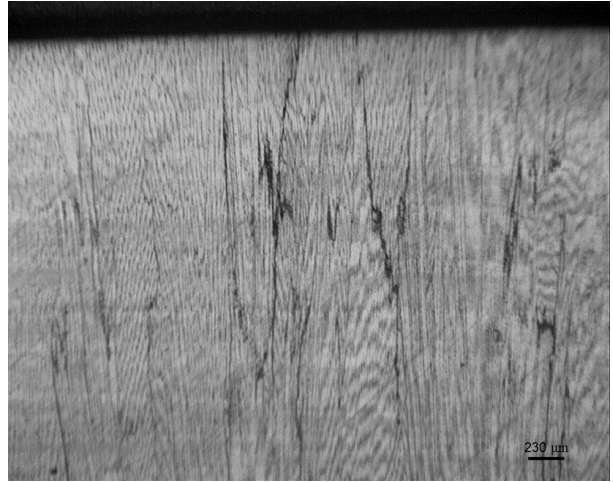
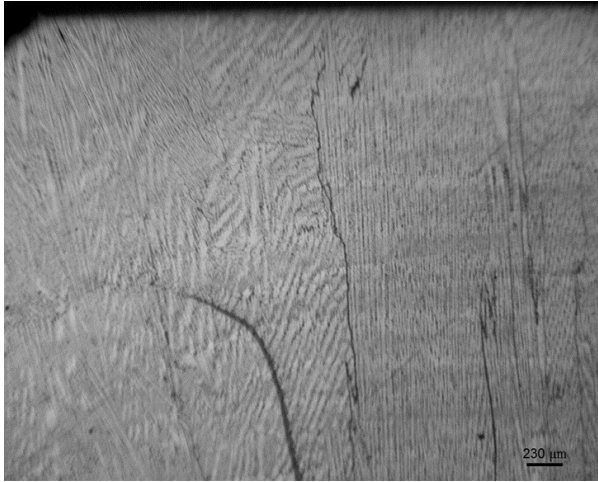
Part #	Current (mA)	Scan Speed (mm/s)	Line order
1	3.5	100	1
2	2	100	1
3	3.5	100	10
4	4	100	10
5	4	100	1



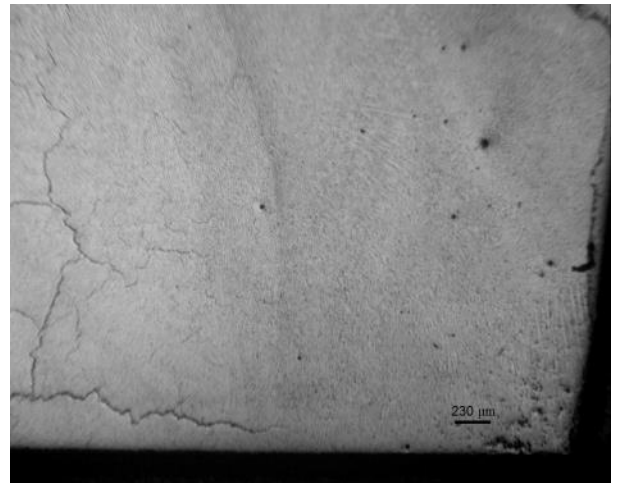
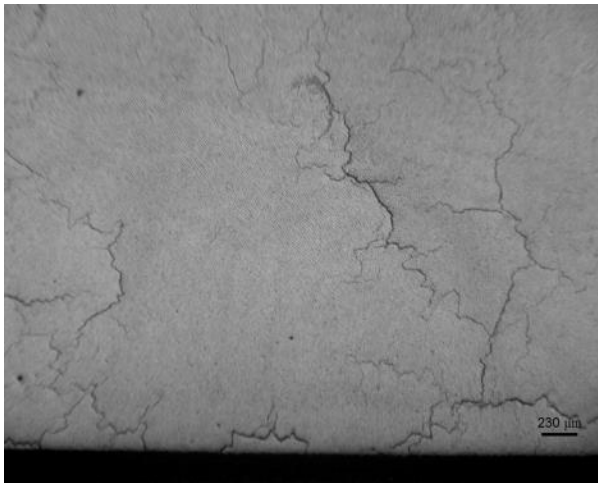
C.R. $\sim -75^{\circ}\text{C/s}$



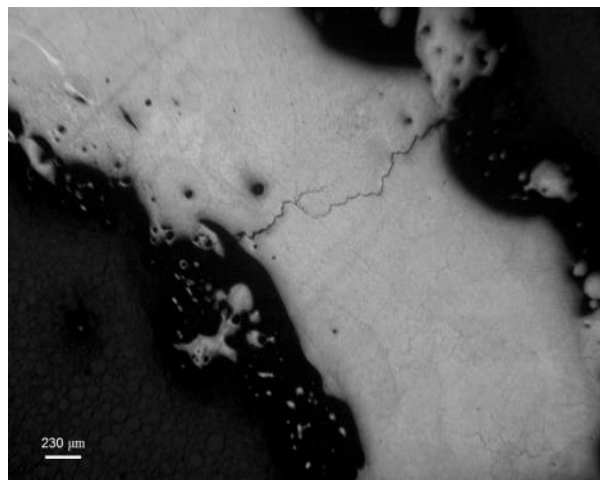
Vertical micrographs of part 5



Horizontal micrographs of part 5



Horizontal micrographs of part 2

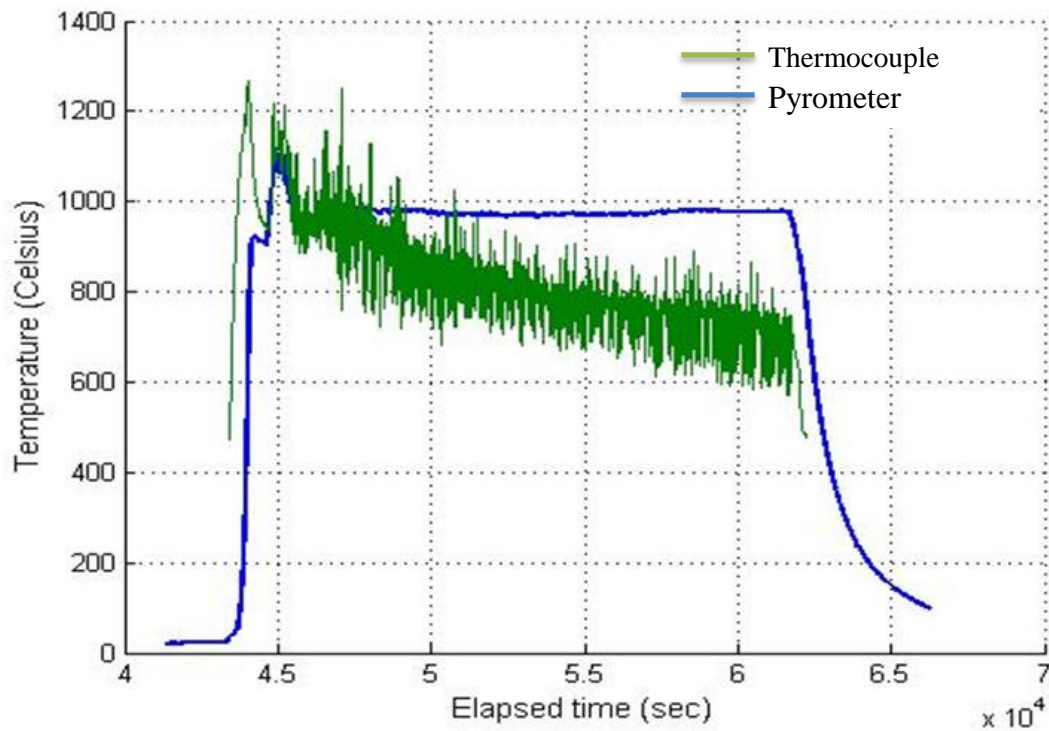


Date: 3/14/14

This build was fabricated using automatic mode and the snake was disabled. No further experimentation or analysis was done for this build. Cracking was clearly evident after cutting the build from the R125 start plate.

Automatic mode:

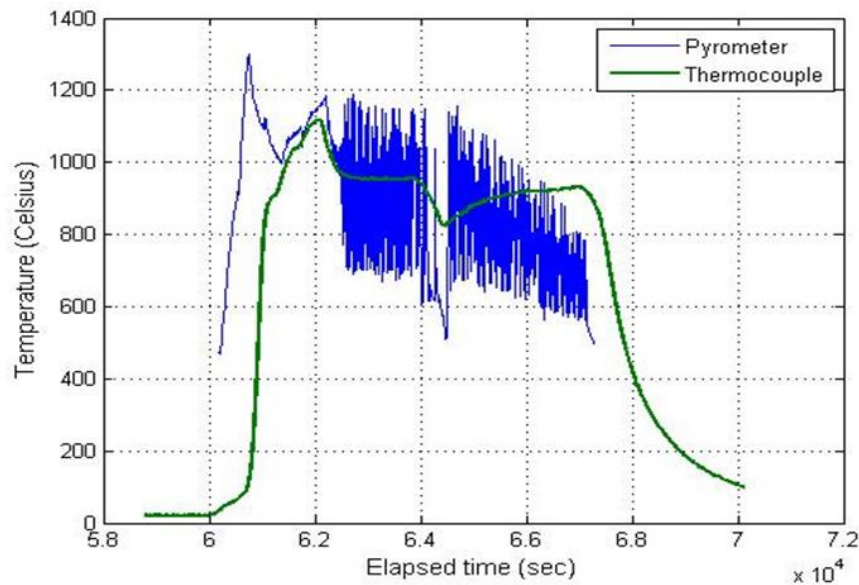
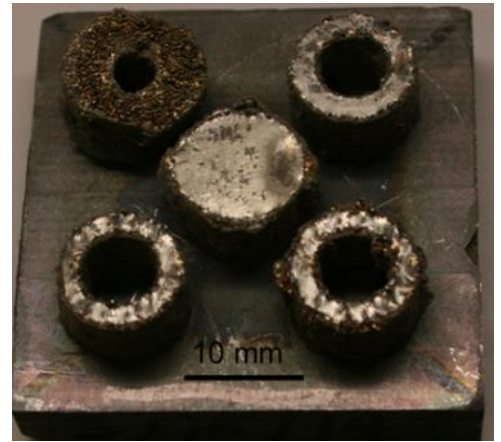
Surface Temp: 1100° C
Speed Function: 30



Date: 3/15/14

For this build, the preheating strategy was changed from slow speed and low current to high speed and high current. This change in strategy caused powder explosion and was changed to the previous strategy half-way through the build to prevent these explosions. Several parameter changes were done to part 2 during fabrication in an attempt to find workable parameters using high speed and high current. No parameters were found to be successful after the build was removed. Part 2 immediately broke away from the start plate.

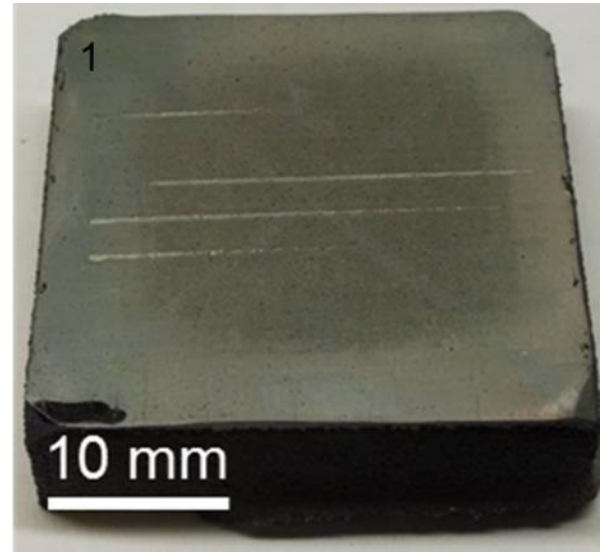
Part #	Current (mA)	Scan Speed (mm/s)	Line order
1	4	100	5
2	10	1000	1
3	4	100	10
4	4	100	15
5	4	100	1



Date: 3/17/14

Another beam pass experiment was performed similar to 2/21/14; however, using faster beam speed and high beam currents. No analysis was done for this experiment due to the difficulty of observing the melted areas with the equipment available.

Pass number	Current (mA)	Scan Speed (mm/s)
1	25	600
2	25	800
3	25	1000
4	20	500
5	20	700
6	20	900
7	20	1100
8	15	400
9	15	600
10	15	800



Date: 3/19/14 (1)

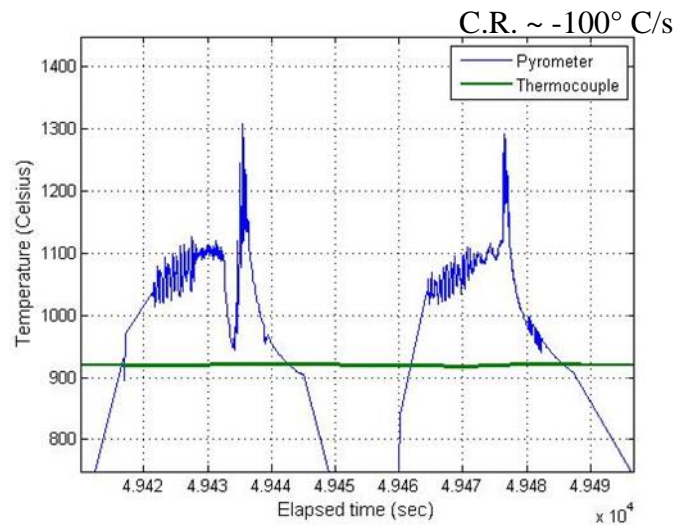
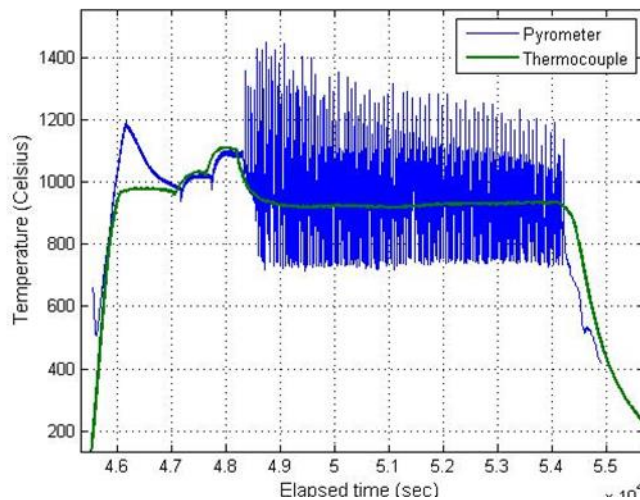
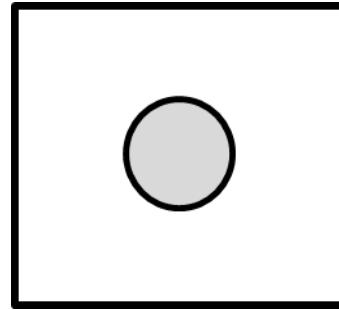
For this build, the geometry was changed to a single cylinder with the same 10mm diameter and 10mm height as previous builds. The pyrometer showed a repeating pattern, shown by the zoomed in temperature plot. This was caused by the positioning of the pyrometer.

Melt themes:

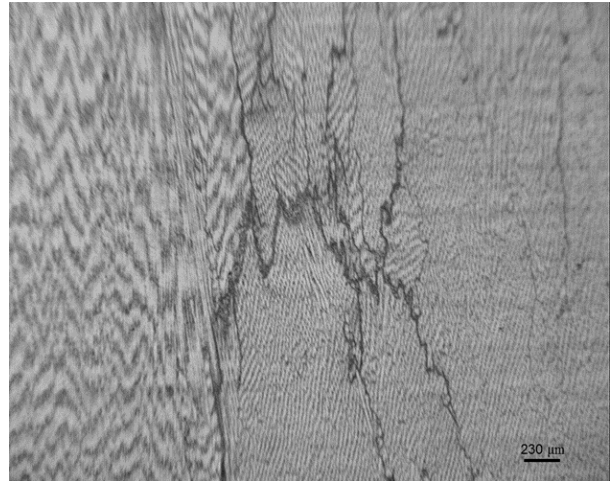
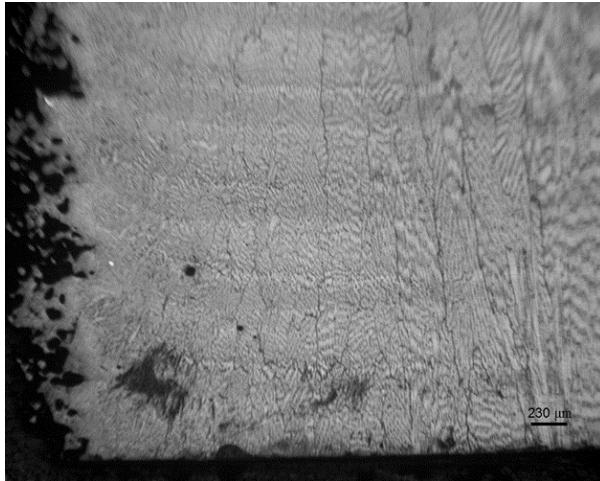
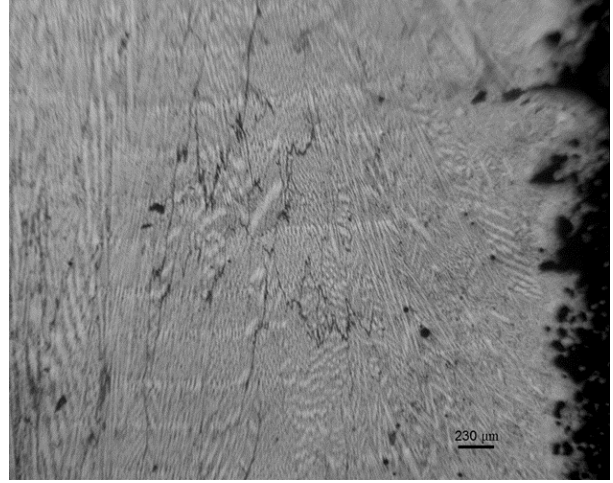
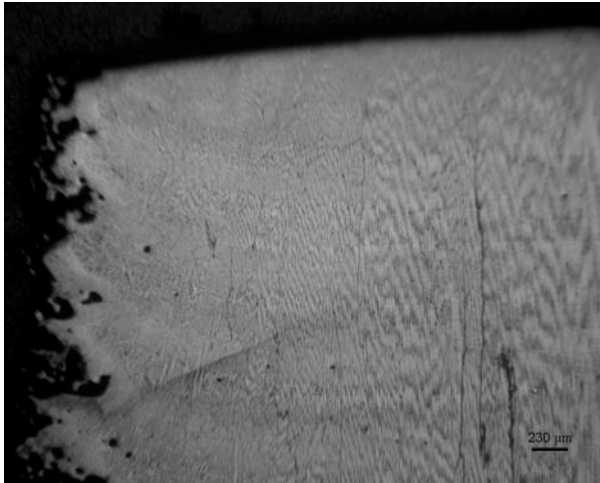
Current: 4mA

Scan Speed: 100mm/s

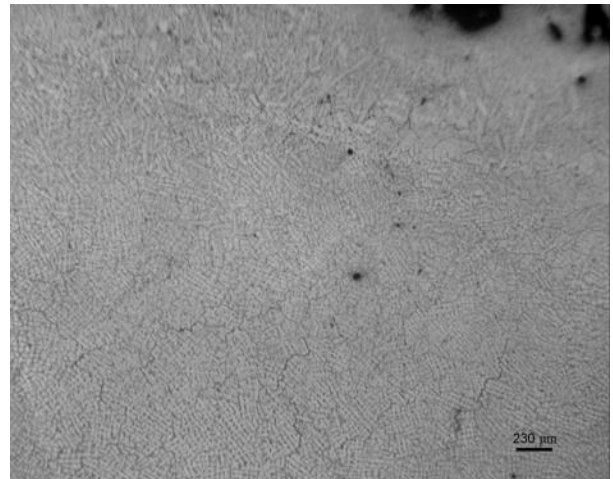
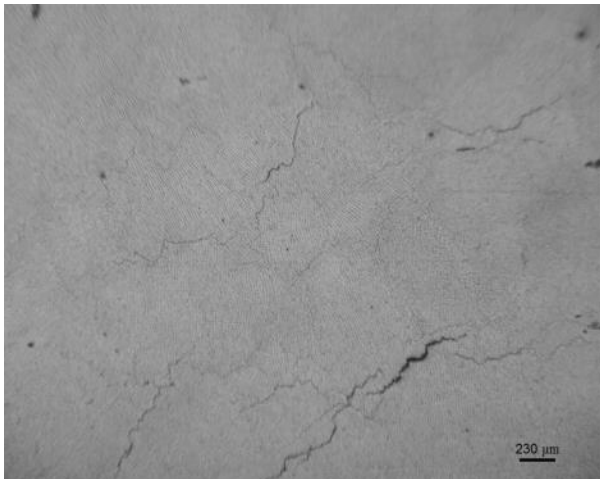
Focus Offset: 19 mA



Vertical micrographs



Horizontal micrographs

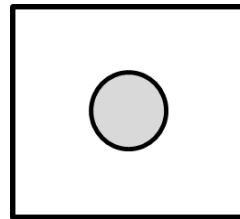


Date: 3/19/14 (2)

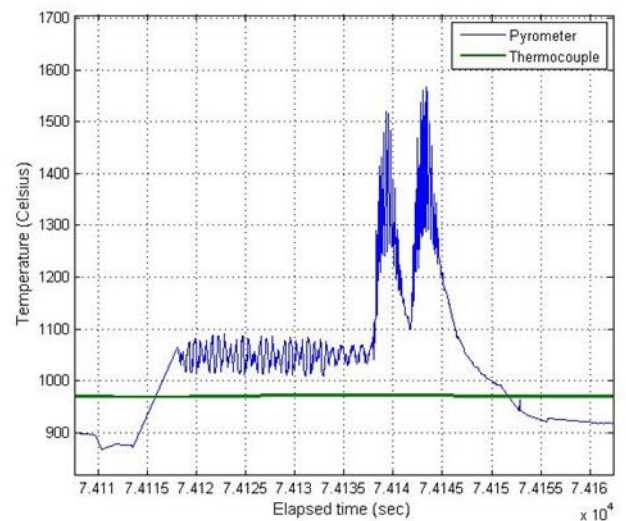
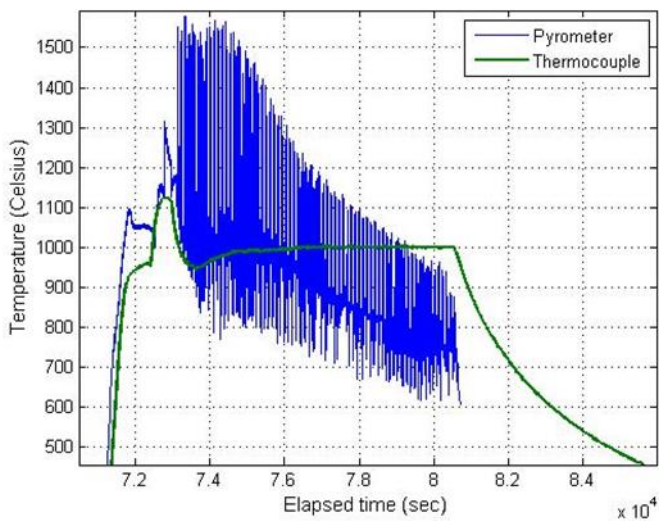
The addition of another melt step was used for this build allowing the melt step to occur twice for each layer. Cracking was not observed in the horizontal micrographs; however, upon analyzing the vertical micrographs, various cracks were observed that were smaller in number compared to previous builds. Multiple melts can improve the crack density of the parts which was further explored with future experiments.

Melt themes:

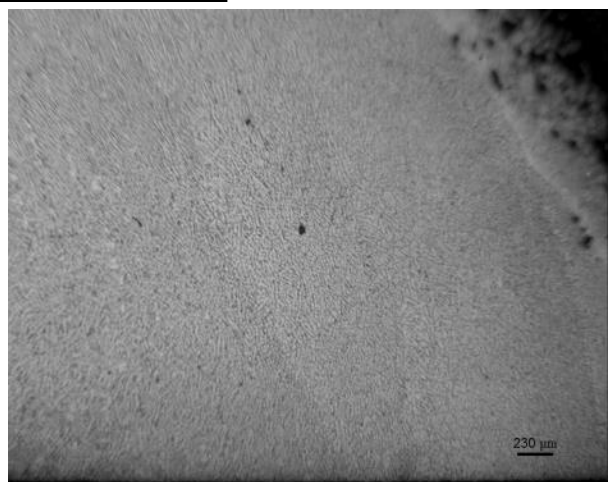
Current: 4, 4.3mA
Scan Speed: 100, 100mm/s
Focus Offset: 19 mA



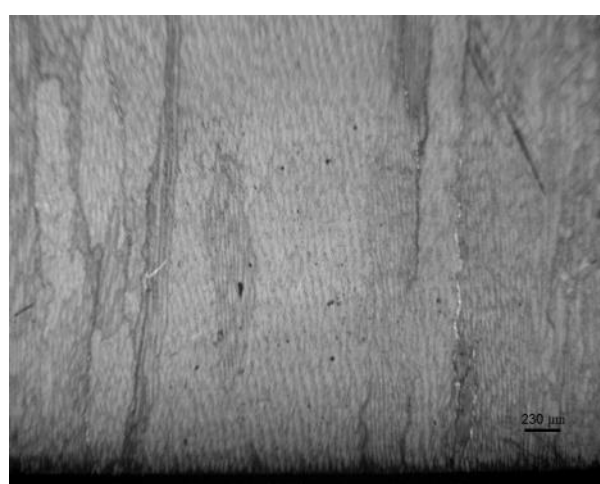
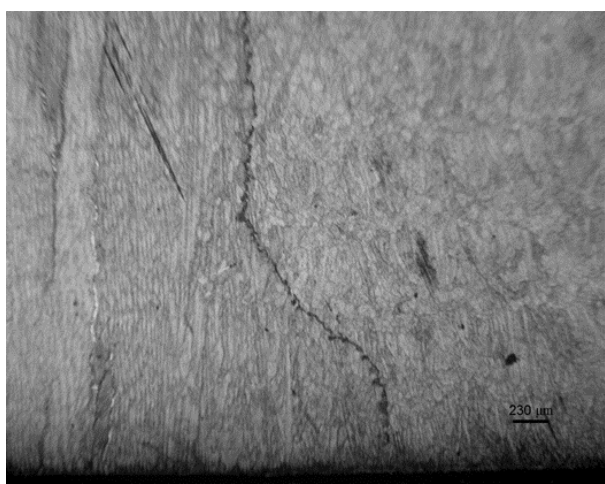
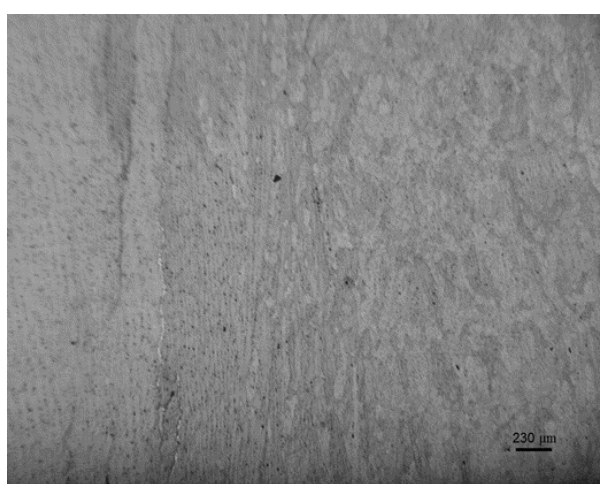
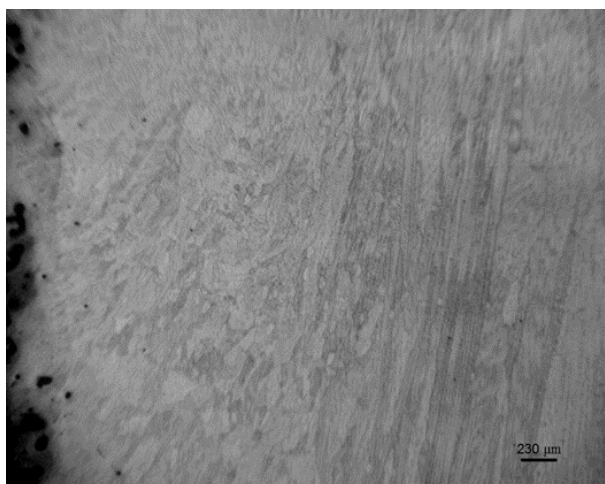
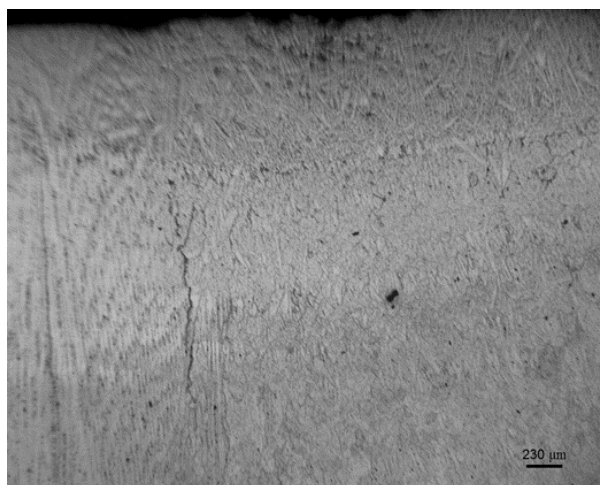
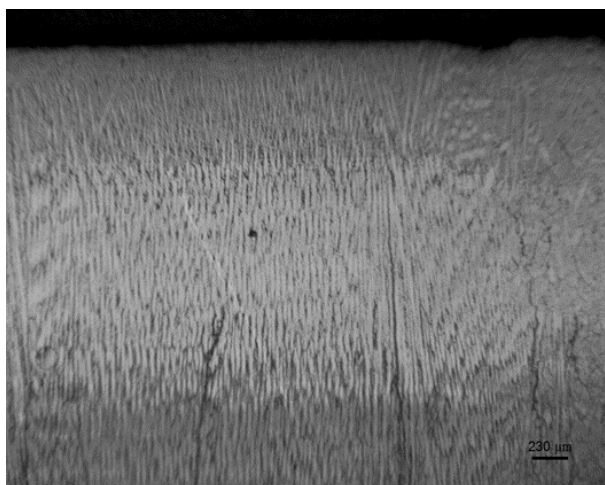
C.R. $\sim -75^{\circ}\text{C/s}$



Horizontal micrographs



Vertical micrographs



Date: 3/24/14

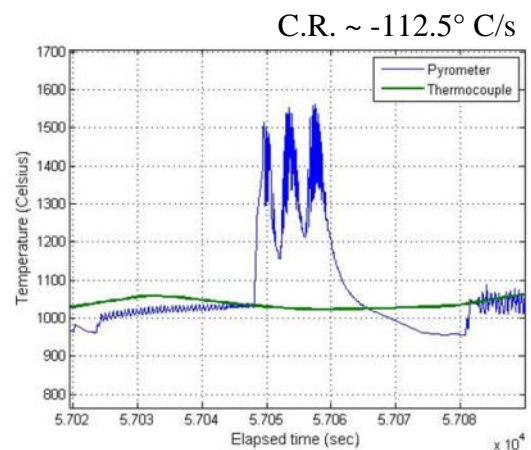
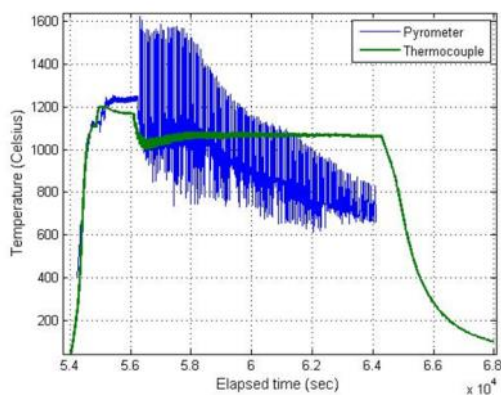
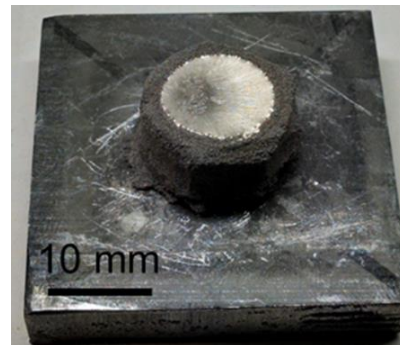
Seeing the reduction in crack density when doing two melts from previous builds, a third melt was added. Only one crack was visible in the vertical micrographs and no cracks were visible in the horizontal micrographs. The only crack seen in the micrographs appeared to stop near the top of the sample. This experiment rendered the most successful results from all experiments performed in this research.

Melt themes:

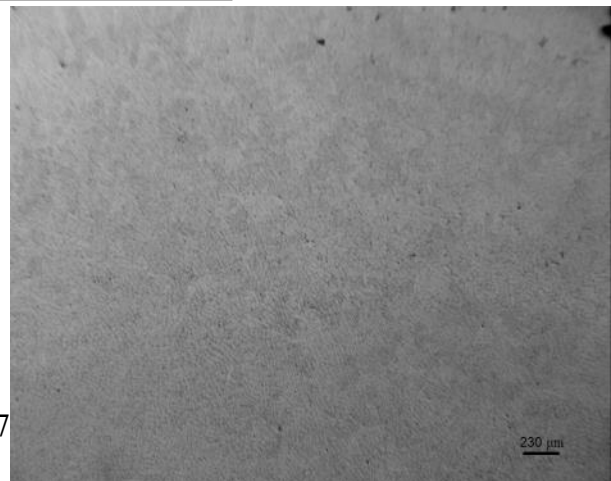
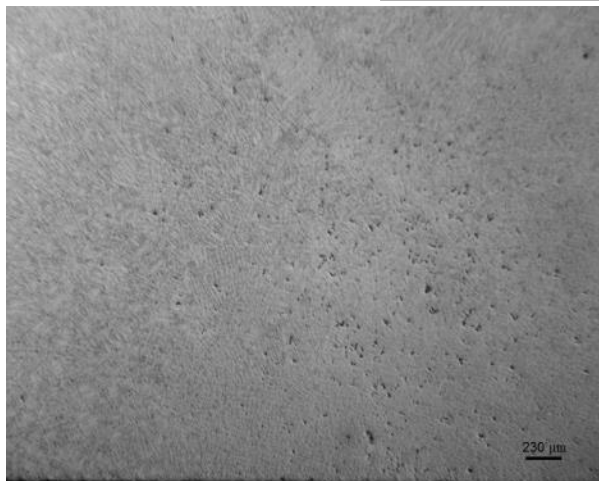
Current: 4, 4.3, 4mA

Scan Speed: 100, 100, and 100mm/s

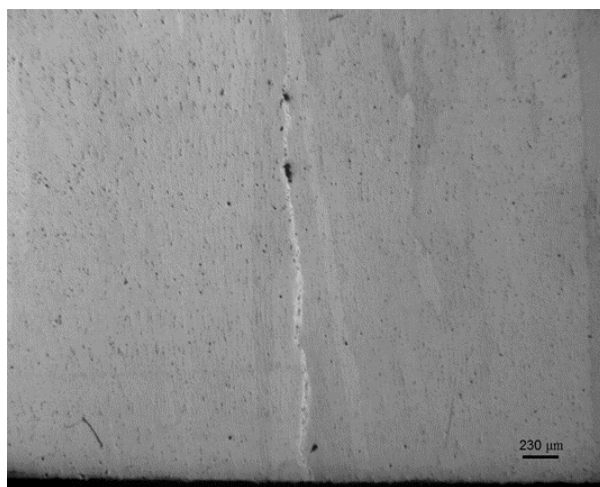
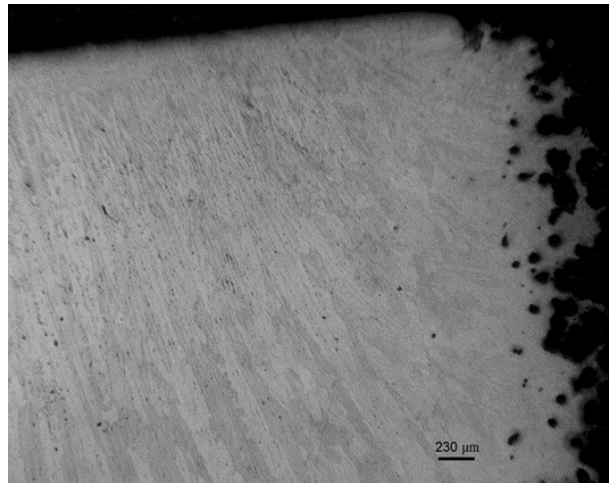
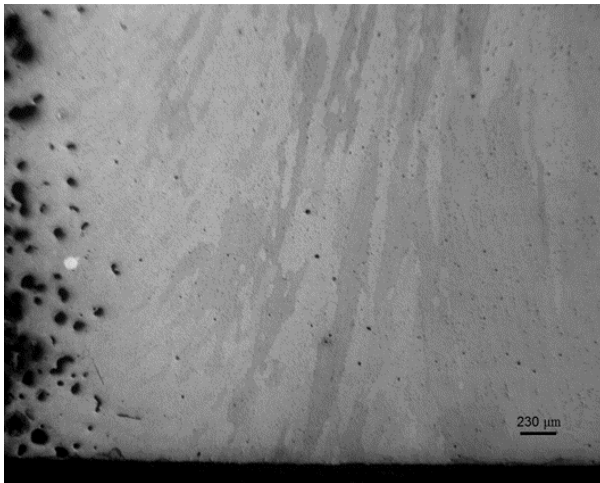
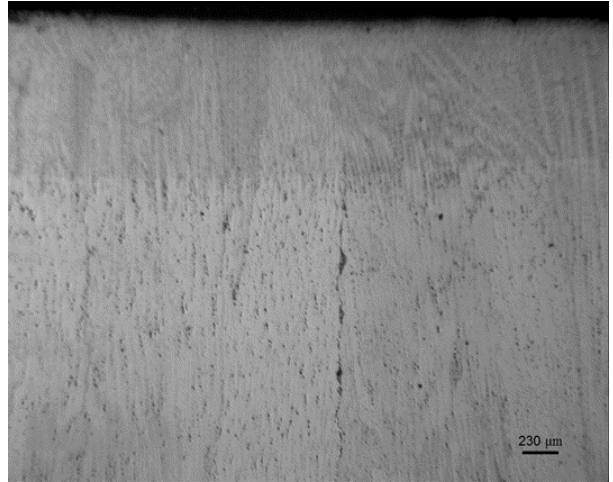
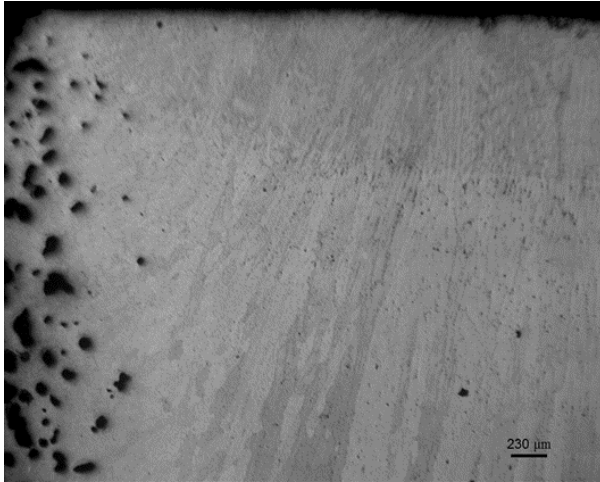
Focus Offset: 19 mA



Horizontal micrographs



Vertical micrographs

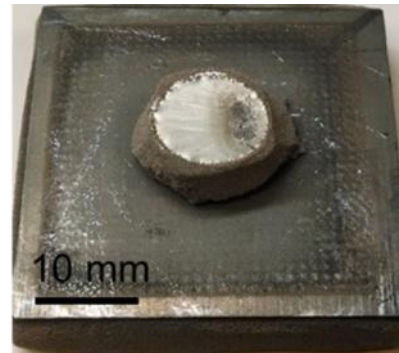
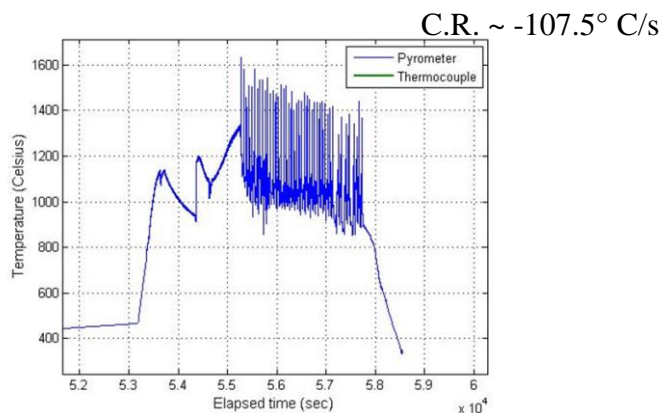


Date: 3/26/14

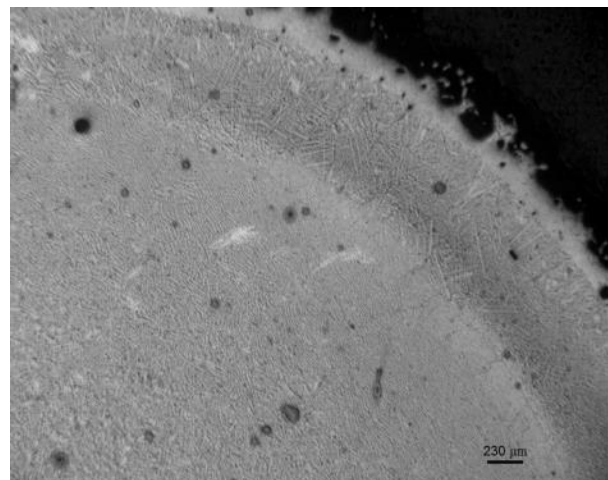
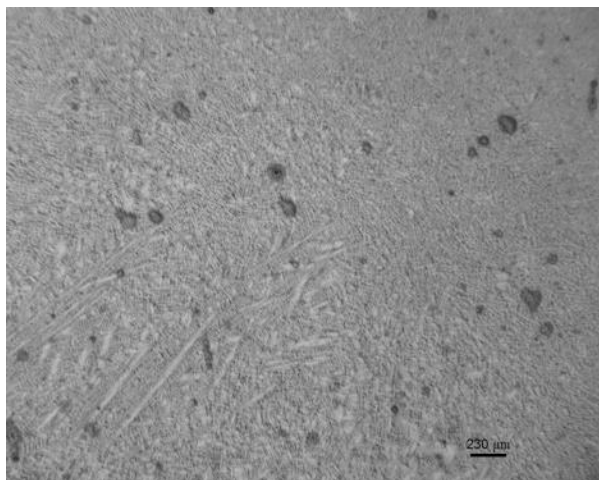
Multiple melts were used in this build, each with a randomized hatch pattern. The vertical micrographs did not appear to have horizontal cracks. The dark lines in the micrographs were due to alcohol staining on the sample. The thermocouple data were not available for this build. A good estimation of the build temperature would be $\sim 1050 - 1100^{\circ}\text{C}$ based on the pyrometer data obtained. Randomizing the hatching pattern increased the crack density showing that the scan method can play a significant role in crack density.

Melt themes:

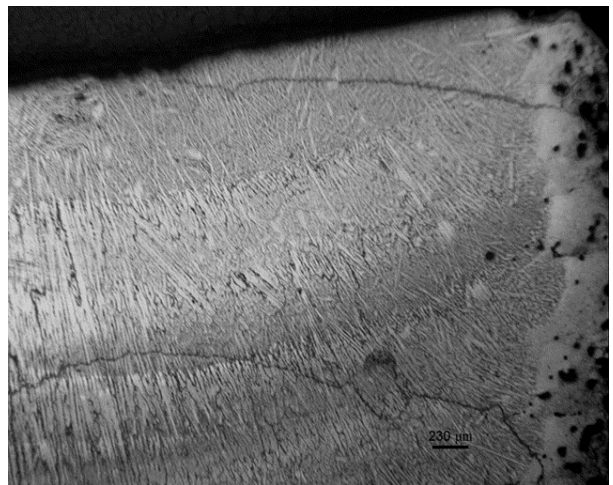
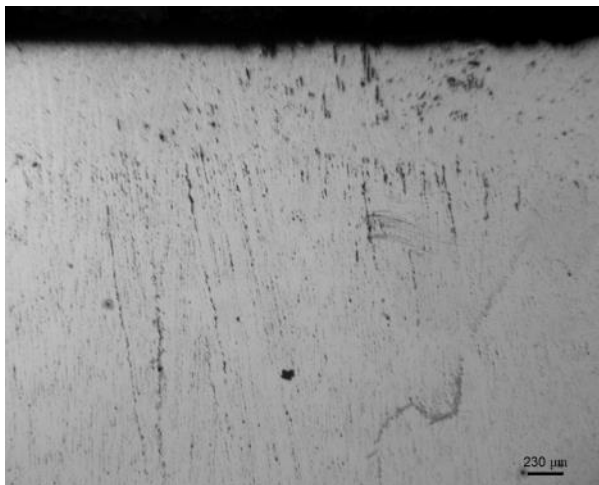
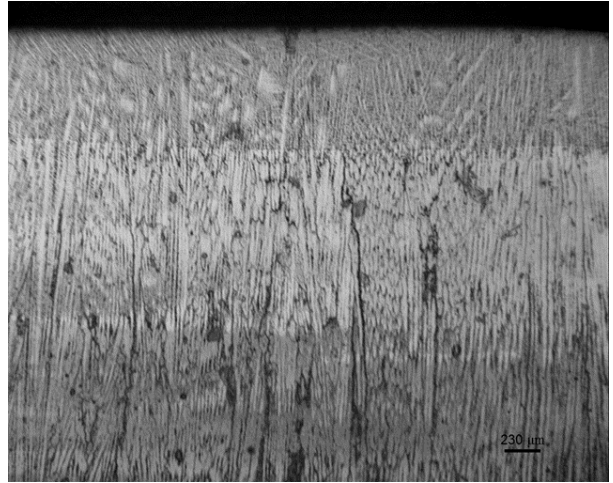
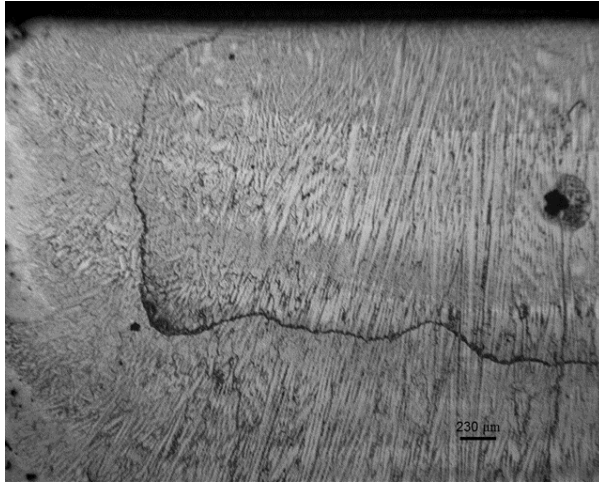
Current: 4.3, 4, 3.5mA
Scan Speed: 100mm/s
Focus Offset: 19 mA



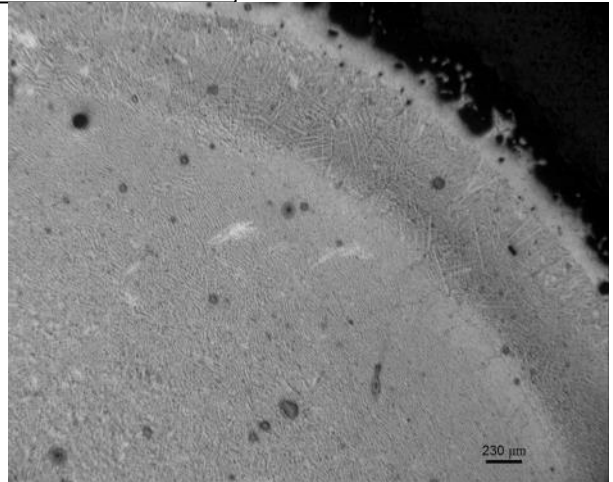
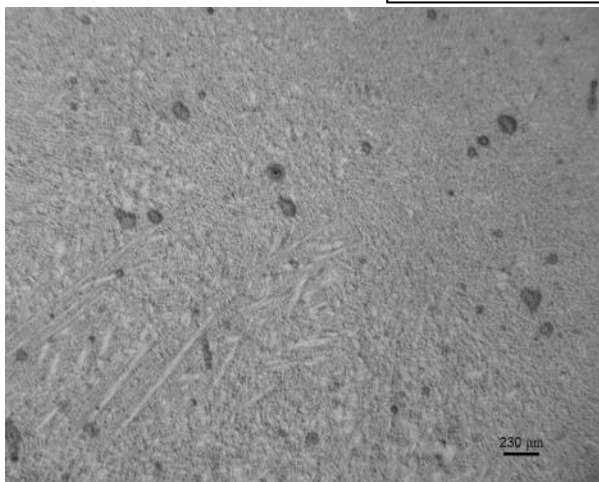
Horizontal micrographs



Vertical micrographs



Horizontal micrographs



Date: 3/27/14 (1)

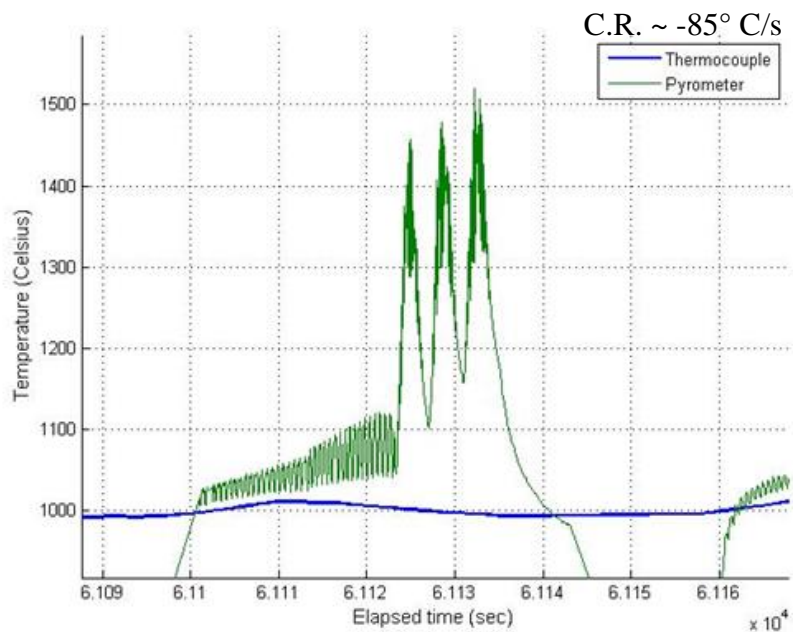
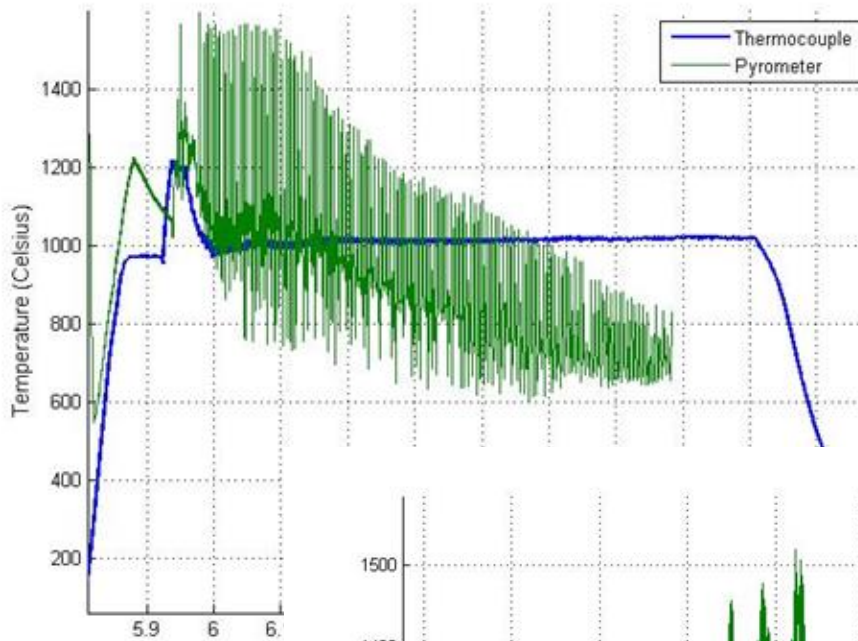
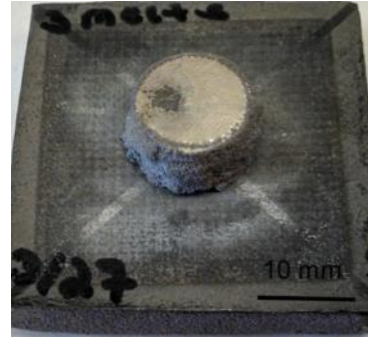
Three melts were used for this build, each increasing in current. No noticeable change was observed in crack density as few cracks were observed in the vertical micrographs and none were observed in the horizontal micrographs.

Melt themes:

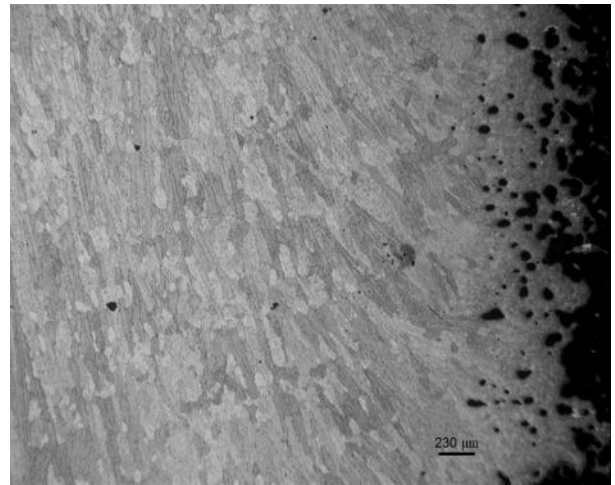
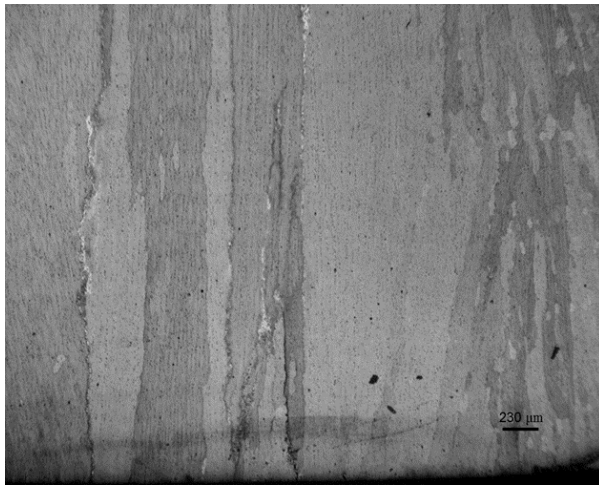
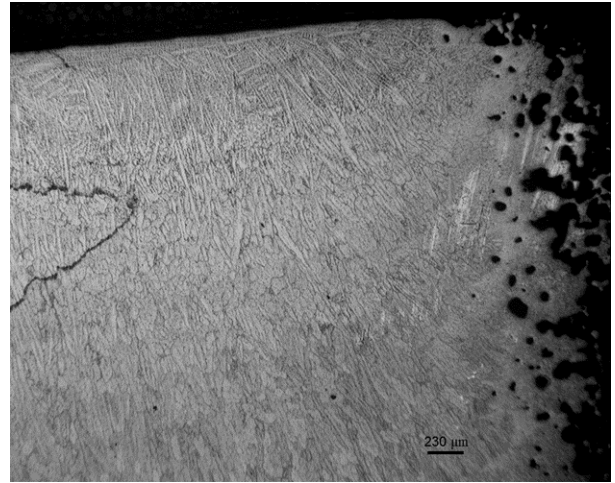
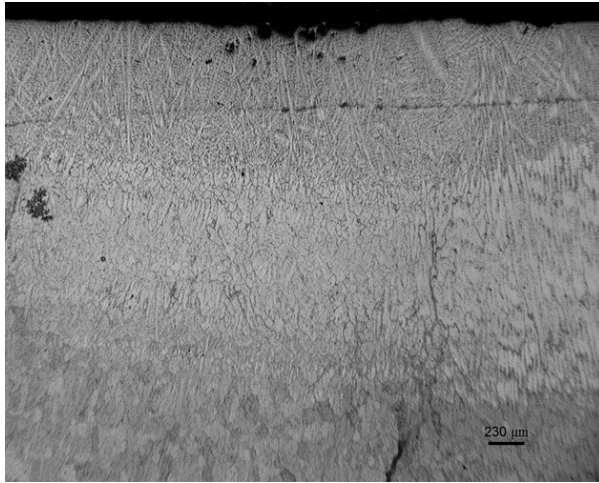
Current: 3.5, 4, 4.3mA

Scan Speed: 100mm/s

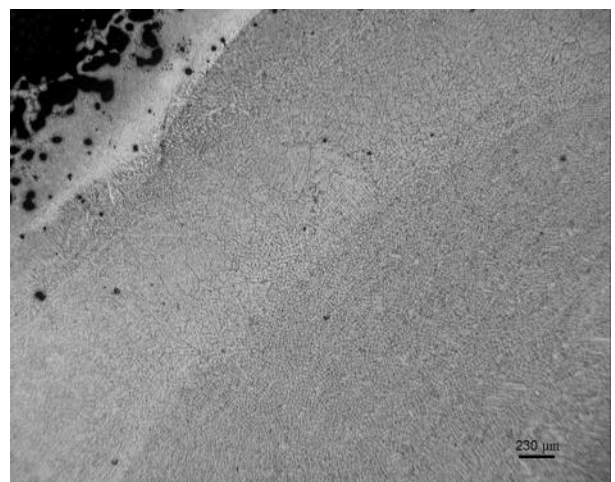
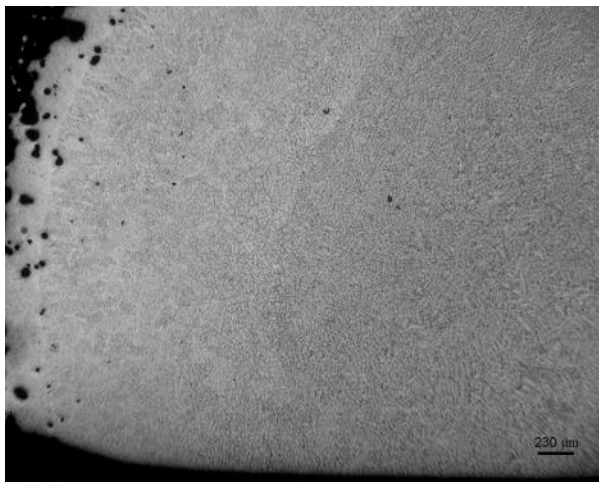
Focus Offset: 19 mA



Vertical micrographs

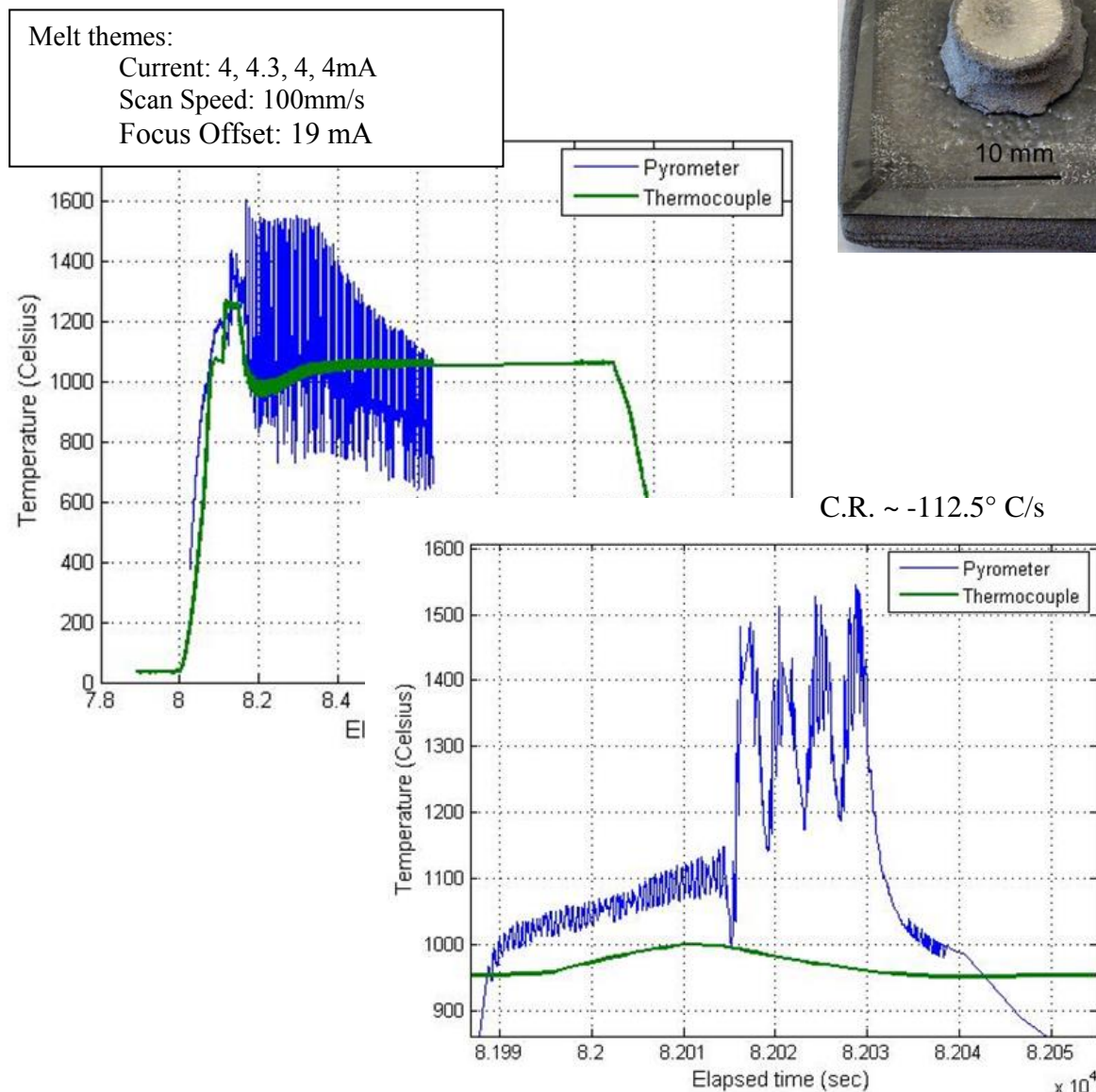


Horizontal micrographs

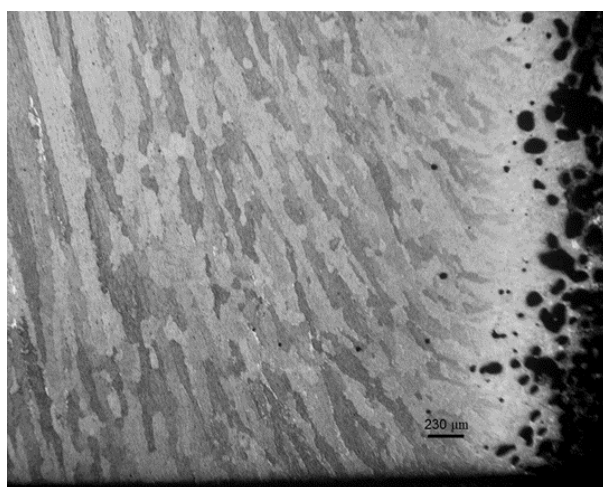
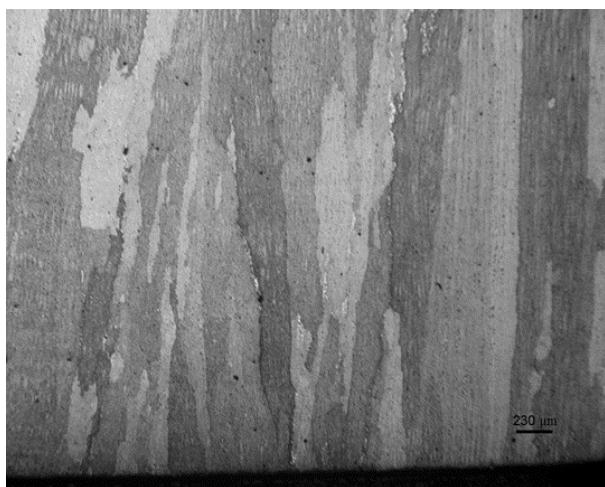
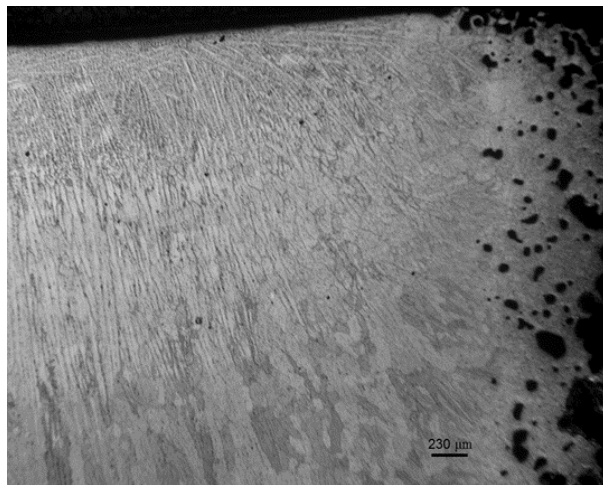
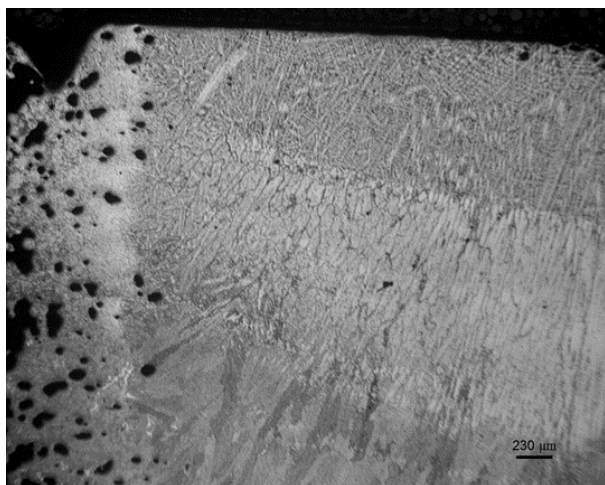


Date: 3/27/14 (2)

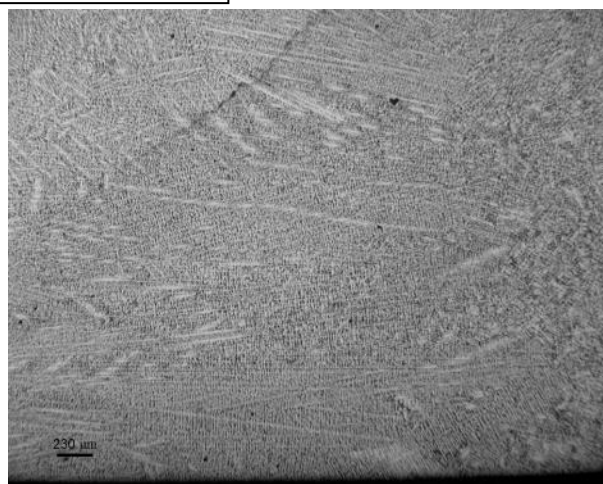
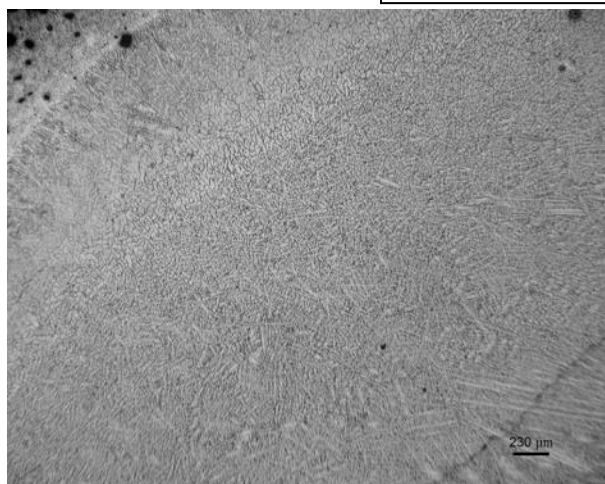
A fourth melt was added to this build in order to assess whether more melts will further improve the crack density. Crack density still remained low, similar to build using three melts. Additional experiments are needed to conclude whether more melts can further improve crack density. It is important to note that utilizing an increased number of melts will begin to change part microstructure and increase porosity at the part's contours as shown by this builds microstructure.



Vertical micrographs



Horizontal micrographs



Date: 3/28/14

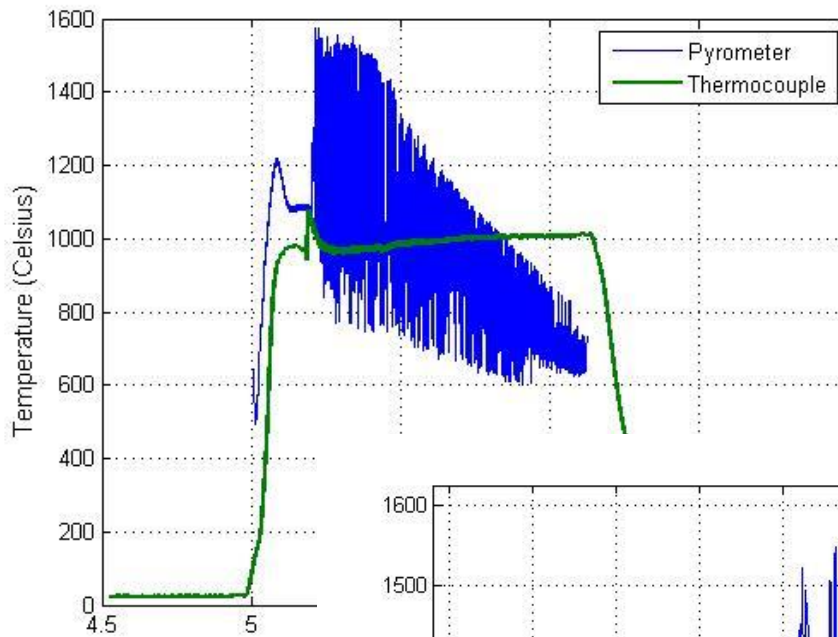
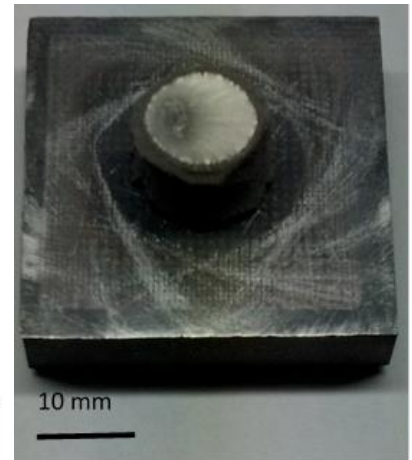
Three melts were used for this build. The first melt started at a high current of 4.3mA and ramped down to a current of 3.5 mA. Crack density still remained low, similar to build on 3/27/2014.

Melt themes:

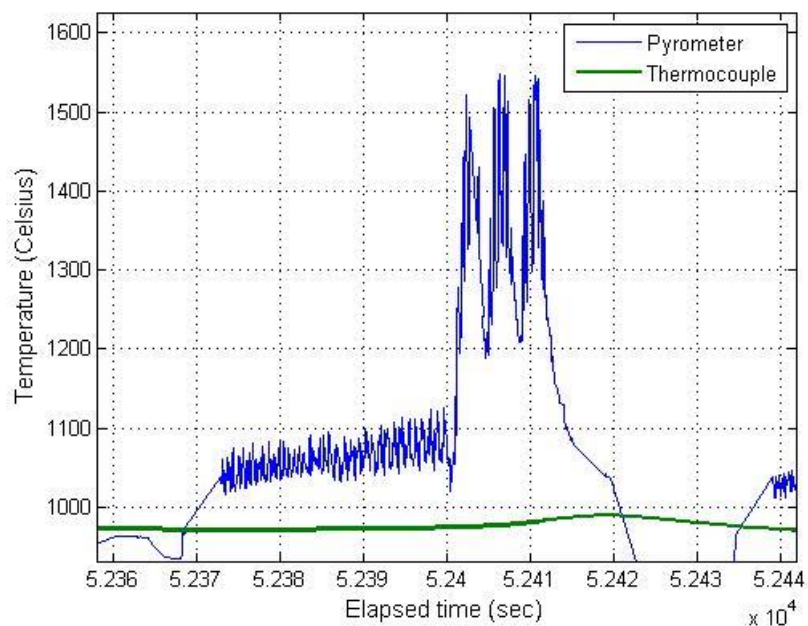
Current: 4.3, 4, 3.5mA

Scan Speed: 100mm/s

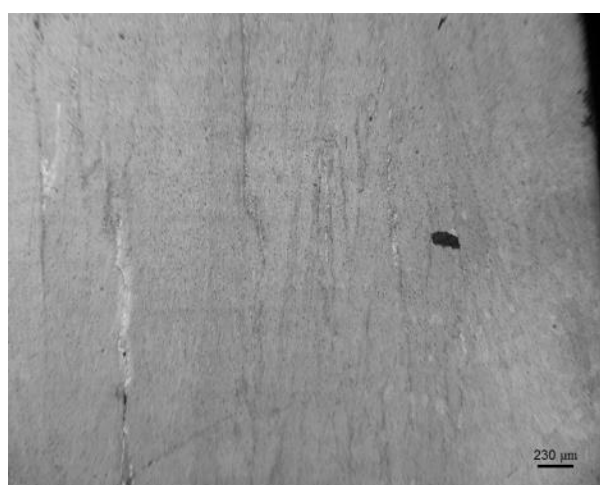
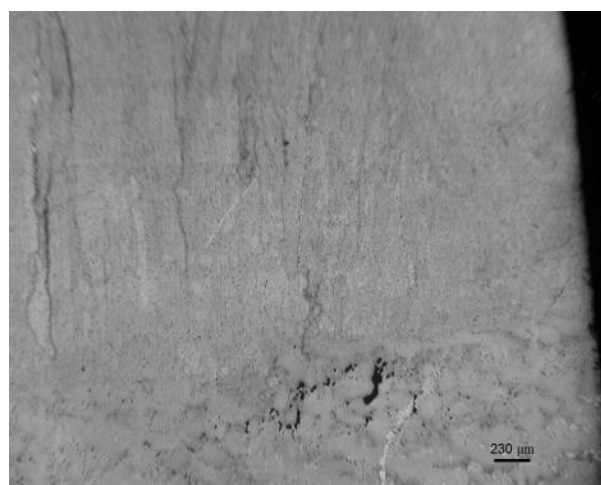
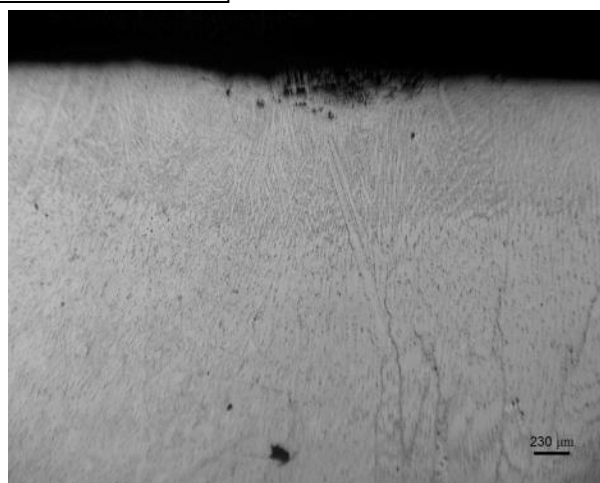
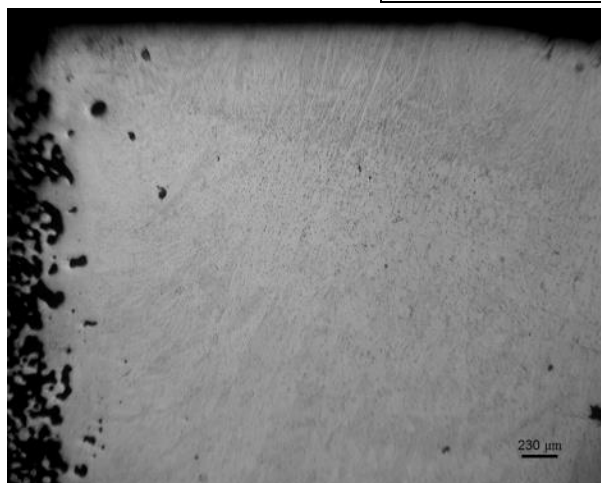
Focus Offset: 19 mA



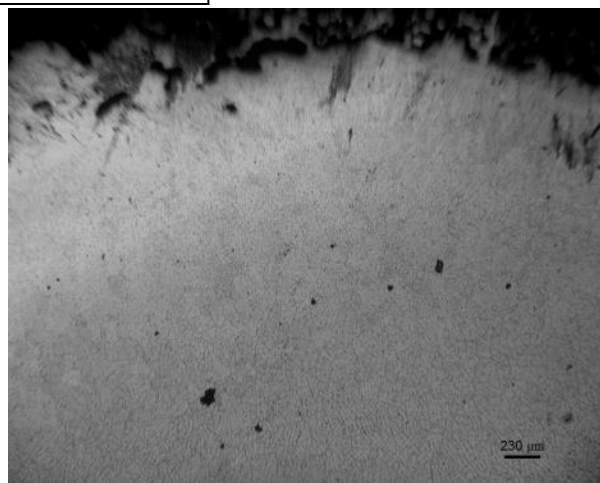
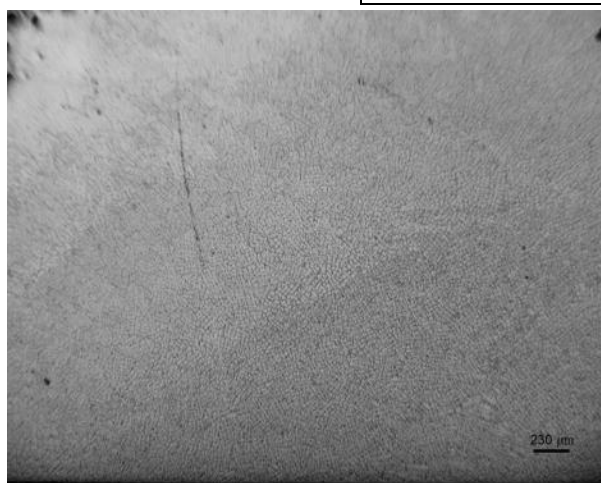
C.R. $\sim -125^{\circ}\text{C/s}$



Vertical micrographs



Horizontal micrographs

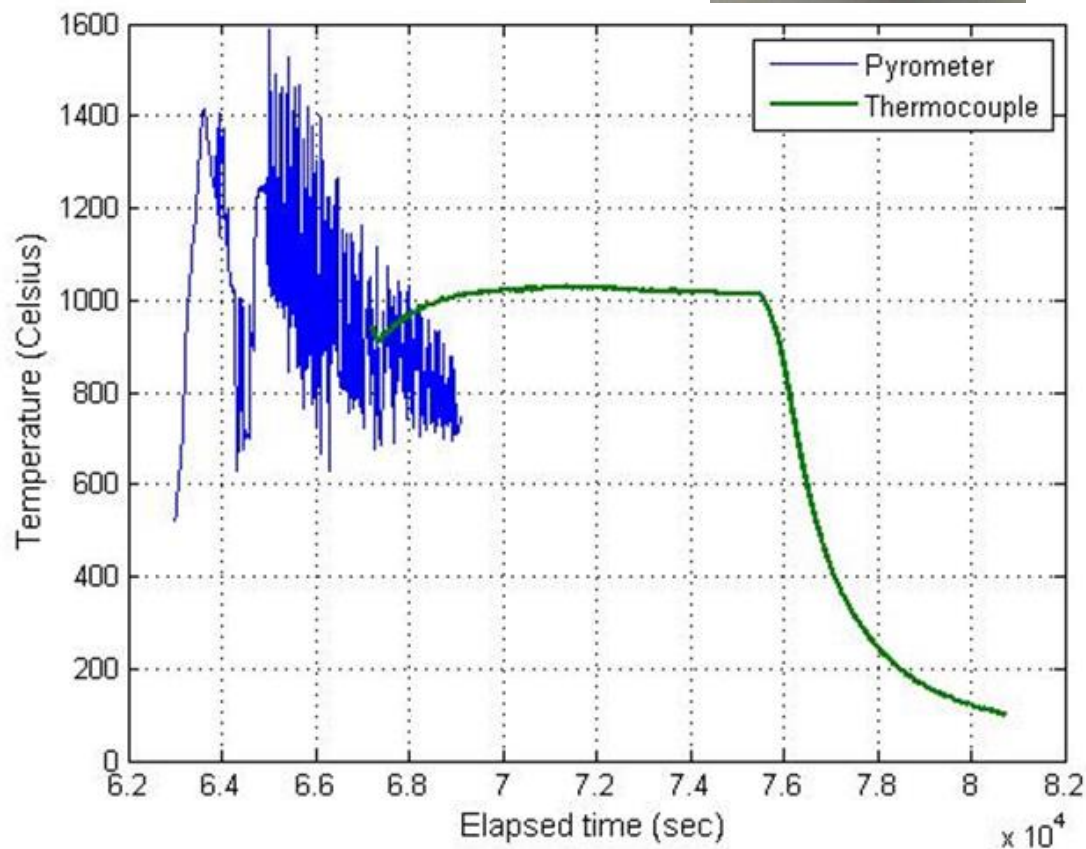
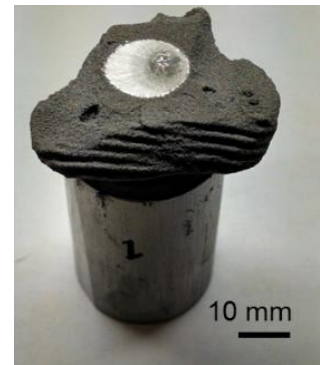


Date: 3/31/14 (1)

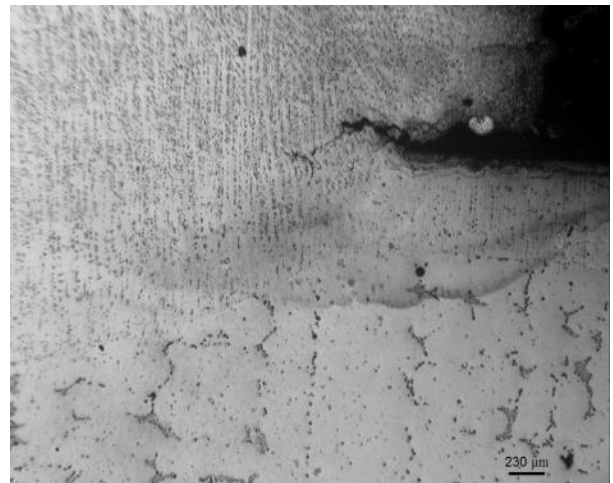
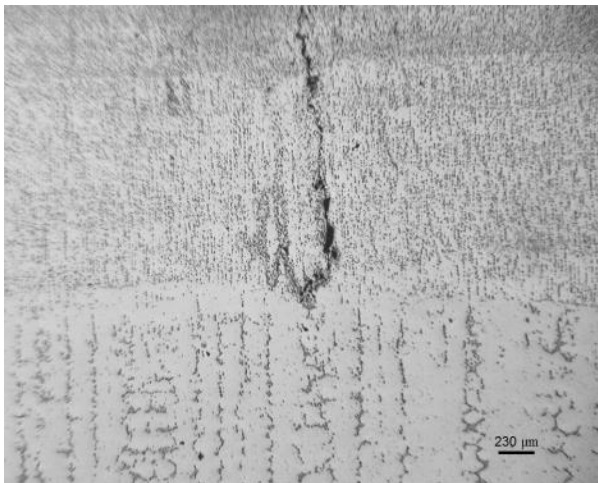
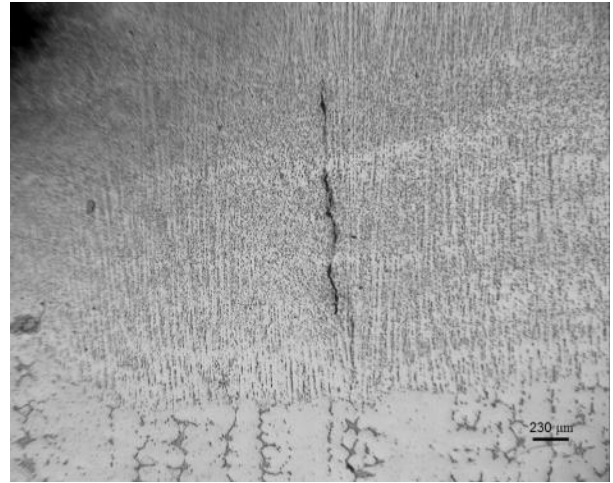
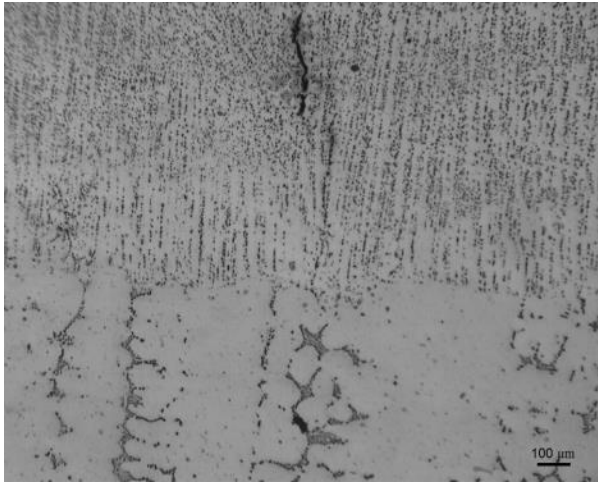
For this build, the start plate was changed to a single crystal N5 cylindrical start plate and preheat themes from previous builds on the same start plates (11/25/13) were utilized. The idea to utilize a single crystal start plate was conceived by the researchers to reduce cracking that may initiate from defected zones or grain boundaries within a non-single crystal start plate. Initially the build temperature was decreasing too rapidly, thus adjustments to the preheat theme were made to stabilize the temperature at a higher temperature. Such decrease in temperature caused arc trips.

Melt themes:

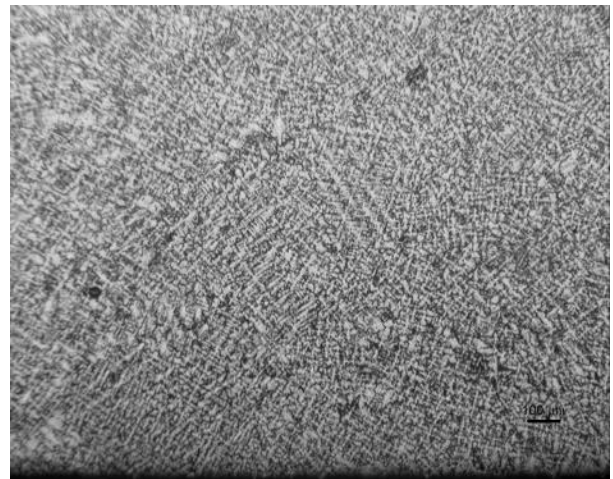
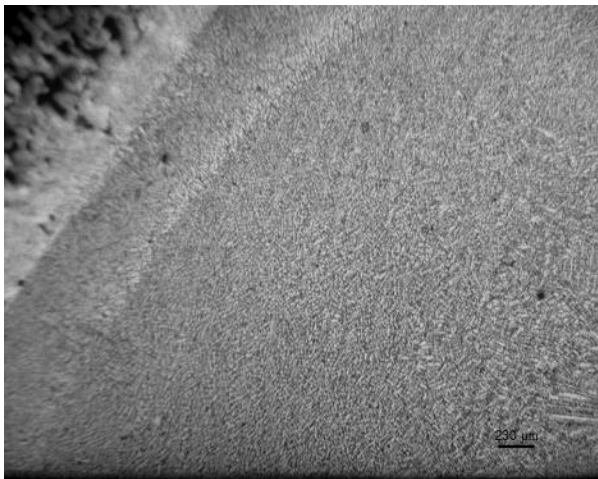
Current: 4, 4.3, 4mA
Scan Speed: 100mm/s
Focus Offset: 19 mA



Vertical micrographs



Horizontal micrographs



Date: 3/31/14 (2)

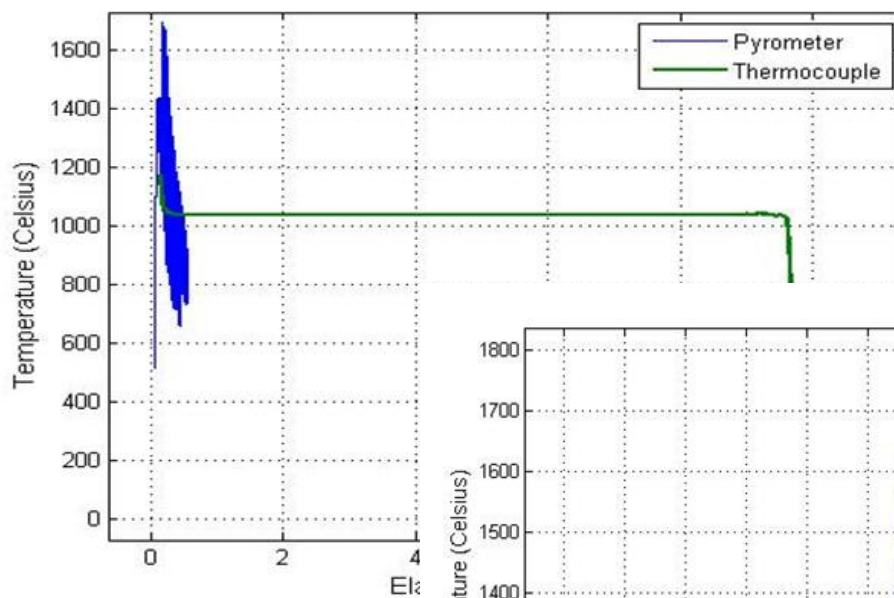
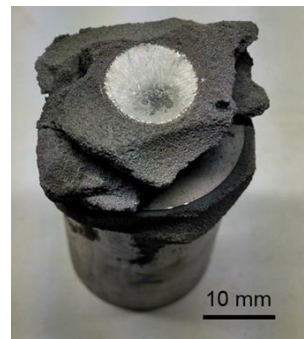
A single crystal N5 start plate was also used for this build. The previous experiment was repeated because the powder was initially cooling rapidly and it was difficult to control the temperature of the build. Repeating the experiment using a fixed preheat theme to stabilize the build temperature yielded good results. Few cracks were seen in the vertical micrographs and the cracks were also thinner than was observed in previous experiments. Cracks could not be differentiated from grain boundaries at low magnifications.

Melt themes:

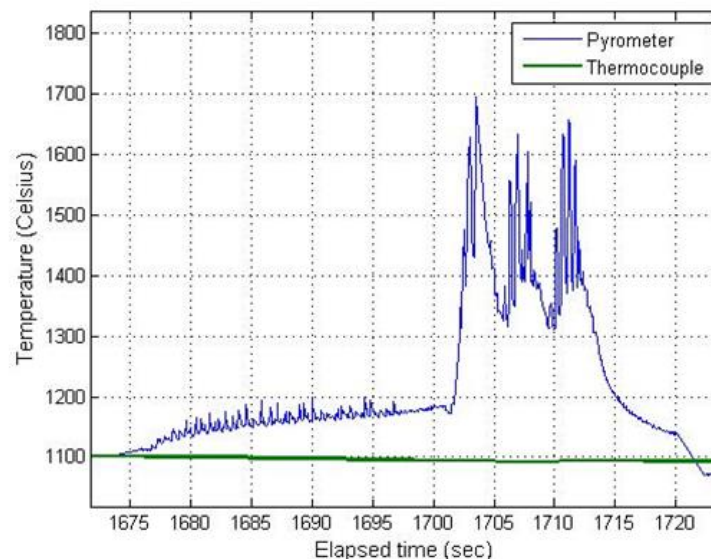
Current: 4, 4, 4mA

Scan Speed: 100, 125, and 150mm/s

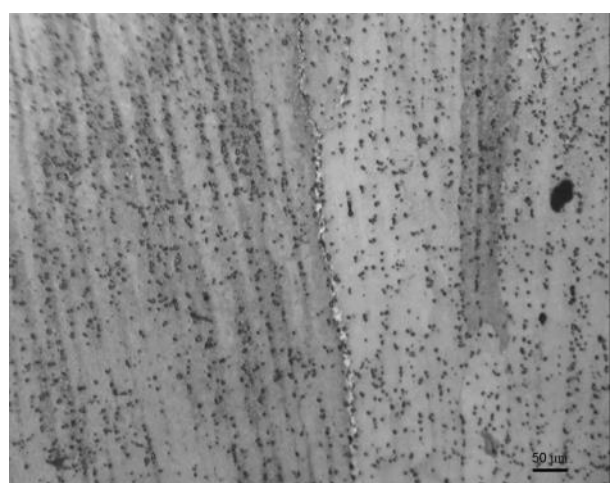
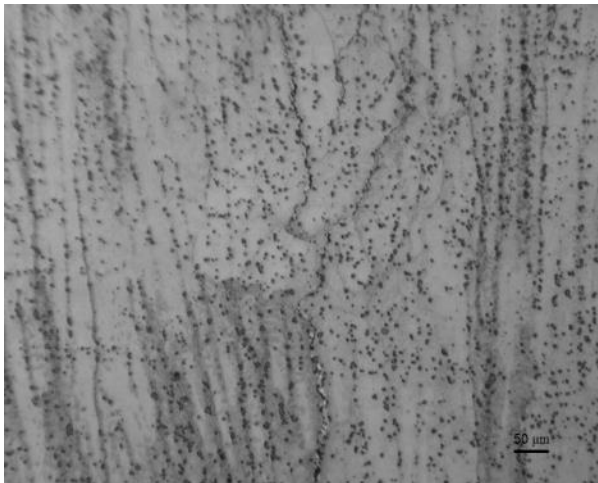
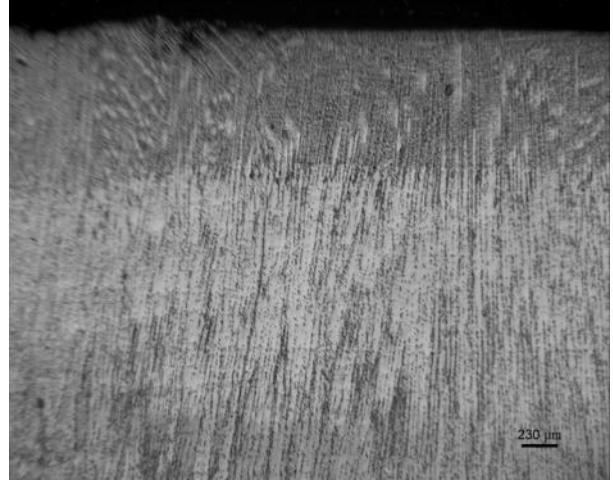
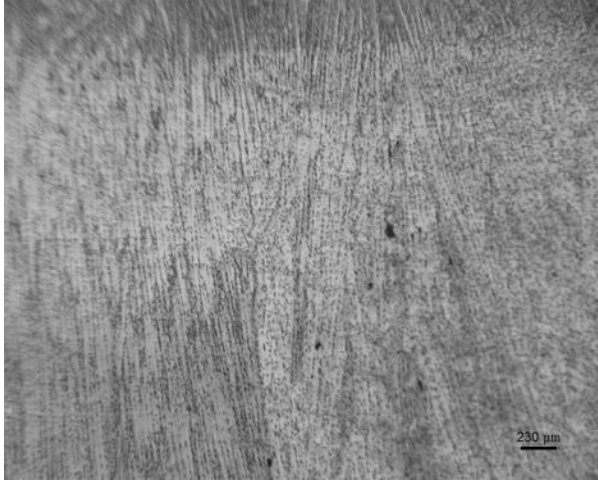
Focus Offset: 19 mA



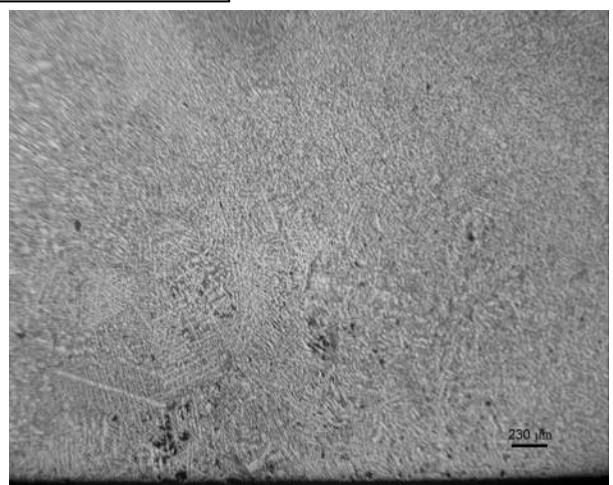
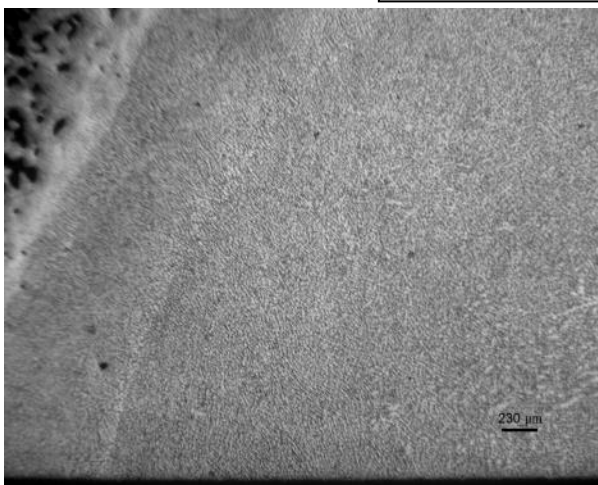
C.R. ~ -75° C/s



Vertical micrographs



Horizontal micrographs



Date: 3/31/14 (3)

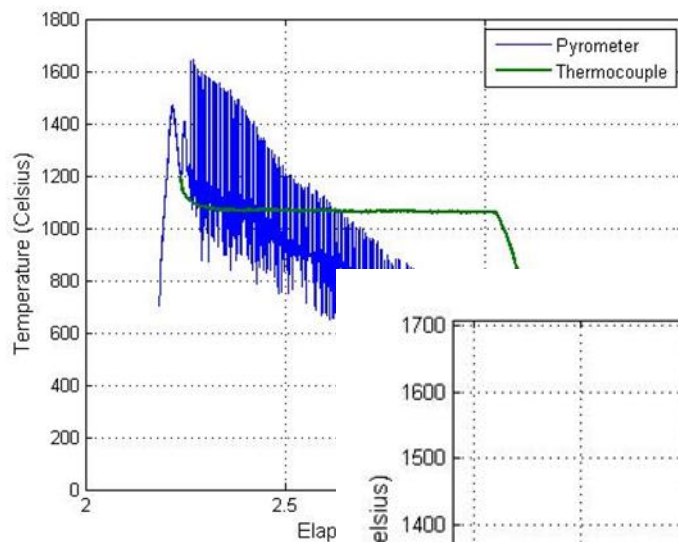
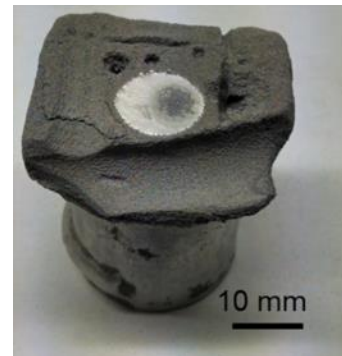
A single crystal N5 start plate was used for this build. A very large crack was observed after polishing the cross section. A crack that penetrated into the start plate was observed by the vertical micrograph. The build temperature was also higher than the previous experiments even though the same parameters were used. This phenomenon may have occurred due to a change in start plate dimension. The N5 cylinder used for this experiment was shorter than the previous two.

Melt themes:

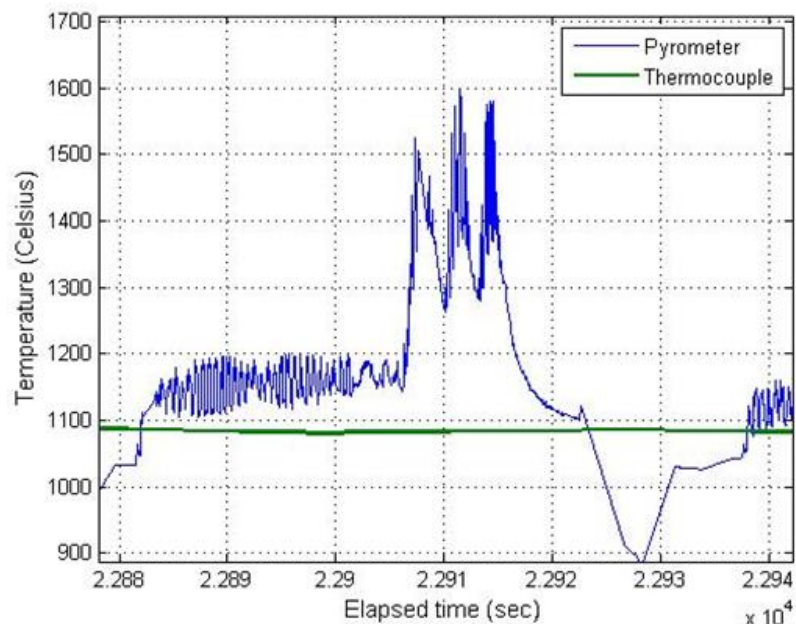
Current: 4, 4.2, 4.2mA

Scan Speed: 100, 125, and 150mm/s

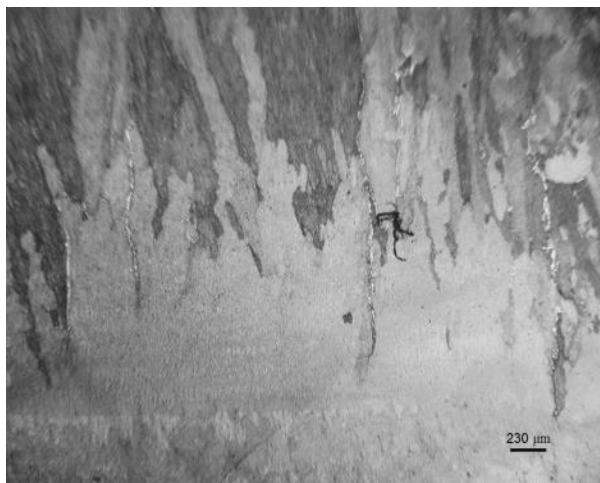
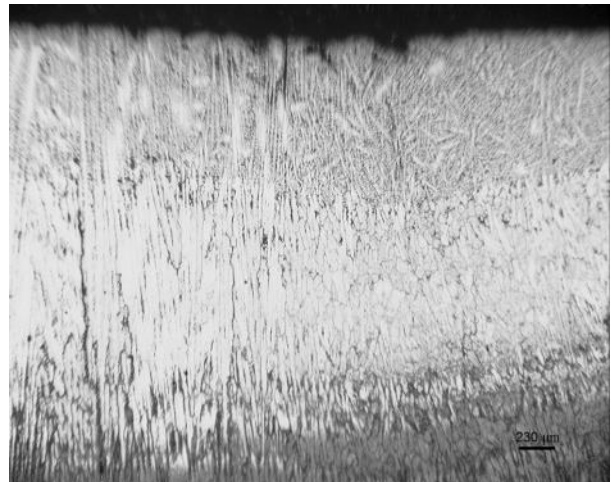
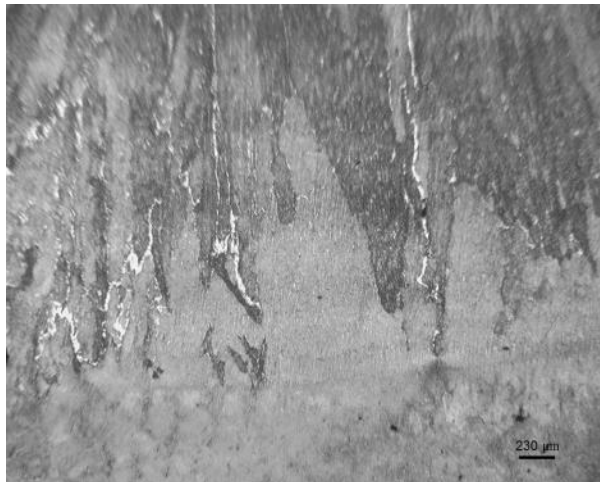
Focus Offset: 19 mA



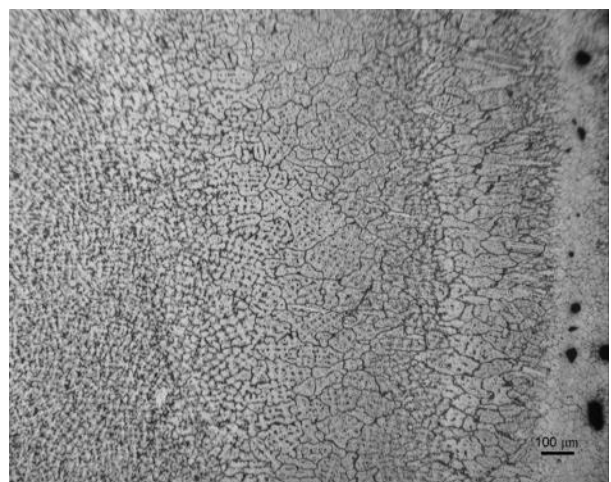
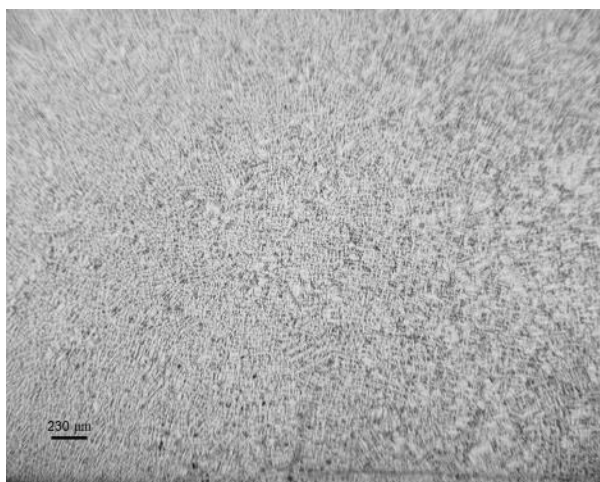
C.R. $\sim -183.3^{\circ}\text{C/s}$



Vertical micrographs



Horizontal micrographs



6.1 DISCUSSIONS

For all the experiments, at least one sample was prepared for metallography. The sample was removed from the start plate, mounted, polished, and micrographs were recorded using an optical microscope. The areas of interest were horizontal and vertical cross sections of the sample. The horizontal plane refers to the layer plane where the electron beam melts the 2D cross section of the build. The top surface of the sample was used for horizontal microscopy. The vertical plane was the Z-axis (height) plane of the build. For vertical pictures, the sample was cut in half from top to bottom and the samples were prepared for metallography. Since the metallography was recorded in only two planes (horizontal and vertical) of the sample, the micrographs may not represent the structure of the entire part. It is noteworthy to understand that cracks might change propagation direction in three dimensions. For example, if a vertical micrograph showed a crack that stops growing at specific points, then two assumptions are possible: 1) the crack stopped growing or 2) the crack grew in a different direction to the plane.

The multi-wavelength pyrometer allowed the researchers to observe the surface temperature throughout the fabrication process. The pyrometer displayed the temperature of the forming layer, permitting the modification of parameters on preheat themes or melting themes while building. On several of the experiments performed, the temperature of the forming layer during the preheat step or the melt step was useful to observe difference in cracking. If the temperature displayed by the pyrometer was not the desired temperature, proper modifications on the themes were performed to achieve the desired layer temperature. The pyrometer feedback on temperature permitted the improvement of system parameters for fabrication of NSAT parts. It is important to note that the micrographs of the samples with the best parameters achieved in this study showed a significant reduction in size and length of cracks in analyzed planes.

6.2 BEST PARAMETERS MODIFICATIONS

There were two major modifications done on the parameters that reduced the cracking on samples significantly, including 1) turning off the snake melting pattern and 2) performing

multiple melts on the same layer. Samples fabricated with these parameter modifications represented the parts containing the least amount and size of cracks when compared to previous samples. A solid cylinder fabricated with unidirectional scanning and multiple melts presented only one crack throughout the build. This sample was considered the best among all the experiments.

Disabling the snake parameter allowed the electron beam to melt the layer in a unidirectional manner. With the snake disabled, heat is distributed more evenly during the melt process than with the snake being enabled due to the unidirectionality of scanning (as discussed in chapter 3). An even distribution of heat during the melting process assisted the fabrication of NSAT parts with reduced cracking due to reduction in heat localization. The localized heat was theorized to produce an additional thermal stresses.

Fabricating using multiple melts with the EBM system can produce swelling and deformation of parts. When deformed, a part expands and deforms in all directions, making an uneven surface and, ending with a part different from the CAD model. Swelling and deformation of parts are caused by the accumulation of heat or overheating the same layer during the melting process. On EBM-fabricated Ti-6Al-4V parts, the grain dimension increase with multiple melts (Murr *et al*, 2009) and also help eliminate defects such as porosity (Medina, 2013).

An experiment was performed to build NSAT parts using multiple melts. Starting with two melts, the part did not present any swelling or deformation and the micrographs revealed reduction in cracking. Interestingly, a NSAT solid cylinder that was fabricated using four melts did not present any critical swelling or deformation. By measuring the diameter of the solid cylinder, it was noticed that the cylinder expanded slightly in the layer plane, but the fabrication process was very stable when building solid cylinders using multiple melts. The process did not involve any undesirable effects during the melting step such as powder explosions, formation of melt-balls, or powder fireworks. By re-melting the 2D cross section, the layer was accumulating heat and possibly melting the forming cracks. The thermal gradient between layers was less when compared to previous builds (shown by the experiment from 3/19/14). Upon

microstructural analysis, it was observed that the accumulation of heat during fabrication formed small carbides on the part. However, the multiple melt process presented parts with a significant reduction in cracking.

6.3 BEST PARAMETERS

One of the best experiments achieved that presented the most significant reduction in cracking was the experiment performed on 03/24/2014. The experiment consisted of fabricating a single solid cylinder of 10mm in diameter and 10mm in height on a Rene 125 start plate using three melt steps. The micrographs of this cylinder did not present visible cracks on the horizontal plane and only contained one visible thin crack on the vertical plane. The heating of the start plate was done in three steps to prevent powder explosions. To slowly increase the temperature, the current of the electron beam was set to 4mA. It was changed to 5mA when the thermocouple recorded $\sim 250^{\circ}\text{C}$. Then, the current was set to 7.5mA when the thermocouple recorded $\sim 900^{\circ}\text{C}$. The desired initial temperature of the start plate was set to 1100°C . The time to hold the desired temperature was 10min. This time was used to sufficiently sinter the powder underneath the start plate and also to stabilize the temperature of the start plate. The preheat area used was 38mm for the 40 by 40 by 10mm start plate. Table 6-1 describes the preheat theme parameters and Table 6-2 describes the melt-theme parameters.

Table 6-1 Preheat theme

Parameters	Preheat I	Preheat II
Liner order	15	15
Line offset	102	1.2
Hatch depth	0.14	0.14
Max beam current	10mA	40mA
Min beam current	4mA	35mA
Beam speed	2500mm/s	7000mm/s
Number of repetitions	20	8
Maximum number of repetitions	40	17
Number of repetitions	30	5

Table 6-2 Melt theme

Parameters	Melt I	Melt II	Melt III
Speed	100mm/s	100mm/s	100mm/s
Current	4mA	4.3mA	4mA
Max Current	4mA	4.3mA	4mA
Focus offset	19mA	19mA	19mA
Snake	FALSE	FALSE	FALSE
Liner order	1	1	1
Line offset	0.2mm	0.2	0.2
Randomized hatch	FALSE	FALSE	FALSE

6.4 POSSIBLE EXPERIMENTS

Additional experiments can be performed to attempt to reduce or eliminate cracks of NSAT parts. To avoid cracking during the fabrication process, a reduction in thermal gradient throughout the part was desired. Possible experiments might be conceived for methods to reduce the thermal gradient during the EBM fabrication process such as implementation of thermal blankets within the system. Thermal blankets can be attached to the hoppers and the build tank to attempt to reduce thermal gradients during fabrication. Implementing thermal blankets to hoppers would allow heating of the metal powder before the rake deposits a new layer onto the hot start plate. This would reduce the temperature difference between the metal powder and the hot start plate, thus potentially minimizing the cooling rate of the start plate. Thermal blankets can also be useful to maintain a constant build tank temperature during the fabrication process. As fabrication takes place, the build tank is lower by one layer thickness, or each time the electron beam finishes melting the 2D cross section. As the part increases in height, the temperature difference between the bottom and the top of the part also increases, thus a greater thermal gradient develops between the top and bottom of a part. If a thermal blanket is added to the build tank, the thermal gradient will be reduced, making the part less prone to cracking.

Another option is to modify the existing heat shield design in an effort to maintain an optimum heat environment for the fabricated parts and further reduce thermal gradients on the

building part due to the fabrication environment. The heat shield is positioned at the top of the build surface to act as an insulator to the build platform which helps conserve the heat generated by the electron beam when entering into the powder bed (Rodriguez, 2013). The heat loss on the forming layer is primarily due to conduction and radiation since EBM fabrication takes place in a vacuum environment. Heat is lost by conduction between the melt pool being in contact with the surrounding powder bed and the rest of the part that was already built. Heat is lost by radiation from the forming layer to walls of the heat shield and into the remaining components of the chamber. The heat shield was designed to be used with start plates of 150 by 150 by 10mm of cross sectional area. Since the 40 by 40 by 10mm start plates were used for parameter development purposes, thus the heat shield may not be efficient in maintaining the heat on the custom sized start plates utilized in this study. A new heat shield design can consist on a reduction of the bottom area of the heat shield to about the size of the start plate. The heat shield can be a rectangular prism positioned from the top of the chamber to the bottom of the start plate. This reduction in area might retain more of the heat during the fabrication process, thus, minimizing the heat loss through radiation and reducing the thermal gradient on the EBM-fabricated part.

An additional option was to implement post-processing treatments to fabricated parts such as hot isostatic pressing (HIP). HIP consists of applying high temperature and pressure to a sample within a vessel. The high pressure is provided by a gas; commonly an inert gas. In such conditions of high temperature and pressure, internal pores, or defects inside a solid part collapse and bond together by diffusion. Thus, HIP may be a possible solution to achieve more dense (by enclosing any prevalent cracking) parts with improved mechanical properties (Aktinson and Davies, 2000) when the cracks are small in size and do not extend to an outer surface. HIP has been performed on CM-681LC nickel-based superalloy tensile specimens fabricated with micro-cast by Wei *et al.* HIP produced refined and spherical carbides and eliminated micro-pores. This post-process may help NSAT parts contain reduced cracks while also improving its mechanical properties through closing of defects since the cracks on NSAT parts were internal.

CHAPTER 7 CONCLUSIONS

7.1 SUMMARY

A multi-wavelength pyrometer was installed in an Arcam S12 EBM system. The incorporation of the multi-wavelength pyrometer included radiation safety. A radiation shield was designed, fabricated, and installed to prevent radiation exposure to the system operator. The multi-wavelength pyrometer was utilized to analyze surface temperature profiles to develop fabrication parameters for NSAT, a crack prone nickel-based superalloy material. The NSAT metal powder was characterized and properties such as powder distribution, apparent density, percent density change, and flowability were obtained. These properties were compared to Ti-6Al-4V properties, since Ti-6Al-4V is a well-known developed material for fabrication on EBM systems.

Experiments for parameter development were designed and performed. Optical metallography was done on fabricated parts to observe microstructure and defects such as cracks. Micrographs were recorded to analyze the presence of cracking. Temperature data of each experiment recorded by the multi-wavelength pyrometer was graphed using MATLAB to analyze surface temperatures of the build and observe thermal phenomena such as temperature decay due to raking, melting temperature of the material, temperature decay after melting, and minimum and maximum temperatures during the preheat step. The multi-wavelength pyrometer enabled the improvement of system parameters for the fabrication of NSAT parts by continuously displaying the surface temperature of build and providing feedback on surface temperatures and cooling rates.

Two major modifications were found that produced a significant reduction in cracking which included disabling the snake pattern parameter and performing multiple melts. It was determined that unidirectional scanning reduced the thermal gradient between hatch lines and that the multiple melts reduced the thermal gradient of the overall part. The system parameters developed for fabrication of NSAT parts using the EBM process such as, starting temperature, beam speed, beam current, beam focus offset, line order, line offset, and the preheat themes,

significantly reduced the amount of cracking of the overall part when compared to initial fabricated parts.

7.2 RECOMMENDATIONS

The system's parameters develop in this study for fabrication of NSAT were developed and improved using feedback from a multi-wavelength pyrometer. Modifications performed helped achieved a significant reduction in crack density of NSAT solid parts fabricated in EBM system. However, to eliminate cracking of NSAT parts using the EBM system, further research must be done. Based on the results of this study, recommendations for experiments provided here can lead to a better understanding of the optimal thermal behavior needed to fabricate NSAT crack free parts. Recommendations include:

- Further explore the multiple melt parameters. Experiments should focus on reducing the thermal gradient on the entire parts. Attempting initial higher temperatures (1200°C or 1300°C), with different beam currents and beam speeds may lead to reduction in cracking.
- Spread the layer of powder on the top of the build faster. During the experiments performed on this study, the rake passed three times over the top surface of the build to spread the powder in a proper manner. By increasing the speed of the raking mechanism the time without the layer being heated by the electron beam reduces. This reduction in time may cause the cooling rate of the layer to minimize.
- Using thermal blankets on components inside the vacuum chamber such as heat shield, hoppers, and envelope. As explained in chapter five the use of thermal blankets can reduce the thermal gradient between the powder and the hot start plate as well as the thermal gradient between the surface layer and the bottom of the build. Reducing the thermal gradient through the entire part may reduce propagation of cracks.
- Design and fabricate a new heat shield for the small start plates. The heat shield used during the experiments performed was designed for maintaining the heat on larger start

plates. A small heat shield that maintains the heat more efficiently on the small start plates would reduce the radiation loss from the start plates, thus, reducing the thermal gradient between layers.

- Perform post-processing treatments such as HIPing. HIPing on fabricated NSAT parts may produce parts with improved density by bonding internal pores and enclosing any prevalent cracking.

REFERENCES

- Arcam, AB. *Arcam EBM user's manual*. Sweden, 2011.
- Askeland, Donald R. and Pradeep P. Phule. *The Science and Engineering of Materials*. Toronto: Thomson, 2006.
- ASTM Standard, B212-13. *Apparent Density of Free-Flowing Metal Powders Using the Hall Flowmeter Funnel*. West Conshohocken, PA: ASTM International, 2012. 2012. <www.astm.org>.
- ASTM Standard, B213-13. *Flow Rate of Metal Powders Using the Hall Flowmeter Funnel*. West Conshohocken, PA: ASTM International, 2013. <www.astm.org>.
- Atkinson, H.V. and S. Davies. "Fundamental Aspects of Hot Isostatic Pressing: An Overview." *Metallurgical and Materials Transactions A* (2000): 2981-3000.
- Boland, M.A. *USGS Science for a Changing world*. 2012. 25 06 2014. <<http://pubs.usgs.gov/fs/2012/3024/pdf/fs2012-3024.pdf>>.
- Bradley, Elihu F. *Superalloys a Technical Guide*. Metals Park: ASM International, 1988.
- Cengel, Yunus A. and Afshin J. Ghajar. *Heat and Mass Transfer Fundamentals and Applications*. The McGraw-Hill Companies, Inc., 2011.
- Cormier, Denis, Ola Harryson and Harvey West. "Characterization of H13 steel produced via electron beam melting." *Rapid Prototyping Journal* (2004): 35-41.
- Distefani, J. *Introduction to Titanium and Titanium Alloys, ASM Metals Handbook*. 1990.

- Ekrami, A., S. Moeinifar and A.H. Kokabi. "Effect of transient liquid phase diffusion bonding on microstructure and properties of a nickel base superalloy Rene 80." *Materials Science and Engineering A* (2006): 93.
- Felice, R.A. "The spectropyrometer- a Practical Multi-wavelength Pyrometer." *The 8th Symposium on Temperature: Its Measurements and Control in Science and Industry*. Macedonia: FAR Associates, 2002. 1-6.
- Felice, Ralph. *FAR Associates*. n.d. 16 04 2014. <<http://pyrometry.com/technology/how-spectropyrometer-technology-works/>>.
- Gibson, I., D.W. Rosen and B. Stucker. *Additive Manufacturing Technologies*. New York: Springer, 2010.
- Gonzalez, M.A., et al. "Microstructural Response to Heat Affected Zone Cracking of Prewelding Heat-treated Inconel 939 Superalloy." *SciVerse ScienceDirect* (2011): 1116.
- Harrison, Thomas R. *Radiation Pyrometry and Its Underlying Principles of Radiant Heat Transfer*. Jon Wiley and Sons, Inc, 1960.
- Hu, D, H Mei and R Kovacevic. *Improving Solid Freeform Fabricagton by Laser-based Additive Manufacturing*. Richardson, Texas: Reserach Center for Advanced Manufactiringm Southern Methodist University, 2002.
- Lippold, J.C. "An Investigation of Heat-Affected Zone Hot Cracking in Alloy 800." *Welding Research* (1983): 1.

- Medina, Francisco. *Reducing Metal Alloy Powder Costs for Use in Powder Bed Fusion Additive Manufacturing: Improving the Economics for Production*. PhD Dissertation. El Paso: Materials Science and Engineering, The University of Texas at El Paso, 2013.
- Mireles, Jorge. *Process Study and Control of Electron Beam Melting Technology Using Infrared Thermography*. Thesis. El Paso: PLC, 2013.
- Murr, L.E., et al. "Effect of Build Parameters and Build Geometries on Residual Microstructures and Mechanical Properties of Ti-6Al-4V Components Built by Electron Beam Melting (EBM)." 2009.
- . "Microstructures of Rene 142 nickel-based superalloy fabricated by electron beam melting." *Acta Materialia* (2013): 4289-4296.
- Office of research and sponsored projects. "Organized research center profile- W.M. Keck Center for 3D Innovation." Web. 9 Nov.2012. Available:
<http://orspprofile.utep.edu/profilesystem/editprofile.php?=1307&onlyview=1>
- Rodriguez, Emmanuel. *Development of a Thermal Imaging Feedback Control System in Electron Beam Melting*. Thesis. El Paso: ProQuest LLC, 2013.
- Ross, Earl W. and Kevin S. O'Hara. "Rene 142: High Strength, Oxidation Resistant DS Turbine." *The Minerals, Metals and Materials society* (1992): 257.
- Sclater, Neil and Nicholas P. Chironis. *Mechanisms and Mechanical Devices Sourcebook*. New York: McGraw-Hill Professional, 2006.

- Sexton, L., S. Lavin, G. Byrne, and A. Kennedy. "Laser cladding of aerospace materials." *Journal of Materials Processing Technology* 122, no. 1 (2002): 63-68.
- Shahsavari, H.A., A.H. Kokabi and S. Nategh. "Effect of preweld microstructure on HAZ liquation cracking of Rene 80 superalloy." *Materials Science and Technology* (2007): 1.
- Sidhu, R.K., O.A. Ojo and M.C. Chaturvedi. "Microstructural Respons of Directionally Solidified Rene 80 Superalloy to Gas-Tungsten Arc Welding." *The Minerals, Metals and Materials society and ASM International* (2008): 150.
- U.S. Environmental Protection Agency. 7 August 2012. 19 April 2014.
<http://www.epa.gov/rpdweb00/understand/health_effects.html>.
- Wang, Huei-Sen, et al. "Microstructure Evolution of Laser Repair Welded Rene 77 Nickel-Based Superalloy Cast." *Materials Transactions* (2011): 2197.
- Wei, Chao-Nan, Hui-Yun Bor and Li Chang. "Effect of Hot Isostatic Pressing on Microstructure and Mechanical Properties of CM-681LC Nickel-Base Superalloy Using Microcast." *Materials Transactions, Vol. 49, No.1* (2008): 193-201.
- Wholers, Terry and Tim Caffrey. *Wholers Report 2013*. Additive Manufacturing and 3D Printing State of the industry Annual Worldwide Progress Report. Fort Collins: Wholers Associates, 2013.
- Wohlers, Terry and Tim Caffrey. *Wohlers Report 2009*. Additive Manufacturing and 3D Printing State of the industry Annual Worldwide Progress Report. Fort Collins: Wohlers Associates, 2009.

Wicker, R. "Additive Manufacturing: A Nexus for Transformation." Solid Freeform Fabrication Symposium. August, 2012. Austin, TX

Griffith, M.L., *et.al.* "Understanding thermal behavior in the LENS process." Materials and Design, 20.2-3 (1999): 107-113.

Office of research and sponsored projects. "Organized research center profile- W.M. Keck Center for 3D Innovation." Web. 9 Nov.2012. Available:

<http://orspprofile.utep.edu/profilesystem/editprofile.php?=1307&onlyview=1>

Appendix

The following table presents all the experiments performed during this project. The table shows the date, the custom experiments, parameters used, and summary of results explaining details of the experiment performed. The main parameters presented in the table are current, beam speed and focus offset (F.O.). The temperature showed in each experiment is the temperature reached when the first layer of powder was deposit. Other parameters are presented when modified such as maximum current (MC), minimum current (MinC), average current (AV), beam speed (SP), line order (LO), number of repetitions (Rep), contour offset (CO), and scan area.

			Parameters				
Date	Experiment	Start plate	Part No.	Current	Speed	F.O	Summary of results
10/8/2013	Nine cubes	Stainless steel	Pre-heat: 700 °C				Start plate deformation and over-melting of the material due to high current. Powder not sintered correctly. Initial temperature of substrates must be higher
			1	19	500	21	
			2	19	500	17	
			3	19	500	19	
			4	17	500	21	
			5	17	500	17	
			6	17	500	19	
			7	21	550	19	
			8	21	450	19	
			9	21	500	19	
10/12/2013	Nine cubes	Stainless steel	Pre-heat: 950 °C				Start plate deformation and over-melting of the material due to high current. Proper powder sintering improved from last build
			1	19	500	21	
			2	19	500	17	
			3	19	500	19	
			4	17	500	21	
			5	17	500	17	
			6	17	500	19	
			7	21	550	19	
			8	21	450	19	
			9	21	500	19	
10/13/2013	Stainless steel mask	Stainless steel	Pre-heat: 1050 °C				Over-melting of the material due to high current. Over sintering of powder during melting. Difficult to setup the system with the stainless steel mask.
			1	19	500	21	
			2	19	500	17	
			3	19	500	19	
			4	17	500	21	
			5	17	500	17	
			6	17	500	19	
			7	21	550	19	
			8	21	450	19	
			9	21	500	19	
10/15/2013	Stainless steel mask	Stainless steel	Pre-heat: 1050 °C				Build finished. Formation of balls occurred during melting due to surface
	with thin rectangular		1	19	500	21	
			2	19	500	17	

	ar blocks						tension. Over sintering of powder during melting. Difficult to setup the system with the stainless steel mask. The stainless steel mask did not present improvement on the parts.
			3	19	500	19	
			4	17	500	21	
			5	17	500	17	
			6	17	500	19	
			7	21	550	19	
			8	21	450	19	
			9	21	500	19	
10/17/2013	Nine cubes	Rene 125	Pre-heat: 950 °C				Start plate did not present any deformation. Geometry of cubes defined by melting of beam. Arc-trips occurred during the melting process causing layer of powder to be removed. Build cancelled due to powder explosions. Initial temperature of the start plate must be higher to avoid powder explosions
			1	8	500	21	
			2	8	500	17	
			3	8	500	19	
			4	6	500	21	
			5	6	500	17	
			6	6	500	19	
			7	10	550	19	
			8	10	450	19	
			9	10	500	19	
10/18/2013 (1)	Nine cubes	Rene 125	Pre-heat: 1000°C FO: 360mA MC: 10ma				Larger sintering underneath start plate. Arc-trips occurred during melting of part 7. To avoid arc-trips initial temperature of substrate must be higher. Build process stop due to arc-trips.
			1	8	500	21	
			2	8	500	17	
			3	8	500	19	
			4	6	500	21	
			5	6	500	17	
			6	6	500	19	
			7	10	550	19	
			8	10	450	19	
			9	10	500	19	
10/18/2013	Nine	Rene	Pre-heat: 1120°C FO: 360mA MC:				Improved

(2)	cubes	125	10ma				sintering under the start plate. Indentation formation on parts due to high currents during melting. Arc-trips removed powder bed causing the build plate to move. Build stop due to movement of start plate.
			1	8	500	21	
			2	8	500	17	
			3	8	500	19	
			4	6	500	21	
			5	6	500	17	
			6	6	500	19	
			7	10	550	19	
			8	10	450	19	
			9	10	500	19	
10/21/2013 (1)	Nine cubes	Rene 125	Pre-heat: 1150°C SP: 8000mm/s				Arc-trips removed powder bed causing the build plate to move. Manually moved rake to refill vat. Build cancelled when start plate moved after four layers.
			1	8	500	21	
			2	8	500	17	
			3	8	500	19	
			4	6	500	21	
			5	6	500	17	
			6	6	500	19	
			7	10	550	19	
			8	10	450	19	
			9	10	500	19	
10/21/2013 (2)	Nine cubes	Rene 125	Pre-heat: 1135°C MC: 12ma				Five layers completed. Arc-trips occurring during melt of part four. Arc-trips removed powder bed causing the build to fail.
			Pre-heat I and II				
			Pre-heat I: current 6mA				
			Pre-heat II: current 7mA				
			1	8	500	21	
			2	8	500	17	
			3	8	500	19	
			4	6	500	21	
			5	6	500	17	
			6	6	500	19	
			7	10	550	19	
			8	10	450	19	
			9	10	500	19	
10/21/2013 (3)	Nine cubes	Rene 125	Pre-heat: 1100°C FO: 50mA				
			1	8	500	21	
			2	8	500	17	

			3	8	500	19	and seven were warped. Powder sintering around parts difficult to remove. Improved melt on parts four and five. Decreasing the speed reduce porosity.
			4	5	150	21	
			5	5	200	17	
			6	6	500	19	
			7	10	550	19	
			8	10	450	19	
			9	4	250	19	
10/23/2013	Nine cubes	Rene 125	Pre-heat: 1115°C FO: 150mA SP: 5000mm/s				Build finished. Sintering around parts difficult to remove. Small dents on top surface. Cubes are defined but presented visible cracks.
			Scan area: 35mm Max current: 12mA				
			1	8	200	21	
			2	8	200	19	
			3	8	200	17	
			4	5	225	21	
			5	5	225	19	
			6	6	225	17	
			7	10	150	21	
			8	10	150	19	
			9	4	150	17	
10/24/2013	Nine cubes	Rene 125	Pre-heat: 1030 °C FO: 200mA SP: 5000mm/s				Sintering around parts difficult to remove. The specimens showed reduce porosity and cracking in horizontal micrographs. Cracking is observed in vertical micrographs of all parts. Scanning speed plays an important role in controlling cracking. Attempt Lower scanning speed
			Scan area: 34mm Max current: 12mA				
			1	4.5	200	21	
			2	4.25	200	19	
			3	4.25	200	17	
			4	4.75	225	21	
			5	4.5	225	19	
			6	4.25	225	17	
			7	4.75	175	21	
			8	4.75	175	19	
			9	4.5	175	17	
10/31/2013	Nine cubes	Rene 125	Pre-heat: 1030 °C FO: 150mA SP: 5000mm/s				Build finished. No explosions of

			Scan area: 35mm Max current: 12mA				powder. Sinter around parts more loose when compared to previous builds. Small dents on top surface of all parts.
			Melting sequence: 5, 1, 3,9,7,2,6,8,4				
			1	4.25	75	21	
			2	4.25	75	19	
			3	4.25	75	17	
			4	4.25	100	21	
			5	4.25	100	19	
			6	4.25	100	17	
			7	4.25	125	21	
			8	4.25	125	19	
			9	4.25	125	17	
11/7/2013	Nine cubes	Rene 125	Pre-heat: 1030 °C FO: 150mA SP: 5000mm/s				Build finished. No explosions of powder. Sinter around parts more loose when compared to previous builds. Small dents on top surface of all parts. Part 5 presented with a reduction on cracks. For this experiment Helium purge was delay and it did not present any effect on reduction on cracking.
			Scan area: 35mm Max current: 12mA				
			Melting sequence: 5, 1, 3,9,7,2,6,8,4				
			1	4	80	20	
			2	4.25	100	19	
			3	4	80	19	
			4	4.25	100	19	
			5	4.25	100	19	
			6	4.25	100	19	
			7	4.25	90	20	
			8	4.25	100	19	
			9	4.25	90	19	
11/13/2013	Nine cubes	Rene 125	Pre-heat: 1030 °C FO: 150mA SP: 5000mm/s				Process failed. Over-melting of powder. During the process it was observed uneven raking and surface balling during the melting.
			Extra Pre-heat after melt sequence				
			No. of scans: 100 MC: 5mA AC: 2.5mA				
			Melting sequence: 1, 3, 9,7,2,6,8,4,5				
			1	4.25	100	19	
			2	4.25	100	19	
			3	4.25	100	19	
			4	4.25	100	19	
			5	4.25	100	19	
			6	4.25	100	19	

			7	4.25	100	19	Powder bed cooling rapidly causing power explosions. Build failed.
			8	4.25	100	19	
			9	4.25	100	19	
11/14/2013	Nine cubes	Rene 125	Pre-heat: 1030 °C FO: 150mA SP:5000mm/s				
			Two Extra Pre-heats after melt sequence				
			I: No. of scans: 50 MC: 1mA AC: 0.75mA				
			II: No. of scans: 15 MC: 0.5mA AC: 0.25mA				
			Melting sequence: 1, 3, 9,7,2,6,8,4,5				
			1	4.25	100	19	
			2	4.25	100	19	
			3	4.25	100	19	
			4	4.25	100	19	
			5	4.25	100	19	
			6	4.25	100	19	
			7	4.25	100	19	
			8	4.25	100	19	
			9	4.25	100	19	
11/15/2013	Nine cubes	Rene 125	Pre-heat: 1030 °C FO: 150mA SP: 5000mm/s				Build failed. Overheating of the powder bed causing uneven melt surface.
			Four Extra Pre-heats after melt sequence				
			I: No. of scans: 25 MC: 2mA AC: 1.75mA				
			II: No. of scans: 25 MC: 2mA AC: 1.25mA				
			III: No. of scans: 25 MC: 2mA AC: 1.5mA				
			IV: No. of scans: 25 MC: 2mA AC: 0.75mA				
			Melting sequence: 1, 3, 9,7,2,6,8,4,5				
			1	4.25	100	19	
			2	4.25	100	19	
			3	4.25	100	19	
			4	4.25	100	19	
			5	4.25	100	19	
			6	4.25	100	19	
			7	4.25	100	19	
			8	4.25	100	19	

			9	4.25	100	19	
11/18/2013	Nine cubes	Rene 125	Pre-heat: 1030 °C FO: 150mA SP: 5000mm/s				Build stopped at 75%. Initially powder bed cooling rapidly. This experiment presented even raking, melting and contours. Part 5 has a smoother surface compared to all other parts. Swelling of contours for part 5. Extra melt sequences helped reduce cooling rates.
			16 Extra Pre-heats on part 5				
			Ramping down current in steps of .25mA				
			Melting sequence: 1, 3, 9,7,2,6,8,4,5				
			1	4.25	100	19	
			2	4.25	100	19	
			3	4.25	100	19	
			4	4.25	100	19	
			5	4.25	100	19	
			6	4.25	100	19	
			7	4.25	100	19	
			8	4.25	100	19	
			9	4.25	100	19	
11/25/2013	7 Parts of Single solid cylinder	N5 single Crystal	Pre-heat: 1150 °C SP: 1500mm/s				Build finished. Process stable ~1000°C. Vertical cross sections presented cracks.
			AC: 7.5mA FO: 140mA Rep: 20				
			Scan area: 16.5mm MC: 12mA				
			1	4	10	19	
1/7/2014	Nine cubes	Rene 125	Pre-heat: 1100°C				Start plate cooling rapidly. Cracks originated from the start plate. Sintering of powder difficult to remove.
			Three melts per block				
			1	4, 2, 1	100,250,450	19	
			2	4, 2, 1	100,200,300	19	
			3	4, 2, 1	100,150,200	19	
			4	4, 1.5, 1	100,200,300	19	
			5	4, 1.5,1	100,200,300	19	
			6	4, 1.5,1	100,150,200	19	
			7	4, 3, 2	100,250,450	19	
			8	4, 3, 2	100,200,300	19	
			9	4, 3, 2	100,150,200	19	
1/9/2014	Electron beam passes (NSAT Start plates)	Rene 125	Pre-heat: 1100°C				Build failed. Powder over sinter around the part. Start plate cooling rapidly.
			Three melts				
				1	4, 2, 1	100,250,450	19
1/14/2014	Solid cylinders	Rene 125	Pre-heat: 1100°C				

			Three melts on some parts				since the start plate was cooling rapidly. Uneven surface. Contours swelling and uneven melting. Large heat affected zone in start plate. In all parts cracks propagated to the top surface.
			1	4	100	19	
			2	4, 2.25, 1.25	100,250,350	19	
			3	4, 2.25, 1.25	100,350,300	19	
			4	4, 1.5,1	100,250,350	19	
			5	4, 1.5,1	100,250,350	19	
1/21/2014	Hollow cylinders	Rene 125	Pre-heat: 1100°C				Build failed. Arc-trips occurred during the first three layers
			Three melts on some parts				
			1	4	100	19	
			2	4, 2.25, 1.25	100,250,350	19	
			3	4, 2.25, 1.25	100,350,300	19	
			4	4, 1.5,1	100,250,350	19	
			5	4, 1.5,1	100,200,300	19	
1/22/2014	Hollow cylinders	Rene 125	Pre-heat: 1100°C				Increased pre-heat current to prevent arc-trips. Cracks started at the start plate.
			Three melts on some parts				
			1	4	100	19	
			2	4, 2.25, 1.25	100,250,350	19	
			3	4, 2.25, 1.25	100,350,300	19	
			4	4, 1.5,1	100,250,350	19	
			5	4, 1.5,1	100,200,300	19	
1/24/2014	Hollow cylinder	Rene 125	Pre-heat: 1100°C				Build failed due to arc-trips
			1	4	100	19	
1/25/2014	Hollow cylinder	Rene 125	Pre-heat: 1100°C				Build failed due to "no heater" warning
			1	4	100	20	
1/27/2014	Hollow cylinder	Rene 125	Pre-heat: 1100°C				Warning fixed by adjusting pre-heat size. Build failed due to start plate movement.
			1	4	100	21	
1/28/2014	Hollow	Rene	Pre-heat: 1100°C				Completed 10

	cylinder	125					layers. Hollow cylinder showed increase in porosity. Build failed
			1	2	20	20	
2/3/2014	Hollow cylinders	Rene 125	Pre-heat: 1100°C				
			Three melts on some parts				
			1	4	100	19	Contours used for first melt. Powder sintering difficult to remove around parts. Pre-heat must be modify using lower currents
			2	4, 2.25, 1.25	100,250,350	19	
			3	4, 2.25, 1.25	100,350,300	19	
			4	4, 1.5,1	100,250,350	19	
			5	4, 1.5,1	100,200,300	19	
2/4/2014 (1)	Hollow cylinders	Rene 125	Pre-heat: 1100°C				
			Three melts on some parts				Pre-heat modified. Build failed due to movement of start plate.
			1	4	100	19	
			2	4, 2.25, 1.25	100,250,350	19	
			3	4, 2.25, 1.25	100,350,300	19	
			4	4, 1.5,1	100,250,350	19	
			5	4, 1.5,1	100,200,300	19	
2/4/2014 (2)	Hollow cylinders	Rene 125	Pre-heat: 1100°C				Pre-heat modified. Build failed due to movement of start plate.
			Three melts on some parts				
			1	4	100	19	
			2	4, 2.25, 1.25	100,250,350	19	
			3	4, 2.25, 1.25	100,350,300	19	
			4	4, 1.5,1	100,250,350	19	
			5	4, 1.5,1	100,200,300	19	
2/5/2014 (1)	Hollow cylinders	Rene 125	Pre-heat: 1100°C				Pre-heat modified. Build failed due to movement of start plate. Powder under the start plate did not
			Three melts on some parts				
			1	4	100	19	
			2	4, 2.25, 1.25	100,250,350	19	
			3	4, 2.25,	100,350,300	19	

				1.25			sinter properly
			4	4, 1.5,1	100,250,350	19	
			5	4, 1.5,1	100,200,300	19	
2/5/2014 (2)	Hollow cylinders	Rene 125	Pre-heat: 1100°C				Pre-heat modified. Powder under the start plate properly sintered. Build failed due to uneven raking. Balling defects formed on the edges of the rings.
			Three melts on some parts				
			1	4	100	19	
			2	4, 2.25, 1.25	100,250,350	19	
			3	4, 2.25, 1.25	100,350,300	19	
			4	4, 1.5,1	100,250,350	19	
			5	4, 1.5,1	100,200,300	19	
2/7/2014	Hollow cylinders	Rene 125	Pre-heat: 1100°C				Sinter powder improved from previous builds. Build finished. Used contours to melt. Cracks presented in horizontal and vertical planes.
			Pre-heat I: MinC: 4mA MC: 6mA Rep: 5				
			Pre-heat II: MinC: 4mA MC: 5mA Rep: 15				
			Three melts on some parts				
			1	4	100	19	
			2	4, 2.25, 1.25	100,250,350	19	
			3	4, 2.25, 1.25	100,350,300	19	
			4	4, 1.5,1	100,250,350	19	
			5	4, 1.5,1	100,200,300	19	
2/10/2014	Hollow cylinders	Rene 125	Pre-heat: 1100°C				Contour offset (CO) modified on parts to observe effect on cracking. Part 1 CO: 1mm. Part 2 CO: 0.1mm. Part 3 CO: 0.2mm. Part 4 CO: 0.2mm. Part 5 CO: 0.2mm. Part 1 presented the least amount of cracking in the horizontal plane.
			Pre-heat I: MinC: 4mA MC: 6mA Rep: 5				
			Pre-heat II: MinC: 4mA MC: 5mA Rep: 15				
			Three melts on some parts				
			1	3	100	19	
			2	3, 2.25, 1.25	100,250,350	19	
			3	3, 2.25, 1.25	100,250,350	19	
			4	3, 2.25, 1.25	100,250,350	25	
			5	3, 2.25, 1.25	100,250,350	15	

2/11/2014	Hollow cylinders	Rene 125	Pre-heat: 1100°C				Contour offset (CO) modified on parts to observe effect on cracking. Part 1 CO: 0.1mm. Part 2 CO: 1mm. Part 3 CO: 0.1mm. Part 4 CO: 0.2mm. Part 5 CO: 1mm. Part 1 had less cracking compare to other parts.
			Pre-heat I: MinC: 4mA MC: 6mA Rep: 5				
			Pre-heat II: MinC: 4mA MC: 5mA Rep: 15				
			Three melts on some parts				
			1	3.7	150	19	
			2	2.6	20	19	
			3	2.6	100	19	
			4	2.6	150	19	
			5	3	20	19	
2/13/2014	Electron beam passes	Rene 125	Pre-heat: 1100°C				Build failed due to Arcam tool path generator. Layers were skipped in the vertical direction.
			1	2	300	19	
			2	2	100	19	
			3	2	20	19	
			4	3	500	19	
			5	3	300	19	
			6	3	100	19	
			7	3	20	19	
			8	4	300	19	
			9	4	100	19	
			10	4	20	19	
2/14/2014	Electron beam passes (NSAT start plate)	Rene 125	Pre-heat: 1100°C				Build failed due to excessive powder explosions causing start plate to move.
			1	3.7	178	19	
2/17/2014	Electron beam passes (NSAT start plate)	Rene 125	Pre-heat: 1100°C				Build finished. Powder explosions though the whole build. Cracking evident on to surface. This start plate can be used for electron beam passes.
			1	3.7	178	19	
2/18/2014	Electron beam	Rene 125	Pre-heat: 1100°C				Build failed due to delamination of

	passes (NSAT start plate)		1	3.7	178	19	the part from start plate. Initial explosions during first layers caused poor bonding with start plate.
2/19/2014	Electron beam passes (NSAT start plate)	Rene 125	Pre-heat: 1100°C				Build completed. Improved surface finish from previous builds. Crack is evident on top surface.
			1	3.7	178	19	
2/21/2014	Electron beam passes	NSAT	Pre-heat: 1100°C				Build finished. Beam passes with high current (4mA) are visible.
			1	2	300	19	
			2	2	100	19	
			3	2	20	19	
			4	3	500	19	
			5	3	300	19	
			6	3	100	19	
			7	3	20	19	
			8	4	300	19	
			9	4	100	19	
			10	4	20	19	
2/24/2014	Hollow cylinders	Rene 125	Pre-heat: 1100°C				Multi-spot on part 5 was causing powder explosions. Melt did not improve from previous experiments
			Melting of parts using single contours				
			Part 5 melting using multi-spot				
			1	4	20	19	
			2	3	20	19	
			3	4	100	19	
			4	3	100	19	
			5	3	20	19	
2/25/2014	Solid cylinders	Rene 125	Pre-heat: 1100°C				Part 5 was melted using line order of 10. Build finished. Part 5 presented the least amount of cracking when compared to the others.
			Parts 1 to 4 hollow cylinders using single contours				
			Part 5 solid cylinder using hatch				
			1	4	20	19	
			2	3	20	19	
			3	4	100	19	
			4	3	100	19	

			5	4	100	19	
2/27/2014	Solid cylinders	Rene 125	Pre-heat: 1100°C MC: 7mA MinC: 6mA				Build stopped due to poor thermocouple contact.
			Parts 1 to 4 hollow cylinders using single contours				
			Part 5 solid cylinder using hatch				
			1	4	20	19	
			2	3	20	19	
			3	4	100	19	
			4	3	100	19	
			5	4	100	19	
2/28/2014	Solid cylinders	Rene 125	Pre-heat: 1100°C MC: 7mA MinC: 6mA				Build stopped due to thermocouple not working properly. Replacement of thermocouple needed.
			Parts 1 to 4 hollow cylinders using single contours				
			Part 5 solid cylinder using hatch				
			1	4	20	19	
			2	3	20	19	
			3	4	100	19	
			4	3	100	19	
			5	4	100	19	
3/3/2014	Solid cylinders	Rene 125	Pre-heat: 1100°C MC: 7mA MinC: 5.5mA				Build finished. Line order (LO) was implemented to the parts. Part 1 LO: 5. Part 2 LO: 10. Part 3 LO: 10. Part 4 LO: 15. Part 5 LO: 1. Part 5 presented the least amount of cracking in the horizontal plane.
			Parts 1 to 4 hollow cylinders using single contours				
			Part 5 solid cylinder using hatch				
			1	4	100	19	
			2	3	100	19	
			3	4	100	19	
			4	4	100	19	
			5	4	100	19	
3/4/2014	Solid Cylinders	Rene 125	Pre-heat: 1100°C MC: 7mA MinC: 5.5mA				Build finished. Line order (LO) was implemented to the parts. Part 1 LO: 2. Part 2 LO: 11. Part 3 LO: 10. Part 4 LO: 1. Part 5 LO: 1. Part 5 presented the least amount of cracking in the
			Parts 1 to 4 hollow cylinders using single contours				
			Part 5 solid cylinder using hatch				
			1	4	100	19	
			2	2.5	100	19	
			3	3.5	100	19	
			4	4	200	19	
			5	4	100	19	

							horizontal plane. Part 5 showed a reduction in cracking but an increase in porosity.
3/6/2014	Solid Cylinders	Rene 125	Pre-heat: 1000°C				Build finished. Line order (LO) was implemented to the parts. Part 1 LO: 5. Part 2 LO: 10. Part 3 LO: 10. Part 4 LO: 1. Part 5 LO: 1. Solid cylinders shifted to the left on the z-axis. This is commonly seen in Ti-6Al-4V during high temperature processes. Part 5 increase in porosity.
			Pre-heat I: MC: 8.7mA Pre-heat II: MC: 9.2mA				
			Parts 1 to 4 hollow cylinders using single contours				
			Part 5 solid cylinder using hatch				
			1	4	100	19	
			2	2.5	100	19	
			3	3.5	100	19	
			4	4	200	19	
			5	4	100	19	
3/12/2014	Solid cylinders	Rene 125	Pre-heat: 1000°C				Build finished. Line order (LO) was implemented to the parts. Part 1 LO: 1. Part 2 LO: 10. Part 3 LO: 10. Part 4 LO: 15. Part 5 LO: 1. Top surface not smooth on parts. Part 5 increase in porosity from previous build.
			Pre-heat I: MC: 8.7mA Pre-heat II: MC: 9.2mA				
			Parts 1 to 4 hollow cylinders using single contours				
			Part 5 solid cylinder using hatch				
			1	4	80	19	
			2	3	100	19	
			3	4	100	19	
			4	3.5	100	19	
			5	4	100	19	
3/13/2014	Solid cylinders	Rene 125	Pre-heat: 1000°C				Build finished. Line order (LO) was implemented to the parts. Part 1 LO: 1. Part 2 LO: 1. Part 3 LO: 10. Part 4 LO: 10. Part 5 LO: 1. Top surface improved
			Pre-heat I: MC: 8.7mA Pre-heat II: MC: 9.2mA				
			Parts 1 to 4 hollow cylinders using single contours				
			Part 5 solid cylinder using hatch				
			1	2.5	100	19	
			2	2	100	19	

			3	2.5	100	19	from previous build.
			4	4	100	19	
			5	4	100	19	
3/13/2014	Solid cylinders	Rene 125	Pre-heat: 1000°C				Build finished. Line order (LO) was implemented to the parts. Part 1 LO: 1. Part 2 LO: 1. Part 3 LO: 10. Part 4 LO: 10. Part 5 LO: 1. Top surface improved from previous build. Part 5 presented smaller cracks compared to previous build.
			Pre-heat I: MC: 8.7mA Pre-heat II: MC: 9.2mA				
			Parts 1 to 4 hollow cylinders using single contours				
			Part 5 solid cylinder using hatch				
			1	3.5	100	19	
			2	2	100	19	
			3	3.5	100	19	
			4	4	100	19	
			5	4	100	19	
3/14/2014	Electron beam passes (NSAT start plate)	Rene 125	Pre-heat: 1100°C				Build finished. Start plate built to repeat beam passes experiment.
			1	3.7	30	19	
3/15/2014	Solid cylinders	Rene 125	Pre-heat: 1000°C				Build finished. Line order (LO) was implemented to the parts. Part 1 LO: 5. Part 2 LO: 1. Part 3 LO: 10. Part 4 LO: 15. Part 5 LO: 1. Part 2 detached from start plate.
			Pre-heat I: MC: 6mA Pre-heat II: MC: 10mA				
			Parts 1 to 4 hollow cylinders using single contours				
			Part 5 solid cylinder using hatch				
			1	4	100	19	
			2	10	100	19	
			3	4	100	19	
			4	4	100	19	
			5	4	100	19	
3/17/2014 (1)	Electron beam passes	NSAT	Pre-heat: 1100°C				Build failed due to a warning "start level error".
			1	25	600	19	
			2	25	800	19	
			3	25	100	19	
			4	25	500	19	
			5	25	700	19	
			6	25	900	19	

			7	25	1,100	19	Build finished. Beam passes are visible.
			8	25	400	19	
			9	25	600	19	
			10	25	800	19	
3/17/2014 (2)	Electron beam passes	NSAT	Pre-heat: 1100°C				
			1	25	600	19	
			2	25	800	19	
			3	25	100	19	
			4	25	500	19	
			5	25	700	19	
			6	25	900	19	
			7	25	1,100	19	
			8	25	400	19	
			9	25	600	19	
			10	25	800	19	
3/19/2014 (1)	Solid cylinder	Rene 125	Pre-heat: 1100°C				Build finished. Part presented reduction in cracking compared to part 5 from previous build.
			Pre-heat I: MC: 10 MinC: 8 SP: 3000 Rep: 15				
			Pre-heat II: MC: 40 MinC35 SP: 7500 Rep: 6				
			1	4	100	19	
3/19/2014 (2)	Solid cylinder	Rene 125	Pre-heat: 1100°C				Build finished. Two melts were applied. Part 5 presented a significant reduction in cracking compared to previous build.
			Pre-heat I: MC: 11 MinC: 9 SP: 3000 Rep: 20				
			Pre-heat II: MC: 45 MinC40 SP: 6800 Rep: 10				
			1	4, 4.3	100,100	19	
3/20/2014	Solid cylinder	Rene 125	Pre-heat: 1100°C				Build failed due to movement of the start plate.
			Pre-heat I: MC: 11 MinC: 9 SP: 3000 Rep: 20				
			Pre-heat II: MC: 45 MinC40 SP: 6800 Rep: 10				
			1	4, 4.5	100,100	19	
3/21/2014	Solid cylinder	Rene 125	Pre-heat: 1100°C				Build failed due to movement of the start plate.
			Pre-heat I: MC: 11 MinC: 9 SP: 3000 Rep: 20				

			Pre-heat II: MC: 45 MinC40 SP: 6800 Rep: 10				Build failed due to movement of the start plate.
			1	4, 4.5	100,100	19	
3/22/2014	Solid cylinder	Rene 125	Pre-heat: 1100°C				
			Pre-heat I: MC: 11 MinC: 9 SP: 3000 Rep: 20				
			Pre-heat II: MC: 45 MinC40 SP: 6800 Rep: 10				Build finished. Three melts were applied. No visible cracks on the horizontal plane. Only one crack was visible on the vertical plane. The microstructure presented formation of carbides.
			1	4, 4.5	100,100	19	
3/24/2014	Solid cylinder	Rene 125	Pre-heat: 1100°C				
			Pre-heat I: MC: 10 MinC: 4 SP: 2500 Rep: 20				
			Pre-heat II: MC: 40 MinC: 35 SP: 7000 Rep: 8				Build finished. Three melts were applied. Randomized hatch was used in this experiment. No visible cracks on the horizontal plane. The part presented cracks on the vertical plane.
			1	4, 4.3,4	100,100,100	19	
3/26/2014	Solid cylinder	Rene 125	Pre-heat: 1100°C				
			Pre-heat I: MC: 11 MinC: 9 SP: 3000 Rep: 20				
			Pre-heat II: MC: 45 MinC40 SP: 6800 Rep: 10				Build finished. Three melts were applied. Unidirectional hatch was used in this experiment. No visible cracks on the horizontal plane. Few cracks were observed in the vertical plane.
			1	4.3, 4, 3.5	100,100,100	19	
3/27/2014 (1)	Solid cylinder	Rene 125	Pre-heat: 1100°C				
			Pre-heat I: MC: 11 MinC: 9 SP: 3000 Rep: 20				
			Pre-heat II: MC: 45 MinC40 SP: 6800 Rep: 10				
			1	3.5, 4, 4.3	100,100,100	19	

3/27/2014 (2)	Solid cylinder	Rene 125	Pre-heat: 1100°C					Build finished. Four melts were applied. No visible cracks on the horizontal plane. Very Few and small cracks were observed in the vertical plane. Formation of carbides increase compared to previous builds.
			Pre-heat I: MC: 11 MinC: 9 SP: 3000 Rep: 20					
			Pre-heat II: MC: 45 MinC40 SP: 6800 Rep: 10					
			1	4, 4.3,4,4	100,100,100,100	19		
3/28/2014	Solid cylinder	Rene 125	Pre-heat: 1100°C					Build finished. Three melts were applied. No visible cracks on the horizontal plane. Very Few and small cracks were observed in the vertical plane.
			Pre-heat I: MC: 11 MinC: 9 SP: 3000 Rep: 20					
			Pre-heat II: MC: 45 MinC40 SP: 6800 Rep: 10					
			1	4.3, 4, 3.5	100,100,100	19		
3/29/2014	Solid cylinder	Rene 125	Pre-heat: 1100°C					Build failed due to movement of the start plate.
			Pre-heat I: MC: 11 MinC: 9 SP: 3000 Rep: 20					
			Pre-heat II: MC: 45 MinC40 SP: 6800 Rep: 10					
			1	4.3, 4, 3.5	100,100,100	19		
3/30/2014	Solid cylinder	Rene 125	Pre-heat: 1100°C					Build failed due to movement of the start plate.
			Pre-heat I: MC: 11 MinC: 9 SP: 3000 Rep: 20					
			Pre-heat II: MC: 45 MinC40 SP: 6800 Rep: 10					
			1	4.3, 4, 3.5	100,100,100	19		
3/31/2014	Solid cylinder	Rene 125	Pre-heat: 1100°C					Build failed due to movement of the start plate.
			Pre-heat I: MC: 11 MinC:9 SP:3000 Rep:20					
			Pre-heat II: MC: 45 MinC40 SP: 6800 Rep: 10					
			1	4.3, 4, 3.5	10,010,010	19		

			3.5				
3/31/2014 (1)	Solid cylinder	N5 start plate	Pre-heat: 1100°C				Build finished. Three melts were applied. No visible cracks on the horizontal plane. Very Few and small cracks were observed in the vertical plane.
			Pre-heat I: MC: 11 MinC: 9 SP: 3000 Rep:20				
			Pre-heat II: MC: 45 MinC40 SP: 6800 Rep:10				
			1	4, 4.3,4	100,100,100	19	
3/31/2014 (2)	Solid cylinder	N5 start plate	Pre-heat: 1100°C				Build finished. Three melts were applied. No visible cracks on the horizontal plane. Very Few and small cracks were observed in the vertical plane.
			Pre-heat I: MC: 11 MinC: 9 SP: 3000 Rep:20				
			Pre-heat II: MC: 45 MinC40 SP: 6800 Rep:10				
			1	4, 4.3,4	100,100,100	19	
3/31/2014 (3)	Solid cylinder	N5 start plate	Pre-heat: 1100°C				Build finished. Three melts were applied. No visible cracks on the horizontal plane. Very Few and small cracks were observed in the vertical plane.
			Pre-heat I: MC: 11 MinC:9 SP:3000 Rep:20				
			Pre-heat II: MC: 45 MinC40 SP: 6800 Rep: 10				
			1	4, 4.2, 4.2	100,125,150	19	

CURRICULUM VITA

Jonathan Minjares was born on July 21, 1989 in Cd. Juarez, Chihuahua, Mexico. He completed his high school studies at the Preparatoria El Chamizal graduating in 2007. In August 2007, Jonathan enrolled at the University of Texas at El Paso (UTEP) and was awarded the Jimmy and Yolanda Janacek scholarship. Jonathan gained access to teaching experience through the physics department starting in 2009 until 2012 working as a teacher assistant. He gave weekly workshops to students to facilitate the learning process of physics' principles. He graduated in May 2012 with a degree in Mechanical Engineering. In August 2012, Jonathan began his graduate studies to pursue a Master's of Science in Mechanical Engineering. He started working at the Lockheed Martin Lab at UTEP where he researched and documented instrumentation and equipment to demonstrate concepts of engineering for educational purposes. In January 2013, Jonathan joined the W.M. Keck Center for 3D Innovation (Keck Center) as a research assistant. He completed various projects focusing on additive manufacturing of metals. The research Jonathan performed to complete his thesis continued at the Keck Center focusing on electron beam melting technology, an additive manufacturing process used to fabricate metal parts.

Permanent address: 1509 Ruth Deerman PL
El Paso, TX 79912

This thesis was typed by Jonathan Minjares